^{138}La-^{138}Ce systematics in terrestrial samples and chondrites

Inaugural-Dissertation

zur

Erlangung des Doktorgrades

der Mathematisch-Naturwissenschaftlichen Fakultät

der Universität zu Köln

vorgelegt von

Christiane Schnabel

aus Wagna

Köln, 2019

Gutachter: Prof. Dr. Carsten Münker
PD. Dr. Erik Strub
Tag der mündlichen Prüfung: 16.01.2020

Table of content

Abstract

The long-lived ^{138}La-^{138}Ce decay system (half-life 1.02 x 10^{11} a) is a potentially useful tool to study the behavior of the light rare earth elements (LREE) and to unravel information about the timing of geological processes and about the interaction of geological reservoirs on Earth. In earth sciences, the ^{138}La-^{138}Ce geochronometer can therefore complement information from the more popular long-lived ^{147}Sm-^{143}Nd and ^{176}Lu-^{176}Hf isotope systems.

This thesis presents a new analytical protocol for the application of the ^{138}La-^{138}Ce geochronometer. An efficient three-step ion-chromatography procedure allows to separate La and Ce in rock matrices from other rare earth elements (REE) and from interfering Ba. Additionally, an analytical protocol was developed to measure Ce isotope compositions and La and Ce concentrations by MC-ICP-MS. For the first time, all stable Ce isotopes (^{136}Ce, ^{138}Ce, ^{140}Ce and ^{142}Ce) were measured simultaneously by employing a 10^{10} Ω amplifier for the most abundant isotope ^{140}Ce. Because the traditionally used JMC-304 Ce reference material is not commercially available anymore, a new reference material was prepared from AMES laboratory Ce metal (Cologne-AMES). In order to compare the new material with the previously reported isotopic composition of AMES material prepared at Mainz (Mainz-AMES), Cologne-AMES and JMC-304 were measured relative to each other in one analytical session. Additionally, for La and Ce concentration measurements by MC-ICP-MS, an isotope tracer enriched in ^{138}La and ^{142}Ce was prepared and calibrated against high purity AMES metals. The new protocols were applied to determine the variations of Ce isotope compositions and La and Ce concentrations of geochemical reference materials: BCR-1, BCR-2, BHVO-2, JR-1, JA-2, JB-1b, JB-3, JG-1, JR-1, AGV-1 and one in-house La Palma basalt standard (LP1).

Subsequently, the protocols were used to determine the important CHUR reference parameter (chondritic uniform reservoir) for the ^{138}La-^{138}Ce isotope system, which is defined by the present-day chondritic ^{138}La/^{136}Ce and ^{138}Ce/^{136}Ce values. This parameter is still poorly determined for the ^{138}La-^{138}Ce decay system but highly significant, once age-corrected initial Ce isotope ratios are calculated for older samples or for the determination of the Ce-Nd mantle array. Therefore, La and Ce concentration as well as Ce isotope measurements were performed combined with ^{147}Sm-^{143}Nd measurements from the same aliquots for 22 different meteorites including carbonaceous chondrites (CM, CK, CV and CO), ordinary chondrites (H, L and LL), and enstatite chondrites (EL and EH). After a detailed data evaluation of previous studies by Bellot et al. (2015) and Willig and Stracke (2019), the recommended chondritic ^{138}Ce/^{136}Ce mean value is 1.33686±3 (2 s.e., n=18) and ^{138}La/^{136}Ce mean value is 0.1868±40 (2 s.e., n=33).

Due to the ongoing debate, which group and petrological type of chondrites reflect the building blocks of the Earth ^{138}La/^{136}Ce and ^{138}Ce/^{136}Ce mean values of carbonaceous and non-

carbonaceous chondrites are determined. The recommended carbonaceous chondritic $^{138}Ce/^{136}Ce$ mean value is 1.33684±2 (2 s.e., n=10) and and $^{138}La/^{136}Ce$ mean value is 0.1946±43 (2 s.e., n=14). The non-carbonaceous chondritic $^{138}Ce/^{136}Ce$ mean value is 1.33689±4 (2 s.e., n=17) $^{138}La/^{136}Ce$ mean value is 0.1823±46 (2 s.e., n=17)

The application of the ^{138}La-^{138}Ce isotope system in combination with the ^{147}Sm-^{143}Nd isotope system is used to define the Ce-Nd mantle array comprising of mid-ocean ridge basalts (MORBs) and oceanic island basalts (OIBs). The chondritic $^{138}Ce/^{136}Ce$ mean value shows no overlap within uncertainties with the Ce-Nd mantle array. In contrast, the non-carbonaceous chondritic $^{138}Ce/^{136}Ce$ mean value intersects within uncertainties the Ce-Nd mantle array.

In the last part of this thesis, ^{138}La-^{138}Ce measurements were performed on Archean mafic and felsic rocks from the Barberton Greenstone Belt and the Ancient Gneiss Complex from South Africa and the Itsaq Gneiss Complex from southwest Greenland, which belong to the oldest rocks on Earth (between 3.8 and 3.2 Ga). Undisturbed samples define a $\varepsilon^{143}Nd(t)$-$\varepsilon^{138}Ce(t)$ correlation trend and intersect with the non-carbonaceous chondritic ^{138}La-^{138}Ce reference value in contrast to the chondritic and carbonaceous chondritic ^{138}La-^{138}Ce reference values. Consequently, the data show that for the ^{138}La-^{138}Ce system the bulk silicate Earth (BSE) is best described with a non-carbonaceous chondrite composition.

Kurzzusammenfassung

Das langlebigen ^{138}La-^{138}Ce Zerfallssystem (Halbwertszeit 1.02 x 10^{11} a) kann verwendet werden, um das Verhalten der leichten Seltenerdelemente (LREE) zu untersuchen und Informationen über den Zeitablauf geologischer Prozesse zu erhalten. Des Weiteren kann das ^{138}La-^{138}Ce Zerfallssystem ergänzende Informationen zu den etablierten ^{147}Sm-^{143}Nd und ^{176}Lu-^{176}Hf Isotopensystemen liefern.

Zunächst wurde für die Anwendung des ^{138}La-^{136}Ce- Geochronometers das neu entwickelte analytische Protokoll beschrieben. Ein effizientes drei-stufiges Ionenchromatographieverfahren wurde entwickelt, um La und Ce von anderen Seltenerdelementen (REE) und Ba zu trennen. Zusätzlich wurde ein analytisches Protokoll entwickelt, um die Ce-Isotopenzusammensetzungen und La- und Ce-Konzentrationen mit MC-ICP-MS zu bestimmen. Erstmals wurden alle stabilen Ce-Isotope (^{136}Ce, ^{138}Ce, ^{140}Ce und ^{142}Ce) gleichzeitig gemessen, indem ein 10^{10} Ohm-Verstärker für das am häufigsten vorkommende Isotop ^{140}Ce verwendet wurde. Da das früher verwendete Referenzmaterial JMC-304 kommerziell nicht mehr erhältlich ist, wurde ein neues Referenzmaterial aus Ce-Metall (Cologne-AMES) hergestellt. Um den neuen Referenzstandard mit dem in der Literatur verwendeten Referenzstandard Mainz-AMES zu vergleichen, wurden die drei Referenzmaterialen innerhalb einer Messserie relativ zueinander gemessen. Für die La- und Ce-Konzentrationsmessungen mit MC-ICP-MS wurde ein mit ^{138}La und ^{142}Ce angereicherter Isotopentracer hergestellt. Das zuvor entwickelte Protokoll wurde für die Bestimmung der Ce-Isotopien und La- und Ce-Konzentrationen von geochemischen Referenzmaterialien verwendet: BCR-1, BCR-2, BHVO-2, JR-1, JA-2, JB-1b, JB-3, JG-1, JR-1, AGV-1 und ein laboreigener Standard (La-Palma Standard (LP 1)).

Zusätzlich wurde das zuvor entwickelte analytische Protokoll für die Bestimmung des wichtigen Referenzparameters CHUR (chondritic uniform reservoir, einheitlich chondritisches Reservoir) angewendet, das durch die heutigen ^{138}La/^{136}Ce- und ^{138}Ce/^{136}Ce-Werte von undifferenzierten Meteoriten definiert ist. Dieser Parameter ist für das ^{138}La-^{138}Ce-System derzeit nur ungenau bestimmt, jedoch von essentieller Bedeutung, wenn alterskorrigierte Ce-Isotopenverhältnisse für ältere Proben oder eine Ce-Nd Mantelentwicklungslinie bestimmt werden soll. Aus diesem Grund wurden La- und Ce-Konzentrationsmessungen und Ce-Isotopenmessungen mit Sm-Nd-Daten aus den gleichen Aliquoten für 22 verschiedene Chondrite bestimmt: kohlige Chondrite (CM, CK, CV und CO), gewöhnliche Chondrite (H, L und LL) und Enstatit Chondrite (EL und EH). Nach einer detaillierten Datenauswertung früherer Studien von Bellot et al. (2015) und Willig und Stracke (2019) wurde der chondritische ^{138}Ce/^{136}Ce Wert = 1.33686±3 (2 s.e., n=18) und chondritische ^{138}La/^{136}Ce Wert 0.1868±40 (2. s.e, n=33) bestimmt.

Aufgrund der aktuellen Debatte, welche Gruppe und petrologische Art von Chondriten die Bausteine der Erde widerspiegeln, wurden die $^{138}Ce/^{136}Ce$-Mittelwerte und $^{138}La/^{136}Ce$-Mittelwerte aus kohligen und nicht-kohlichen Chondriten berechnet. Der empfohlene $^{138}Ce/^{136}Ce$-Mittelwert beträgt 1.33689±4 (2 s.e., n=17) und der $^{138}La/^{136}Ce$-Mittelwert beträgt 0.1946±43 (2 s.e., n=14) für kohlige Chondriten. Der empfohlene $^{138}Ce/^{136}Ce$-Mittelwert beträgt 1.33684±2 (2 s.e., n=17) und der $^{138}La/^{136}Ce$-Mittelwert beträgt 0.1823±46 (2 s.e., n=17) für nicht-kohlige Chondriten.

Die Kombination von ^{138}La-^{138}Ce mit dem ^{147}Sm-^{143}Nd Zerfallssystem wird benutzt um aus mittelozeanischen Rückenbasalte (MORBs) und ozeanischen Inselbasalte (OIBs) eine Ce-Nd-Mantelentwicklungslinie zu definieren. Der in dieser Arbeit bestimmte chondritischen $^{138}Ce/^{136}Ce$-Mittelwert zeigt innerhalb der statistischen Unsicherheiten keine Überschneidung mit der Ce-Nd-Mantelentwicklungslinie. Der $^{138}Ce/^{136}Ce$-Mittelwert für kohlige Chondrite schneidet jedoch innerhalb der statistischen Unsicherheiten die Ce-Nd-Mantelentwicklungslinie.

In Kapitel 4 wurde das ^{138}La-^{138}Ce Geochronometer auf archaische mafische und felsische Proben aus dem Barberton Greenstone Belt und dem Ancient Gneiss Complex aus Südafrika und dem Itsaq Gneiss Complex aus Südwestgrönland angewendet, die zu den ältersten Proben (3.8-3.2 Ga) der Erde gehören. Proben, die nur wenig Alteration zeigen, definieren einen Ce-Nd-Korrelationstrend und dieser Korrelationstrend schneidet sich innerhalb des Messfehlers mit dem ^{138}Ce-^{136}Ce Mittelwert aus nicht-kohligen Chondriten. Der chondritische ^{138}Ce-^{136}Ce-Mittelwert oder der ^{138}Ce-^{136}Ce-Mittelwert aus nicht-kohligen Chondriten schneidet sich im Gegensatz dazu nicht mit dem Ce-Nd Korrelationstrend. Diese Ergebnisse deuten darauf hin, dass die Bausteine der Erde durch einen ^{138}La-^{138}Ce-Wert aus nicht-kohligen Chondriten gekennzeichnet sind.

Chapter 1

Introduction

1.1. The origin of the elements

This thesis focuses on the development of an analytical protocol (separation technique and measurement procedure) for the ^{138}La-^{138}Ce isotope system and the following application of the ^{138}La-^{138}Ce isotope systems on chondrites and terrestrial samples. The following part of the introduction provides the scientific background for the origin of the elements to understand how the involved elements Lanthanum and Cerium were produced and to explain the elemental abundances of these two elements.

1.2. Aim of this study and overview of the chapters

In modern earth sciences, radioactive decay systems are an essential tool to unravel absolute age information of geological processes and the interaction of geological reservoirs on Earth. In the 1980s, the ^{138}La-^{138}Ce isotope system (half-life 1.02 x 10^{11} a) was first introduced by Tanaka and Masuda (1982). This system is based on the branched decay from ^{138}La to ^{138}Ce through β^- and ^{138}Ba through electron capture. The ^{138}La-^{138}Ce isotope system has been used rarely because of analytical difficulties. Ce isotope analyses are challenging because of the low abundances of ^{136}Ce (0.185 %) and ^{138}Ce (0.251 %) relative to ^{140}Ce (88.45 %) and ^{142}Ce (11.11 %). Additionally, there are strong isobaric interferences from ^{142}Nd on ^{142}Ce and ^{138}Ba on ^{138}Ce. Other studies only measured ^{136}Ce, ^{138}Ce and ^{142}Ce and could perform Ce isotope measurements by thermal ionization mass spectrometry (TIMS) with large uncertainties (e.g. up to 0.4 ε^{138}Ce, Bellot et al. (2015)). The use of different reference materials in older studies (JMC-304) and recent studies (Mainz-AMES) makes a comparison between literature data difficult.

The chondritic uniform reservoir (CHUR) reference value is an important reference parameter because the value allows direct comparison of terrestrial data to that expected in a chondritic Earth. This important reference parameter has been determined from few meteorite samples with large uncertainties by three older studies (Shimizu et al. (1984), Makashima and Masuda (1993), Makashima and Masuda (1993)). Recent studies (Bellot et al. (2015) and Willig and Stracke (2019)) show inconsistent ^{138}La-^{138}Ce CHUR values.

A combination of ^{138}La-^{136}Ce with the more popular ^{147}Sm-^{143}Nd and ^{176}Lu-^{176}Hf isotope systems for older samples is rarely applied (Shimizu et al. (1988)) because of the analytical difficulties and the unprecisely determined ^{138}La-^{138}Ce CHUR value.

Because of these issues, the key points of this study are to:

- Improve the analytical procedure (separation and measurement procedure),
- investigate the ^{138}La-^{138}Ce system for meteorites and terrestrial samples,
- define chondritic, carbonaceous chondritic and non-carbonaceous chondritic ^{138}La-^{138}Ce values.

After an introduction in Chapter 1, Chapter 2 describes the results to overcome the above mentioned analytical difficulties through the development of an efficient three-step ion-exchange chromatography. An analytical protocol was developed to perform simultaneously high precision Ce measurements of all four Ce isotopes (136, 138, 140 and 142) using Multicollector - inductively coupled plasma - mass spectrometry (MC-ICP-MS). An enriched ^{138}La and ^{142}Ce tracer was prepared and calibrated to perform isotope dilution measurements by MC-ICP-MS. Additionally, a new reference standard (Cologne-AMES) was prepared and characterized because the traditionally used reference standard JMC-304 is not commercially available anymore. In comparison with recent studies, where Mainz-AMES (Willbold (2007)) was used, and older studies, the three reference standards (JMC-304, Cologne-AMES and Mainz-AMES) were calibrated against each other in one analytical session. The results show that the three reference materials are isotopically heterogeneous.
In Chapter 3 the analytical protocol was applied to different meteorites to define a more accurate chondritic uniform reservoir (CHUR) reference value. In addition, the question was addressed if the Earth is in general chondritic with respect to the ^{138}La-^{138}Ce isotope system because there is an ongoing debate which chondrite class reflects the building block for the Earth (e.g. Warren (2011) and Boyet et al. (2018)). Therefore, non-carbonaceous and carbonaceous chondritic ^{138}La-^{138}Ce values were determined. Using Ce and Nd literature data from mid ocean ridge basalts (MORBs) and ocean island basalts (OIBs) (Willig and Stracke (2019), Makashima and Masuda (1994) and Boyet et al. (2019)) the Ce-Nd mantle array intersects within uncertainties using the non-carbonaceous chondritic ^{138}Ce-^{136}Ce value. In Chapter 4 the ^{138}La-^{138}Ce isotope system was applied to mafic and felsic rocks from southwest Greenland and South Africa and is combined with ^{147}Sm-^{143}Nd and ^{176}Lu-^{176}Hf data from literature (Kröner et al. (1994), Hoffmann et al. (2011), Hoffmann et al. (2014), Kröner et al. (2014), Schneider et al. (2018), Schneider et al. (2019) and van de Löcht et. al. (2019)). The samples were screened for alteration, Cerium anomalies and effects on sediment recycling. Undisturbed samples define a ε^{143}Nd- ε^{138}Ce correlation trend and intersect within uncertainties with the non-carbonaceous chondritic ^{138}La-^{136}Ce value.

1.2.1. **Primordial nucleosynthesis**

The origin of the universe, the Earth and the elements are key questions in cosmo- and geochemistry and there are still a lot of open questions. The evolution of the universe began 13.7 billion years (Ga) ago with the big bang (e.g., Burbidge et al. (1957)). In the first three minutes of its existence, the universe had cooled down to ~10^9 K and the light elements (H 75%, He 25% and traces of ^{7}Li) were synthesized through nuclear fusion (primordial nucleosynthesis):

$n+p \rightarrow d+\gamma$

$p+d \rightarrow {}^3He+\gamma$ and $n+d \rightarrow {}^3H+\gamma$

^{3}He and ^{3}H underwent further reactions that produced ^{4}He. A=5 nuclei are not produced because there are no stable nuclei with this mass number. A small amount of ^{7}Li was also produced:

$^4He+{}^3H \rightarrow {}^7Li+\gamma$.

^{7}Li is very weakly bound and decays rapidly. As a result, the production of larger nuclei were blocked and the primordial nucleosynthesis ceased.

1.2.2. **Stellar nucleosynthesis**

Heavier elements are primarily produced in the interior of stars (stellar nucleosynthesis) (Burbidge et al. (1957), Merrill (1952)). The first step of this stellar nucleosynthesis is hydrogen burning where protons are converted into ^{4}He nuclei. Due to the absence of neutrons the first reaction is different from primordial nucleosynthesis:

1) $p+p \rightarrow d+e^+ + \nu_e$

2) $p+p+ e^- \rightarrow d+\nu_e$

3) $d+p \rightarrow {}^3He+\gamma$

4) $^3He+{}^3He \rightarrow {}^4He+2p$ or $^3He+{}^4He \rightarrow {}^7Be+\nu_e$

1+2+3+4) $4p \rightarrow {}^4He+2e^- +2\ \nu_e$ $e^- + {}^7Be \rightarrow {}^7Li+\nu_e$

$p+{}^7Li \rightarrow 2\ {}^4He$

A small fraction of ^{7}Be can undergo proton capture to produce two nuclei of ^{4}He. The CNO-cycle (or Bethe-Weizsäcker-cycle) is another fusion reaction by which stars can burn hydrogen. It occurs mainly in heavier stars with masses of at least 1.3 times the mass of the sun (population II and population I stars). In these stars, heavy elements such as C, N and O are present from pre-existing stars.

$^{12}C+p \rightarrow {}^{13}N+\gamma$

$^{13}N \rightarrow {}^{13}C + e^+ + \nu_e$

$^{13}C+p \rightarrow {}^{14}N+\gamma$

$^{14}N+p \rightarrow {}^{15}O+\gamma$

$^{15}O \rightarrow {}^{15}N+ e^{+}+\nu_e$

$^{15}N + p \rightarrow {}^{12}C+{}^{4}He$

The second step of stellar nucleosynthesis is helium burning. If hydrogen burning stops a gravitational collapse will occur. This will increase the temperature and as a consequence, in a so called red giant Helium burning will start: $3\ {}^{4}He \rightarrow {}^{12}C+\gamma$. After a sufficient amount of ^{12}C has formed in massive stars an α- capture reaction can occur to produce ^{16}O:

$^{4}He+{}^{12}C \rightarrow {}^{16}O+\gamma$

$^{4}He+{}^{16}O \rightarrow {}^{20}Ne+\gamma$

When the helium burning stops, a further gravitational collapse with a temperature increase will occur. As a consequence, carbon and oxygen burning occurs in massive stars by charged particle reactions such as:

$^{12}C+{}^{12}C \rightarrow {}^{20}Ne+{}^{4}He$

$^{12}C+{}^{12}C \rightarrow {}^{23}Na+p$

$^{12}C+{}^{12}C \rightarrow {}^{23}Mg+n$

$^{12}C+{}^{12}C \rightarrow {}^{24}Mg+\gamma$

$^{16}O+{}^{16}O \rightarrow {}^{24}Mg+2\ {}^{4}He$

$^{16}O+{}^{16}O \rightarrow {}^{28}Si+\ {}^{4}He$

$^{16}O+{}^{16}O \rightarrow {}^{31}P+p$

$^{16}O+{}^{16}O \rightarrow {}^{31}S+n$

$^{16}O+{}^{16}O \rightarrow {}^{32}S+\gamma$

The neutrons produced by these reactions above are the main source for the s-process (slow neutron process, see chapter on nucleosynthesis of heavier elements). The last step of the stellar nucleosynthesis is silicon burning:

$^{28}Si+\ \gamma \rightarrow {}^{24}Mg+{}^{4}He$

$^{28}Si + {}^{4}He \rightarrow {}^{32}S+\gamma$

Nucleosynthesis of heavier elements via α-capture proceeds only until ^{56}Ni because further α-capture reactions would be endotherm. ^{56}Ni decays to ^{56}Fe and ^{56}Fe, which is the endpoint of stellar nucleosynthesis by fusion.

1.2.3. **Nucleosynthesis of heavier elements**

Nuclei with masses > 56 are produced by neutron capture processes. In the core of massive stars, the reaction $^{56}Fe \rightarrow 26p+30n$ leads to collapse of the stellar core through shock waves (supernova event). An extremely compact, hot (10^6 K surface temperature) and rapidly rotating (milliseconds) neutron star with only a few (100 km) diameter remains. The explosion shell of the supernova is ejected into interstellar space at several dozen kilometers per second and

enriches the interstellar matter with many heavy elements of the periodic table. This is due to the fact that extremely high neutron fluxes are available in the vicinity of the neutron nucleus. Energetically favored for nuclei A≥56 are neutron capture reactions because no Colomb barriers must be overcome. There are two types of neutron capture processes: s-process (slow neutron capture) and r-process (rapid neutron capture) (Burbidge et al. (1957), Cameron (1957)). The difference between the r- and s-process is the rate of neutron capture relative to the beta decay rates of unstable isotopes. At low neutron densities n_n ~10^8 cm^{-3} (Busso et al. (1999)), a neutron capture occurs every 10^3-10^4 years because the beta decays are faster than the neutron capture reactions ($\tau_{(n,\gamma)} >> \tau_{(\beta)}$). Therefore, the beta decay occurs before the newly produced unstable nuclei can capture another neutron. In contrast, the r-process occurs at extremely high neutron densities n_n >10^{22} cm^{-3} (Kratz et al. (2007)). Neutron capture in this case is more rapid than the beta decay ($\tau_{(n,\gamma)} << \tau_{(\beta)}$). The r- and s-processes are accounting for the heavier stable isotopes of a given element. The end of the s-process chain is ^{209}Bi because when ^{209}Pb captures a neutron ^{210}Bi is produced (half-life 5d), which decays to ^{210}Po. ^{210}Po undergoes alpha decay back to ^{206}Pb. Examples of s- and r-processes are given in Figure 1 for the elements La to Nd. The neutron capture repeats from ^{137}Ba to ^{139}Ba and ^{139}Ba decays into ^{139}La with a half-life of 85 min. At ^{139}La the neutron capture continues until the short-lived ^{140}La which decays into ^{140}Ce. ^{140}Ce also captures a neutron to produce ^{141}Ce which decays to ^{141}Pr. The half-life of ^{141}Ce is shorter than the timescale of neutron capture. Therefore, ^{142}Ce cannot be produced via the s-process and is a r-process only nucleus. As also seen in Figure 1 ^{142}Nd is a p-process (discussed below) and s-process nuclei because the stable nuclei ^{142}Ce shield the r-process.

Another important process for the synthesis of proton-rich nuclei is the p-process. Isotopes produced by the p-process undergo photonuclear reactions (r*p*-process, γ-process and ν*p*-process). The p-process is responsible for the lighter stable isotopes of a given element. P-process isotopes often have lower abundances, because these processes occur much less likely than neutron capture.

1.2.4. **Consequences of nucleosynthesis for Ce**

Cerium has 4 naturally occurring isotopes: ^{136}Ce (0.19%), ^{138}Ce (0.25%), ^{140}Ce (88.4%), and ^{142}Ce (11.1%). The isotope abundances of Cerium can be explained by the nucleosynthetic pathways described above. Figure 1 shows a portion of the nuclide chart including the elements Ba to Nd and the production of each isotope by the s-, r- or p-processes. The isotopes ^{136}Ce and ^{138}Ce are p-process only elements and therefore both isotopes only occur at low abundances. ^{140}Ce is an s- and r-process isotope and has the highest abundance, while ^{142}Ce

is an r-process only isotope. Furthermore, Figure 1 shows that ^{138}La (0.1%) is a p-process only nucleus and the much more abundant ^{139}La (99.9%) is a s- and r-process nucleus.

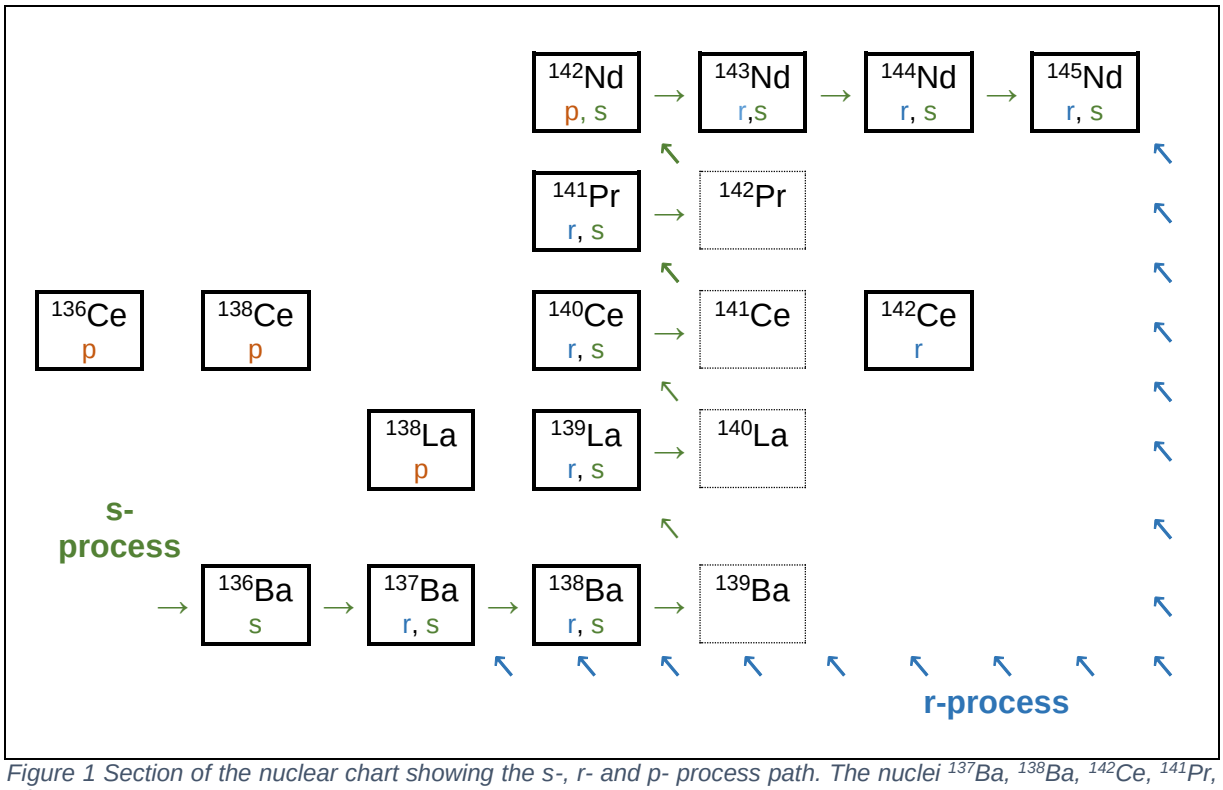

Figure 1 Section of the nuclear chart showing the s-, r- and p- process path. The nuclei ^{137}Ba, ^{138}Ba, ^{142}Ce, ^{141}Pr, ^{143}Nd, ^{144}Nd and ^{145}Nd are produced via rapid neutron capture (blue arrow). The slow neutron capture process path from ^{136}Ba to ^{139}Ba for example is shown by green arrows. The isotopes ^{136}Ce, ^{138}Ce and nuclide ^{138}La are produced via photonuclear reaction. The production path influences the abundances of the elements. P-process nuclei are the rarest heavy elements (A>56) in the universe and nuclei which can be produced both by r- and s-process are the most common heavy elements in the universe..-

1.3. Evolution of the solar system

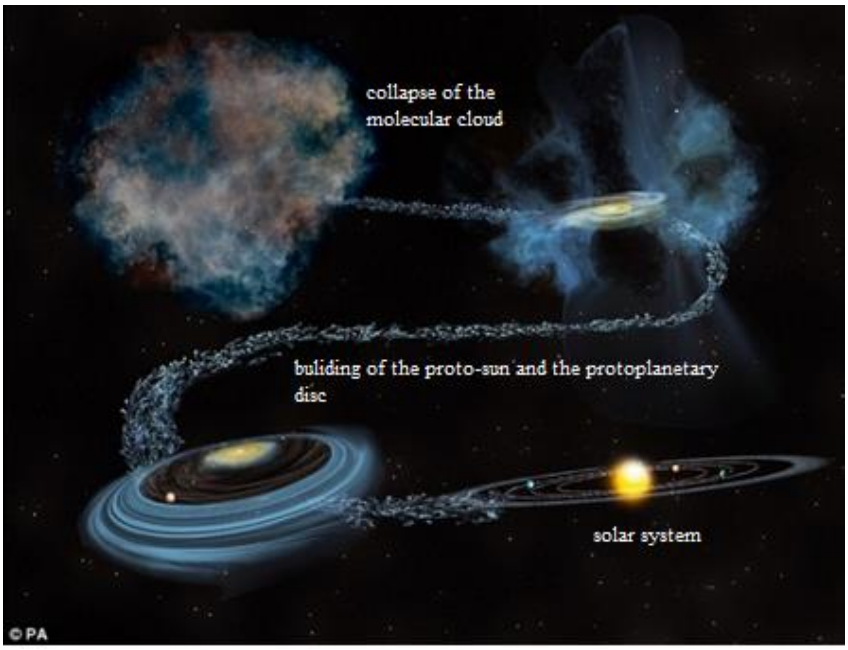

Figure 2 schematic concept of the solar system formation. Starting with the collapse of the molecular cloud and the building of the proto-sun and the protoplanetary disc to the building of the solar system. Image credit: modified after Bill Saxton/NSF/AUI/NRAO

At this point only a very brief overview about the evolution of the solar system is given (Figure 2). The formation of the solar system started about 4.57 Ga ago (Bouvier and Wadhwa, (2010)) through the collapse of the molecular cloud. Out of the molecular cloud, the protoplanetary disc was formed. In its center, the Sun was formed from the greatest part of the collapsing mass. Later, the protoplanetary disc broke up into clumps of solid particles and the development of the first planetesimal. Planetesimals are the precursors of terrestrial planets (e.g. Earth) and the accretion of planetesimals from the nebular dust are the first part of Earth formation. The second step is the growth of planetary embryos by collision of the planetesimals and the collision of planetary embryos to form terrestrial planets is the last step.

1.4. Meteorites

Meteorites are fragments of asteroids and originate from the asteroid belt between Mars and Jupiter. The asteroid belt consists of planetesimal leftovers.

Meteorites are subdivided into undifferentiated and differentiated meteorites (Figure 3). Differentiated meteorites originate from larger bodies that have been broken apart. In contrast, undifferentiated meteorites are considered pristine and therefore reflecting the composition of the solar nebula. Achondrites, iron meteorites and stone-iron meteorites belong to the differentiated meteorites and chondrites belong to the undifferentiated meteorites. In this thesis, chondrites are used because they are the most primitive meteorites and offer the only

direct access to study the origin of our solar system. Chondrites are the most common meteorites they have their name from mm-size small silicate spherules that are called chondrules. Chondrules are quickly cooled down melt droplets from the solar nebula. These chondrules can occupy between 0 and 90% of the meteorite volume.

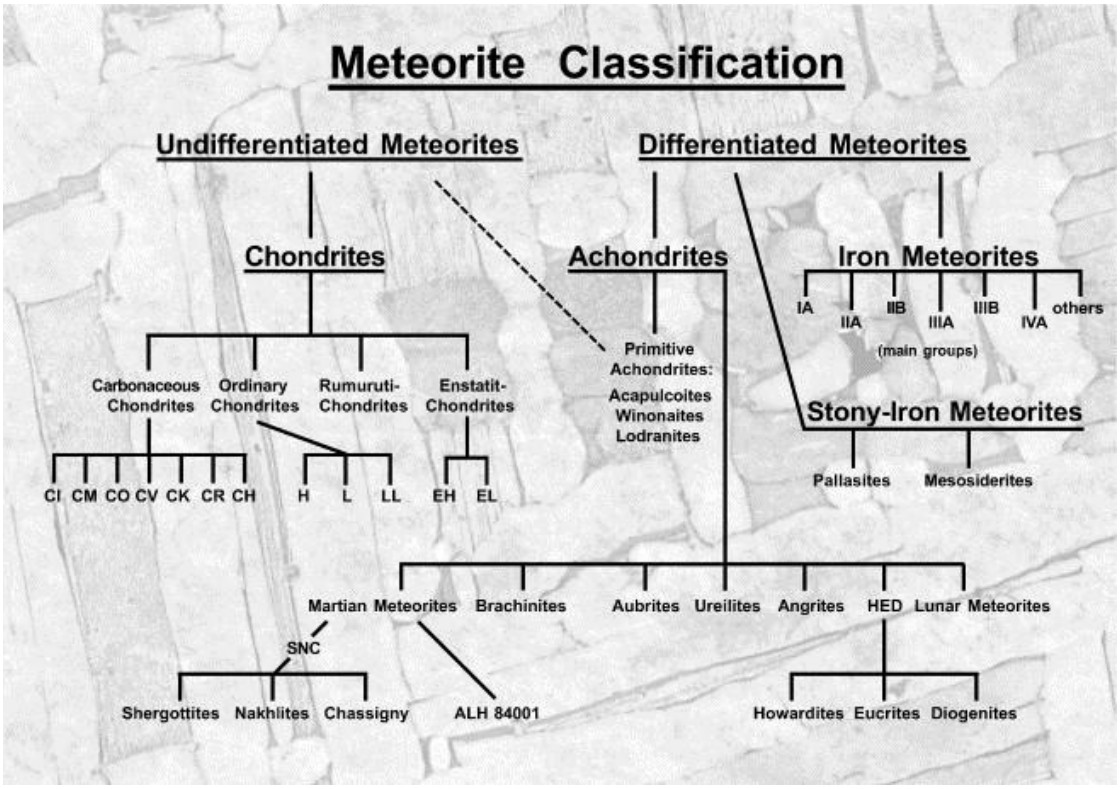

Figure 3 classification of meteorites taken from Bischoff (2001). Meteorites are subdivided into differentiated (achondrites, iron and stony-iron) and undifferentiated (chondrites) meteorites.

1.4.1. **Chondrite classes**

Chondrites are divided into three classes based on their bulk chemical compositions: Carbonaceous (CC), ordinary (OC) and enstatite (EC) chondrites and are additionally subdivided into six petrological types based on their degree of aqueous and thermal alteration.

Carbonaceous chondrites

Four percent of all chondrites are classified as carbonaceous chondrites because their matrices contain carbonates and complex organic compounds. The carbonaceous chondrites are further subdivided into seven groups (CI, CM, CV, CO, CK, CR and CH) depending on their composition. They are named after prominent representative members of their class. CI-chondrites which are named after the fall of Ivuna, Tanzania, contain virtually no visible chondrules (mm-sized enamel beads), but a water content of up to 20% and contain numerous organic compounds such as amino acids. CM-chondrites, which are named after the fall of Mighei, Ukraine, contain organic substances such as amino acids and in addition they have

clearly visible chondrules and inclusions of so-called CAIs (calcium-aluminum rich inclusions). CV chondrites are named after the fall of Vigarano, Italy, but the best-known CV chondrite is Allende, Mexico. In contrast to CI chondrites, CV chondrites just contain traces of water, organic substances and especially many and large chondrules and CAIs. CO chondrites are named after Ornans, France, and they differ already at first sight from the other groups because of their black appearance. CO chondrites have small chondrules and only sparse inclusions of CAIs. They also contain clearly visible inclusions of nickel/iron. Chemically, the CO chondrites are similar to CV chondrites. CH chondrites are not named after a location, the term “H” stands for “High Iron” and describes the high proportion of nickel/iron (more than 50%) of the total mass. CR chondrites are named after Renazzo, Italy. They usually have large, clearly separated chondrules and in contrast to the CM chondrites, they contain relatively much nickel/iron, and iron sulfide. CK-chondrites are named after the fall of Karoonda, Australia. They contain a high proportion of magnetite and therefore the cut slices appear matt and black. They also contain chondrules of different sizes and occasional inclusions of CAIs.

Ordinary chondrites

85% of all found meteorites are ordinary chondrites that are subdivided into H, L, LL-chondrites. The “H” in H-chondrites stands for “High Iron” (25 to 31% total iron) and they consist of olivine and orthopyroxene. L chondrites where the “L” stands for “Low Iron” (20-25% total iron) consist of olivine and the orthopyroxene hypersthene. The “LL” in LL chondrites stands for "Low Iron" (19 to 22% total iron) and "Low Metal".

Enstatite chondrites

Enstatite chondrites are subdivided into 2 classes: EH and EL depending on their metal content (EH: high metal with 29% total iron; EL: low metal with 22% total iron). Enstatite chondrites differ from the ordinary and carbonaceous chondrites in the fact that the iron component is present almost only in reduced, metallic form.

Figure 4 shows the different classes of chondrites and the corresponding petrological types (Weisberg et al. (2006)). The classification into the different petrological types is based on the presence of chondrules, matrix, as well as the carbon and water content. Type 1 meteorites have no chondrules, high carbon (3-5%) and high water (18-22%) content. The carbon and water contents decrease from type 1 to 6, and from type 2 on there are always chondrules. There are several additional classification criteria such as homogeneity of olivine composition or structural state of low Ca-pyroxene. In general, the petrological type 3 is the most pristine class, and from type 3 to type 1 there is an increase in the degree of aqueous alteration and

from type 3 to type 6 there is an increase in the degree of thermal metamorphism (Weisberg et al. (2006)).

classification	Petrological type					
	1	2	3	4	5	6
Carbonaceous	CI1					
	CM1	CM2				
	CR1	CR2				
			CH3			
			CV3			
			CO3			
			CK3	CK4	CK5	CK6
Ordinary			H3	H4	H5	H6
			L3	L4	L5	L6
			LL3	LL4	LL5	LL6
Enstantite			EH3	EH4	EH5	EH6
			EL3	EL4	EL5	EL6

Figure 4 classification of chondrites modified after Van Schmus and Wood (1967) and Weisberg et al. (2006). The carbon and water contents decrease from type 1 to 6. The carbonaceous chondrites are subdivided into seven groups (CI, CM, CV, CO, CK, CR and CH) depending on their place of origin in the solar nebula they are very different. Ordinary and enstatite chondrites only occur as petrological types 3 to 6 and are subdivided into three groups (H,L and LL) based on the iron content (H: 25-30% iron, L: 20-25% iron and LL: 19-22% iron). However, there are several more classifying criteria such as the appearance of chondrules or the homogeneity of olivine composition.

1.5. The Geochemistry of Lanthanum and Cerium

Lanthanum with the atomic number 57 and Cerium with the atomic number 58 are the first two elements of the lanthanides or rare earth elements (REEs). Lanthanum was named after the Ancient Greek lanthanein (= “to lie hidden”) and Cerium was named after the asteroid Ceres, which had been discovered shortly before. Cerium is the most abundant REE and La the second most common REE in the Earth’s crust. Cerium has the same abundance as the transition metals copper or nickel which reflects that there is one isotone of La and Ce with the magic neutron-number N=82 (^{139}La and ^{140}Ce). In the environment, most REEs occur in the oxidation state +III such as La and Nd. Europium and Ce can further occur in the oxidation states +II and +IV, respectively. The reason is the electronic configuration [Xe]$4f^1$ in the trivalent state of cerium. With a standard reduction potential E^0_{red}=+1.74 V (Ce^{3+}/Ce^{4+}) Ce has a stable electronic configuration in the tetravalent state. This chemical property is used to separate Ce from other REEs like La and Nd during chromatography column chemistry

(Chapter 2). In geochemistry, Ce anomalies are used to describe the enrichment (positive anomaly) or depletion (negative anomaly) of Ce relative to the other REE based on the redox potential of this element. In this thesis, Ce anomalies (Ce/Ce*) are calculated after Equation 1 or Equation 2. Cerium anomalies are defined as the difference between the actually measured and predicted Ce concentration, where the latter is interpolated from the La and Nd or Pr concentration of the individual samples:

$$Ce/Ce^* = Ce_{sample} \Big/ \frac{2\frac{La}{La_{CI}} + \frac{Nd}{Nd_{CI}}}{3} \qquad \text{Equation 1}$$

$$Ce/Ce^* = Ce_{sample} \Big/ \sqrt{\frac{La}{La_{CI}} * \frac{Pr}{Pr_{CI}}} \qquad \text{Equation 2}$$

A Ce/Ce* value of 1 means that La, Ce,Pr and Nd have crust-like components and that no fractionation of Ce from La, Pr and Nd occurred. Ce/Ce* values between 0 and 1 are by definition called negative anomalies while values greater than 1 are called positive anomalies. For example, a negative Ce anomaly indicates that Ce might be selectively depleted in contrast to La and Nd. In Chapter 3 no Pr data are available for the analyzed chondrites and therefore Equation 1 is used. In Chapter 4 Pr data are available from literature and Equation 2 is used.

An aperiodic physical property is the decrease of the ionic radius with increasing nuclear charge number of the lanthanides (lanthanide contraction). Lanthanum has the largest ionic radius of the lanthanides and Lu the smallest. Larger occurrences of lanthanides can be found in Scandinavia, South India, South Africa, Brazil, Malaysia, China and Russia. Due to their chemical similarity, lanthanides are mostly associated in nature. The two most important lanthanide minerals are bastnaesite (REE)[CO_3F] and monazite (REE)[(P, Si)O_4]. Other lanthanide minerals are allanite ($CaCe(Al_2Fe^{2+})[O|OH|SiO_4|Si_2O_7]$, $CaLa(Al_2Fe^{2+})[O|OH|SiO_4|Si_2O_7]$) or ceranite CeO_2.

After the classification from Victor M. Goldschmidt (1937) La and Ce belong geochemically to the lithophile elements because they tend to form silicates and oxides. Cosmochemically, La and Ce belong to the refractory elements that condense at high temperatures between 1850 - 1355 K and would condensate first from cooling gas of solar composition.

1.6. The ^{138}La-^{138}Ce Geochronometer

Since the mid 20th century, long-lived radioactive decay chains have been used to date geological events and to put time constraints on the differentiation history of Earth's mantle–crust system. The most prominent decay systems are Lu-Hf, Sm-Nd, Re-Os and Rb-Sr. The Lu-Hf system is based on the beta- emission from radioactive ^{176}Lu to ^{176}Hf (half-life ~37.1 Ga) and the Sm-Nd system is based on the alpha decay from radioactive ^{147}Sm to ^{143}Nd (half-life ~106 Ga). Both isotope systems behave identically in that during mantle melting the daughter nuclides ^{176}Hf and ^{143}Nd are more incompatible than the parent nuclides ^{176}Lu and ^{147}Sm. The

Rb-Sr geochronometer is based on the beta decay of radioactive ^{87}Rb to ^{87}Sr (half-life of ~ 49 Ga) and in contrast to the Lu-Hf and Sm-Nd systems the parent nuclide ^{87}Rb is highly incompatible during mantle melting. The ^{187}Re-^{187}Os isotope system is based on the beta decay of ^{187}Re to the ^{187}Os (half-life of 42 Ga) and during mantle melting the parent nuclide ^{187}Re is more incompatible than the parent isotope ^{187}Os. As a consequence, mantle melting causes higher Lu/Hf and Sm/Nd values but lower Rb/Sr and Re/Os values in the residual mantle and lower Lu/Hf and Sm/Nd values but higher Rb/Sr and Re/Os values in the magma. These four geochronometers have commonly been used to track the history of Earth's mantle-crust system (e.g., Moorbath et al. (1977); Patchett and Tatsumoto (1981), Patchett (1983), Jacobsen (1988), Collerson et al. (1991), Bennett et al. (1993), Bowring and Housh (1995), Vervoort and Blichert-Toft et al. (1999), Bennett et al. (2002)).

The ^{138}La-^{136}Ce geochronometer used in this thesis has been introduced in the 80's (Tanaka et al. (1982)) and is based on the branched decay of ^{138}La to ^{138}Ce and ^{138}Ba with a half-life of 102 billion years by β^- decay and electron capture, respectively. Equation 3 describes the decay:

$$\left(\frac{^{138}Ce}{^{136}Ce}\right)_0 = \left(\frac{^{138}Ce}{^{136}Ce}\right)_t + \frac{^{138}La}{^{136}Ce}\left(e^{\lambda_\beta t} - 1\right) \qquad \text{Equation 3}$$

where 0 is the present day and t the appropriate age of the different samples.

In the past, the ^{138}La-^{138}Ce geochronometer has been successfully used for the age determination of rocks and as a geochemical tracer (Nakamura et al. (1984), Shimizu et al. (1984), Tanaka et al. (1987), Dickin (1987), Dickin et al. (1987), Dickin (1988), Shimizu et al. (1988), Shimizu et al. (1990), Amakawa et al. (1991), Shimizu (1992), Tanimizu and Tanaka (2002)). For example Tanaka et al. (1987) used the ^{138}La-^{138}Ce isotope system to determine the age of a gabbro from the upper zone of the Bushveld complex, South Africa. The study combined the ^{138}La-^{138}Ce isotope system with the ^{147}Sm-^{143}Nd isotope system and both age determinations are in good agreement. Dickin (1987) also combined the ^{138}La-^{138}Ce with the ^{147}Sm-^{143}Nd isotope system to unravel the source for ocean island basalts. Tanimizu and Tanaka (2002) combined both isotope systems for lunar samples to constrain the evolution of the Moon. This geochronometer is a unique tool to study the behavior of the LREE because the mother isotope ^{138}La behaves incompatible during the partial melting of the mantle and the daughter isotope ^{138}Ce is more compatible.

In general, the ^{138}La-^{138}Ce geochronometer has rarely been used because ^{138}La has a low abundance (0.0902%) and because of its long half-life the variation of relative ^{138}Ce abundances ratios due to the radiogenic ingrowth is small. Therefore, highly precise measurements of ^{138}Ce/^{136}Ce ratios are necessary. Additionally, the measurement of ^{138}Ce is analytically challenging in terms of possible tailing from the main isotope ^{140}Ce (88.5%) and the interfering isotope ^{138}Ba during mass spectrometric analysis. Therefore, an efficient chemical separation technique is needed to separate Ce from the other REE and Ba

quantitatively. In Chapter 2 an improved three-step ion chromatographic procedure was developed. In the first step, REEs are separated from the matrix using cation exchange chromatography. In the second step, Ce is separated employing an Ln Spec column and selective oxidation. In the last step, a cation clean-up chemistry is performed to remove all traces of remaining interferences especially Ba. Previously published analytical protocols for Ce isotope measurements have been limited to thermal ionisation mass spectrometry (TIMS) (e.g. Nakamura et al. (1984), Shimizu et al. (1984), Tanaka et al. (1987), Dickin (1987), Dickin et al. (1987), Dickin (1988), Shimizu et al. (1988), Shimizu et al. (1990), Amakawa et al. (1991), Shimizu (1992), Tanimizu and Tanaka (2002), Tazoe et al. (2007), Tazoe et al. (2011), Bellot et al. (2015), Willig and Stracke (2019)). The protocol of Chapter 2 was developed specifically for MC-ICP-MS to improve precision and sensitivity. In most previous studies, ^{138}Ce abundances have been reported as ^{138}Ce/^{142}Ce (Bellot et al. (2015), Masuda et al. (1988), Amakawa et al. (1991), Shimizu et al. (1996), Lee et al. (2001)). In contrast, in this study ^{138}Ce/^{136}Ce mass bias corrected to ^{136}Ce/^{140}Ce is used because of a better external reproducibility. The external reproducibility was verified by multiple analyses of JMC-304 and was significantly better once ^{136}Ce/^{140}Ce was used for mass bias correction (±25 ppm) rather than ^{136}Ce/^{142}Ce (±40 ppm, all 2 r.s.d).

Additionally, an isotope tracer enriched in ^{138}La and ^{142}Ce is established to perform precise absolute determination of La and Ce. A new reference material was prepared from AMES laboratory Ce metal (Cologne-AMES) because the previously used JMC-304 Ce reference material is not commercially available anymore. Both reference materials (Cologne-AMES and JMC-304) were calibrated against AMES material prepared at Mainz (Mainz-AMES) in the same analytical session. The results demonstrate an isotope heterogeneity between Cologne-Ames, Mainz-Ames and different JMC-304 batches used in the literature that make comparisons and evaluation of older literature data difficult. The new protocol was applied to different geochemical reference materials: BCR-2, BCR-1, BHVO-2, JR-1, JA-2, JB-3, JG-1, JR-1, JB-1b, AGV-1 and one in-house La Palma standard (LP1) to determine the variations of Ce isotope compositions and La-Ce concentrations. Additionally, different cone combinations were tested (Ni sample cones and H-type skimmer cones; Ni sample cones and X-Skimmer cones; “Jet” sample cones with H-type skimmer cones, and “Jet” sample cones with X-type skimmer cones) to improve the sensitivity for Ce isotope measurements.

1.7. Chondritic Earth: CHUR value

As mentioned above, chondrites can be seen as time capsules from the early solar system because they offer the only direct access to study the origin of our solar system. CI chondrites are the most primitive class of chondrites. In Figure 5 the abundances of the elements in the

bulk silicate Earth are expressed relative to abundances in CI chondrites and normalized to Mg and plotted against 50% condensation temperature [K]. All REEs belong to the refractory lithophile elements (blue filled squares) which should not have been fractionated during condensation or volatilization processes in the early solar system or by metal/silicate differentiation during core formation in terrestrial planets. Due to the absence of these significant fractionations, their relative abundances are the same as in CI chondrites.

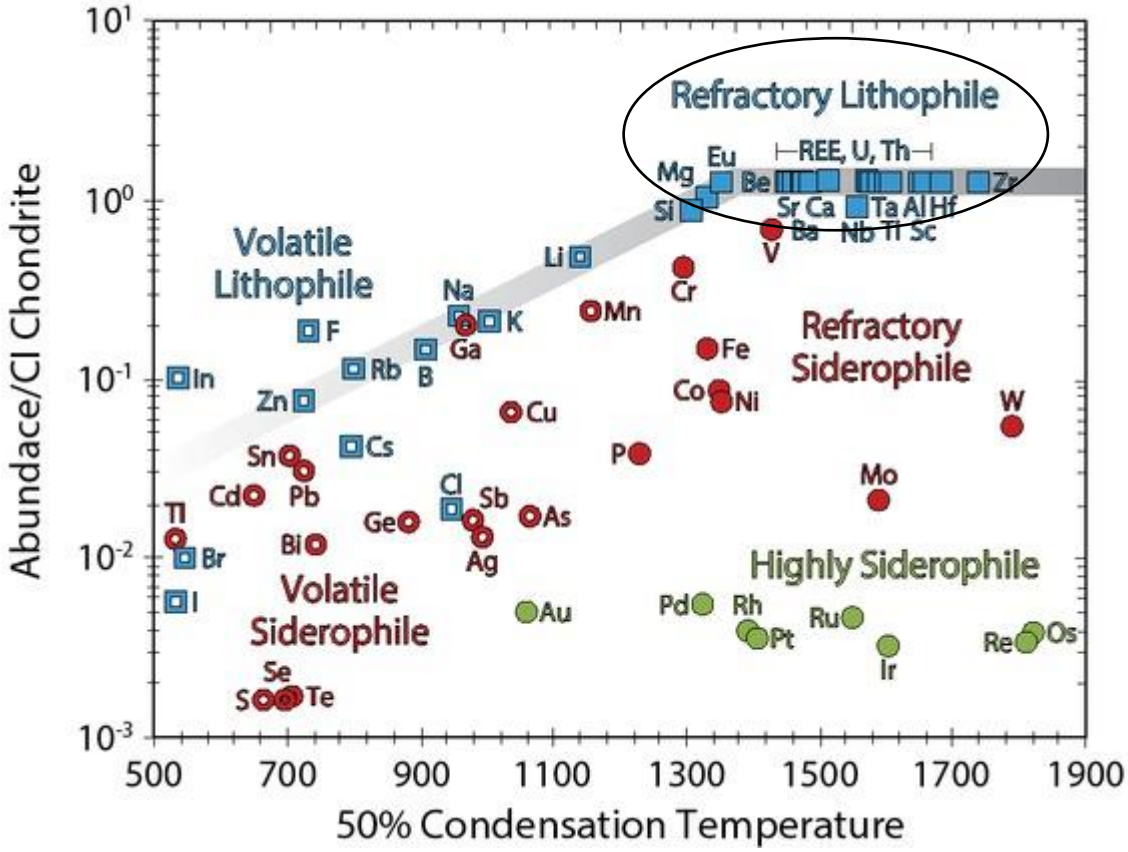

Figure 5 Elemental abundances in the silicate Earth normalized to CI chondrites and Mg modified after Wood et al. (2019). The abundances are plotted against 50 % condensation temperature [K] (50% of the element would be condensed from a gas of solar composition at 10^{-4} bar). Lanthanum and Ce are part of the REEs and belong to the refractory lithophile elements. REEs are marked with a blue square. Refractory lithophile elements such as the REEs are present in chondritic proportions in the silicate Earth.

For this reason, the term “chondritic uniform reservoir” (CHUR) was introduced first for the Sm-Nd isotope system by DePaolo and Wasserburg (1976) which denotes the bulk silicate Earth’s isotope composition. The ^{138}La-^{138}Ce CHUR parameter that is determined in Chapter 3 is based on the present-day ^{138}La/^{136}Ce and ^{138}Ce/^{136}Ce isotopic ratios of different chondrites. Until now, this important parameter has not been well constrained. The ^{138}La-^{138}Ce CHUR value has been determined from a small dataset of meteorite samples in three older studies (Shimizu et al. (1984), Makashima and Masuda (1993), Makashima and Masuda (1993)). Recent studies with an improved analytical setting show inconsistent ^{138}La-^{138}Ce CHUR values (Bellot et al. (2015) and Willig and Stracke (2019)).

The precise determination of the ^{138}La-^{138}Ce isotope composition of CHUR is needed to unravel the processes during the first few hundred million years after the formation of the Earth. By convention, variations in ^{138}Ce/^{136}Ce ratios in planetary reservoirs are expressed in parts per 10^4 relative to the reference parameter CHUR, using the epsilon notation:

$$\varepsilon^{138}Ce = [(^{138}Ce/^{136}Ce)_{sample}/(^{138}Ce/^{136}Ce)_{CHUR}-1]*10^4 \quad \text{Equation 4}$$

This convention is also used for the more popular geochronometers such as Lu-Hf and Sm-Nd:

$$\varepsilon^{143}Nd = [(^{143}Nd/^{144}Nd)_{sample}/(^{143}Nd/^{144}Nd)_{CHUR}-1]*10^4 \quad \text{Equation 5}$$

$$\varepsilon^{176}Hf = [(^{176}Hf/^{177}Hf)_{sample}/(^{176}Hf/^{177}Hf)_{CHUR}-1]*10^4 \quad \text{Equation 6}$$

The CHUR parameters for the Sm-Nd and Lu-Hf systems ($^{143}Nd/^{144}Nd_{CHUR}$=0.512630±11, $^{147}Sm/^{144}Nd_{CHUR}$=0.1960±4 and $^{176}Hf/^{177}Hf_{CHUR}$=0.282785±11, $^{176}Lu/^{177}Hf_{CHUR}$=0.0336±1) parameters that are presently used are those of Bouvier et al. (2008). The Lu-Hf and Sm-Nd CHUR parameters are based on the mean value of unequilibrated chondrites because the Lu/Hf mean value of equilibrated chondrites have a much larger variation (28%) (Bouvier et al. (2008)). Therefore Bouvier et al. (2008) recommended using only the mean values of unequlibrated chondrites for the Lu-Hf and Sm-Nd CHUR values. On the other hand, the Sm-Nd CHUR values of unequilibrated and equilibrated chondrites overlap with each other, in contrast to Lu-Hf where no overlap between unequilibrated and equilibrated chondrites occurs (Bouvier et al. (2008). For the Rb-Sr geochronometer, the determination of a CHUR value is impossible because Rb is a volatile element (i.e., elements predicted to condense at 50% condensation temperature below ~1250 K). The loss of volatile elements during early solar system processes, such as impact vaporization or incomplete condensation, causes a large variation of Rb/Sr values in chondrites. For the Rb-Sr geochronometer, the term BABI (Basaltic Achondrite Best Initial) was introduced by Papanastassiou and Wasserburg (1969). Ca-Al-rich inclusions (CAI) from the CV 3 meteorite Allende has the most primitive Sr isotope composition and is used as a reference parameter for the Rb-Sr isotope system (Hans et al. (2013)). However, the Sm-Nd, Lu-Hf and La-Ce isotope systems involve refractory lithophile elements that have not undergone fractionation during condensation or volatilization processes in the early solar system. Due to the absence of significant fractionation, their relative abundances and also $^{143}Nd/^{144}Nd$ and $^{176}Hf/^{177}Hf$ in the Earth and other terrestrial planets are the same as those of the building blocks. Thus, terrestrial $^{143}Nd/^{144}Nd$ and $^{176}Hf/^{177}Hf$ are chondritic according to the chondritic Earth Model (e.g. DePaolo and Wasserburg (1976), Blichert-Toft (1997)). The bulk silicate Earth (BSE) represents the Earth except the metallic core (Jacobsen and Wasserburg (1980)). As a consequence, the Lu-Hf and Sm-Nd CHUR values are equal to the BSE, because all four elements are strongly lithophile.

1.8. Non-chondritic Earth

As mentioned above, long-lived chronometers such as the $^{147}Sm/^{143}Nd$ and $^{176}Lu/^{176}Hf$ can be used to trace processes such as the evolution of the BSE. Short-lived chronometers like ^{146}Sm-^{142}Nd (half-life: 103 million years (Myrs)) can track early events (within the first 500 Myrs) of Earth`s differentiation. Figure 6 shows the decay of a long-lived decay system such as ^{138}La-^{138}Ce and a short-lived decay system such as ^{146}Sm-^{142}Nd.

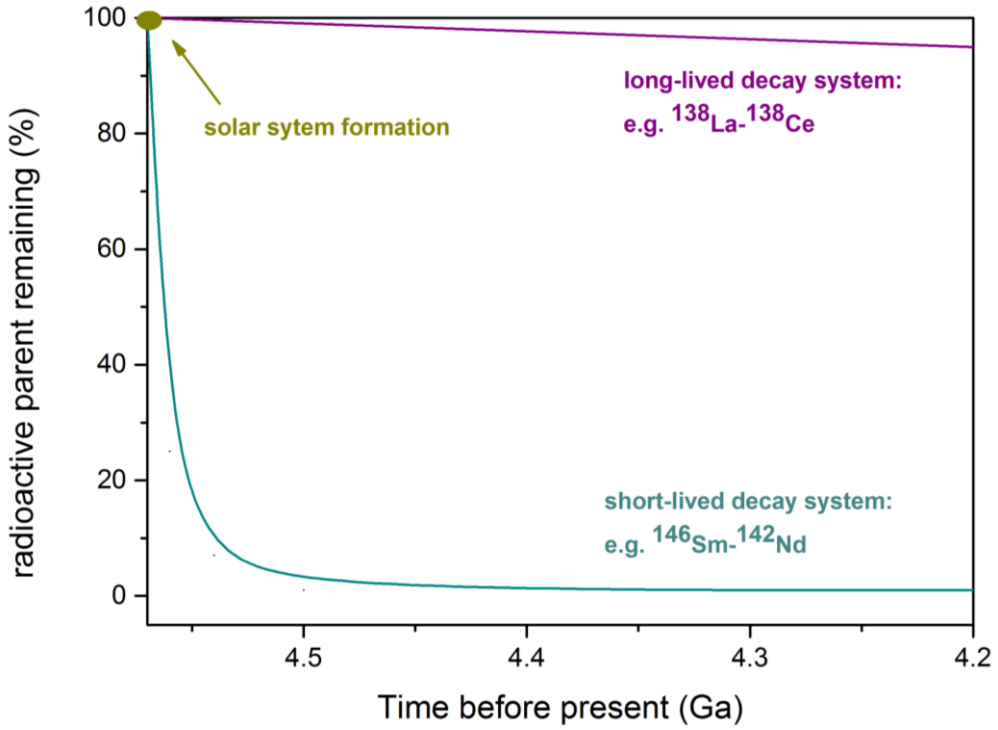

Figure 6 schematic concept of dating with short-lived (e.g. ^{146}Sm-^{142}Nd) and long-lived isotope decay systems (^{138}La-^{138}Ce).

The pioneering study of Harper and Jacobsen (1992) showed first the terrestrial variability (+30 ppm) in ^{142} Nd /^{144}Nd between ~3.8 Ga old supracrustal rocks from Isua, West Greenland and BCR-1. The study of Boyet and Carlson (2005) determined that measured chondrites show an offset of about -0.2 ε^{142}Nd relative to the La Jolla terrestrial Nd standard.

High-precision Nd isotope analyses of bulk meteorites have subsequently been performed by several authors (Andreasen and Sharma (2006)), Fukai and Yokoyama (2017), Bouvier and Boyet (2016), Gannoun et al. (2011)). Andreasen and Sharma (2006) showed that carbonaceous chondrites display a deficit of ^{144}Sm in contrast to other meteorites and terrestrial standards and therefore about 11 ppm decrease in $^{142}Nd/^{144}Nd$ ratio. The authors conclude that p-process isotopes of samarium and neodymium were heterogeneously distributed in the solar nebula.

The study of Gannoun et al. (2011) confirmed the ε^{142}Nd excess of about +0.2 for ordinary and carbonaceous chondrites relative to the terrestrial samples/standard as found in Boyet and Carlson (2005). In contrast to carbonaceous chondrites, enstatite chondrites (EH and EL) have

a ε^{142}Nd mean value of -10±12 (Gannoun et al. (2011)). Moreover, Boyet et al. (2018) proposed based on ^{146}Sm-^{142}Nd measurements that the enstatite subgroup EL3 reflect the Earth's building blocks because EL 3 samples show similar μ^{142}Nd values (μ^{142}Nd = ε^{142}Nd*100, - 0.8±7.0 (2 s.d.)) ppm as the terrestrial La Jolla Nd standard.

Until now, three main models have been discussed to explain the non-chondritic ε^{142}Nd value in terrestrial samples: 1) the BSE has higher Sm/Nd values than measured for chondrites (Non-chondritic Earth model), e.g. Boyet and Carlson (2005), Carlson et al. (2007)) or 2) a reservoir with sub-chondritic ^{142}Nd/^{144}Nd was generated and has stayed isolated (e.g. Boyet and Carlson (2005), Boyet and Carlson (2006), enriched "hidden" reservoir model) 3) nucleosynthetic anomalies. μ^{142}Nd variations in chondrites and terrestrial standards are caused by the heterogeneous distribution of s-process nuclides in the solar system and the BSE has a chondritic Sm/Nd ratio (Burkhardt et al. (2016)), Bouvier and Boyet (2016) and Fukai and Yokoyama (2017).

Other examples for the isotopically variabilities between different chondrites classes and the Earth are Ti, Cr and Ni (Warren (2011) references therein), Tm/Tm* anomalies (Barrat et al. (2016)) and variable Y/Ho ratios (Pack et al. (2007)). In detail, the study of Warren (2011) and references therein showed that the positive (0 to +5) ε^{50}Ti values of carbonaceous chondrites are well separated from negative (0 to -2) ε^{50}Ti values of non-carbonaceous chondrites, the Earth, the Moon and the Mars. In the case of ε^{54}Cr values the carbonaceous chondrites showed positive (0 to +1.6) ε^{54}Cr values in contrast to non-carbonaceous chondrites which show negative (+0.2 to -1.0) ε^{54}Cr values. This separation between carbonaceous and non-carbonaceous chondrites can also be seen for ε^{62}Ni where carbonaceous chondrites show positive (0 to +0.3) ε^{62}Ni values and non-carbonaceous chondrites show negative (0 to -0.2) ε^{62}Ni. In the study of Barrat et al. (2016) and references therein Tm/Tm* anomalies were determined in different chondrites. Relative to CI values carbonaceous chondrites show Tm/Tm* ratios ≥ 1 and non-carbonaceous chondrites show Tm/Tm* values ≤ 1. The study of Pack et al. (2007) demonstrated that carbonaceous chondrites have a Y/Ho ratio of 25.94 ± 0.08 (2 σ) and the non-carbonaceous chondrites show higher average Y/Ho ratios: 1.3% for L- and H-chondrites and 5.1% for EL 6 enstatite chondrites.

In Chapter 3, 22 different meteorites including carbonaceous chondrites (CM, CK, CV and CO), ordinary chondrites (H, L and LL), and enstatite chondrites (EL and EH) were analyzed to determine La and Ce concentrations as well as Ce isotope measurements combined with Sm-Nd measurements. Chondrite, carbonaceous chondritic and non-carbonaceous chondritic ^{138}La-^{138}Ce values are determined to discuss whether the Earth is chondritic or non-chondritic for the ^{138}La-^{138}Ce isotope system.

1.9. Earth's oldest rocks

Mantle-crust differentiation is subject of ongoing discussions because the terrestrial geological record is very limited; especially for the Hadean eon. The only known Hadean remnants are zircon (4.38 Ga) grains from the Jack Hills region in Western Australia (e.g., Compston and Pidgeon (1986), Wilde et al. (2001) Harrison et al. (2007), Menneken et al. (2007), Valley (2008), Kemp et al. (2010), Nebel-Jacobsen et al. (2010)). A combination of REE and oxygen isotope signatures of silicate inclusions of these Hadean zircons indicate the presence of differentiated magmas and that the temperature of the Earth's surface was cold enough to condensate water, forming the first oceans (e.g., Wilde et al. (2001), Harrison et al. (2007)). The oldest non-controversially dated rocks on Earth are the Acasta gneisses from Canada (ca. 4.03 Ga years, e.g., Stern and Bleeker (1998), Bowring and Williams (1999), Iizuka et al. (2007)).

Studying the Archean crustal evolution yields direct geological information of early planetary differentiation of the Earth. At this time, important geodynamic processes began to establish such as the formation of the first continental crust (CC), and larger scale crustal recycling processes into the mantle. However, the availability of Archean rocks is limited. There are only a few areas such as northern Canada (Acasta gneiss), South Africa (Shabani, Barberton), Western Australia (Narryer, Pilbarablock), Northern Antarctica (Enderby Land), Brazil (São Francisco), Greenland (Itsaq Gneiss Complex), Northwest Russia (Ladoga) and East Asia (Aldan, Anshan, Stanovoy, Omolon) which contain remnants of Archean continental crust (Figure 7). Moreover, studying the early crust formation is complex because of the constant rejuvenation of Earth's crust and thus younger crustal rocks reflect later production/differentiation, recycling processes and metamorphism of rocks.

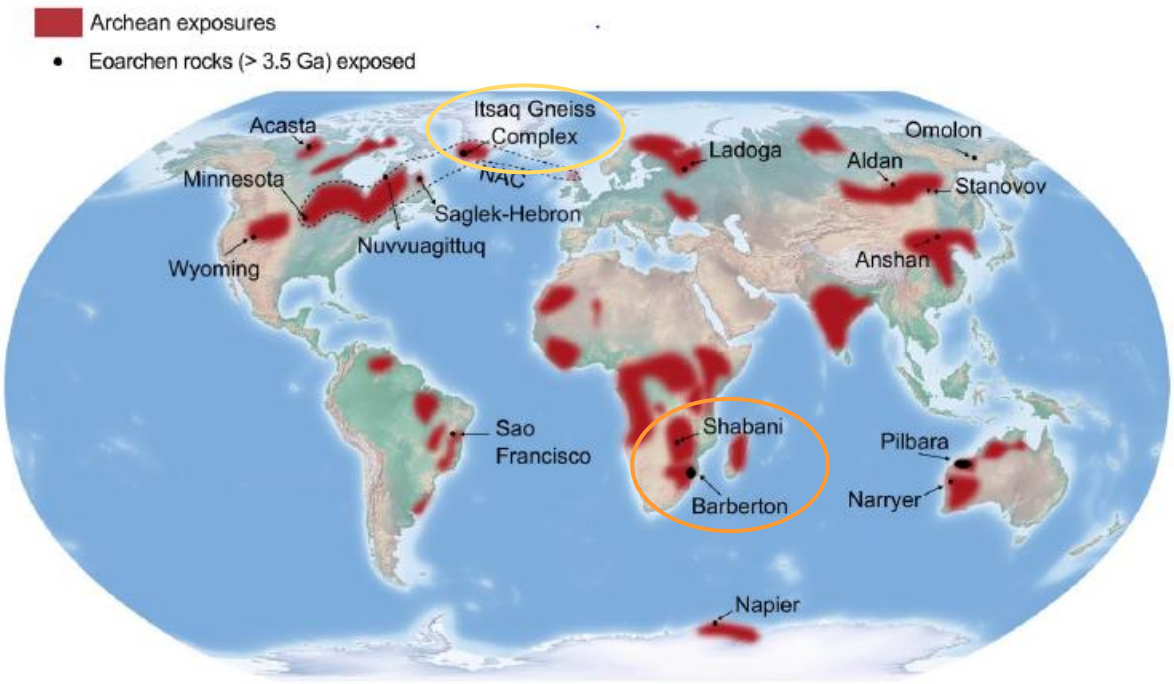

Figure 7 Overview showing the distribution of the Earth's oldest rocks modified after van de Löcht (2019). The areas of Archean cratons are shown in red. Black points show rocks older than 3.5 Ga. In Chapter 4 samples from the Itsaq Gneiss Complex of southern West Greenland (yellow circle), the Barberton Greenstone Belt and Ancient Gneiss Complex of South Africa (orange circle) were analyzed to track Earth's mantle-crust history.

The Itsaq Gneiss Complex of southern West Greenland, the Barberton Greenstone Belt and the Ancient Gneiss Complex of South Africa are key locations for studying Early Earth's mantle-crust differentiation processes. These localities host well preserved exposures of felsic and mafic Archean crustal rocks. In Chapter 4 analyzed samples include mafic, ultramafic and felsic samples from all three localities. Mafic and ultramafic rocks are rich in magnesium (≥ 5 %) and iron. Felsic rocks have a higher SiO_2 content (SiO_2 > 66 %) than mafic (SiO_2: 45-52 %) or ultramafic (SiO_2: < 45 %) rocks. Felsic rocks are mainly produced by partial melting of mafic rocks, whereas the SiO_2 decreases with an increase of the melt proportion. The degree of partial melting depends on temperature and pressure and fluid content, water lowers the melting point of rock and thus, promotes melting. In this study, Tonalite-trondhjemite-granodiorites (TTG) are analyzed. They are the main component of the Archean continental crust. Two models for the TTG (main component of the Archean continental crust) formation in the Archean are commonly assumed (1) formation associated with a subduction-related setting (e.g., Martin (1986), Defant and Drummond, (1990), Kamber et al. (2002)) or (2) formation due to melting of thickened mafic crust (e.g., Smithies (2000), Condie (2005), Bédard (2006), Hoffman et al. (2011)).

1.9.1. Crust-Mantle Models

During decades of research activities several models for the development of Earth's crust and mantle have been proposed based on radiogenic isotope data from felsic and mafic crustal rocks. Figure 8 illustrates the schematic evolution of $\varepsilon^{143}Nd$ and $\varepsilon^{138}Ce$ of the depleted mantle and continental crust relative to CHUR. The CHUR value has by definition $\varepsilon^{138}Ce=0$ and $\varepsilon^{143}Nd=0$. The depleted mantle with lower $^{138}Ce/^{136}Ce$ ratios than CHUR has increasingly negative $\varepsilon^{138}Ce$ over time (presently as low as -1.5, Tazoe et al. (2007), Tazoe et al. (2011), Willig and Stracke (2019), Bonnand et al. (2019)), the continental crust with higher $^{138}Ce/^{136}Ce$ ratios than CHUR has increasingly positive $\varepsilon^{138}Ce$ (present average value: +1.2, Tazoe et al. (2007) and Tazoe et al. (2011)). Because of the covariation of Sm/Nd and La/Ce, the isotope systems behave differently during mantle-crust differentation. The mother nucleus ^{138}La is more incompatible than the daughter nucleus ^{138}Ce during mantle melting and in the case of the ^{147}Sm-^{143}Nd isotope system the daughter nucleus ^{143}Nd is more incompatible during mantle melting than the mother nucleus ^{147}Sm. Therefore, the depleted mantle developed increasing positive $\varepsilon^{143}Nd$ (+12, Salters and Stracke (2004)) over time and the continental crust increasingly negative $\varepsilon^{143}Nd$ (-20, Salters and Stracke (2004)) over time.

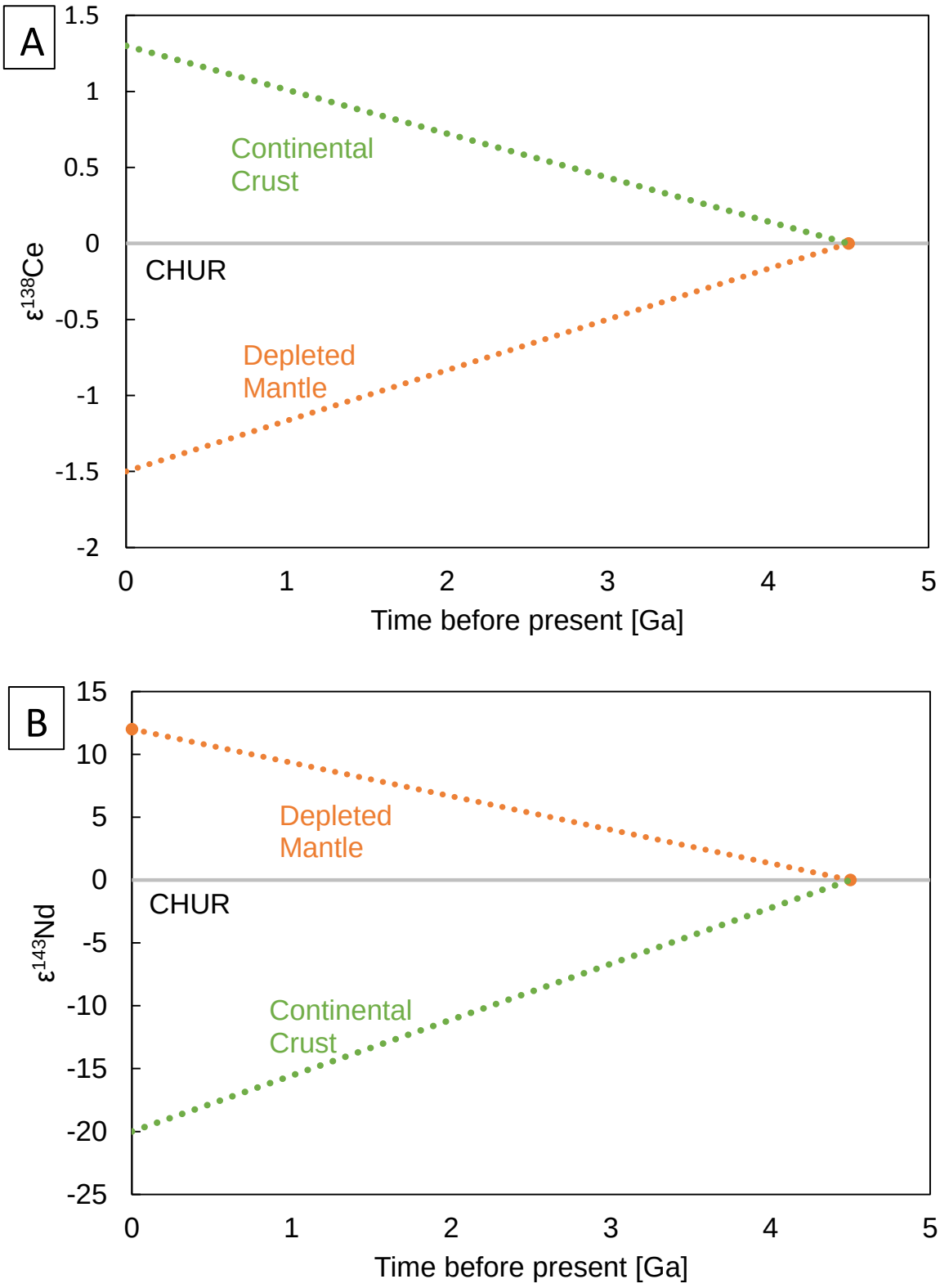

Figure 8 Schematic evolution of $\varepsilon^{143}Nd$ and $\varepsilon^{138}Ce$ of the depleted mantle and continental crust relative to CHUR based on the data from Salters and Stracke (2004), Tazoe et al. (2007) and Tazoe et al. (2011). As mentioned above, the chemical covariation of the ^{147}Sm-^{143}Nd and ^{138}La-^{138}Ce geochronometer during mantle-crust evolution depending on time can be seen. The reason for challenging measurements can also be seen because $\varepsilon^{143}Nd$ measurements would cause results of about +12 for the depleted mantle and -20 for the continental crust. Instead $\varepsilon^{138}Ce$ measurements would cause results of about -1.5 for the depleted mantle and +1.2 for the continental crust.

The first study about mantle-crust differentiation has been published by DePaolo and Wasserburg (1976). Demonstrated, that $\varepsilon^{143}Nd_{initial}$ values in Archean and Proterozoic rocks

(400 to 541 Myrs) were close to that which are expected for the primitive mantle with chondritic Sm/Nd values and $^{143}Nd/^{144}Nd$ ratios. The authors conclude that there was no very early mantle-crust differentiation and no re-mixing of ancient crust and mantle reservoirs before the formation of the oldest cratons. However, at present-day it is well established that mafic rocks (>3.8 Ga) show positive $\varepsilon^{143}Nd_{initial}$ values through time (e.g. Blichert-Toft et al. (1999), Moorbath et al. (1997), Caro (2011) and references therein).

As example, three popular/standard mantle-crust differentiation models that assume a chondritic BSE and explain the positive $\varepsilon^{143}Nd_{initial}$ values in terrestrial rocks are shortly discussed in the following: the constant crust model (Amstrong, (1991)), the early enriched reservoir model (EER, e.g., Boyet and Carlson (2005), Boyet and Carlson (2006)), and the 4-reservoir model (Hoffmann et al. (1986) and Caro and Bourdon (2010)).

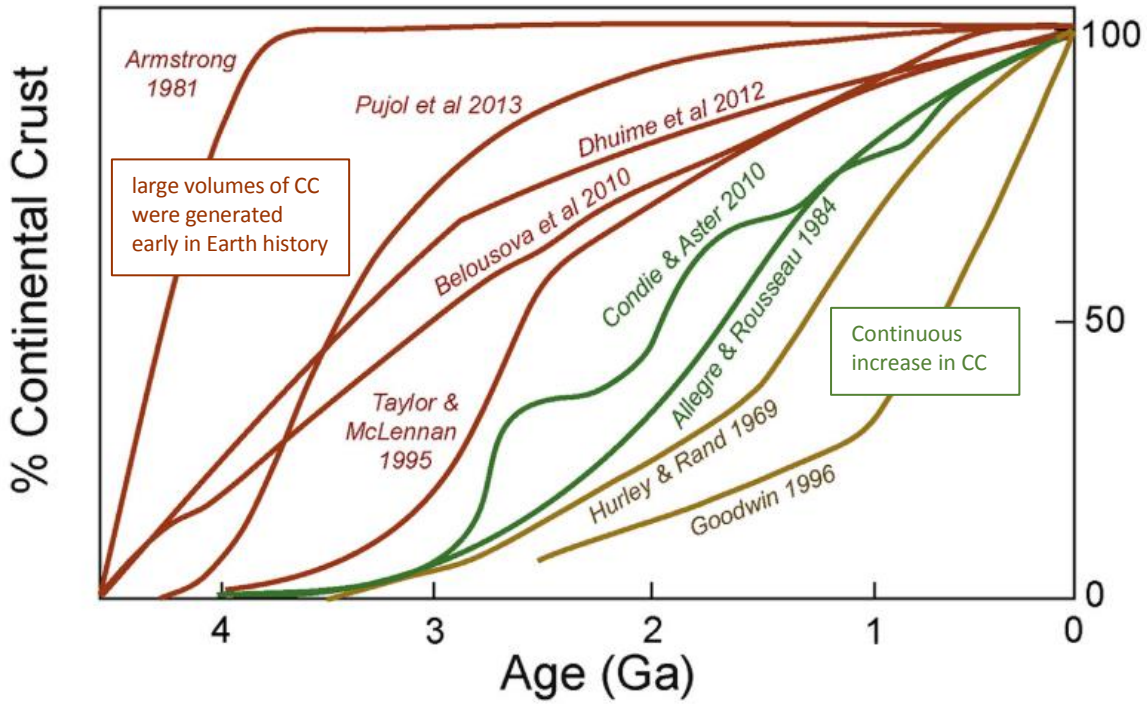

Figure 9 crustal growth models modified after Hawkesworth et al. (2019). The different colors show different models of crustal growth. The brown curves are based on the models where large volumes of continental crust (cc) were generated early in Earth history (e.g. Armstrong (1981)). The green colored lines invoke a continuous increase in the net volume of continental crust [%] from the Archean to the present day (e.g. Allegre and Rousseau (1984)).

One endmember model is the Constant Crustal Mass (CCM) model presented by Armstrong (1991) (Figure 9). The author concludes that positive observed $\varepsilon^{143}Nd$ values in the Archean mantle can be explained by formation of the continental mass prior to 4 Ga. According to this model, the continental mass has remained in a steady-state under balanced production and recycling back into the mantle. However, several studies (Allegre et al. (1980), Christensen and Hofmann (1994), Sun (1980), Tatsumoto (1978)) report evidence for mantle-crust exchanges in relatively recent times. Vervoot et al. (1999) showed constant depleted mantle

evolution for $\varepsilon^{143}Nd$ and $\varepsilon^{176}Hf$ using samples of different ages (from 0 to 3.8 Ga). A schematic depleted mantle evolution for $\varepsilon^{143}Nd$ is shown in Figure 8.

Common mantle-crust differentiation models (early enriched reservoir: EER) that assume a chondritic BSE, postulate early depletion of large parts of the Earth's mantle due to continuous continental crust formation. Such a significantly depleted mantle was the source of MORB that exhibit positive $\varepsilon^{143}Nd_{initial}$ values. The models further postulate a long-lived reservoir with low Sm/Nd and subchondritic $\varepsilon^{143}Nd$ in order to balance the accessible silicate reservoirs (i.e., the crust and the source reservoirs of oceanic basalts) (e.g. Shirey et al. (2008) and references therein). This model only works if the depleted mantle represents about 25% of the bulk silicate Earth because otherwise the extraction of the present-day continental mass would only generate $\varepsilon^{143}Nd$=+2 in the depleted mantle (Caro, (2011)). $\varepsilon^{143}Nd$ composition for MORB are between +7 and +12 (DePaolo and Wasserburg (1976), Richard et al. (1976), Salters and Stracke (2004)).

An alternative mantle-crust evolution model (4-reservoir model) was presented by Caro and Bourdon (2010) and based on the results from the pioneering study of Hoffmann et al. (1986). The 4-reservoir model involves a first stage differentiation from the primitive mantle into the continental crust and residual mantle, followed by a second differentiation of the residual mantle into the depleted mantle and recycled oceanic crust. This model is also limited to reach the observed $\varepsilon^{143}Nd$ +9 units for MORB samples (assuming chondritic BSE) (Figure 10).

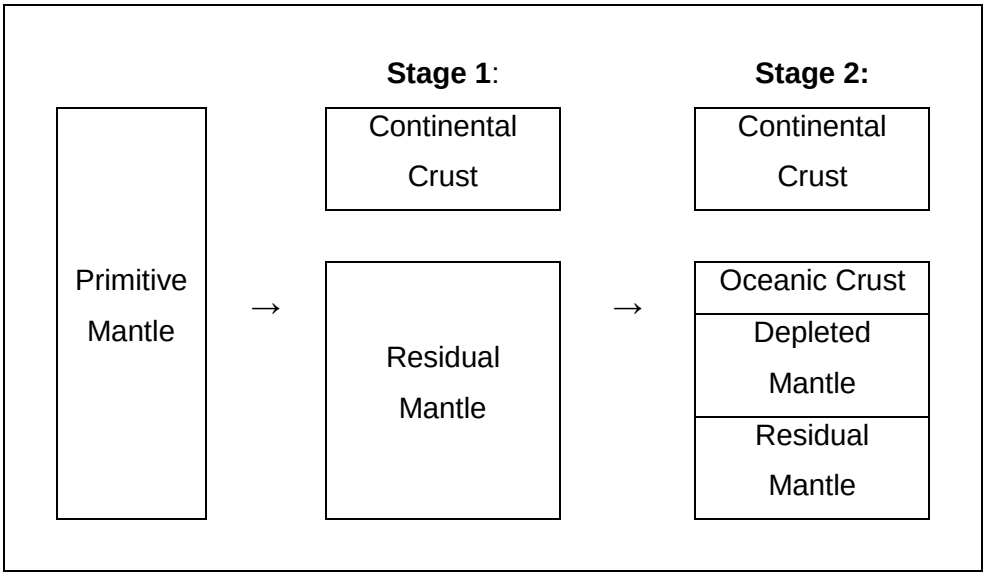

Figure 10 schematic illustration of the 4-reservoir model modified after Caro and Bourdon (2010). This model is based on a first stage differentiation from the primitive mantle into the continental crust and residual mantle, followed by a second differentiation of the residual mantle into the depleted mantle and recycled oceanic crust.

In Chapter 4 samples from South Africa and Greenland were analyzed and the ^{138}La-^{138}Ce isotope system was applied to track the Earth's mantle-crust history. The sample set comprises previously studied felsic, mafic and ultramafic Archean crustal rocks from the Isaq Gneiss

Complex, southwest Greenland (Hoffmann et al. (2011), Hoffmann et al. (2014), van de Löcht et al. (2018), van de Löcht (2019)) and from Barberton Greenstone Belt and Ancient Gneiss Complex South Africa (Schneider et al. (2018), Schneider et al. (2019)). These samples have been previously investigated in terms of their Lu-Hf and Sm-Nd isotope composition used for the Lu-Hf and Sm-Nd isotopes system.

As outlined in this chapter, there are still open questions regarding mantle-crust differentiation and chemical composition of the building blocks of Earth and further research is required. An additional geochronometer such as ^{138}La-^{138}Ce will contribute important information to this discussion. The ^{138}La-^{138}Ce isotope system behaves covariant to the ^{147}Sm-^{143}Nd isotope system because during mantle melting the mother nuclide ^{138}La is more incompatible than the daughter nuclide ^{138}Ce. In the case of ^{147}Sm-^{143}Nd the daughter nuclide ^{143}Nd is more incompatible during mantle melting than the mother nuclide ^{147}Sm. Due to the inverse compatibility of these isotope systems the ^{138}La-^{138}Ce isotope system can be used to evaluate the model of a non-chondritic Earth.

Chapter 2

La–Ce isotope measurements by multicollector- ICPMS

2.1. Introduction

The nuclide ^{138}La (relative abundance 0.089%) decays by branched decay to both ^{138}Ce (0.25%) and ^{138}Ba (71.66%) with a long half-life ($1.02*10^{11}$ years, Sonzogni (2003)) by β^- decay and electron capture (EC), respectively (Figure 11).

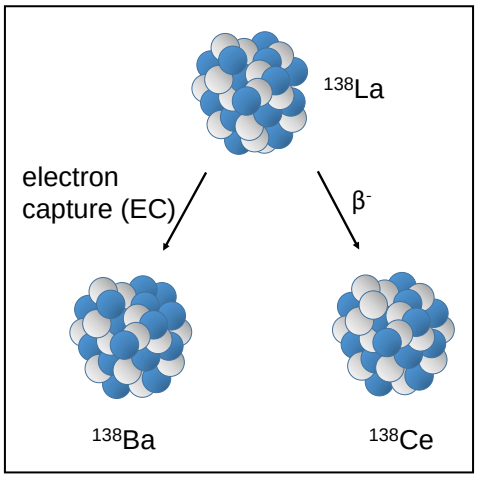

Figure 11 Sketch illustrating decay of ^{138}La to stable ^{138}Ba (electron capture (EC), 65.5%) and ^{138}Ce (β^- decay, 34.4%, $t_{1/2}=1.02*10^{11}$ years)

Due to a different behavior of La and Ce during geological processes, the ^{138}La-^{138}Ce isotope system can provide viable geological information, especially when coupled with other radiogenic isotope systems like ^{147}Sm-^{143}Nd and ^{176}Lu-^{176}Hf. So far, previously published analytical protocols for the ^{138}La-^{138}Ce decay system focused on thermal ionisation mass spectrometry (TIMS) (Willbold (2007), Bellot et al. (2015), Tanaka and Masuda (1982), Masuda et al. (1988)).

Pioneering studies on the ^{138}La-^{138}Ce geochronometer in the 1980's focused on age determinations (Tanaka and Masuda (1988)). Since this first geochemical application, the ^{138}La-^{138}Ce isotope system has also been used as a geochemical tracer (Nakamura et al. (1984), Simizu et al. (1984), Tanaka et al. 1987, Dickin (1987), Dickin et al. (1987), Dickin (1988), Shimizu et al. (1988), Shimizu et al. (1990), Amakawa et al. (1991), Shimizu (1992), Tanimizu and Tanaka (2002)). In the past, Ce isotope measurements have shown to be very challenging because of the isobaric interference from ^{138}Ba (relative abundance 71.7%) on ^{138}Ce (0.251%) and of ^{142}Nd (27.2%) on ^{142}Ce (11.114%). A further challenge is the simultaneous measurement of all Ce isotopes due to the extremely high abundance of ^{140}Ce

(88.450%) relative to the much smaller ^{136}Ce (0.185%) and radiogenic ^{138}Ce (0.251%) (Berlund and Wieser (2011)).

Interfering elements such as Ba and Nd can be separated from Ce by cation-exchange chromatography. The first routine protocol for Ce separation was introduced by Tanaka and Masuda using α-hydroxy-isobutyric acid (α-HIBA) and a AG50W-X8 resin columns (Tanka and Masuda (1982)). Similar procedures based on this separation scheme have been further developed for rock samples (Nakamura et al. (1984), Makashima and Nakamura (1991), Makashima and Masuda (1994), Makashima and Masuda (1994), Doucelance et al. (2014)). The separation of Ce from other REE using an oxidative extraction technique was first proposed by Rehkämper et al. (1996). Tazoe et al. (2007) proposed the separation of Ce using oxidative extraction technique with chelating resin (Ln Spec). Ohno and Hirata (2013) used a combination of a TRU Spec resin column and a LN Spec column to separate Ce.

Previous isotope measurements of Ce in geological material have been performed using TIMS or MC-ICP-MS (Willbold (2007), Bellot et al. (2015), Tanaka and Masuda (1982), Masuda et al. (1988), Ohno and Hirata (2013)). In all of these studies, only the isotopes ^{136}Ce, ^{138}Ce and ^{142}Ce were measured, with two exceptions where ^{140}Ce was also measured (Dickin (1982), Dickin et al. (1987)). In most previous studies, ^{138}Ce abundances were reported as ^{138}Ce/^{142}Ce (Bellot et al. (2015), Masuda et al. (1988), Amakawa et al. (1991), Shimizu et al. (1996), Lee et al. (2001)). As reference material, JMC-304 Ce has been predominantly used as a synthetic standard, and BCR-1 as a natural geological standard (Makashima and Masuda (1994), Makashima and Masuda (1994), Makashima and Masuda (1993), Makashima et al. (1993)). In few studies, no measurements of reference materials were explicitly reported, making direct comparisons of reported Ce isotope values for geological samples difficult (Dicken et al. (1987), Dickin (1988), Xiao et al. (1994)). In more recent studies, AMES Ce metal prepared at MPI Mainz was introduced (below referred to as Mainz-AMES) and proposed as a reference standard material, as the original stock of JMC-304 is not commercially available anymore (Willbold (2007), Bellot et al. (2015), Doucelance et al. (2014)). A direct comparison of Ce isotope data from different studies is therefore not straightforward and there is an urgent need for validated and widely available reference material.

Precise and accurate concentration measurements of La and Ce are required for age correction of measured Ce isotope values and for isochron dating. However, sufficiently precise measurements by employing isotope dilution have rarely been performed (Nakamura et al. (1984), Shimizu et al. (1992), Makashima and Masuda (1994), Makashima and Masuda (1993)). The goal of this work is the development of an analytical protocol for sufficiently precise and accurate Ce isotope and La-Ce concentration measurements for geological samples using MC-ICP-MS. Two new synthetic reference standards (Cologne-AMES and JMC-304 batch number: 15952) were prepared and calibrated against the Mainz-AMES

standard used in previous studies. Additionally, for concentration measurements, a ^{138}La-^{142}Ce spike was prepared and calibrated. The new protocol has been validated by performing combined Ce isotope and La-Ce concentration measurements by isotope dilution on a variety of geological reference materials.

2.2. Analytical Protocols

2.3. Reagents and sample digestion procedures.

For comparison with previous studies, a new JMC-304 solution was prepared from an own batch of JMC-304 Ce-oxide (batch number: 15952). In 2007, Willbold prepared a new reference material from Ce-AMES metal (Mainz-AMES). In addition to this reference material, a new solution was also prepared from Ce-AMES metal during the course of this study (below referred to as Cologne-AMES), expecting that both synthetic Ce-AMES standards are isotopically indistinguishable. These 3 different standards (Mainz-AMES, Cologne-AMES and Cologne-JMC-304) were all used as reference solutions for Ce-IC and Ce-ID measurements in our study and were also calibrated relative to each other in terms of their Ce isotope composition. Additionally, a diluted La-Alfa Aesar^{TM} standard solution and a La solution prepared from AMES metal were used as reference materials for La-ID measurements.
Concentrated HF (24M), HCl (12M) and HNO_3 (14M) were single-distilled to minimize acid blanks which were monitored before each batch of samples. Reagent grade H_2O_2 (30%) and $KBrO_3$ (purity ≥99.8%) were used. The total Ce chemistry blanks for isotope measurements ranged from 286 pg to 567 pg and can be neglected. Depending on the Ce concentrations, 70-240 mg of sample was used for measurements. The reference materials BHVO-2, BCR-2, JG- 1, BCR-1, JB-3 and BIR-1 provided by USGS and GSJ and an in house standard (La Palma basalt LP-1) were analyzed during the course of this study. These samples were digested in a 1:1 mixture of HF (24N) and HNO3 (14N) at 120°C in Savillex® Beakers on a hotplate. The standards AGV-1, JR-1, JB-1b and JA-2 also provided by USGS and GSJ were digested in a 1:1 mixture of HF (24N) and HNO3 (14N) at 180°C in Parr® bombs to ensure complete dissolution of refractory minerals. After both digestion steps, 1mL of $HClO_4$ was added to prevent precipitation of La/Ce-bearing fluorides. Following this step, the samples were dried down, re-dissolved once in 2mL HNO_3 (14N), and evaporated to dryness on the hotplate again. Complete dissolution was ensured by dissolving in 6N HCl solution overnight. After digestion, each sample solution was split into two aliquots. One aliquot, typically ca. 90% of the aliquot, was used for Ce isotope measurements (IC cut) while the remaining 10% aliquot (ID cut) was spiked with a mixed La-Ce isotope tracer prepared during the course of this study (see below). The spiked ID cut was put on the hotplate for at least 12 hours to ensure full

sample-spike equilibrium. Both cuts were dried down and each was taken up in 1mL 1N HCl/(0.1N HF) prior to ion exchange chemistry.

2.4. Chemical separation procedures for Cerium isotope measurements (Ce-IC) and La-Ce concentration measurements (La-Ce-ID).

The ion chromatographic procedure for Ce separation consists of three steps (Table 1). In the first step (modified from Patchett and Tatsumoto (1980)), the REE fraction was separated from the bulk matrix using 5 mL cation resin (height = 23.5 cm, internal diameter = 8 mm, BIORAD® AG-50W-X8, 200-400 mesh, hydrogen form). The column was preconditioned in 2 resin volumes (rv) 1N HCl (optional 1N HCl /0.1N HF). The centrifuged sample was loaded in 1mL 1N HCl/(0.1 N HF). After loading, the matrix was eluted with 2.8rv 1N HCl/(0.1N HF). Strontium and Ba were eluted with 10rv 2.5N HCl and 4rv 3N HNO_3, respectively. Finally, the REEs were eluted with 7rv 6N HCl (Figure 12).

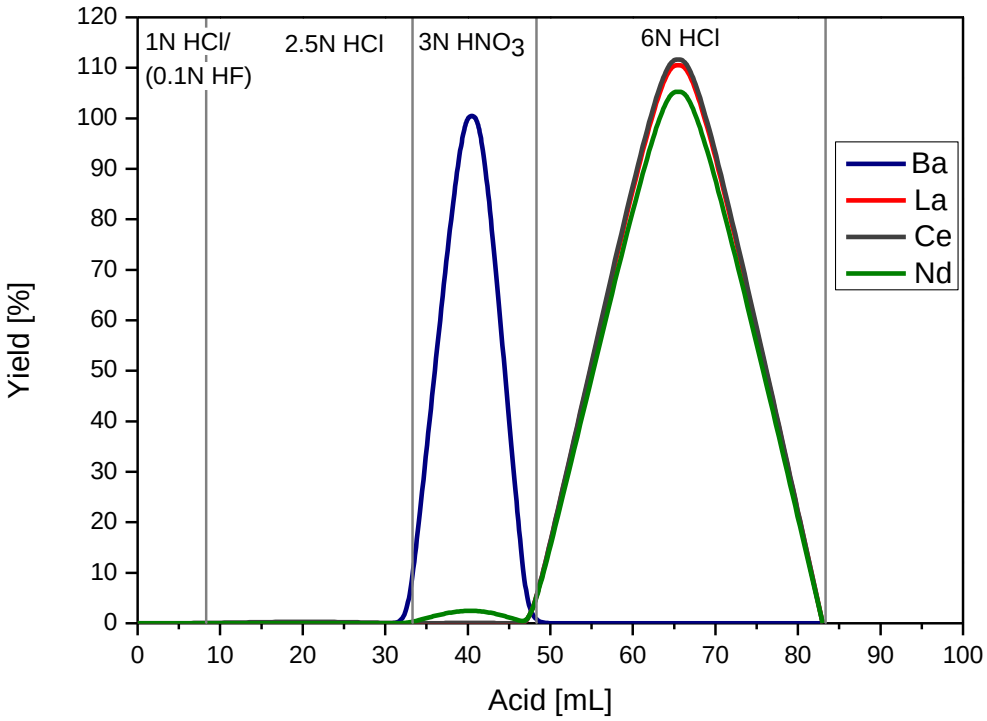

Figure 12 Elution scheme illustrating separation of the REEs from the matrix using cation resin in stage 1

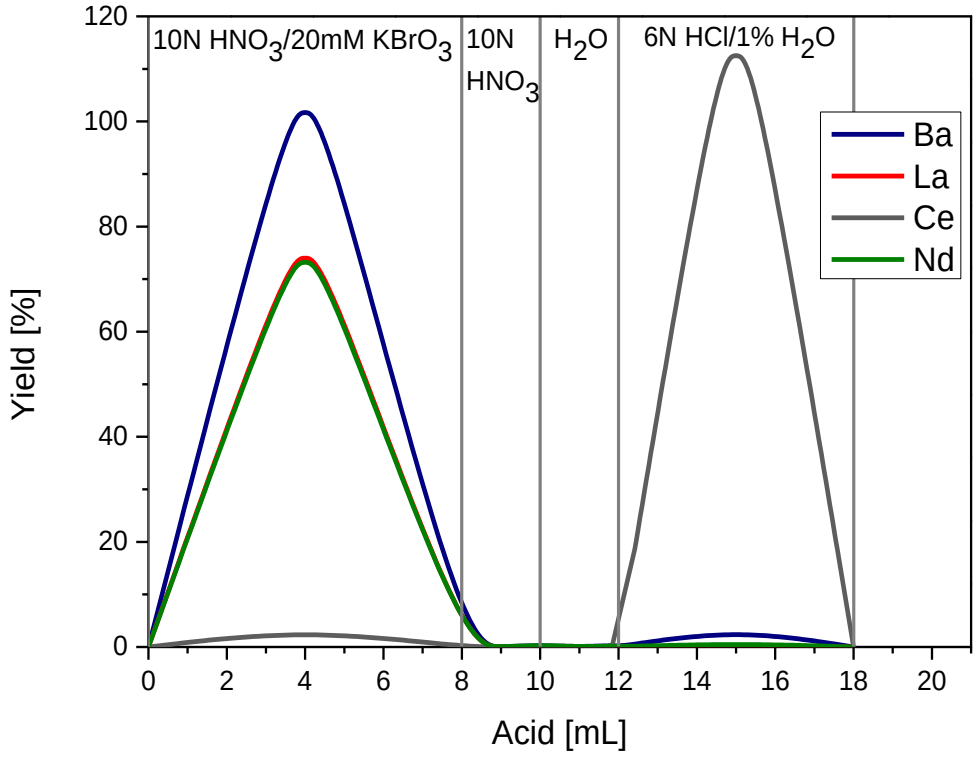

Figure 13 Elution scheme illustrating separation of Ce from REEs using Ln Spec (stage 2)

The second step is based on protocols in Tazoe et al. (2003) and Hirahara et al. (2012). The extracted REE fraction was dissolved in 10N HNO_3/20mM $KBrO_3$ and loaded onto a 0.5mL Ln Spec® resin column (height = 8.5 cm, internal diameter = 5 mm). In this step, Ce^{3+} is oxidized to Ce^{4+}, while all other REEs remain in trivalent state. For cleaning, the column was rinsed two times with 4rv 10N HNO_3 and conditioned three times with 4rv 10N HNO_3/20mM $KBrO_3$. Trivalent REEs were subsequently eluted with 16rv 10N HNO_3/20mM $KBrO_3$ and Ce was eluted as Ce^{3+} after reduction with 6N HCl/1% H_2O_2 (Figure 13). The yields of Ce were generally very high, with more than 95%. The collected Ce fraction was dried down and re-dissolved two times in 250µL 14N HNO_3 with 10µL H_2O_2 and subsequently taken up in 0.5mL 3N HNO_3 for clean-up chemistry.

In the third step, a clean-up of the Ce was performed to remove remaining Ba and K. This separation step is based on the last 2 steps of the first stage chemistry employing cation resin. The dissolved Ce cut was loaded onto a 2 mL AG50-X8 column (height=17cm, internal diameter=7mm) and Ba and K were eluted with 3rv 3N HNO_3. Ce was stripped with 7.5rv mL 6N HCl. The yield of this 3 step column calibration was better than 80%.

In contrast to hitherto published ion-chromatographic procedures, the technique presented here is rapid, because the resin volumes could be reduced and pH-dependent α-HIBA is not used anymore (Bellot et al. (2015)). In addition, this technique could be used for samples sizes up to 250mg (Hirahara et al. (2012)) and an efficient clean-up chemistry was developed to remove all remaining impurities. Otherwise, no accurate measurement by MC-ICP-MS is possible.

For La- and Ce-ID measurements, the same ion exchange procedure as described above was used, except for collecting the complete REE^{3+} fraction in the 2nd column stage and a small modification in the clean-up chemistry. During the clean-up chemistry, the first 3rv 6N HCl in the stripping step was discarded and only the following 7.5rv 6N HCl was collected because only then all of the La is eluted from the column.

Table 1 Column dimensions and three-stage column separation procedures for our La-Ce protocols: (1) separation of REE from matrix elements; (2) separation of Ce from all other REE or La using redox conditioning; (3) clean- up chemistry for La and Ce cuts.

1	**BIORAD AG-50W-X8** (Resin Volume: 5mL)	
Step	Resin Volumes (rv)	Acid
precondition	2 rv	1N HCl/(0.1N HF)
load sample	0.2 rv	1N HCl/(0.1N HF)
rinse matrix	2.8 rv	1N HCl/(0.1N HF)
Sr	10 rv	2.5 N HCl
Ba	4 rv	3N HNO3
REE	7 rv	6N HCl
cleaning	10 rv	6N HCl
	10 rv	3N HNO_3

2	**LN-SPEC®** (Resin Volume: 0.5mL)	
Step	Resin Volumes (rv)	Acid
cleaning	12 rv	10N HNO_3
precondition	12 rv	10N HNO_3/20mM $KBrO_3$
eluting REE^{3+}	16 rv	10N HNO_3/20mM $KBrO_3$
washout	4 rv	10N HNO_3
washout	4 rv	Milli Q
eluting Ce^{3+}	10 rv	6N HCl/1% H_2O_2

3	**BIORAD AG-50W-X8** (Resin Volume: 2mL)			**BIORAD AG-50W-X8** (Resin Volume: 2mL resin)	
Step	Resin Volumes (rv)	Acid	Step	Resin Volumes (rv)	Acid
precondition	5 rv	3N HNO_3	precondition	5 rv	3N HNO_3
load sample	0.25 rv	3N HNO_3	load sample	0.25 rv	3N HNO_3
eluting Ba, K	3.25 rv	3N HNO_3	eluting Ba,K	3.25 rv	3N HNO_3
washout	3 rv	6N HCl	eluting Ce	7.5 rv	6N HCl
eluting La	7.5 rv	6N HCl	cleaning	10 rv	6N HCl
cleaning	10 rv	6N HCl		10 rv	3N HNO_3
	10 rv	3N HNO_3			

2.5. Preparation of a mixed La-Ce isotope tracer

In order to accurately calibrate the mixed La-Ce tracer solution, gravimetric dilution was performed by using a Mettler Toledo analytical balance to prepare one mixed standard solution from concentrated stock solutions of each element, using 99.996% pure La and 99.996% pure Ce metal ingots provided by AMES laboratory as starting material. The metals were first dissolved in 14N HNO_3 and then ultimately diluted to a 1.4N HNO_3 solution. The element concentrations of the La-Ce normal are known to within 0.1% including all propagated errors (characterization was performed using MC-ICP-MS). A mixed isotope tracer was prepared using two individual concentrated solutions of isotopically enriched ^{138}La and ^{142}Ce, respectively. To prepare these concentrated solutions, ca. 0.87mg of $^{138}La_2O_3$ powder (^{138}La enrichment 7%, Oak Ridge National Laboratory, USA) and ca. 47mg of $^{142}CeO_2$ powder (^{142}Ce enrichment 95.1%, Campro Scientific, Germany) were each dissolved in 14N HNO_3. Prior to mixing, the purity of both tracer solutions was verified by MC-ICP-MS through the measurement of potentially interfering isobars. The ^{138}La isotope trace solution was checked for the masses 136, 137, 140, 142 and 144 and the ^{142}Ce isotope trace solution was checked for the masses 137, 139 and 144.

The isotope tracer was calibrated using variable mixtures of tracer and normal solutions. For the separation of La and Ce fractions from these mixtures, two different separation procedures were used. In the first calibration run, a 2.5mL Ln Spec column (height=25cm, internal diameter=3.2mm) was preconditioned in 7.5rv 0.15N HCl. The spike/normal mixtures were loaded onto a 2.5mL Ln Spec column in 0.5mL 0.15N HCl, and La was eluted in 7.5rv 0.15N HCl. Cerium was eluted with 17.5rv 6N HCl (Table 2, Figure 14). This method was also tested for the Ce separation of rock samples but for two reasons the method is not used anymore. First, a substantial fraction of Pr was collected together with Ce. Saji et al. (2016) have pointed out that the molecular interference of ^{141}PrH affects the mass ^{142}Nd during MC-ICP-MS measurements. Secondly, the yield of this method varies between different sample matrices, possibly due to non-reproducible redox conditions on the column (Ce^{3+}/Ce^{4+}).

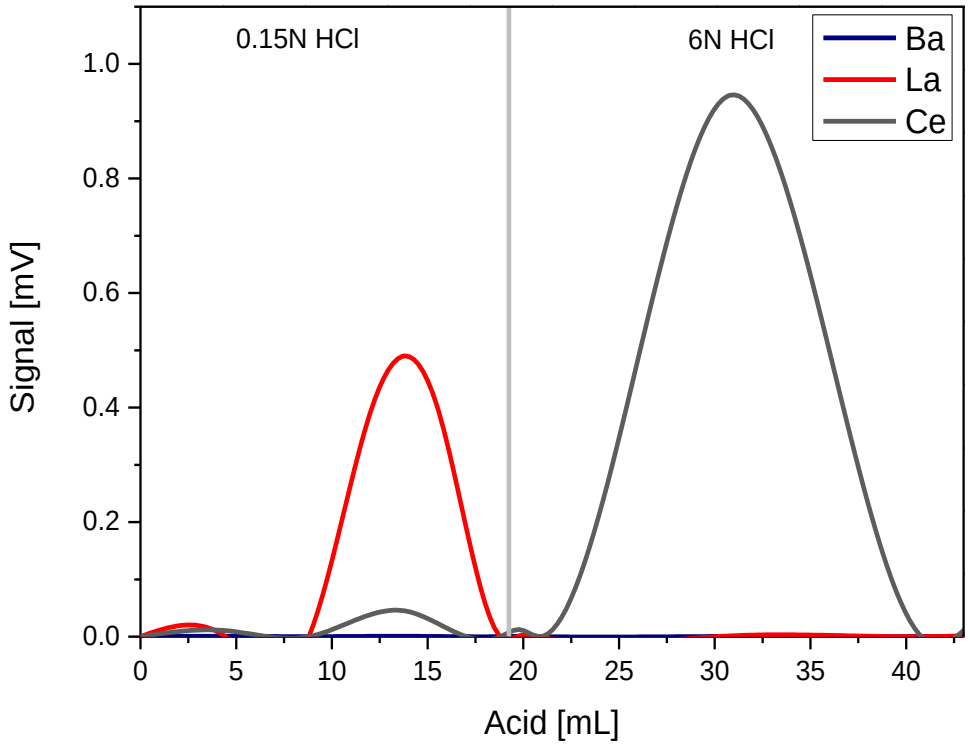

Figure 14 Elution scheme illustrating separation of La and Ce from REEs using a long Ln Spec column (see also Table 2)

The second calibration run was performed employing steps 2-3 of the standard procedure described above (Table 1).

Table 2 Miniaturized separation procedure for La and Ce used for spike calibrations.

	Ln SPEC	
	(Resin Volume: 2.5 mL)	
Step	Resin Volumes	Acid
precondition	7.5 rv	0.15N HCl
load sample	0.2 rv	0.15N HCl
La	7.5 rv	0.15N HCl
REE	17.5 rv	6N HCl
Cleaning	20 rv	6N HCl

In order to determine the isotope compositions and the concentrations of each element in the mixed La-Ce tracer, 9 different mixtures of the spike and diluted AMES metal solution (La-Ce Normal I) were prepared and analyzed after chemical separation. The mass fraction of Ce and La in the mixed spike La-Ce Mix I are 922.6±0.2 ng/g Ce (2r.s.d) and 126.1±1.1 ng/g La (2 r.s.d), respectively. The La/Ce ratio was calculated as 0.1370±0.00004 (2 r.s.d, corresponding to ±0.22%), where errors denote the external reproducibility obtained by the different mixtures. Details and abundances of minor isotopes in the mixed isotope tracer are given in Table 3.

Table 3 Details of the La-Ce mixed isotope tracer

Isotope	^{138}La [µmol/g] [2 r.s.d]	^{142}Ce [µmol/g] [2 r.s.d]	^{138}La/^{139}La [2 s.e.]	^{136}Ce/^{142}Ce [2 s.e.]	^{138}Ce/^{142}Ce [2 s.e.]	^{140}Ce/^{142}Ce [2 s.e.]
	7.128E-05 ±0.16 %	6.183E-03 ±0.12 %	0.08507 ±0.12 %	0.00006 ±0.92 %	0.00010 ±1.42%	0.05200 ±0.01 %

2.6. La-Ce measurements by MC-ICP-MS

2.7. Ce-IC Measurements.

All isotope ratio measurements were performed on a Thermo Finnigan™ Neptune MC-ICP-MS at joint Cologne-Bonn isotope facility. The mass spectrometer was equipped with a Cetac ARIDUS II™ desolvation system to improve the elemental sensitivity. The PFA nebulisers operated at uptake rates of ca. 100µL/min, using 0.14N HNO_3 as measurement solution. If not mentioned otherwise, standard Ni sample cones and H-type skimmer cones were used. All measurements were performed in low resolution mode (R=300). Typical operating conditions are given in Appendix A Table 14. A 10^{10} Ohm amplifier was used for mass ^{140}Ce and two 10^{12} Ohm amplifiers were used for ^{134}Xe and ^{137}Ba, monitoring interferences of ^{136}Xe and ^{138}Ba. The detailed Faraday cup configuration and interferences are shown in Faraday cup configuration for Ce isotope measurements using the Neptune MC-ICP-MS at Cologne/Bonn (Table 4).

Table 4 Faraday cup configuration for Ce isotope measurements using the Neptune MC-ICP-MS at Cologne/Bonn. Isobaric interferences from Ba, La and Nd are shown as well. All measurements were performed in low resolution mode (R=300).

cup	L4	L3	L2	L1	C	H1	H2	H3	H4
measured isotopes	^{134}Xe	^{135}Ba	^{136}Ce	^{137}Ba	^{138}Ce	^{139}La	^{140}Ce	^{142}Ce	^{144}Nd
amplifier	10^{12}	10^{11}	10^{11}	10^{12}	10^{11}	10^{11}	10^{10}	10^{11}	10^{11}
interferences			^{136}Xe, ^{136}Ba		^{138}Ba, ^{138}La			^{142}Nd	

Each analysis consisted of 60 cycles (2 blocks of 30 cycles with 8.389 sec integration time), resulting in ca. 10 minutes of data collection. All Ce isotopes (136, 138, 140 and 142) were measured in static mode. During the different measurement sessions, the ^{140}Ce ion beam intensity was kept at 250-280 V for both standards and samples. Measured Ce isotope ratios were normalized to both ^{136}Ce/^{140}Ce 0.002124072 (Makashima and Nakamura (1991), Makashima et al. (1987)) and ^{136}Ce/^{142}Ce of 0.01688 (Makashima et al. (1987)) to correct for mass bias using the exponential law. The accuracy of measured Ce isotopes ratios is affected by the isobars ^{136}Xe, ^{136}Ba, ^{138}Ba, ^{138}La, and ^{142}Nd. To correct the ^{142}Ce signal, the measured signal on mass 144 was monitored, using a ^{142}Nd/^{144}Nd ratio of 1.141870 (Thirlwall (1991)) that was artificially fractionated using the measured ^{136}Ce/^{140}Ce mass bias and then subtracted from the ^{142}Ce signal. Likewise, the ^{138}Ce signal was corrected for ^{138}Ba and ^{138}La using the measured masses 137 and 139 and artificially fractionated Ba and La isotope abundances

ratios of $^{138}Ba/^{137}Ba$=6.383458 (Berglund and Wieser (2011)) and $^{138}La/^{139}La$=0.000902414 (Makashima et al. 1997). The ^{136}Ce signal was corrected using the measured masses ^{134}Xe and ^{137}Ba and artificially fractionated Xe and Ba isotope abundance ratios of $^{136}Xe/^{134}Xe$=0.848750 (Berglund and Wieder, 2011) and $^{136}Ba/^{137}Ba$=0.699163105 (Berglund and Wieder, 2011), respectively.

The external reproducibility achieved for ^{138}Ce measurements, as determined by multiple analyses of JMC-304, was significantly better, once $^{136}Ce/^{140}Ce$ was used for mass bias correction (±25 ppm) rather than $^{136}Ce/^{142}Ce$ (±40 ppm, all 2 r.s.d). Samples were measured using the standard-sample bracketing approach with our in house JMC-304 solution as standard. In recent studies, Mainz-AMES has been used as reference standard but the amounts of Mainz-AMES available were insufficient to perform larger amounts of measurements (Willbold 2007, Bellot et al. 2015, Doucelance et al. 2014). Therefore, the Mainz-AMES and Cologne-AMES standards were measured relative to our in house JMC-304 solution ca. 3 times before and after the standard-sample bracketing sequence. The daily mean value of the JMC-304 standard were used to calculate $\varepsilon^{138}Ce$ (Equation. 7)

$$\varepsilon^{138}Ce_{JMC\text{-}304} = [(^{138}Ce/^{136}Ce)_{sample}/(^{138}Ce/^{136}Ce)_{JMC\text{-}304}\text{-}1]*10^{4}. \quad \text{Equation 7}$$

Details for re-calculating $\varepsilon^{138}Ce$ from $\varepsilon^{138}Ce_{JMC\text{-}304}$ relative to Cologne-AMES, Mainz-AMES and CHUR can be found below.

The effects of interfering Ba, La and Nd on the accuracy of measured Ce isotope ratios measurements were evaluated using a ca. 600 ppb JMC-304 Ce standard solution doped with each interfering element at different concentrations (Appendix A Table 15 and Figure 15). The accuracy of measured $\varepsilon^{138}Ce$ values is compromised at $^{137}Ba/^{140}Ce$ higher than ca. $4*10^{-6}$, $^{139}La/^{140}Ce$ higher than $2*10^{-2}$, and the accuracy of measured $\varepsilon^{142}Ce$ values is affected at $^{144}Nd/^{140}Ce$ higher than $2.5*10^{-4}$.

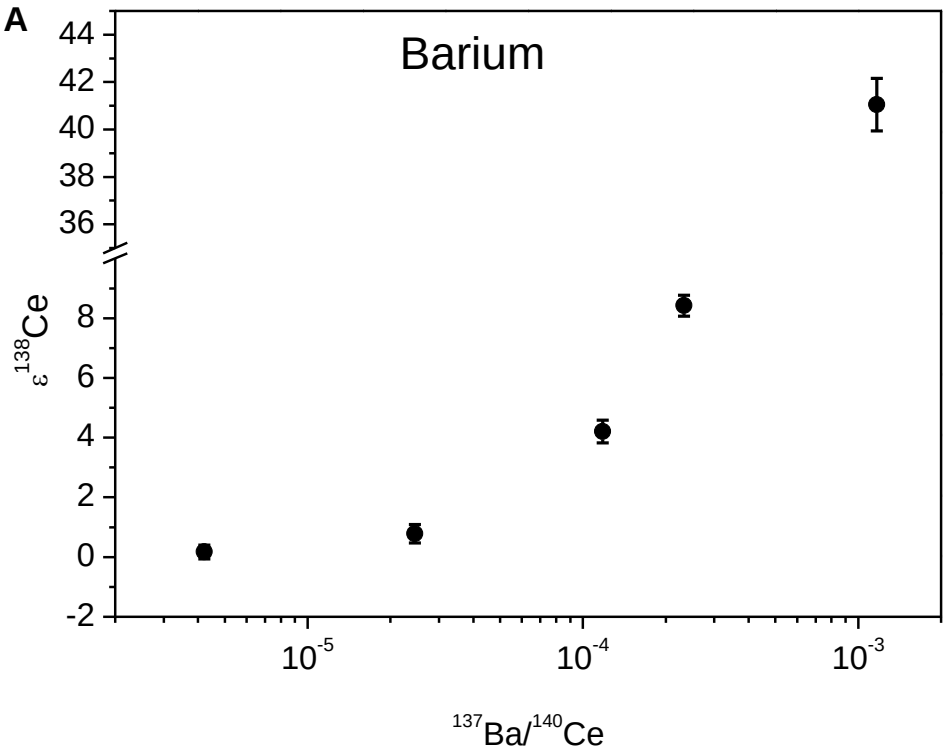
A
Barium
44
42
40
38
36
8
6
4
2
0
-2
ε^{138}Ce
10^{-5}
10^{-4}
10^{-3}
^{137}Ba/^{140}Ce

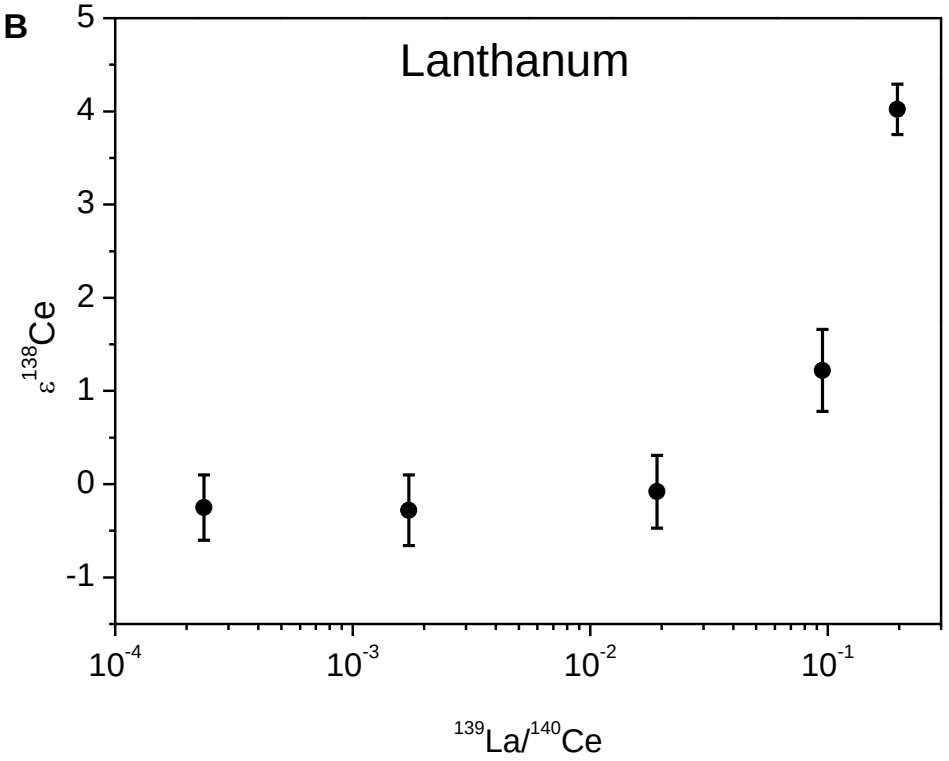
B
Lanthanum
5
4
3
2
1
0
-1
ε^{138}Ce
10^{-4}
10^{-3}
10^{-2}
10^{-1}
^{139}La/^{140}Ce

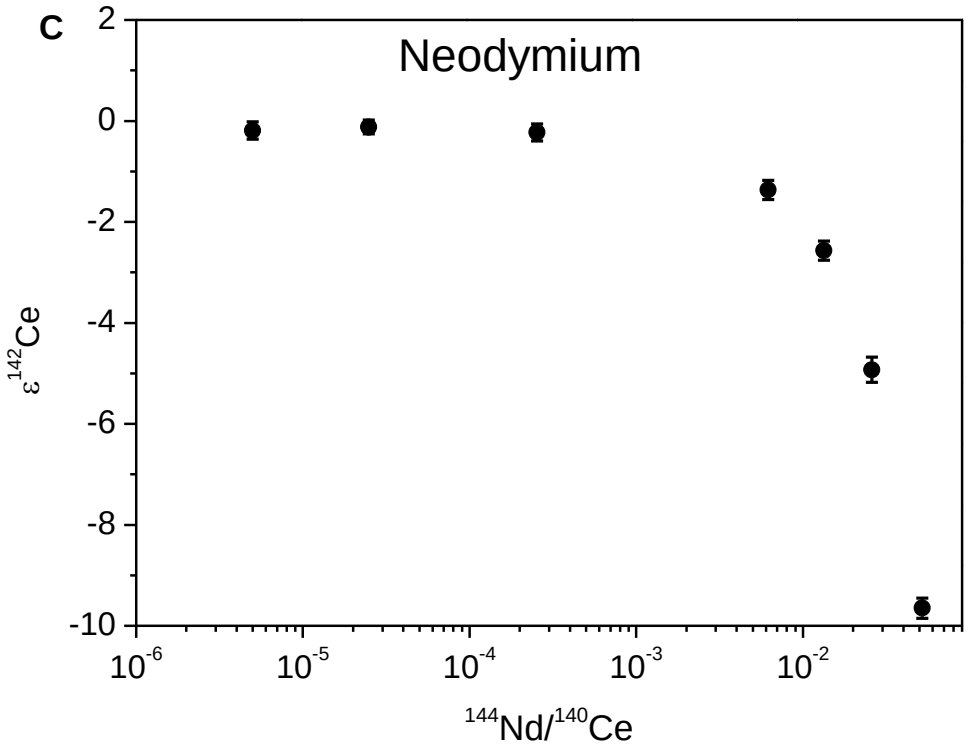

Figure 15 Measured ε[138]Ce values and ε[142]Ce value plotted against measured ratios of (A) [137]Ba/[140]Ce (B) [139]La/[140]Ce (C) [144]Nd/[140]Ce.

Given the typical abundance sensitivity of MC-ICP-MS instruments (during the course of measurements ca. 2 ppm), a tailing correction may be required for isotopes on the low mass side of ^{140}Ce with a relative abundance by a factor of ca. 100 higher than those of ^{138}Ce and ^{136}Ce. In contrast to TIMS measurements, where the instrumental back end vacuum may vary during the course of a single measurement, vacuum conditions during MC-ICP-MS measurements are more stable, as the system is operated in steady-state (Bellot et al. (2015)). Consequently, tail measurements were only made at the beginning and at the end of each analytical session using the JMC-304 standard with the cup configuration shown in Table 5. The integration time was 8.389 seconds with a total number of 30 integrations. Although both tail measurements typically are consistent within the uncertainty, sample standard bracketing was always applied in order to monitor putative short term variations in instrumental vacuum conditions. The tail correction was made offline after the measurement using an algorithm fit (Equation 8) through the individual half mass data points to obtain the best-fit parameters a(1), a(2), and a(3) (Willbold (2007), Pfeifer et al. (2017)).

$$I(m) = a(1) * \exp\left(\frac{m-134.5}{a(3)}\right) + a(4) \qquad \text{Equation 8}$$

Typical values were a(1)=1*10^{-15}-1*10^{-10}, a(3)=0.3-0.2 and a(4)= 1*10^{-5}-1*10^{-6}. The tailing ratio ^{138}Ce/^{140}Ce was then calculated by dividing I(m) by the ^{140}Ce intensity. Throughout the course of our measurements peak tailing varied between 1*10^{-7} and 1*10^{-8}, which is regarded as

negligible, as it only would cause shifts in the measured ^{138}Ce abundances between 0.001 ε-units and 0.0001 ε-units.

Table 5 Faraday cup configuration for ^{140}Ce tail measurements on half masses using the MC-ICP-MS at Cologne/Bonn. Measured values are used together with the corresponding ^{140}Ce intensity to calculate the abundance sensitivity.

Cup	L4	L3	L2	L1	C	H1	H2	H3	H4
Measured mass		135.5		137.5	138.5	139.5	140.5	142.5	144.5
Amplifier		10^{11}		10^{12}	10^{11}	10^{11}	10^{10}	10^{11}	10^{11}

2.8. La/Ce-isotope dilution (ID) measurements

For geochronology the measurement of parent/daughter ratios at high precision and accuracy is necessary. Due to the rapid measurement protocol (5 minutes) MC-ICP-MS is used for isotope dilution measurements. All isotope dilution measurements were performed on a Thermo Finnigan™ Neptune MC-ICP-MS at Cologne/Bonn, but using a different sample introduction system than for the IC measurements (Scott-type glass spray chamber and 50µl PFA nebulizer) in order to avoid memory effects. The Faraday cup configuration for Ce-ID measurements was the same as used for Ce-IC measurements (Table 4) except for the 10^{10} Ohm amplifier on mass 140 that was replaced by a 10^{11} Ohm amplifier. The detailed Faraday cup configuration for La is shown in Table 6. Isotope dilution measurements of La and Ce were performed by measuring ^{138}La/^{139}La and ^{142}Ce/^{140}Ce. Both ratios were mass bias corrected employing doped Ba (Ce) and Nd (La) and using the exponential law for mass bias correction. For external normalization a ^{137}Ba/^{135}Ba value of 1.70383 (Berglund and Wieser (2011)) for Ce and a ^{142}Nd/^{144}Nd value of 1.14187 (Thirlwall (1991)) for La were used, respectively.

Table 6 Faraday cup configuration for La isotope dilution measurements using the MC-ICP-MS at Cologne-Bonn

Cup	L4	L3	L2	L1	C	H1	H2	H3	H4
Isotope	^{136}Ce	^{137}Ba	^{138}La(Ce)	^{139}La	^{140}Ce	^{142}Ce	^{144}Nd	^{146}Nd	^{147}Sm
Amplifier	10^{12}	10^{11}	10^{11}	10^{12}	10^{11}	10^{11}	10^{11}	10^{11}	10^{11}
Interference	^{136}Xe, ^{136}Ba		^{138}Ce(La), ^{138}Ba			^{142}Nd			

2.9. Cerium isotope compositions of synthetic reference materials and rock standards

2.10. Synthetic Reference Materials (JMC-304, Cologne and Mainz-AMES batches).

In this study, three different Ce reference materials were used to evaluate analytical precision, reproducibility and accuracy of the Ce measurements by MC-ICP-MS. The three solutions are (i) Johnson Matthey reference material JMC-304 (batch 15952), (ii) AMES metal solution distributed by M. Willbold (Mainz-AMES) and (iii) AMES metal solution prepared at Cologne (Cologne-*AMES*) As already described above, two highly concentrated (1000 ppm) stock solutions of Ce have been prepared by dissolving 1g high-purity CeO_2 powder (JMC-304 (batch 15952)) and 1g of AMES Laboratory Ce metal (Cologne-AMES) in 14N HNO_3. Splits of these solutions were diluted in 0.1N HNO_3 to running solutions with typical concentrations of 450 ppb.

Results of repeated measurements in one analytical session are shown as example in Figure 16. The mean values for $\varepsilon^{138}Ce$ relative to JMC-304 for this session are -0.03±0.12 (2 r.s.d) for JMC-304, +0.73±0.11 for Cologne-AMES and +2.44±0.14 for AMES. Figure 16 shows also clearly discernable $\varepsilon^{138}Ce$ compositions of the three standards, indicating that Cologne-AMES and Mainz-AMES are isotopically heterogeneous.

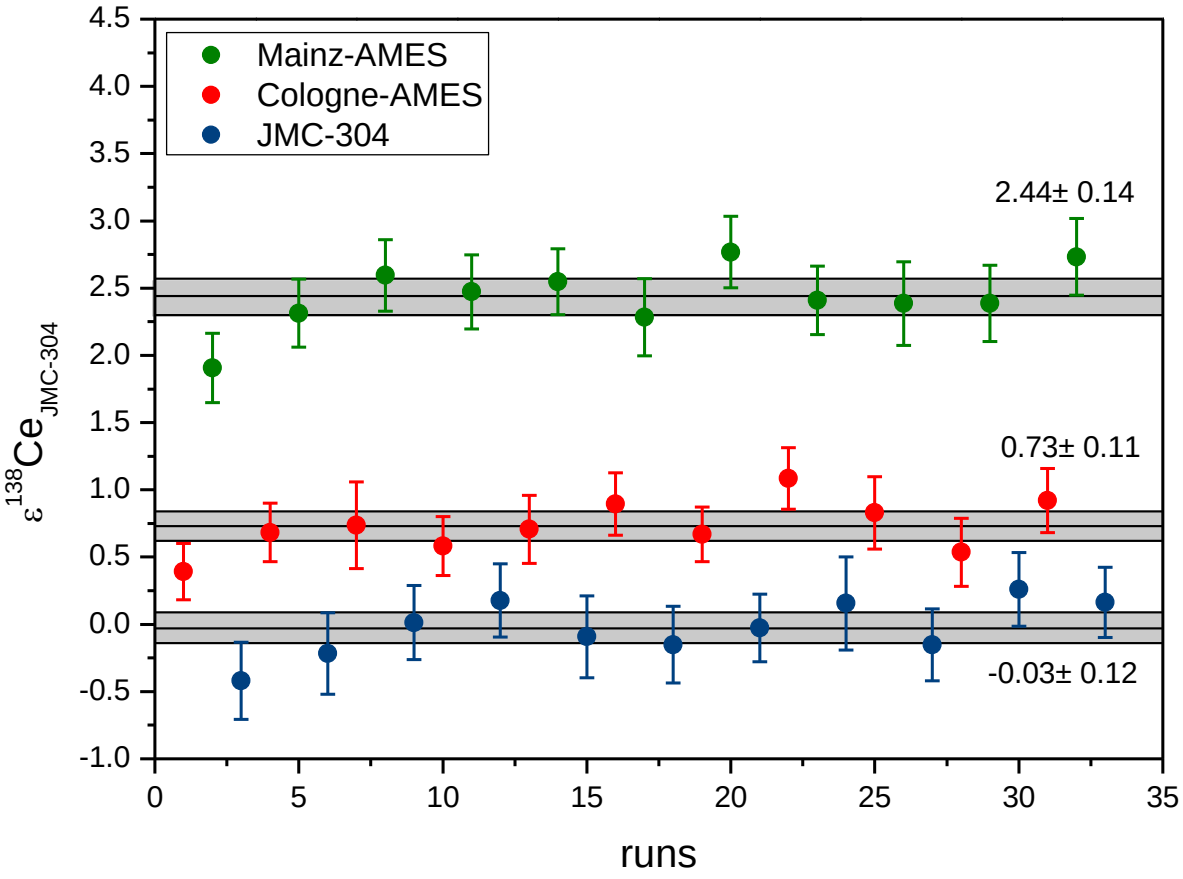

Figure 16 Comparison of ^{138}Ce compositions of (i) JMC-304 reference material, (ii) Cologne-AMES and (iii) Mainz-AMES for a single analytical session (March 2015). All values are given relative to JMC-304. The $\varepsilon^{138}Ce$ value is calculated as $^{138}Ce/^{136}Ce$, normalized to $^{136}Ce/^{140}Ce$ using a $^{136}Ce/^{140}Ce$ of 0.002124072[18,33] and the exponential law. The weighted means of $\varepsilon^{138}Ce$ are -0.03±0.12 for JMC-304, +0.73±0.11 for Cologne-AMES and +2.44±0.14 for Mainz-AMES (all 2 r.s.d).

Results of long term measurements for the standards Cologne-AMES and Mainz-AMES are shown in Appendix A Table 16 and Figure 17. The means for $\varepsilon^{138}Ce$ relative to the JMC-304 are +0.83±0.10 for Cologne-AMES and +2.61±0.09 for Mainz-AMES, respectively. The results are in a good agreement with the results of the single analytical session illustrated in Figure 16.

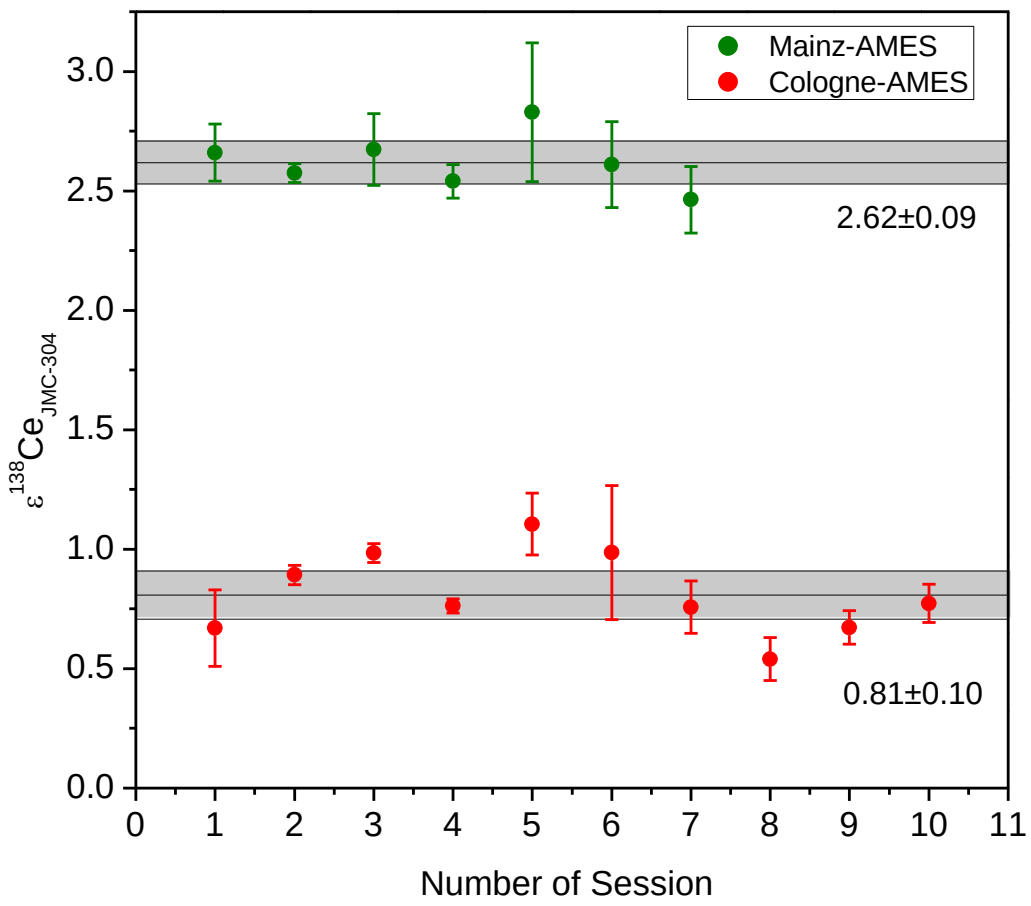

Figure 17 Long term comparison of the ^{138}Ce compositions of Cologne-AMES and Mainz-AMES. All values are given relative to JMC-304, measured during 10 analytical sessions. The weighted means are $\varepsilon^{138}Ce$ +0.81±0.10 for Cologne-AMES and +2.62±0.09 for Mainz-AMES (all 2 r.s.d).

The hitherto published ^{138}Ce isotope values for the JMC-304 standard display a large scatter even after adjusting for the different mass fractionation procedures being applied.[3] A probable source of these differences is the use of different JMC-304 batches that appear to be isotopically heterogeneous. Therefore, any direct data comparison with older studies is difficult because the individual JMC-304 batches used in the different studies have not always been specified. Comparison of data obtained using two different JMC-304 batches relative to Mainz- AMES (this study and Bellot et al. (2015) confirm that the two JMC-304 batches used are compositionally different. Whereas the $\varepsilon^{138}Ce$ value for the JMC-304 batch relative to Mainz-AMES in Bellot et al. (2015) is given as -1.15±0.38 (2 r.s.d), the $\varepsilon^{138}Ce$ value for the JMC-304 batch used in this study relative to Mainz-AMES is -2.46±0.28 (2 r.s.d). Both values are outside analytical uncertainty, confirming that the two JMC-304 batches are clearly isotopically distinguishable.

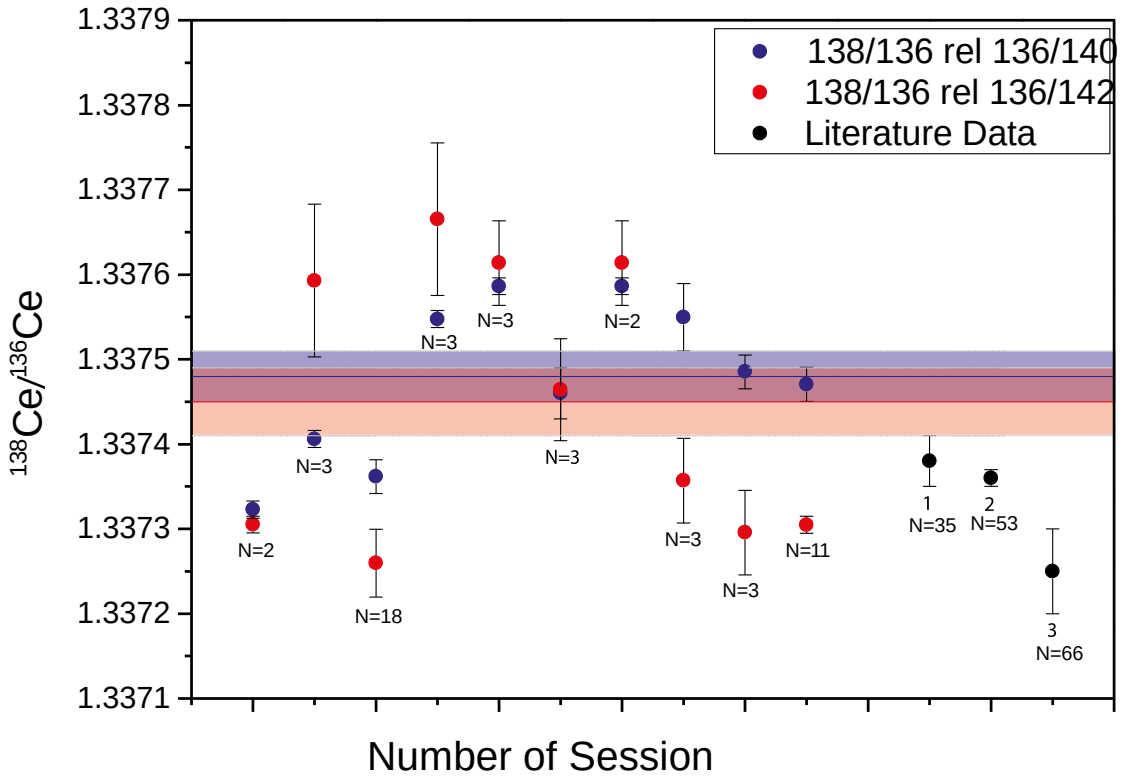

Figure 18 Absolute $^{138}Ce/^{136}Ce$ composition (error bars 2 r.s.d.) obtained for the Mainz AMES standard for 10 different analytical sessions (red/blue dots). The black dots are literature data: 1 Willbold 2007, 2 Doucelance et al.2014, 3 Bellot et al. 2015

Appendix A Table 17 and Figure 18 shows the results of absolute $^{138}Ce/^{136}Ce$ ratio measurements for the Mainz-AMES standard that has previously been characterized (Willbold (2007)). As mentioned above, the tailing effects in this study were negligible and no offline tailing correction was applied. A ratio of $^{136}Ce/^{140}Ce$ of 0.002124072 (Makashima and Nakamura (1991), Makashima et al. (1987)) was initially used in our study to correct the mass bias (blue dots in Figure 16) because the external reproducibility is significantly better. To compare our measured $^{138}Ce/^{136}Ce$ ratios with those obtained in recent TIMS studies (Willbold (2007), Doucelance et al. (2014) and Bellot et al. (2015)), the measured $^{138}Ce/^{136}Ce$ ratios were also normalized to $^{136}Ce/^{142}Ce$ of 0.01688 (Makashima et al. (1987)) and these data are additionally shown in Appendix A Table 17 and Figure 18 (red dots). Importantly, Doucelance et al. (2014) and Bellot et al. (2015) both used this $^{136}Ce/^{142}Ce$ ratio for normalization.

The average absolute $^{138}Ce/^{136}Ce$ normalized to $^{136}Ce/^{142}Ce$ were 1.33738±0.00001 in Willbold (2007), 1.33736±0.00001 in Doucelance et al. 2014, 1.33725±0.00005 in Bellot et al. (2015) and 1.33745±0.00004 in this study (10 individual sessions). The absolute $^{138}Ce/^{136}Ce$ normalized to $^{136}Ce/^{140}Ce$ obtained in this study was 1.33748±0.00003. Both values agree within error, but a tentative systematic difference of +0.52ε-units for $^{138}Ce/^{136}Ce$ normalized to $^{136}Ce/^{142}Ce$ compare to Willbold (2007) and the larger scatter in our study can be explained through non-ideal mass bias correction and cup efficiency. Importantly, the external

reproducibility of our analytical protocol within an individual session is significantly better (±0.25 ε-units), because run parameters are not changed and measured sample values are always referenced to the standards measured in the individual session.

2.11. Recalculation relative to the chondritic uniform reservoir (CHUR) value.

By direct measurements of meteorite samples, Makashima and Nakamura (1991) and Makashima and Masunda (1993) defined the average chondritic uniform reservoir (CHUR) value by an $^{138}Ce/^{142}Ce$ value of 0.0225652±0.0000024 which is in a good agreement with the $^{138}Ce/^{142}Ce$ value of 0.0225654±0.0000007 obtained for two chondrites (Bellot et al. (2015)). Both studies used the same $^{136}Ce/^{138}Ce$ value ($^{136}Ce/^{138}Ce$=0.01688, Makashima et al. (1987)) for mass bias correction. In this study, no meteorites were measured but the same reference standards (Mainz-AMES, JMC-304) were used. A comparison with CHUR values reported in older studies is not straightforward, as the JMC-304 batches used in the different studies do not appear to be homogenous, as pointed out above. If the $\varepsilon^{138}Ce$ of JMC-304 from Makashima and Nakamura 1991 is recalculated relative to their own CHUR value, an $\varepsilon^{138}Ce_{CHUR}$ of +1.46 is obtained for JMC-304. In contrast, the reported $\varepsilon^{138}Ce_{CHUR}$ for JMC-304 relative to CHUR in the study of Bellot et al. (2015) is +2.30. This indicates that the different JMC-304 batches used in these two studies are not identical. If the JMC-304 measurements relative to Mainz-AMES in the Bellot et al. (2015) study ($\varepsilon^{138}Ce_{AMES}$ = -0.93) and in our study ($\varepsilon^{138}Ce_{AMES}$ = -2.61) are now considered, there appears to be clear evidence that different JMC-304 batches have been utilized in all three studies. In summary, our results indicate that JMC-304 is not a suitable standard to accurately cross-reference CHUR values reported from older studies. In our study, the $\varepsilon^{138}Ce$ value reported for Mainz-AMES relative to CHUR of +3.24±0.23 from the study of Bellot et al. (2015) was used for calculating the standard data reported in this study relative to CHUR because two unambiguously identical splits of the same reference standard were used in both studies.

2.12. Cerium isotope composition and La-Ce concentration measurements for geological reference materials.

Both accuracy and precision of our new MC-ICP-MS protocol were further tested by La-Ce measurements of replicate digestions of the geological reference material BCR-2. Five fractions of this basaltic reference standard were digested following the procedure described above. The measured mean $\varepsilon^{138}Ce$ value obtained using a standard Ni sample cone and a H- type skimmer cone (H) is 0.11±0.14 (2 r.s.d) relative to CHUR. Furthermore, the same solutions were measured with an X-Skimmer cone in combination with a standard Ni sample

cone (X) to improve sensitivity. The sensitivity for Ce was improved by a factor of ca. 2.4 using the X-skimmer cone, and a mean ε^{138}Ce value of 0.28±0.33 (2 r.s.d) relative to CHUR was obtained which is indistinguishable within uncertainty. The mean values obtained for the element concentrations of BCR-2 were 24.97±0.22 (2 r.s.d) for La [ppm] and 53.21±0.54 for Ce [ppm], the La/Ce ratio is 0.4693±0.0008. The data are reported in Appendix A Figure 38 and Table 7.

The ε^{138}Ce values obtained for different cone combinations are in a good agreement. As a result, Ce isotope composition studies can also be performed by using a standard Ni sample cone and an X-type skimmer cone, where the amount of sample being required can be decreased by a factor of ca. 2.4. The study of Raczek et al. (2003) showed, that the two rock standards BCR-1 and BCR-2 have indistinguishable Nd isotope compositions. Therefore, it can be assumed that the Ce isotope compositions are also identical (cf. Bellot et al. (2015)). Independent of the cone combination our ε^{138}Ce(CHUR) results are in a good agreement with the result of BCR-1 (Tanaka et al. (1987)). But the ε^{138}Ce(CHUR) value obtained for BCR-2 of this study overlaps barely with a recent TIMS study (Bellot et al. (2015)). Notably, Bellot et al. 2015 assume an analytical bias as cause for the discrepancy of their BCR-2 data and the BCR- 1 data of Tanaka et al.1987. The La-Ce isotope dilution data obtained BCR-2 are in a good agreement with the studies of Raczek et al. (2003) and Baker et al. (2002) that also employed isotope dilution. In addition to multiple analyses of the BCR-2 reference material, further La-Ce analyses were performed for 9 reference rock samples (BCR-1, BHVO-2, JR-1, JA-2, JB-3, JG-1, JB-1b, AGV-1, JR-1) and one La Palma basalt (LP-1, in-house standard). The results are reported in Table 7 and Figure 19.

Table 7 Cerium isotope compositions and La-Ce elemental concentrations obtained for geological reference materials and different types of skimmer cones (X/H) for BCR-2. Ce isotope data are given relative to the average JMC-304 ratio measured during one analytical session and relative to CHUR[3]

Sample	Type of cone	$\varepsilon^{138}Ce$ (JMC-304)	2 r.s.d [ppm]	$\varepsilon^{138}Ce$ (CHUR)	2 r.s.d [ppm]	$\varepsilon^{138}Ce$ (CHUR)/ Literature Data	Ce [ppm]	La [ppm]	La/Ce	$^{138}La/^{136}Ce$	$^{138}La/^{142}Ce$	La/Ce Literature Data
1 BCR-2	H	-0.78	0.30	-0.15	0.30		53.0	24.9	0.4695	0.2280	0.003852	
	X	-0.44	0.36	0.19	0.36							
2 BCR-2	H	-0.46	0.34	0.17	0.34		52.8	24.8	0.4695	0.2280	0.003853	
	X	-0.51	0.29	0.12	0.29							
3 BCR-2	H	-0.37	0.23	0.26	0.23		53.4	25.1	0.4694	0.2280	0.003852	
4 BCR-2	H	-0.59	0.25	0.04	0.25		53.3	25.0	0.4696	0.2281	0.003853	
	X	-0.80	0.39	0.17	0.39							
5 BCR-2	H	-0.88	0.22	0.25	0.22		53.5	25.1	0.4685	0.2276	0.003845	
	X	-1.28	0.25	0.63	0.25							
Mean ± 2 r.s.e	**H**	**-0.61**	**0.14**	**0.11**	**0.14**		**53.2**	**25.0**	**0.4693**	**0.2279**	**0.003851**	
	X	**-0.76**	**0.33**	**0.28**	**0.33**							
JR-1 Batch 1		-1.78	0.31	-1.15	0.31	-1.0±0.4[8]	58.9	36.5	0.6192	0.3014	0.005092	
JB-1b Batch 1	H	-1.41	0.21	-0.78	0.21		68.8	39.6	0.5752	0.2800	0.004730	
JB-1b Batch 2	H	-1.13	0.30	-0.50	0.30		69.2	39.7	0.5746	0.2797	0.004750	
JB-1b Batch 3	H	-0.90	0.24	-0.27	0.24		68.9	39.8	0.5783	0.2815	0.004756	
AGV-1 Batch 1	H	-1.39	0.20	-0.76	0.20		58.8	36.3	0.6164	0.3000	0.005069	0.5651 (Raczek et al. 2003)
AGV-1 Batch 2	H	-1.33	0.20	-0.70	0.20		59.0	37.3	0.6325	0.3078	0.005200	
LP-1 Batch 1	H	-1.95	0.24	-1.32	0.24		170	85.3	0.5008	0.2438	0.004118	
LP-1 Batch 2	H	-1.92	0.19	-1.29	0.19		170	85.0	0.4998	0.2433	0.004110	
BHVO-2 Batch 1	H	-1.93	0.22	-1.30	0.22	-0.35±0.76[3]	37.8	15.4	0.4056	0.1974	0.003335	0.4053 (Raczek et al. 2003)
BHVO-2 Batch 2	H	-2.25	0.24	-1.62	0.24		37.9	15.4	0.4050	0.1971	0.003330	
BCR-2 Batch 1	H	-0.70	0.26	-0.07	0.26	0.39±0.31[3]	53.4	25.3	0.4735	0.2305	0.003894	0.4707 (Raczek et al. 2003)
BCR-2 Batch 2	H	-0.85	0.22	-0.22	0.22		53.4	25.2	0.4714	0.2296	0.003879	0.4712 (Baker et al. 2002)
JG-1 Batch 1	H	-0.57	0.21	+0.06	0.21	-0.8±1.1[8]	54.5	26.3	0.4831	0.2351	0.003973	

Table 7 continued

Sample	Type of cone	ε^{138}Ce (JMC-304)	2 r.s.d [ppm]	ε^{138}Ce (CHUR)	2 r.s.d [ppm]	ε^{138}Ce (CHUR)/ Literature Data	Ce [ppm]	La [ppm]	La/Ce	^{138}La/^{136}Ce	^{138}La/^{142}Ce	La/Ce Literature Data
JG-1 Batch 2	H	-0.20	0.22	+0.43	0.22		39.4	18.6	0.4705	0.2290	0.003870	
JA-2 Batch 1	H	-0.87	0.21	-0.24	0.21		33.6	16.1	0.4791	0.2332	0.003939	
JA-2 Batch 2	H	-0.88	0.21	-0.25	0.21		33.8	16.1	0.4782	0.2327	0.003932	
BCR-1 Batch 1	H	-0.80	0.24	-0.17	0.24	-0.3±0.4[8]	53.8	25.4	0.4714	0.2294	0.003877	0.4709 (Raczek et al. 2003)
BCR-1 Batch 2	H	-0.79	0.26	-0.16	0.26		54.0	25.5	0.4720	0.2298	0.003882	0.4716 (Baker et al. 2002)
JB-3 Batch 1	H	-2.20	0.22	-1.57	0.22	-1.6±1.1[8]	21.3	8.4	0.3958	0.1927	0.003255	
JB-3 Batch 2	H	-2.24	0.22	-1.61	0.22		21.3	8.4	0.3957	0.1926	0.003254	

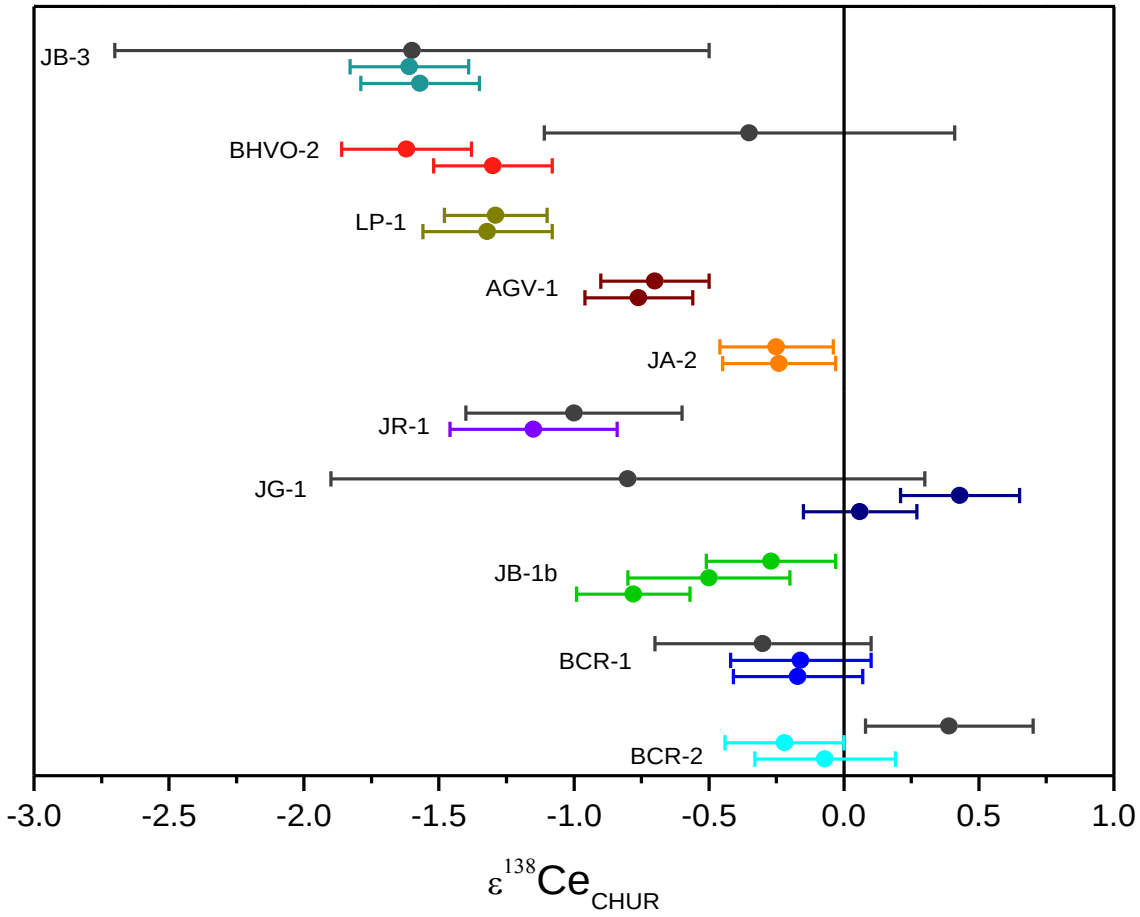

Figure 19 Measured Ce isotope ratios for rock reference samples given in ε-units relative CHUR. Reported uncertainties correspond to 2 r.s.d. Grey dots are literature data from Tanaka et al. (1987) (JR-1, JG-1, JB-3 and BCR-1) and Bellot et al. (2015) (BHVO-2 and BCR-2).

The external reproducibility of our new analytical protocol was tested by multiple processing of BCR-2 (Table 7 and Appendix A Figure 38). The uncertainty for BCR-2 using a standard Ni sample cone and an H-type skimmer cone is ±0.14ε, which is significantly smaller than in previous studies (±0.31ε to ±1.1ε) (Bellot et al. (2015), Tanaka et al. (1987)). The external reproducibility was also assessed for other reference materials by double processing of each sample. The mean $\varepsilon^{138}Ce$ value for all BCR-2 sample using a standard Ni sample cone and an H-type skimmer cone is 0.04±0.14 (2 r.s.d) which overlaps only slightly within error with the value reported in a recent TIMS study. As discussed in the previous section, it is possible that an analytical bias causes a discrepancy of 0.5ε-units (Bellot et al. (2015)). The study of Raczek et al. (2003) showed, that the two rock standards BCR-1 and BCR-2 have the same Nd isotope composition. Therefore, it was previously assumed (Bellot et al. (2015)) that the Ce isotope compositions are also identical which is confirmed by our results (Table 7 and Appendix A Figure 35). The data obtained for BCR-1 in our study are also in a good agreement with literature data for BCR-1, if normalized relative to

CHUR (Tanaka (1987)). The analytical bias mentioned above might also be an explanation for the difference of the BHVO-2 data between our study and the study of Bellot et al. (2015).

The Ce isotope composition and the La-Ce concentration data obtained in this study are in an excellent agreement between two duplicates for the samples BCR-1, BCR-2, BHVO-2, JB-3, JA-2, LP-1, JB-1b, JR-1 and AGV-1. The granite sample JG-1 shows good agreement with respect to measured Ce isotope compositions (Tanaka et al. (1987)), but also shows deviations in measured La-Ce concentration data which could be an indication of sample heterogeneity.

By the advent of special interface cone designs like wide-angle skimmer cones (X-cones) or "Jet"- sample cones with wider aperture, the sensitivity of MC-ICP-MS instruments could be increased by up to an order of magnitude of 4-6.5 for Nd measurements (Newman (2012)). To assess the potential of MC-ICP-MS for high sensitivity measurements, the effects of four different Ni-cone combinations were investigated: standard sample cone with H-type skimmer cone (H), standard sample. cone with X-type skimmer cone (X), "Jet" sample cone with H-type skimmer cone (J), and "Jet" sample cone with X-type skimmer cone (J/X). By using "Jet" sample cone and H-type skimmer cone, the signal sensitivity for a given concentration of Ce could be improved by a factor of 2.4. The same factor can be achieved by using X-type skimmer cone and standard Ni sample cone. By using a combination of X-type skimmer cone and "Jet" sample cone, the signal sensitivity for Ce could be improved by a factor of ca. 4. The Ce isotope results for the different cone combinations are shown in Appendix A Table 18 and Figure 20. In general, the Ce isotope data are in a good agreement, independent of the cone combination used, and no increase of the standard error of the mean is observed at a given intensity. This observation indicates that our ion exchange protocol produced sufficiently clean Ce-cuts to avoid matrix effects, in particular during the use of "Jet" sample cone (Schulz et al. (2013), Peters et al. (2015)).

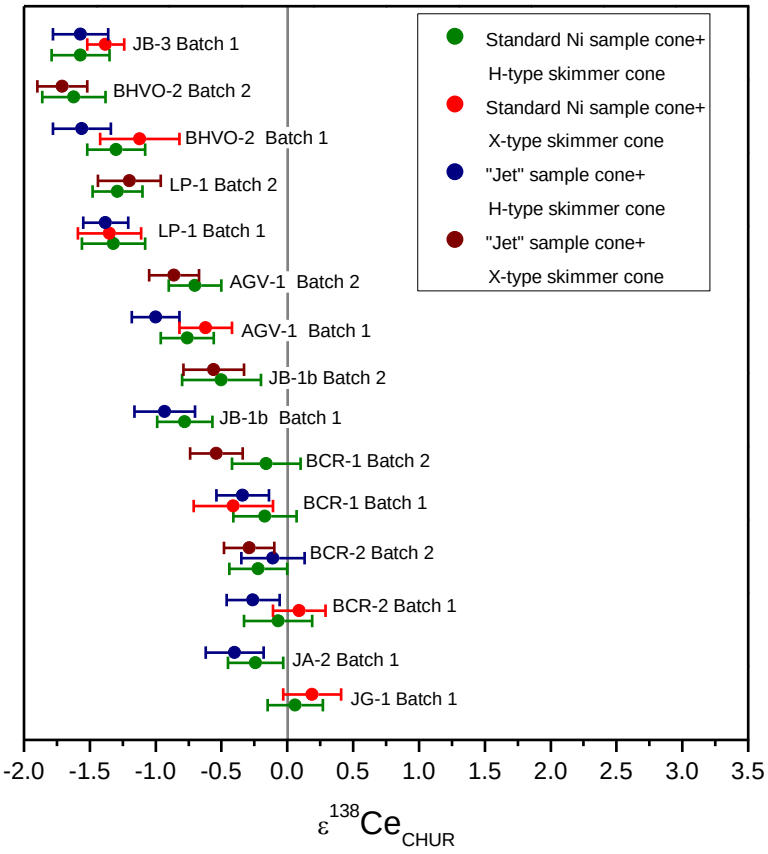

Figure 20 Measured Ce isotope ratios for rock reference samples using different interface cone combinations. $^{138}Ce/^{136}Ce$ ratios are expressed in ε-units relative to CHUR. Reported uncertainties correspond to 2 s.e.

2.13. Conclusions

Our study presents the first complete MC-ICP-MS protocol for separation of La-Ce from rock matrices and measurements of Ce isotope compositions as well as La-Ce concentrations by isotope dilution. The protocol enables static measurements of all Ce isotopes (^{136}Ce, ^{138}Ce, ^{140}Ce and ^{142}Ce), also including the large abundance isotope ^{140}Ce that is measured with an 10^{10} Ohm amplifier. The external reproducibility achieved for ^{138}Ce measurements was significantly better, once $^{136}Ce/^{140}Ce$ was used for mass bias correction (±0.25), rather than $^{136}Ce/^{142}Ce$ (±0.40, all 2 r.s.d.). Two synthetic reference solutions (Cologne-AMES and JMC-304 batch 15952) were prepared and were measured relative to each other and relative to the Mainz-AMES reference material in 10 analytical sessions. The weighted means relative to JMC-304 of $\varepsilon^{138}Ce$ are 0.0±0.12 (all 2 r.s.e) for JMC-304, 0.83±0.11 for Cologne-AMES and 2.61±0.09 for Mainz-AMES, with better external reproducibilities than have been previously reported (Willbold (2017)). The average $^{138}Ce/^{136}Ce$ value measured in this study is 1.33745±4 (2 r.s.e, N=51) for Mainz-AMES; the

deviation of +0.52ε-units from the value published by Willbold 2007 can be explained through non-ideal mass bias correction and possibly by cup efficiency.

A comparison with other TIMS studies demonstrates isotopic heterogeneity between different JMC-304 batches and shows that there are at least 3 different batches being analyzed in different laboratories (Bellot et al. (2015), Tanaka et al. 1(987)). There is also a clearly resolvable isotopic heterogeneity between the Cologne-AMES batch prepared during the course of this study and the Mainz-AMES batch. This underlines that there is an urgent need for a consensus on reference materials being used for Ce isotope measurements.

For La-Ce concentration measurements by isotope dilution, a mixed $^{138}La/^{142}Ce$ isotope tracer was prepared and calibrated against a solution prepared from high-purity AMES metal. The external reproducibility achieved for replicate digestions of the BCR-2 basaltic reference material was ±1.02 (2 r.s.d., %) for La and ±0.90 (2 r.s.d., %) Ce concentration measurements and ±0.19 (2 r.s.d., %) for La/Ce ratios.

Measurements of Ce isotope compositions and La-Ce concentrations were performed on 10 geological reference material (JG-1, JA-2, BCR-2, BCR-1, JB-1b, AGV-1, BHVO-2, JR-1 and JB-3) and one in house La Palma basalt standard (LP-1). Replicate digestion of 5 BCR-2 splits has shown the high accuracy and precision of the presented analytical method (±0.38, 2 r.s.d). A repetitive measurement of different rock samples using variable interface/cone combinations involving “Jet”-sample cones and X-skimmer cones showed a good agreement of the results within analytical resolution. The signal sensitivity of Cerium could be improved by a factor of 2.4 by using the X–skimmer cones and by a factor of 4 by using X–skimmer cones and “Jet”-sample cones.

In summary, the new analytical protocol for MC-ICP-MS measurements presented here opens new avenues for applying the La-Ce geochronometer to a variety of terrestrial rock samples and meteorites. The results will open new avenues to investigate geodynamic processes on Earth and to better understand processes active during the formation of the Earth and the solar system.

Chapter 3

The Ce isotope composition and La/Ce value of CHUR

3.1. Introduction

The branched decay of ^{138}La with a half-life $1.02*10^{11}$ years results in ^{138}Ce from β^- decay (34.4%) and ^{138}Ba from electron capture (65.6%). The ^{138}La-^{138}Ce isotope system can be used as a geochronometer and as isotope tracer in geo- and cosmochemistry. It provides complementary information when coupled with the more popular ^{176}Lu-^{176}Hf and ^{147}Sm-^{143}Nd decay systems, because of the anti-correlated relative compatibilities during silicate melting processes: the parent La is more incompatible than its daughter Ce, while the parents Sm and Lu are more compatible than their daughter elements Nd and Hf (e.g., Hofmann (1988)). The cosmochemical behavior of all three parentss is similar (all highly refractory, e.g., Lodders (2003)). The ^{138}La-^{138}Ce system has first been introduced in the 1980s (Tanaka and Masuda (1982)) and since then, the system has rarely been used. The main reason for this is the very challenging isotope ratio measurement because of isobaric interferences (from ^{138}Ba on ^{138}Ce and from ^{142}Nd on ^{142}Ce). Moreover, it is difficult to measure all Ce isotopes, because the abundance of ^{140}Ce (88.450%) is more than 80 times higher abundance than ^{136}Ce (0.185%) and ^{138}Ce (0.251%). However, these problems are overcome by efficient separation techniques (e.g. Tazoe et al. (2007), Ohno and Hirata (2013), Bellot et al. (2015), Chapter 2) and the use of Faraday amplifiers with higher ohmic $10^{10}\,\Omega$ resistors in their feedback loop for the collection of the ^{140}Ce ion current during mass spectrometry (Chapter 2).

Due to these analytical challenges, important reference parameters for the ^{138}La-^{138}Ce decay system are still poorly known. Amongst these parameters is the ^{138}La-^{138}Ce CHUR value, which is defined by the present-day ^{138}La/^{136}Ce and the ^{138}Ce/^{136}Ce value of meteorites. First coined by DePaolo and Wasserburg (1976) for the ^{147}Sm-^{143}Nd decay system, the term “chondritic uniform reservoir” (CHUR) denotes the bulk Earth parent-daughter and radiogenic isotope composition, assuming that bulk Earth has a refractory trace element and radiogenic isotope composition similar to chondrites. This assumption has recently been challenged based on ^{146}Sm-^{142}Nd isotope data for chondrites (e.g., Boyet and Carlson (2005), Burkhardt et al. (2016), Bouvier and Boyet (2016)), but can still be regarded as broadly valid for long-lived radiogenic isotope systems.

Recent analytical improvements for the ^{138}La-^{138}Ce system (Chapter 2) in combination with the ^{147}Sm-^{143}Nd system allow for a better evaluation of the CHUR model.

This study reports the ^{138}La/^{136}Ce and ^{138}Ce/^{136}Ce composition of a representative set of chondrites, covering all major classes and petrological types. Based on this dataset and the detailed evaluation of two more recent studies (Bellot et al. (2015), Willig and Stracke (2019)), a more accurate chondritic ^{138}Ce/^{136}Ce value was determined in this study. For ^{138}La/^{136}Ce, our average chondritic value was determined by isotope dilution in contrast to Willig and Stracke (2019).

3.1.1. Previous CHUR estimates for the ^{138}La–^{138}Ce system and data comparison

For chondrites and achondrites, Ce isotope ratio and especially La and Ce concentration measurements by isotope dilution have rarely been performed. A compilation of previously reported data are listed in Table 8. Shimizu et al. (1984) provided the first ^{138}La-^{138}Ce CHUR parameter by measuring Juvinas (eucrite), Pasamonte (eucrite), ALH-78132 (eucrite) and Jilin (H5 chondrite). Makishima and Masuda (1993) determined the Ce isotope compositions and ^{138}La-^{142}Ce using Murchison (CM2 chondrite), Granés (L6 chondrite), Holbrook (L/LL6 chondrite), Barwise (H5 chondrite) and four eucrite sample: Camel Donga, Juvinas and two pieces of Millbillillie. In a follow up study, Makashima and Masuda (1994) analyzed two pieces of Allende (CV3 chondrite). In a more recent study, Bellot et al. (2015) used Allende (CV3) and Sahara 97072 (EH3) to redetermine the ^{138}Ce/^{136}Ce CHUR value. Based on TIMS measurements at higher precision, Willig and Stracke (2019) proposed a chondritic ^{138}Ce/^{136}Ce value based on the measurement of 12 different meteorites: Allende (CV3), Homestead (L5), Indarch (EH4), Knyahinya (LL5), Murchison (CM2), Ninqiang (CK3), NWA6015 (CO3), Ornans (CO3), Parnallee (LL3.6), Pultusk (H5), Tuxtuac (LL5), Holbrook (LL6), Jbilet Winselwan (CM2) and Saratov (L4). All previous meteorite data had been reported as ^{138}Ce/^{142}Ce, which were corrected for mass fractionation using the exponential law and ^{136}Ce/^{142}Ce = 0.01688 (Makashima et al (1987)). Willig and Stracke (2019) however, measured ^{138}Ce/^{136}Ce and corrected offline for mass fractionation using the exponential law and ^{136}Ce/^{142}Ce = 0.01688 (Makashima et al. (1987)).

Until now, the La/Ce value of meteorites have been determined in four studies (Shimizu et al. (1984), Makashima and Masuda (1993), Makashima and Masuda (1994), Willig and Stracke (2019)) whereas the older studies employed isotope dilution but no detailed description about the used isotope tracer and measurements procedures are available. However, Makashima and Masuda (1993) determined a La/Ce value of 0.3770±66 (2 r.s.d.). Willig and Stracke determined

a La/Ce ratio of 0.3839±39 (2 r.s.d) by sector field-inductively coupled plasma-massspectrometry (SF-ICP-MS).

As in Willig and Stracke (2019), all four Ce isotopes (136, 138, 140, and 142) were measured in our study. In contrast to Willig and Stracke (2019), we mass bias corrected $^{138}Ce/^{136}Ce$ relative to $^{136}Ce/^{140}Ce=0.002124072$ (Mahashima and Nakamura (1991), Makashima et al. (1987)) using the exponential law, in order to achieve a better external reproducibility (Chapter 2). The $^{138}Ce/^{136}Ce$ isotope ratios in this study are all reported relative to Mainz-AMES 1.33738±1 (2 s.e.) Willbold (2007).

Different reference materials (JMC-304, BCR-1 and Mainz-AMES) and different Ce isotope ratios ($^{138}Ce/^{142}Ce$ and $^{138}Ce/^{136}Ce$) have been used in previous studies. For a better comparison with this study the $^{138}Ce/^{142}Ce$ data of Makashima and Masuda (1993), Makashima and Masuda (1994) and Bellot et al. (2015) were recalculated to $^{138}Ce/^{136}Ce$ (see Table 8) using the $^{136}Ce/^{142}Ce$ of 0.01688 (Makashima et al. (1987)). The uncertainties on $^{138}Ce/^{136}Ce$ originating from the recalculation were propagated.

It was shown in Chapter 2 that different batches of JMC-304 and AMES metal are isotopically heterogeneous in their Ce isotope composition. Because of the isotopic heterogeneity between the JMC-304 batches, a recalculation for the results of the study by Shimizu et al. (1984) is impossible. Consequently, these results are only expressed in $\varepsilon^{138}Ce$ (JMC-304). In contrast to JMC-304, the rock reference standards BCR-1 and BCR-2 are isotopically homogenous in their Ce isotope compositions (Chapter 2). In the studies of Makashima and Masuda (1993) and Makashima and Masuda (1994) BCR-1 was used whereas in the recent studies of Bellot et al. (2015), Willig and Stracke (2019) and in this study, Mainz-AMES was used as reference material. Both standards, BCR-1 and Mainz-Ames, were analyzed in Chapter 2. Therefore, the Ce isotope results of Makashima and Masuda (1993) and Makashima and Masuda (1994) can now be re-normalized relative to Mainz-AMES = 1.33738±1 (2 s.e.) (Willbold (2007)). In addition, the Ce isotope compositions of Bellot et al. (2015) and Willig and Stracke (2019) were also recalculated relative to Mainz-AMES = 1.33738±1 (2 s.e.). The rock reference standard BCR-2 was used in all three recent studies. If recalculated relative to Mainz-AMES there is no agreement between Willig and Stracke (2019) (1.33693±1) and Bellot et al. (2015) (1.33688±2). We analyzed BCR-2 two times and the results (1.33694±3 and 1.33692±2, Chapter 2) are in an excellent agreement with Willig and Stracke (2019) and barely overlap with Bellot et al. (2015). A recalculation of data for the Allende meteorite that was also processed in both studies also shows no overlap between the study of Bellot et al. (2015) (1.33685±2) and Willig and Stracke (2019) (1.33691±3 and 1.33692±1). This systematic offset of about ~0.5 $\varepsilon^{138}Ce$ is also found when comparing the mean

$^{138}Ce/^{136}Ce$ value of Bellot et al. (2015) (1.33684±3, 2 s.e.) and Willig and Stracke (2019) (1.33692±1, 2 s.e.). Willig and Stracke (2019) have argued that there are problems with the tail correction applied in Bellot et al. (2015). However, the offset in the chondrite data of both recent studies is a problem because the precise knowledge of the ^{138}La-^{138}Ce CHUR value is a prerequisite to accurately understand the behavior of the LREE in magmatic systems and the location of the Ce-Nd isotope mantle array.

Table 8 Previous La-Ce isotope data obtained for meteorites. For comparison data were recalculated as $^{138}Ce/^{136}Ce$ using the $^{136}Ce/^{142}Ce = 0.01688$ (Makashima et al. (1987)) and expressed relative to Mainz-AMES with $^{138}Ce/^{136}Ce = 1.33738\pm1$ (Willbold (2007)). See section discussion for detailed description. Additionally, the results are also expressed as $\varepsilon^{138}Ce$ relative BCR-1/BCR-2 because this rock reference standard was used in all studies with the exception of Shimizu et al. (1984). The results of Shimizu et al. (1984) are only expressed as $\varepsilon^{138}Ce$ relative JMC-304 because the Ce isotope heterogeneity of the JMC-304 standard (Chapter 2) makes recalculation relative Mainz-AMES impossible.

data source	Meteorite	La/Ce	$^{138}La/^{142}Ce$	$^{138}Ce/^{142}Ce$	2 s.d.	$^{138}Ce/^{136}Ce$	2 s.d.	$\varepsilon^{138}Ce$ (BCR-1/BCR-2)	$\varepsilon^{138}Ce$ (JMC-304)
Shimizu et al. (1984)	Jilin 1 (H5)		0.00307	0.0225667	0.0000058.				-0.9±2.5
	Jilin 2		0.00315	0.0225650	0.0000114				-1.7±5.0
	Pasamonte (Eucrite-pmist)		0.00311	0.0225647	0.0000026				-1.8±1.1
	Juvinas (Eucrite-mmict)		0.00303	0.0225662	0.0000026				-1.1±1.1
Makishima and	Murchison (CM2)	0.3916	0.00320	0.0225674	0.0000005	1.33706	0.00003	1.0±0.22	
Masuda (1993)	Granes (L6)	0.3768	0.00308	0.0225636	0.0000010	1.33683	0.00006	-0.71±0.44	
	Holbrook1 (L/LL6)	0.3705	0.00303	0.0225653	0.0000015	1.33694	0.00009	0.04±0.66	
	Holbrook2		0.00303	0.0225644	0.0000008	1.33688	0.00005	-0.35±0.35	
	Barwise1 (H5)	0.3794	0.00310	0.0225638	0.0000007	1.33685	0.00004	-0.62±0.31	
	Barwise2		0.00310	0.0225665	0.0000007	1.33701	0.00004	0.58±0.31	
	Camel Donga (Eucrite-mmict)	0.3803	0.00311	0.0225659	0.0000011	1.33697	0.00007	0.31±0.49	
	Juvinas	0.3805	0.00311	0.0225665	0.0000008	1.33701	0.00005	0.58±0.35	
	Millbillillie1 (Eucrite-mmict)	0.3568	0.00292	0.0225636	0.0000008	1.33683	0.00005	-0.71±0.35	
	Millbillillie2/1	0.3799	0.00311	0.0225650	0.0000007	1.33692	0.00004	-0.09±0.31	
	Millbillillie2/2		0.00311	0.0225659	0.0000006	1.33697	0.00004	0.31±0.27	
Makashima and	Allende (CV3)#1	0.4028		0.0225681	0.0000023	1.33710	0.00013	0.62±1.00	
Masuda (1994)	Allende (CV3)#2	0.3701		0.0225678	0.0000001	1.33708	0.00001	0.47±0.06	
Bellot et al. (2015)	Allende (CV3)			0.0225657	0.0000004	1.33683	0.00002	-0.27±0.18	
	Sahara97072 (EH3)			0.0225652	0.0000003	1.33680	0.00002	-0.49±0.13	
Willig and Stracke	Allende A (CV3)	0.3916				1.33689	0.00003	-0.25±0.22	
(2019)	Allende B (CV3)	0.3917				1.33690	0.00001	-0.11±0.08	
	Homestead (L5)	0.3809				1.33693	0.00002	0.10±0.15	
	Indarch (EH4)	0.3841				1.33690	0.00002	-0.12±0.16	

Table 8 continued

data source	Meteorite	La/Ce	$^{138}La/^{142}Ce$	$^{138}Ce/^{142}Ce$	2 s.d.	$^{138}Ce/^{136}Ce$	2 s.d.	$\varepsilon^{138}Ce$ (BCR-1/BCR-2)	$\varepsilon^{138}Ce$ (JMC-304)
	Knyahinya (LL5)	0.3824				1.33688	0.00002	-0.28±0.12	
	Murchinson (CM2)	0.3898				1.33690	0.00003	-0.16±0.19	
	Ninqiang (CK3)	0.3917				1.33690	0.00001	-0.12±0.08	
	NWA6015 (CO3)	0.3897				1.33691	0.00002	-0.09±0.12	
	Ornans (CO3)	0.3884				1.33690	0.00002	-0.16±0.12	
	Parnallee (LL3.6)	0.3772				1.33688	0.00002	-0.32±0.13	
	Pultusk (H5)	0.3807				1.33688	0.00001	-0.27±0.09	
	Tuxtuac (LL5)	0.3723				1.33690	0.00002	-0.11±0.13	
	Holbrook (LL6)	0.3846				1.33688	0.00002	-0.29±0.17	
	Jbilet Winselwan (CM2)	0.4101				1.33690	0.00002	-0.13±0.17	
	Saratov (L4)	0.5019				1.33694	0.00002	0.19±0.13	

3.2. Analytical methods and samples

3.2.1. Meteorite samples analyzed in this study

In this study, 22 different meteorites were analyzed to determine the ^{138}La-^{138}Ce CHUR value. We have chosen these samples to represent a wide range of meteorite classes and petrological types. Nine meteorites are carbonaceous chondrites (CM, CK, CV, and CO groups). Five meteorites are ordinary chondrites (H, L and LL), and six meteorites are enstatite chondrites (EL and EH). Ten of these meteorites (Karoonda, Nogoya, Cold Bokkeveld, Vigarano, Allende, Chainpur, Ramsdorf, Khairpur, Neuschwanstein and Abee) are falls, while the other meteorites are finds (Table 9). The meteorite falls were selected such that the material had been collected within a few days after the fall, before any terrestrial weathering could have caused changes in the REE patterns (see discussion). The consideration of the different meteorite types for the calculation of the ^{138}La-^{138}Ce CHUR value is discussed in more detail below. The sample and collection list is given in Table 9.

Table 9 Sample list of bulk chondrites, NC = Nuclear Chemistry (Cologne), MfN = Museum für Naturkunde (Berlin), MWG = Meteorite working group (NASA), NHM = Natural History Museum (London)

Meteorite name	Group/Type		Source
Carbonaceous chondrites			
Karoonda	*CK4*	*fall*	*MfN Berlin*
MET 01070	*CM1*	*find*	*MWG Nasa*
Nogoya	*CM2*	*fall*	*MfN Berlin*
Cold Bokkeveld	*CM2*	*fall*	*NHM London*
Vigarano	*CV3*	*fall*	*J. Schlüter, Universität Hamburg*
Acfer 082	*CV3*	*Find*	*A. Bischoff, Universität Münster*
Isna	*CO3.8*	*Find*	*NC Cologne*
Dar al Gani 067	*CO3*	*Find*	*A. Bischoff, Universität Münster*
EET 92002	*CK5*	*Find*	*MWG Nasa*
Allende - MS	*CV3*	*Fall*	*Cologne collection*
Ordinary chondrites			
Dimmitt	*H3.7*	*find*	*NC Cologne*
Roosevelt	*H3.4*	*find*	*NC Cologne*
Chainpur	*LL3.4*	*fall*	*NC Cologne*
Etter	*L5*	*find*	*NC Cologne*
Ramsdorf	*L6*	*fall*	*NC Cologne*

Table 9 continued

Meteorite name	Group/Type		Source
Enstatite chondrites			
Khairpur	*EL6*	*fall*	*NC Cologne*
EET 96341	*EH4/5*	*find*	*MWG Nasa*
Happy Canyon	*EL6/7*	*find*	*NC Cologne*
Atlanta	*EL6*	*find*	*NC Cologne*
Neuschwanstein	*EL6*	*fall*	*NC Cologne*
Abee	*EH4*	*fall*	*NC Cologne*
Differentiated meteorite			
Ilafegh 002	*Mesosiderite*	*find*	*NC Cologne*

3.2.2. **Sample preparation and ion-exchange chromatography**

Our analytical protocol for sample preparation broadly follows that of Chapter 2. Single-distilled concentrated HF (24M), concentrated HCl (10M), concentrated HNO_3 (14M) and reagent grade H_2O_2 (30%) and $KBrO_3$ (purity ≥ 99.8%) were used. Total chemistry blanks were less than 750 pg Ce and can be neglected. Ca. 250 mg of meteorite sample powder were weighted into Savillex® beakers, spiked with a mixed ^{149}Sm-^{150}Nd tracer and digested in a 1:1 vol. mixture of HF (24M) and HNO_3 (14M) at 120°C in Savillex® beakers on a hotplate. After 24h on the hotplate, the acids were dried down and the residue was re-dissolved in a 3:2 (v/v) mixture of HF (24M) and HNO_3 (14M) and digested at 180°C for 36 hours in Parr Bombs® to ensure complete dissolving of refractory minerals. Subsequently, 1mL of reagent grade $HClO_4$ was added to prevent the precipitation of redissolved secondary fluorides during dry down. To get rid of remaining $HClO_4$ and fluoride precipitates the samples were re-dissolved three times in 2mL HNO_3 (14M) and dried down again. Complete dissolution for most of the samples was achieved by re-dissolving and heating in 10 mL 6M HCl solution for 12 h at 120 °C. If dissolution was incomplete at this point, samples were dried down again, re-dissolved in 2mL HNO_3 (14M) and put on the hotplate for additional 12h at 120°C. Following this additional step, the samples were slowly dried down at 70°C and again re-dissolved in 10 mL 6M HCl. After these digestion steps, all samples were completely dissolved. Each meteorite sample was split into a cut of ca. 90% for Ce isotope measurement (Ce IC) and a cut of ca. 10% for La/Ce isotope dilution, (La-Ce ID). The ID cuts were spiked with a mixed ^{138}La-^{142}Ce isotope tracer (for details see Chapter 2). Both cuts were dried down and Ce (and La) were isolated from major elements following the separation procedure described in Chapter 2. In short, this protocol employs separation of the REE from major elements through cation ion exchange columns followed by the oxidation of Ce using $KBrO_3$ and subsequent separation of Ce^{4+} from the remaining REE via Ln-Spec column separation. The Ce cut was then further cleaned-up using another cationic ion-exchange column. After matrix and Ce separation, the remaining REE^{3+} ID cuts were used

to separate La by the clean-up chemistry and the remaining REE^{3+} IC cuts were used to separate Sm and Nd using Eichrom Ln-spec® resin as described by Pin and Zalduegui (1997).

3.2.3. **Mass spectrometry**

Isotope analyses of La and Ce were performed at the University of Cologne using a ThermoFinnigan™ Neptune MC-ICP-MS, broadly following the protocol of Chapter 2. Cerium isotope measurements were performed from solutions containing 0.14M HNO_3, using a Cetac ARIDUS II™ desolvation system and a PFA nebulizer with an uptake rate of ca. 50 µL min^{-1}. A standard sample cone and a X-skimmer cone were used to further increase the instrumental sensitivity. All Ce isotopes (136, 138, 140 and 142) were measured in static and low resolution mode (R = 300). In order to collect the extremely high ion current of ^{140}Ce relative to the much smaller ^{136}Ce and ^{138}Ce ion currents, an amplifier equipped with a 10^{10} Ω resistor was used for mass 140. In contrast to Chapter 2, three amplifiers equipped with 10^{13} Ω resistors were applied to monitor ^{134}Xe, ^{137}Ba and ^{144}Nd ion beams for interference correction.

Each analysis consisted of 60 cycles (2 blocks of 30 cycles with 8.389s integration time). Interference corrections for the isobars ^{136}Xe, ^{136}Ba, ^{138}Ba, ^{138}La and ^{142}Nd as well as the mass bias correction followed the method of Chapter 2. Measured $^{138}Ce/^{136}Ce$ ratios were mass bias corrected to $^{136}Ce/^{140}Ce = 0.002124072$ (Makashima and Nakamura (1991), Makashima et al. (1987)) using the exponential law, resulting in a better external reproducibility than normalization to $^{138}Ce/^{142}Ce$.

In this study, three different pure Ce solutions were used as reference materials: Johnson Matthey JMC-304 (batch 15952), Mainz-AMES (Willbold (2007)) and Cologne-AMES with a different isotope composition than Mainz-AMES (Chapter 2). Due to the limited amount of Mainz-AMES, our in house JMC-304 standard was used to measure all meteorites employing standard-sample bracketing, while the other two reference solutions were occasionally interspersed for quality control. All three reference materials were calibrated against each other (Chapter 2) and the $\varepsilon^{138}Ce$ mean values relative to Mainz-AMES are presented in Table 10.

Table 10 Comparision of $\varepsilon^{138}Ce$ mean values of JMC-304 and Cologne-AMES relative to Mainz-AMES

	JMC-304	***Cologne-AMES***
Chapter 2	-2.41±0.12 (2 r.s.d)	-1.71±0.11 (2 r.s.d)
This study	-2.56±0.12 (2 r.s.d)	-1.77±0.14 (2 r.s.d)

As described in Chapter 2, typical tail contributions on mass 138 from ^{140}Ce ion beams increased ε^{138}Ce by 0.001 and 0.0001 and are insignificant. All reported data are reported relative to ^{138}Ce/^{136}Ce of 1.33738±1 (2 s.e.) for the Mainz-AMES standard (Willbold (2007)). Age corrected ε^{138}Ce values were calculated using the CHUR values determined below and the ^{138}La decay constant λ_{β^-} = 2.37 (±0.10)*10^{-12} y^{-1} (Tanimizu (2000)).

All La-Ce concentration measurements by isotope dilution were also performed on the Thermo Finnigan Neptune MC-ICP-MS at Cologne, but a dual glass spray chamber (Thermo SIS) and a 50 µL glass nebulizer were used to suppress memory effects. The La and Ce abundances were calculated from measured ^{138}La/^{139}La and ^{142}Ce/^{140}Ce. Both ratios were mass bias corrected employing doped Nd and Ba solutions, respectively, and using the exponential law for mass bias correction. For external normalization, a ^{137}Ba/^{135}Ba value of 1.70383 (Berglund and Wieser (2011)) for Ce and a ^{142}Nd/^{144}Nd value of 1.14187 (Thirwall (1991)) for La were used, respectively. Accurate interference corrections of Ce and Ba (for La) and Nd (for Ce) were ensured by measurements of doped solutions.
Neodymium isotope compositions as well as Sm and Nd concentrations were obtained on the Thermo Finnigan Neptune MC-ICP-MS at Cologne using an ARIDUS desolvating system and isotope dilution for the concentration measurements, employing a mixed ^{149}Sm-^{150}Nd tracer. All measured ^{143}Nd/^{144}Nd data were mass bias corrected to a ^{146}Nd/^{144}Nd value of 0.7219 using the exponential law. During this study, the measured ^{143}Nd/^{144}Nd for the La Jolla Nd standard was 0.511852±15 (2 s.d., n = 2). All reported data are corrected to achieve ^{143}Nd/^{144}Nd of 0.511859 for the La Jolla standard. The external reproducibility for ^{143}Nd/^{144}Nd measurements was ±40 ppm. Age corrected ε^{143}Nd were calculated using the CHUR values 0.5112630 for ^{143}Nd/^{144}Nd and 0.1960 for ^{147}Sm/^{144}Nd (Bouvier et al. (2008)) and λ^{147}Sm = 6.539(±0.061)* 10^{-12} y^{-1} (Nica (2009)). Total procedural blanks during the measurements were 16-260 pg for Sm and 21-432 pg for Nd.

3.3. Results

In this study, we combine ^{138}La-^{138}Ce and ^{147}Sm-^{143}Nd data from the same aliquots for 22 different meteorites. The data are reported in Table 11. For one sample, the Allende CV3 chondrite, the digestion and analyses were replicated. The La/Ce and the Sm/Nd concentration data are in an excellent agreement with each other (within 0.2%) and also the ^{138}Ce/^{136}Ce and ^{143}Nd/^{144}Nd isotope data are in a good agreement (within 5 and 60 ppm, respectively). The mean values of each chondrite class (carbonaceous, ordinary and enstatite) are also shown in Table 11, but some meteorites were excluded (see detailed discussion below). Bouvier et al. (2008) recommended to calculate the CHUR means only from unequilibrated chondrites for

the Lu/Hf and Sm/Nd systems, because Lu/Hf showed a large variation for ordinary and enstatite chondrites of types 4 to 6. As a result of their Lu/Hf study, Bouvier et al. (2008) also defined the Sm-Nd CHUR value only on unequilibrated chondrites, although the mean values of unequilibrated and equilibrated chondrites in their study overlap within uncertainty. In our study, we also observe an overlap between unequilibrated and equilibrated chondrites for Sm/Nd and therefore we use data from both unequilibrated and equilibrated chondrites for calculation of the ^{138}La-^{138}Ce CHUR value.

Table 11 La-Ce and Sm-Nd data and averages for bulk chondrite samples. All $^{138}Ce/^{136}Ce$ values were corrected to Mainz-AMES = 1.33738±1 (2 s.e.) (Willbold (2007)). For the calculation of the mean value see text for data that was excluded from the calculation

Sample	Group	La [ppm]	Ce [ppm]	La/Ce	$^{138}La/^{136}Ce$	$^{138}La/^{142}Ce$	$^{138}Ce/^{136}Ce$	2 s.e.	Ce/Ce*	Sm [ppm]	Nd [ppm]	Sm/Nd	$^{147}Sm/^{144}Nd$	$^{143}Nd/^{144}Nd$	2 s.e.
Carbonaceous chondrites															
Nogoya	CM 2	0.337	0.842	0.3996	0.1945	0.003286	1.33685	4	1.00	0.636	0.605	1.053	-	0.512607	12
Karoonda	CK 4	0.790	1.56	0.5069	0.2467	0.004168	1.33686	3	0.902	0.272	0.844	0.3222	0.1948	0.512633	15
MET 01070	CM 1	0.386	0.909	0.4252	0.2069	0.003496	1.33683	5	0.973	0.198	0.613	0.3234	0.1955	0.512619	13
Cold Bokkeveld	CM 2	0.487	0.974	0.4997	0.2432	0.004108	1.33690	4	0.887	0.191	0.596	0.3196	0.1932	0.512629	10
Vigarano	CV 3	0.498	1.24	0.4026	0.1959	0.003310	1.33681	5	1.00	0.280	0.875	0.3193	0.1931	0.512596	18
Acfer 082	CV 3	0.465	1.18	0.3928	0.1912	0.003230	1.33682	2	1.00	0.276	0.864	0.3200	0.1934	0.512563	15
Isna	CO 3	0.388	1.01	0.3862	0.1880	0.003176	1.33686	3	1.01	0.237	0.740	0.3197	0.1932	0.512578	15
Dar al Gani 067	CO 3	0.369	0.962	0.3837	0.1867	0.003154	1.33685	6	1.02	0.225	0.693	0.3247	0.1963	0.512653	16
Allende#1	CV 3	0.673	1.55	0.4332	0.2108	0.003561	1.33685	5	0.988	0.311	0.967	0.3216	0.1944	0.512744	35
Allende #2	CV 3	0.671	1.56	0.4312	0.2098	0.003545	1.33677	4	0.992	0.313	0.976	0.3213	0.1942	0.512741	29
EET 92002	CK 5	0.492	1.00	0.4913	0.2390	0.004039			0.801	0.294	0.917	0.3206	0.1938	0.512547	13
Mean carbonaceous chondrites (±2 s.e.)					**0.1980±65 (n = 10)**		**1.33684±2 (n = 10)**						**0.1942±6 (n = 10)**	**0.512630±41 (n = 10)**	
Ordinary chondrites															
Etter	L 5	0.268	0.715	0.3750	0.1825	0.003083			1.04	0.164	0.509	0.3223	0.1948	0.512646	21
Chainpur	LL 3	0.342	0.898	0.3807	0.1852	0.003130	1.33685	6	1.05	0.198	0.613	0.3225	0.1950	0.512640	22
Ramsdorf	L 6	0.359	0.945	0.3802	0.1850	0.003125	1.33703	5	1.05	0.210	0.648	0.3235	0.1956	0.512624	23
Roosevelt	H 3	0.915	1.45	0.6295	0.3063	0.005175	1.33689	3	0.707	0.282	1.10	0.2561	-	0.512420	12
Dimmitt	H 3	0.410	0.967	0.4238	0.2062	0.003484	1.33692	4	0.889	0.905	0.871	1.0340	-	0.512563	16
Mean ordinary chondrites (±2 s.e.)					**0.1921±115 (n = 3)**		**1.33693±8 (n=3)**						**0.1951±4 (n = 3)**	**0.512638±8 (n = 3)**	
Enstatite chondrites															
Happy Canyon-1	EL 6/7	0.268	0.391	0.3206	0.1561	0.002637			1.00	0.157	0.389	0.4029	-	0.513893	14
Happy Canyon-2	EL 6/7	0.0878	0.245	0.3576	0.1744	0.002946	1.33682	*5*							
EET 96341	EH 4/5	0.201	0.552	0.3652	0.1777	0.003002	1.33688	6	1.06	0.127	0.393	0.3240	0.1959	0.512642	24
Khairpur-1	EL 6	0.243	0.708	0.3428	0.1668	0.002818			1.10	0.160	0.501	0.3195	0.1932	0.512639	30
Khairpur-2	EL 6	0.310	0.810	0.3823	0.1862	0.003145									
Abee	EH 4	0.559	1.23	0.4528	0.2205	0.003725	1.33682								

Table 11 continued

Sample	Group	La [ppm]	Ce [ppm]	La/Ce	$^{138}La/^{136}Ce$	$^{138}La/^{142}Ce$	$^{138}Ce/^{136}Ce$	2 s.e.	Ce/Ce*	Sm [ppm]	Nd [ppm]	Sm/Nd	$^{147}Sm/^{144}Nd$	$^{143}Nd/^{144}Nd$	2 s.e.
Atlanta	EL 6	0.127	0.389	0.3253	0.1602	0.002707									
Neuschwanstein	EL 6	0.264	0.720	0.3669	0.1795	0.003032									
Mean enstatite chondrites (±2 s.e.)					**0.1807±147 (n = 7)**		**1.33682±8 (n = 3)**						**0.1945±19 (n = 2)**	**0.512640±2 (n = 2)**	
Mesosiderite															
Ilafeg002	Mesos	0.582	1.530	0.3803	0.1851	0.003128	1.33688	6	1.03	0.369	1.11	0.3326	0.2011	0.512804	14
Mean unequlibrated chondrites (± 2 s.e.)					**0.1964±59 (n = 11)**		**1.33685±2 (n = 12)**						**0.1943±7 (n = 9)**	**0.512640±41 (n = 9)**	
Mean all chondrites (± 2 s.e.)					**0.1864±66 (n = 20)**		**1.33686±3 (n = 18)**						**0.1948±9 (n = 16)**	**0.512643±33 (n = 16)**	
Mean carbonaceous chondrites (± 2 s.e.)					**0.1980±65 (n = 8)**		**1.33684±2 (n = 8)**								
Mean non-carbonaceous chondrites (± 2 s.e.)					**0.1804±80 (n = 11)**		**1.33688±6 (n = 7)**								
Mean BCR-2 (± 2 s.e., n = 2)		25.2	53.4		0.4725	0.003867	1.33693±3								
Mean BHVO-2 (± 2.s.e., n = 2)		15.4	37.9		0.4053	0.003333	1.33676±4								

In contrast to Bouvier et al (2008), Patchett et al. (2004), Boyet and Carlson (2005) and Carlson et al. (2007) where the Allende Smithsonian powder was used, the Münster Allende powder (Allende-MS) was used in this study. The measured $^{147}Sm/^{144}Nd$ values for the two Allende-MS replicates overlap within the uncertainties with the mean value of the eight Sm-Nd analyses of Bouvier et al. (2008), Patchett et al. (2004), Carlson et al. (2007) and Boyet and Carlson (2005), but the $^{143}Nd/^{144}Nd$ values show a ≅3 ε-units difference between our and their studies. The measured $^{143}Nd/^{144}Nd$ values of Willig and Stracke (2019) display only a smaller ≅0.6 ε-units difference to the mean value of the Smithsonian powder. Three other meteorites (Vigarano, Chainpur and Karoonda) were analyzed in this study as well as in previous studies (Bouvier et al. (2008), Patchett et al. (2004)). These $^{147}Sm/^{144}Nd$ values are also in good agreement with each other (better than 0.2 %) and the Nd isotope values are also in a good agreement to each other (to better than 70 ppm), as shown in Appendix B Table 19.

3.3.1. Selection of data for the CHUR determination

For determination of the $^{147}Sm/^{144}Nd$ and $^{143}Nd/^{144}Nd$ mean values, 15 of the 22 different meteorites were used. For Abee, Happy Canyon-2 and Khairpur-2 no Sm-Nd data have been available. Nogoya (CM 2), Dimmit (H 3), Roosevelt (H 3) and Happy Canyon (EL 6/7) were excluded for the determination of $^{147}Sm/^{144}Nd$ and $^{143}Nd/^{144}Nd$ mean values. The $^{147}Sm/^{144}Nd$ values of 0.1548 for Roosevelt and 0.2436 for Happy Canyon-1, both of which are meteorite finds, deviate significantly from the mean range of 0.1931-0.2011. This deviation likely mirrors REE redistribution by terrestrial alteration, as also supported by the La-Ce systematics discussed below. The $^{147}Sm/^{144}Nd$ value of 0.6363 for Dimmit is for unknown reasons significantly higher than the $^{147}Sm/^{144}Nd$ mean chondritic value and therefore excluded. Determination of Sm for Nogoya was impossible because the Sm cut was accidentally lost. On the basis of these observations, these four meteorites were not included in the calculation of mean chondritic values. The mean value obtained for $^{147}Sm/^{144}Nd$ is then 0.1948±9 (2 s.e., dark shaded field) and the mean value for $^{143}Nd/^{144}Nd$ is 0.512643±33 (2 s.e., dark shaded field). For comparison, the weighted mean of the literature data (Bouvier et al. (2008)) for $^{147}Sm/^{144}Nd$ is 0.1960±4 (2 s.e., light grey shaded field) and 0.512630±11 (2 s.e., light grey shaded field) for $^{143}Nd/^{144}Nd$ (Figure 21). Both mean values show a good agreement with each other and the results are consistent within uncertainty.

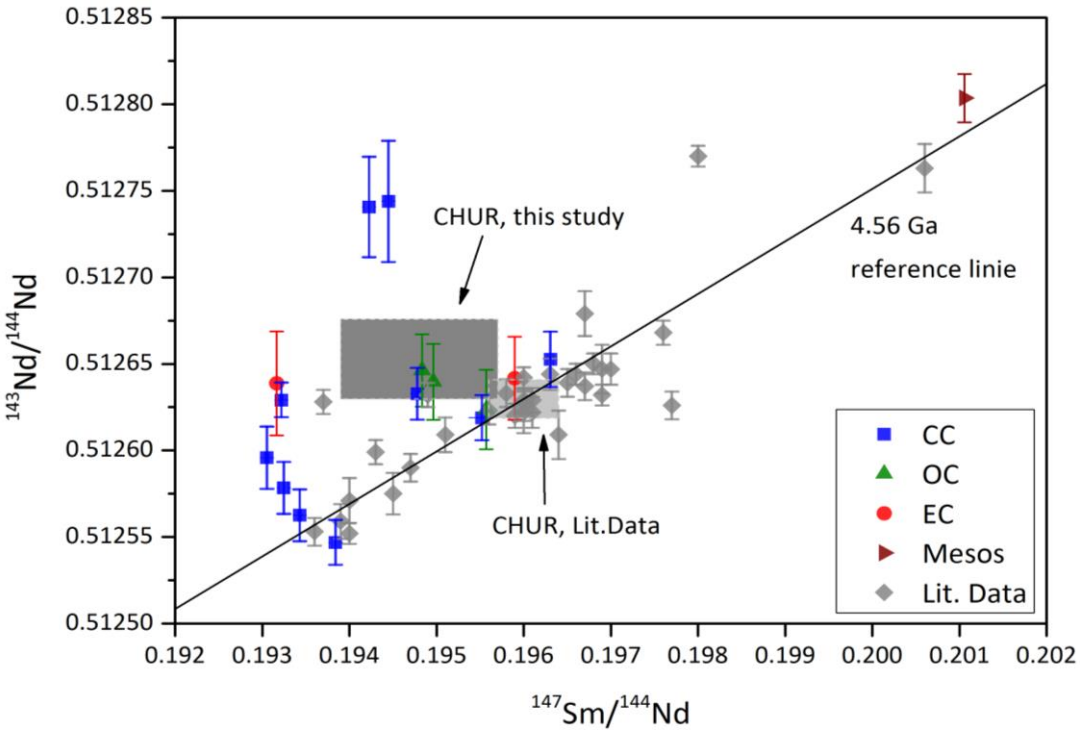

Figure 21 Sm-Nd data for carbonaceous (CC, blue), ordinary (OC, green) and enstatite (EC, red) chondrites and one mesosiderite (Mesos., brown) from this work and from literature data (Lit. data, grey; Bouvier et al. (2008)). In this study, our mean value of $^{147}Sm/^{144}Nd$ is 0.1948±9 and for $^{143}Nd/^{144}Nd$ is 0.512643±33 (dark grey shaded field). The weighted means of the literature data for $^{147}Sm/^{144}Nd$ are 0.1960±4 and for $^{143}Nd/^{144}Nd$ 0.512630±11 (light grey shaded field). Both mean values agree with uncertainty

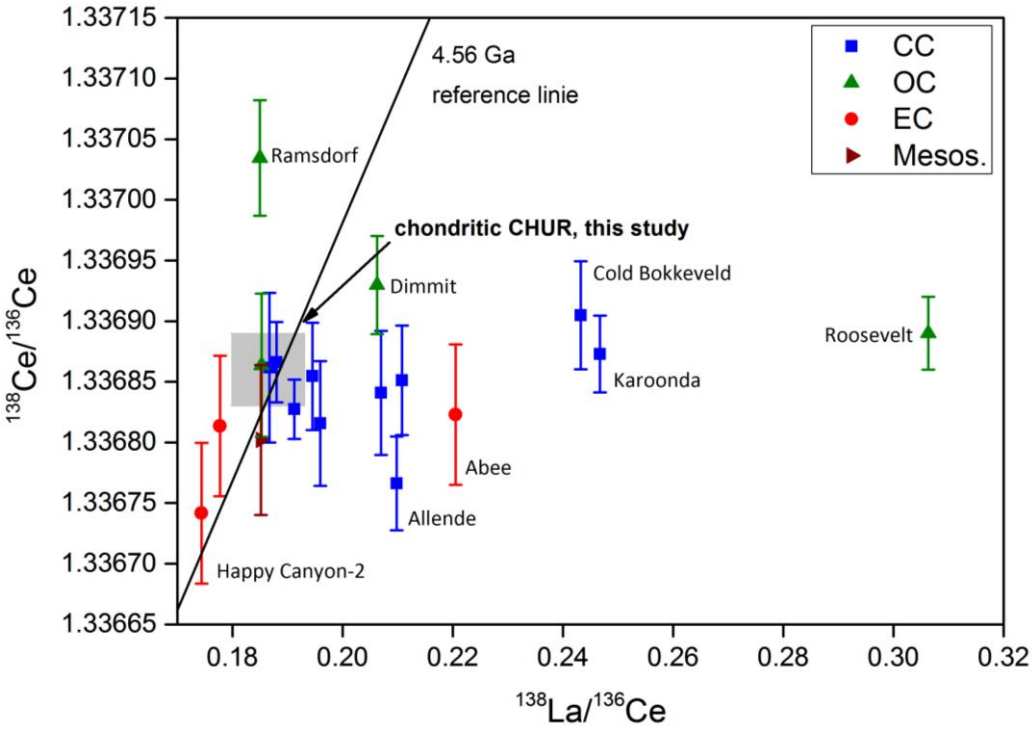

Figure 22 La-Ce data for carbonaceous (CC, blue), ordinary (OC, green), enstatite chondrites (EC, red) and mesosiderite (Mesos., brown) from this study, plotted in ^{138}La-^{138}Ce isochron space. The meteorite Ramsdorf shows a slightly higher $^{138}Ce/^{136}Ce$ value and the meteorites Abee, Cold Bokkeveld, Karoonda and Roosevelt a higher $^{138}La/^{136}Ce$ value than the other meteorites of this study The chondritic mean value of $^{138}La/^{136}Ce$ (n = 20) is 0.1864±66 (2 s.e.). The $^{138}Ce/^{136}Ce$ chondritic mean value (n = 18) is 1.33686±3 (2 s.e.). Happy Canyon-1; Khairpur-1 and Khairpur-2 are not shown.

The La-Ce data are presented in Table 11. Most meteorites show $^{138}La/^{136}Ce$ values between 0.1561 and 0.2108 and $^{138}Ce/^{136}Ce$ values between 1.33680 and 1.33701. The meteorite Ramsdorf shows a slightly higher $^{138}Ce/^{136}Ce$ value and the meteorites Abee, Cold Bokkeveld, Karoonda and Roosevelt show markedly higher $^{138}La/^{136}Ce$ values. For calculation of the $^{138}Ce/^{136}Ce$ value, we used 18 $^{138}Ce/^{136}Ce$ ratios (Figure 22). The meteorites Happy Canyon- 1, Etter, EET92002, Roosevelt, Khairpur-1 and Khairpur-2 were excluded and for Neuschwanstein and Atlanta no $^{138}Ce/^{136}Ce$ ratio were determined. A sufficiently precise determination of the Ce isotope composition was impossible for Happy Canyon-1 and Khairpur-1, because the specimen was too small. Roosevelt was excluded because of its negative Ce anomaly (Ce/Ce* = 0.8, see section discussion below). In addition, Abee, Cold Bokkeveld, EET92002 and Karoonda were excluded because of their high $^{138}La/^{136}Ce$ values. The probable reason for the deviation in these samples is a secondary La/Ce disturbance (see Figure 22 and Figure 25 and discussion of data selection below).

The calculated CHUR value of the $^{138}La/^{136}Ce$ ratio is 0.1864±66 (2 s.e., n = 20) and for $^{138}Ce/^{136}Ce$ is 1.33686±3 (2 s.e., n = 18).

3.4. Discussion

3.4.1. Cerium isotope data and standard reference materials

In recent studies, AMES metal standard has become established as a Ce isotope standard reference material (Boyet et al. (2019), Doucelane et al. (2014), Bellot et al. (2015), Willig and Stracke (2019)). An investigation in Chapter 2 has indicated a ^{138}Ce isotope heterogeneity between different AMES batches and also most likely between different batches of JMC-304 that have been used earlier as reference material. Besides the Mainz-AMES standard that was introduced by Willbold (2007) and used in the studies of Doucelane et al. (2014), Bellot et al. (2015), Willig and Stracke (2019), in Chapter 2 the Cologne-AMES reference material was also proposed. In this study, Mainz-AMES and Cologne-AMES were both used together with our JMC-304 batch that was prepared in house (see Chapter 2 for details). The $\varepsilon^{138}Ce$ mean values relative to Mainz-AMES for JMC-304 (-2.41±0.12 (2 r.s.d)) Chapter 2, -2.56±0.13 (2 r.s.d), this study) and Cologne-AMES (-1.71±0.11 (2 r.s.d)) Chapter 2, -1.77±0.21 (2 r.s.e), this study) are in excellent agreement.

As described in detail above, the measured $^{138}Ce/^{136}Ce$ ratios were renormalized to a $^{136}Ce/^{142}Ce$ of 1.33738±1 for Mainz-AMES (Willbold (2007)). In Figure 23, only the results of the current measurement session are shown for Mainz-AMES. The mean Mainz-AMES value in this study for $^{138}Ce/^{136}Ce$ normalized to $^{136}Ce/^{142}Ce = 0.01688$ is 1.33737±2 (2 r.s.d.), and is in a good agreement with the published value of Willbold (2007) (1.33738±1, 2 r.s.d., grey-

shaded field, Figure 23). Our $^{138}Ce/^{136}Ce$ ratio normalized relative to the $^{136}Ce/^{140}Ce$ ratio of 0.002124072 (Makashima and Nakamura (1992)) yields a $^{138}Ce/^{136}Ce$ value of 1.33736±1 (2 r.s.d). This small offset most likely results from the inconsistency of the used normalization ratios. We also recalculated data from other studies that used Mainz-AMES relative to this value, as outlined in detail above.

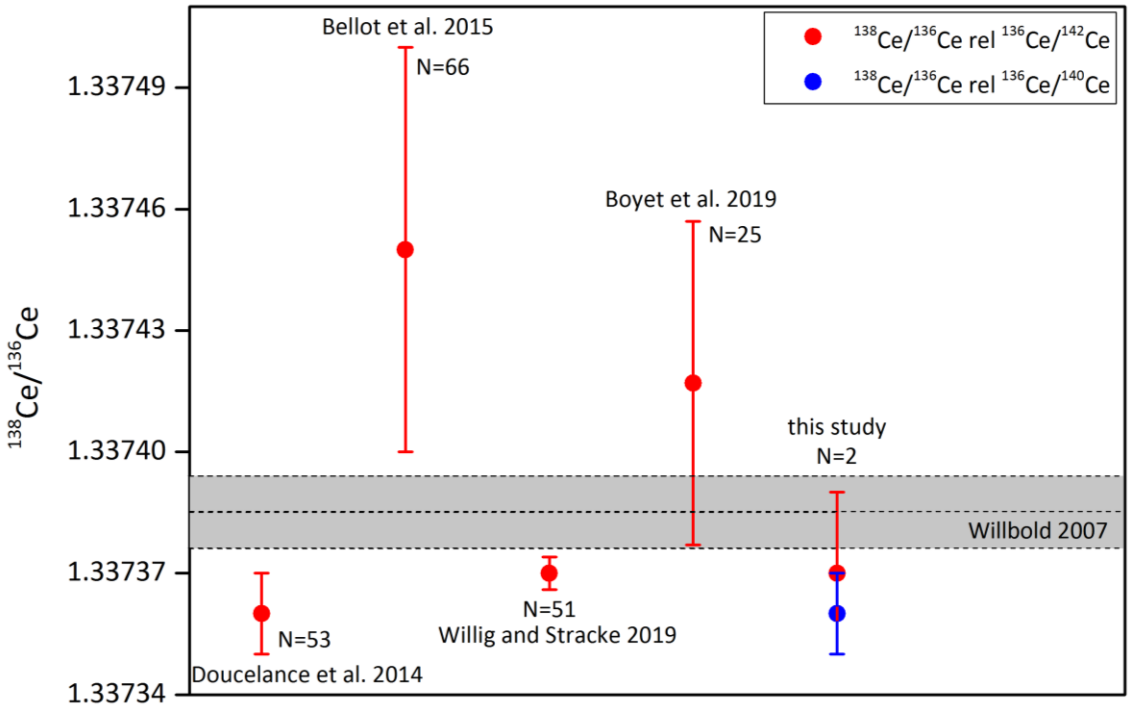

Figure 23 Absolute $^{138}Ce/^{136}Ce$ isotope ratios (error bars 2 r.s.d.) obtained for the Mainz-AMES standard in recent studies. Measured $^{138}Ce/^{136}Ce$ were corrected for mass fractionation using the exponential law and $^{136}Ce/^{142}Ce$ = 0.01688 (Makashima et al 1987) (red dots). Measured $^{138}Ce/^{136}Ce$ were mass bias corrected to $^{136}Ce/^{140}Ce$ 0.002124072 (Makashima and Nakamura (1991), Makashima et al. (1987) (blue dot). The grey shaded area (1.33738±1) show the mean value of Willbold (2007).

3.4.2. **Lanthanum-Cerium concentration data**

So far, four previous meteorite studies performed La and Ce concentration measurements along with Ce isotope measurements (Shimizu et al. (1984), Makashima and Masuda (1993), Makashima and Masuda (1994) and Willig and Stracke (2019), see Table 8). Three of these employed isotope dilution (Shimizu et al. (1984), Makashima and Masuda (1993), Makashima and Masuda (1994)), but no detailed description about the isotope tracer and the protocol for La-Ce determination was provided. In contrast to our study, where an accurately calibrated $^{138}La/^{142}Ce$ tracer and isotope dilution-MC-ICP-MS were employed, in the recent study of Willig and Stracke (2019), the La and Ce concentrations had only been determined by SF-ICP-MS relative to a multielement calibration solution with known quantities of La and Ce including 16 isotopically enriched elements (but not La and Ce, Stracke et al. (2012)). In additional studies (Barrat et al. (2012), Pourmand et al. (2012) and Braukmüller et al. (2018)), highly precise determinations of REE in meteorites (e.g. Allende, Nogoya, Cold Bokkeveld, Jiblet Winselwan

and MET1070) and standard materials (BCR-2 and BHVO-2) have been performed (Appendix B Table 21). These studies employed SF-ICP-MS or MC-ICP-MS and calibration was done either against BHVO-2 (Barrat et al. (2012)), against chondrite-matched calibration solutions (Braukmüller et al. (2018)), or against certified multielement solution by SPEX CertiPrep (Pourmand et al. (2012)). In order to evaluate potential systematic differences in La-Ce results, data for homogeneous rock reference materials need to be compared as these are better characterized and less heterogeneous than typical meteorite samples. Among these reference materials, BCR-2 and BHVO-2 are the best candidates, as they have been analyzed in most relevant studies. Moreover, Raczek et al. (2001) employed isotope dilution-TIMS and an accurately calibrated isotope tracer to determine a full set of REE concentration data for these two standards. Results are shown in Table 20 (Appendix B) and show an excellent agreement between our study and Raczek et al. (2001) in La/Ce ratios obtained for BCR-2 and BHVO-2 (to better than 0.2 %). When comparing the data for both standard materials BCR-2 and BHVO-2 (Chapter 2) and Braukmüller et al. (2018), the measured La/Ce ratios in Braukmüller et al. (2018) (external chondrite matched calibration) are systematically lower by ≅6%. Comparison of the La/Ce ratios for Allende-MS, Nogoya and MET 01070 measured in both studies on the same powder aliquots show a lower difference of 3-10% in the study of Braukmüller et al. (2018). Only the meteorite Cold Bokkeveld shows a difference of about 30% between both studies, likely reflecting sample heterogeneity. The La/Ce ratio in Pourmand et al. (2012), Barrat et al. (2012) and Stracke et al. (2012) is about 1% lower in La/Ce for BCR-2 and BHVO-2 reference material compared to Chapter 2, but their La/Ce value for the Allende meteorite is up to 10% lower. The La/Ce ratios obtained for BCR-2 and BHVO-2 in the study of Stracke et al. (2012) are ~5% lower than in the study of Braukmüller et al. (2018). While the La/Ce value of Allende in the study of Willig and Stracke (2019) is also about 5% lower than in the study of Braukmüller et al. (2018), Jiblet Winselwan is ca. 10% higher. Consideration of analytical uncertainties (1-8% RSD in the study of Barrat (2012), Pourmand et al. (2012), Braukmüller et al. (2017), Willig and Stracke (2019), Stracke et al. (2012) and 0.3% RSD in the study of Chapter 2 and this study), most results obtained for the chondritic La/Ce ratios overlap within their uncertainties. Apart from potential sample artifacts, most of the disagreement between the carbonaceous chondrite data reported above might be largely caused by the heterogeneous distribution of refractory inclusions such as Calcium Aluminum-rich inclusions (CAIs). Importantly, REE like La, Ce, Sm and Nd are highly enriched in CAIs. The REE patterns of CAIs are classified into six groups (Martin and Mason (1974)). The group II pattern is the most common in the CAIs and shows a flat CI chondrite-like LREE pattern but the LREEs are enriched over the middle REE (MREE) and high REE (HREE). In Typ II CAIs the mean La/Ce ratio of ca. 0.35 (Dauphas and Pourmand (2015)) is substantially lower than the proposed CI mean La/Ce ratio of 0.3897 (Palme and O'Neill (2014)) and our value obtained

for chondrites (0.3828). With a La/Ce mean value of CAIs that is about 10% lower than the La/Ce mean value in CI chondrites, the addition of 0.35% fine-grained CAI with group II REE pattern to a CI chondritic composition can reproduce the CV3 Allende meteorite pattern (Dauphas and Pourmand (2015)). Hence, heterogeneously distributed CAIs might quantitatively explain the La-Ce heterogeneity found for chondrites in the different studies (e.g. Stracke et al. 2012).

Cerium anomalies allow to asses the pristinity of La-Ce isotope data in meteorites. Under oxidizing conditions or weathering, Ce^{4+} may fractionate from REE^{3+}. In meteorites, terrestrial weathering can therefore result in modified La/Ce ratios, particularly in finds. The Cerium anomaly (Ce/Ce*; Equation 1) is defined as the difference between the actually measured and predicted Ce concentration, where the latter is interpolated from the La and Nd concentration of the individual samples.

For the calculation of the Ce anomalies (Equation 1), the La and Nd data obtained here by isotope dilution were used and normalized to the CI abundances of Lodders (2003). In most cases, the measured Ce concentrations in our samples agree with the predicted Ce concentrations, (Ce/Ce* ~1). This indicates that Ce behaved similarly to other LREE. However, Dimmitt (H3), Roosevelt (H3), and EET92002 (CK5), Karoonda (CK4) and Cold Bokkeveld (CM2) display small negative Ce anomalies (Ce/Ce* = 0.71 to 0.90) (Table 11, Figure 24). This indicates that Ce might be selectively depleted, or more likely, other REE were selectively enriched. As a consequence, La/Sm(CI) were plotted against Ce anomalies, an enrichment in La can be seen for Rooseveld, Karoonda and Cold Bokkeveld. Dimmit and Nogoya are not shown (details see above). Taking into account that these three meteorites plots at very high $^{138}La/^{136}Ce$ but with chondritic $^{138}Ce/^{136}Ce$ in Figure 22 it appears reasonable that a significant portion of terrestrial LREE including La were added during weathering.

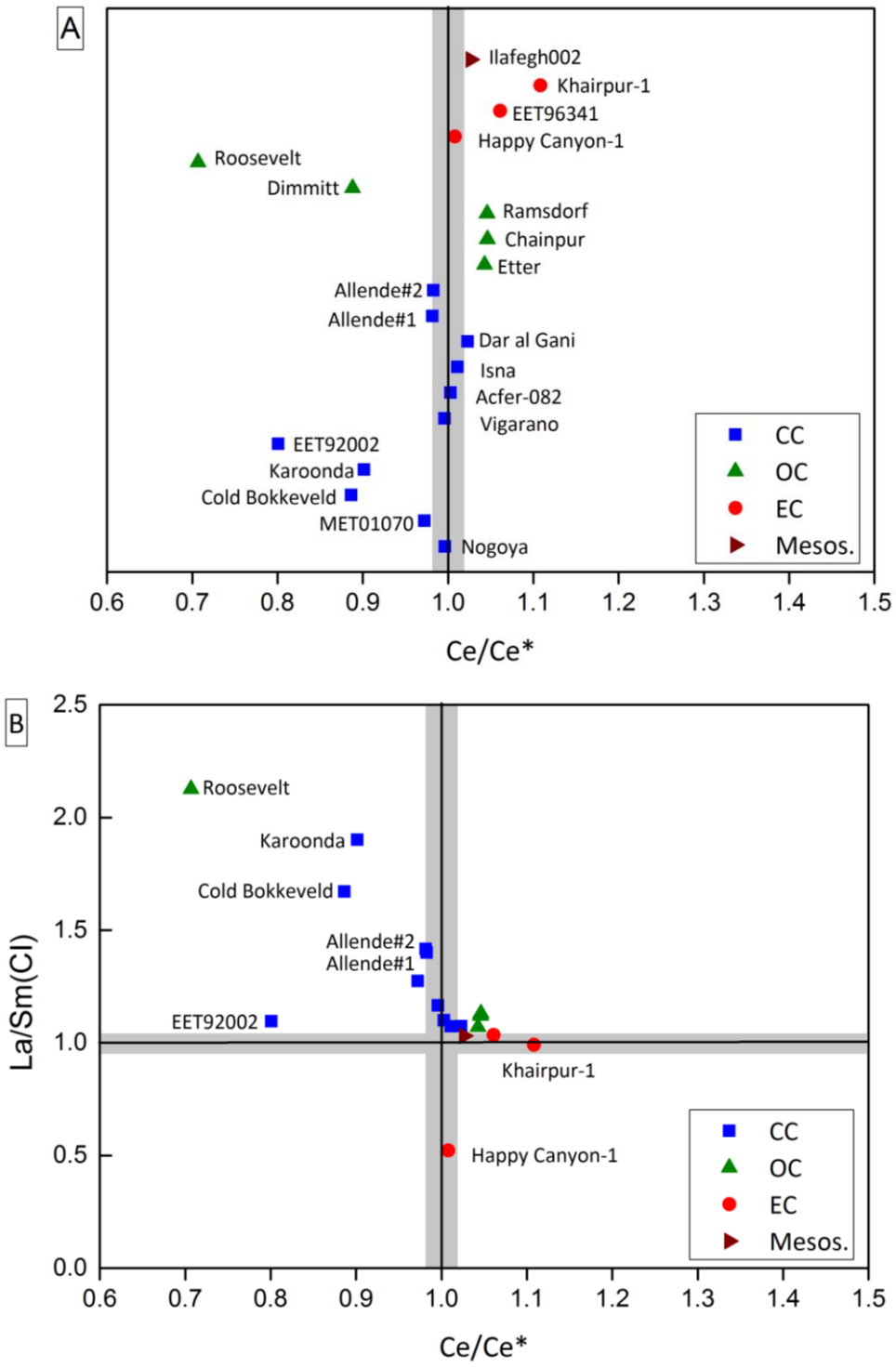

Figure 24 Cerium anomalies of the meteorite samples analyzed. Three different meteorites from two different classes (Dimmitt (H3), Roosevelt (H3), EET92002 (CK5), Karoonda(CK4) and Cold Bokkeveld (CM2)) show significant small negative Ce anomalies (Ce/Ce<1) and Khairpur displays a small positive anomaly (Ce/Ce*>1). The meteorites Roosevelt, Karoonda and Cold Bokkeveld also show a higher La/Sm (CI) value which indicates enrichment in La.*

Combined $^{138}Ce/^{136}Ce$ and La/Ce provide further insight in regard to whether the LREE gain occurred during terrestrial weathering or on the meteorite parent body early in solar system history. In the case of young terrestrial weathering, the Ce isotope ratio should overlap with those of the other meteorites (if not much Ce was added), in case of early parent body La/Ce

increase, ε^{138}Ce should be mostly radiogenic due to the additional long-term ingrowth of ^{138}Ce from ^{138}La decay. Figure 22 shows that Abee, Karoonda, Cold Bokkeveld and Roosevelt are clearly offset from the 4.56 Ga reference line because of their higher ^{138}La-^{136}Ce values but the Ce isotope ratios overlap with those of other meteorites. This indicates that their anomalous ^{138}La-^{136}Ce ratios might be caused by terrestrial weathering. Hence, these meteorites were excluded from the calculation of the mean chondritic ^{138}La/^{136}Ce value. In contrast, the ^{138}La/^{136}Ce ratio of Dimmit (0.2062) overlaps the typical range and was included in the calculation of the ^{138}La/^{138}Ce mean. As a consequence of the alteration effects described above, 20 out of 25 ^{138}La/^{138}Ce values were considered sufficiently robust and were used for the calculation of the mean ^{138}La/^{136}Ce value. These meteorites define a range in La/Ce and ^{138}La/^{136}Ce ratios 0.3828±139 and 0.1864±66 respectively.

3.4.3. Calculation of the mean ^{138}Ce/^{136}Ce and ^{138}La/^{136}Ce CHUR values

As mentioned above, the previous studies of Shimizu et al. (1984), Makashima and Masuda (1993) and Bellot et al. (2015) reported their Ce isotope data as ^{138}Ce/^{142}Ce relative to ^{136}Ce/^{142}Ce. For comparability, all literature data were recalculated to ^{138}Ce/^{136}Ce relative to ^{136}Ce/^{140}Ce and the uncertainties on ^{138}Ce/^{136}Ce relative to ^{136}Ce/^{142}Ce were propagated (see above and Table 8). Common to all more recent studies is that the Allende meteorite had been measured. The available ^{138}Ce/^{136}Ce data for Allende show small but significant differences between the various studies. If recalculated to the Mainz-AMES value of Willbold (2007) (1.33738±1), our measured ^{138}Ce/^{136}Ce values for Allende (1.33677±4 and 1.33685±5) are in excellent agreement with the results of Bellot et al. (2015) (1.33685±2) and also partially overlap with one Allende result of Willig and Stracke (2019) that are shifted towards higher values (1.33691±3 and 1.33692±1).

The chondritic mean ^{138}Ce/^{136}Ce value was calculated here using 18 different meteorites. When comparing the mean ^{138}Ce/^{136}Ce value of this study (1.33686±3, 2 s.e.) with recent studies, there is an excellent agreement with Bellot et al. (2015) (1.33684±3, 2 s.e.) but no overlap within uncertainties with the Ce isotope data by Willig and Stracke (2019) (1.33692±1, 2 s.e.). To get a more robust assessment, the confidence interval (95%) was calculated for each dataset to determine the respective analytical uncertainties for ^{138}Ce/^{136}Ce. For calculation Equation 9 was used.

$$\mu = x \pm t * \frac{s}{\sqrt{n}} \qquad \text{Equation 9}$$

where x is the mean, t is the statistic factor, s is the standard deviation and n the number of samples. The μ ^{138}La/^{136}Ce value for Willig and Stracke (2019) is 0.1884±6 and in this study 0.1864±19. The calculated 95% confidence interval confirms the interpretation made from standard errors. Our determined chondritic ^{138}La-^{136}Ce value overlaps within uncertainties with

the chondritic $^{138}La/^{136}Ce$ of Willig and Stracke (2019) and our recommended chondritic $^{138}La/^{136}Ce$ mean value is 0.1868±40 (2 s.e.).

The $\mu^{138}Ce/^{136}Ce$ value for Bellot et al. (2015) is 1.33684±6, for Willig and Stracke (2019) 1.33692±2 and in this study 1.33686±3. The $^{138}Ce/^{136}Ce$ CHUR value determined in this study overlaps within uncertainties with the results of Bellot et al. (2015) but is statistically distinguishable from the results of Willig and Stracke (2019). Therefore, we prefer to calculate the chondritic $^{138}Ce/^{136}Ce$ CHUR value only from the results of the study of Bellot et al. (2015) and this study. Our recommended weighted mean (n = 21) for $^{138}Ce/^{136}Ce$ is 1.33685±3 (2 s.e.). Our own mean $^{138}Ce/^{136}Ce$ value of 1.33686±3 (n = 18) shows a difference of only +0.07 ε-units from the recommended weighted mean value of 1.33685±3 that includes the Bellot et al. (2015) data (mean value$^{138}Ce/^{136}Ce$ of 1.33684±3), while mean value of Willig and Stracke (2019) deviates by +0.49 ε-units from relative to our recommended weighted value.

Back calculation of the present-day $^{138}Ce/^{136}Ce$ ratios in the different meteorites to the initial ratios at their time of formation (ca. 4.562 Ga) can provide further insights into the pristinity of their La/Ce values. If the actually measured La/Ce values were pristine, it would be expected that a back-calculation should generate a more narrow range of initial $^{138}Ce/^{136}Ce$ ratios. If this is not the case, this hints to a secondary La/Ce disturbance. For this purpose, all measured $^{138}Ce/^{136}Ce$ data were calculated to $4.562*10^9$ years (approximate time of chondrite formation), using $\lambda^{138}La = 2.37*10^{-12}$ (Tanimizu (2000)) and our individual measured $^{138}La/^{136}Ce$ values for each meteorite. The same calculation was done for the chondrite samples of Willig and Stracke (2019). In the study of Bellot et al. (2015) no concentration data for the meteorites are available so these values could not be recalculated. The results are shown in Figure 25. While some meteorites yield markedly unradiogenic outliers, most meteorites data scatter around a well-defined initial $^{138}Ce/^{136}Ce$ value. The unradiogenic outliers are evidently generated by an over-correction of present-day $^{138}Ce/^{136}Ce$, and these samples were already identified as candidates for young, most likely terrestrial disturbance in La/Ce (Cold Bokkeveld, Karoonda (blue circles), Abee (red dots) and Roosevelt (green triangle) in Figure 25). Excluding these outliers and, as discussed above, the meteorites Etter and EET92002, our mean $^{138}Ce/^{136}Ce_{4.562}$ value is 1.33461±16 (2 s.e.). The $^{138}Ce/^{136}Ce_{4.562}$ mean value for all meteorites of Willig and Stracke (2019) is 1.33483±8 (2 s.e.), by +1.63 ε-units higher than the age-corrected recommended weighted mean from this study. Willig and Stracke (2019) excluded Jbilet Winselwan and Saratov because of high La/Ce values. Excluding these both meteorites the $^{138}Ce/^{136}Ce_{4.562}$ mean value is 1.33488±2, yielding a difference of 2.00 ε-units to the age-corrected recommended weighted mean from this study. Using the mean value determined in this study ($^{138}La/^{136}Ce$ = 0.1864±66 and $^{138}Ce/^{136}Ce$ = 1.33685±3 recalculated to Mainz-AMES = 1.33738±1) and the mean value from the study of Willig and Stracke (2019)

(^{138}La/^{136}Ce = 0.1884±19 (2 s.e.) and ^{138}Ce/^{136}Ce = 1.33692±1 (2 s.e.) normalized to Mainz-AMES = 1.33738±1) recalculation of each result to the time of formation (ca. 4.562 Ga) yields a difference of +0.36 ε^{138}Ce.

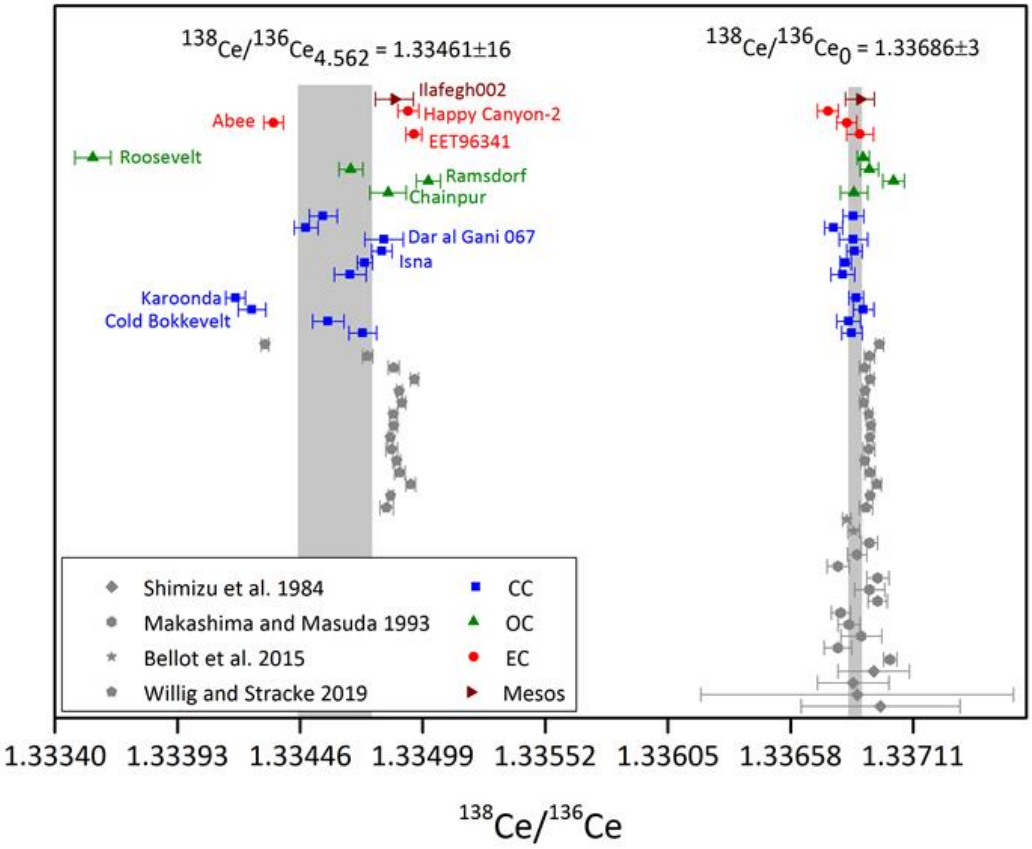

Figure 25 Measured (right) and age-corrected (left) ^{138}Ce/^{136}Ce ratios for chondrites and eucrites measured in this and previous studies. Reported uncertainties correspond to 2 s.e. Colored dots are data from this study. Grey symbols are literature data from Shimizu et al. (1984) (diamond), Makashima and Masuda (1993) (hexagon), Bellot et al. (2015) (star) and Willig and Stracke (2019) (pentagon). The mean ^{138}Ce/^{136}Ce$_0$ value of this study is 1.33686±3 (2 s.e.), and the mean ^{138}Ce/^{136}Ce$_{4.562}$ value is 1.33468±12 (2 s.e.). The back calculated meteorites Cold Bokkeveld, Karoonda (blue square), Abee (red dot) and Roosevelt (green triangle) define outliers because of a young La/Ce disturbance and were therefore excluded from the calculation of the ^{138}La/^{136}Ce mean value.

As mentioned above, the combination of the La-Ce and Sm-Nd chronometers is a unique tool to study the behavior of the LREE in terrestrial silicate reservoirs due to the opposite relative compatibilities of La-Ce and Sm-Nd pairs, where an anti-correlation between the two radiogenic isotope ratios is expected. Selected meteorites (see caption for details) are shown in the ^{143}Nd/^{144}Nd and ^{138}Ce/^{136}Ce space at present time (Figure 26 A) and recalculated, the estimated age for chondrite formation at 4.562 Ga (Figure 26 B). For the recalculation of the ^{143}Nd/^{144}Nd$_{4.562}$ and ^{138}Ce/^{136}Ce$_{4.562}$ value the individual ^{147}Sm/^{144}Nd, ^{144}Nd/^{143}Nd, ^{138}La/^{136}Ce and ^{138}Ce/^{136}Ce were used. Figure 26 A shows, as expected, a widespread in ε^{143}Nd (from -2 to +4) and a small spread in ε^{138}Ce (from -0.25 to +1.4), as the meteorite samples show a greater variation in Nd than in Ce mainly because of the much larger abundance of ^{147}Sm compared to ^{138}La relative to the daughter isotopes. As expected ε^{138}Ce$_{4.562}$ does not show any significant variations except the ordinary chondrite Ramsdorf which shows a slight deviation from ε^{138}Ce$_{4.562}$ of ~+1.2 ε^{138}Ce. Literature data of Willig and Stracke (2019) show the same

spread in $\varepsilon^{138}Ce_{4.562}$ and $\varepsilon^{143}Nd_{4.562}$ as in this study. In Figures 26 A and 26 B a systematic offset of about +0.5 in $\varepsilon^{138}Ce_{today}$ and $\varepsilon^{138}Ce_{4.562}$ the data of Willig and Stracke (2019) and in this study can be seen. Interestingly, the meteorites Pultusk, Parnalle and Sarastow from Willig and Stracke (2019) show a significant offset in $\varepsilon^{143}Nd_{4.562}$ (+0.5 until +5) and $\varepsilon^{138}Ce_{4.562}$. (-3 until +2).

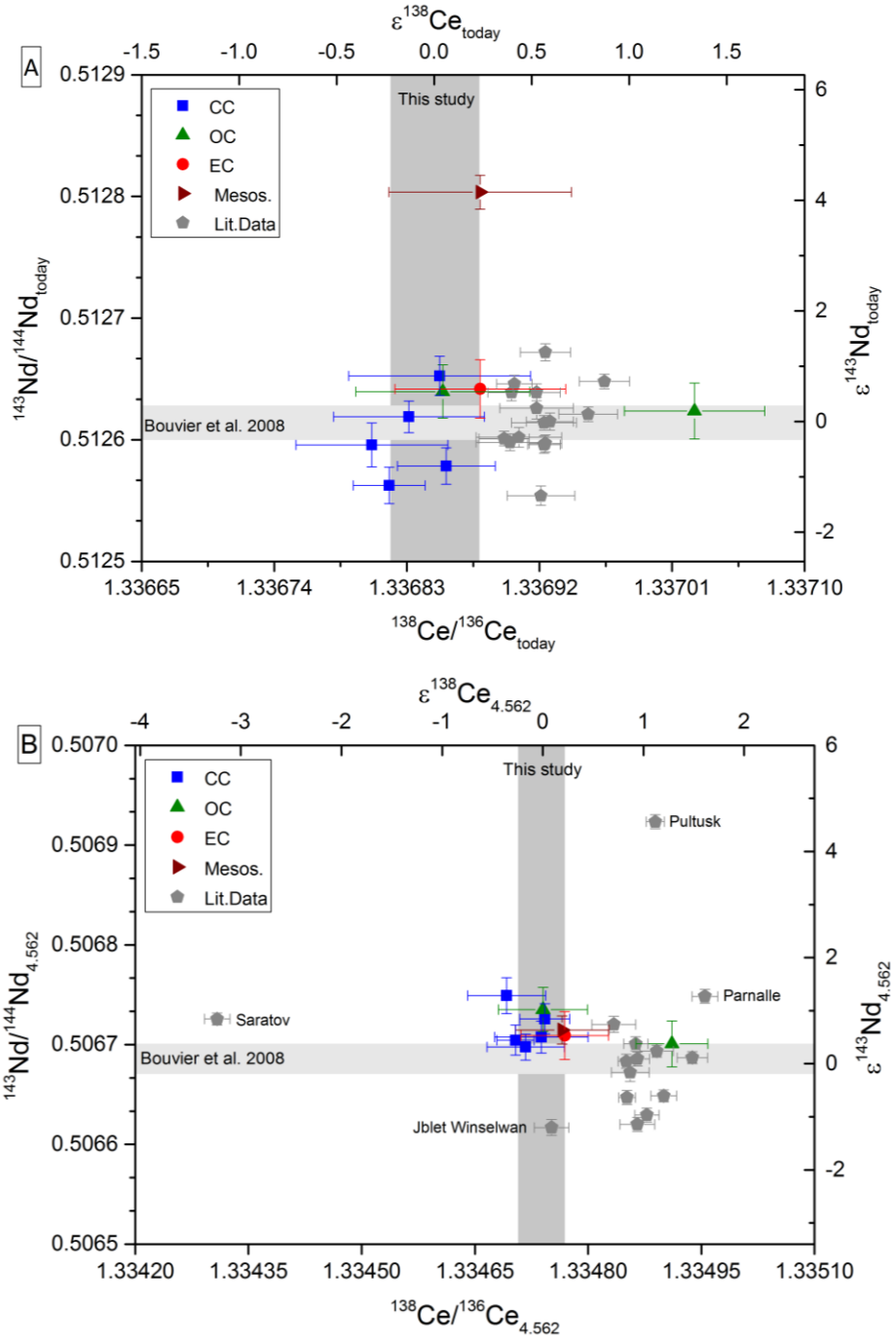

Figure 26 $^{143}Nd/^{144}Nd$ vs. $^{138}Ce/^{138}Ce$ at present day (A) and recalculated at 4.562 Ga (B). Some meteorites were excluded due to low Ce concentrations in the respective element cut (Khairpur), large Ba interferences (EET92002, Happy Canyon-1, Etter, Khairpur-1 and Khairpur-2), Ce anomaly (Roosevelt), secondary La/Ce disturbance (Cold Bokkeveld and Karoonda) and Sm/Nd fractionation (Nogoya and Dimmit)(see section results). Literature data are taken from Willig and Stracke (2019). For the recalculation of the individual $^{138}La/^{136}Ce$ and $^{138}Ce/^{136}Ce$ value of each meteorite was used.

3.4.4. **Implications for terrestrial La-Ce systematics**

The difference between the $^{138}La/^{138}Ce$ CHUR value obtained in our study to that proposed by Willig and Stracke (2019) may have important implications for the interpretation of combined Ce-Nd isotope patterns in terrestrial rocks. Figure 27 shows available Ce and Nd data for MORBs and OIBs from various studies (Makashima and Masuda (1994), Willig and Stracke (2019) and Boyet et al. (2019)) that define the terrestrial Ce-Nd isotope mantle array. All data were recalculated to a $^{138}Ce/^{136}Ce$ for Mainz-AMES of 1.33738±1. Using the $^{138}Ce/^{136}Ce$ CHUR value of Willig and Stracke (2019) (1.33692±1 relative Mainz-AMES) some Gough sample (green triangle, Boyet et al. (2019)) show negative $\varepsilon^{143}Nd$ and $\varepsilon^{176}Hf$ values but also negative $\varepsilon^{138}Ce$, which is contrary to the predicted opposing behavior of the three isotope systems. Using the $^{138}Ce/^{136}Ce$ value of this study (1.33685±3 relative Mainz-Ames) all MORB and OIB data show the expected co-variation, starting from positive $\varepsilon^{143}Nd$ values and negative $\varepsilon^{138}Ce$ values in MORBs. The MORB and OIB data define a linear Ce-Nd isotope mantle array given by the empirical equation $\varepsilon^{143}Nd = -8.7 \times \varepsilon^{138}Ce + 3.4$. Within uncertainty, the Ce-Nd mantle array intersects with non of the $^{138}Ce/^{136}Ce$ values (this study, Willig and Stracke (2019)).

In this study and in the study of Willig and Stracke (2019) all chondrites were used for the calculation of the $^{138}La/^{136}Ce$ CHUR value but there is an ongoing debate if non-carbonaceous (enstatite and ordinary) or enstatite chondrites only are the buildings block of the Earth (e.g. Warren (2011), Boyet et al. (2018)). In this debate it is still unclear 1) if the Earth accreted from a homogenous isotopic reservoir which was isotopically similar to non-carbonaceous or enstatite chondrites or 2) if the Earth accreted from different diverse embryos whose mixture resembles non-carbonaceous or enstatite meteorites. Additionally, there is an ongoing debate about which subgroup of enstatite chondrites (EH or EL) and which petrological type reflects the building blocks of the Earth. Enstatite chondrites are rare and most of the enstatite chondrites that are found on Earth are affected by weathering. However, enstatite chondrites and the Earth are indistinguishable in many isotope systems, i.e. Cr, Ti, O, Ni (Dauphas (2017) and references therein, Boyet et al. (2018). Exceptions are Si, Mo and Ru (Chen et al. (2010), Becker and Walker (2003), Fitoussi and Bourdan (2012), Burkhardt et al. (2011), Yokoyama and Walker (2016), Fischer-Gödde and Kleine (2017)). The assumption is that the Si isotope ratio does not reflect the initial composition of the starting material because Si has been fractionated during nebular processes (Savage and Moynier (2013), Zambardi et al. (2013), Dauphas et al. (2015)). For Mo and Ru no known combination of meteorites can reconstruct the Earth. All classes of meteorites show positive εMo and negative εRu values relative to terrestrial samples. Boyet et al. (2018) proposed based on ^{146}Sm-^{142}Nd measurements that the enstatite subgroup EL3 reflects the Earth's building blocks.

In this study, the determination of the $^{138}Ce/^{136}Ce$ value was only possible for three enstatite chondrites. For the meteorites Abee and Happy Canyon-2 no Sm-Nd data have been available and as a consequence, no Cerium anomalies could be calculated. As illustrated in Figure 22 Abee plots offset from the 4.56 Ga reference line because of the slightly higher $^{138}La/^{136}Ce$ value. It cannot be ruled out that Abee such as the meteorites Cold Bokkeveld and Karronda added a significant portion of terrestrial LREE including during weathering. However, it is possible to calculate the $^{138}La/^{136}Ce$ and $^{138}Ce/^{136}Ce$ mean value for carbonaceous and non-carbonaceous chondrites (Warren (2011)). The carbonaceous chondritic $^{138}Ce/^{136}Ce$ mean value of this study is 1.33684±2 (2 s.e., n = 10, relative to Mainz-AMES) and overlaps within uncertainties with the carbonaceous chondritic $^{138}Ce/^{136}Ce$ value 1.33685±2 (2 s.d. relative to Mainz-AMES) of Bellot et al. (2015) but shows no overlap with the carbonaceous chondritic $^{138}Ce/^{136}Ce$ mean value 1.33692±1 (2 s.e., n = 7) of Willig and Stracke (2019). As a consequence, we recommend to calculate the carbonaceous chondritic $^{138}Ce/^{136}Ce$ mean value from this study and the$^{138}Ce/^{136}Ce$ value of Bellot et al. (2015) resulting in a mean value 1.33684±2 (2 s.e., n = 11, relative to Mainz-AMES). The non-carbonaceous chondritic $^{138}Ce/^{136}Ce$ mean value of this study is 1.33688±6 (2 s.e., n = 7, relative to Mainz-AMES) and overlap within uncertainties with the non-carbonaceous chondritic $^{138}Ce/^{136}Ce$ mean value 1.33692±1 (2. s.e., n = 7 relative to Mainz-AMES) of Willig and Stracke (2019)) and with the enstatite chondrite value 1.33680±2 (2 s.d.) of Bellot et al. (2015). As a consequence, we recommend to calculate the non-carbonaceous chondritic $^{138}Ce/^{136}Ce$ mean value from all recent studies and the non-carbonaceous chondritic $^{138}Ce/^{136}Ce$ mean value is 1.33689±4 (2. s.e., n = 14). The MORB and OIB data define a linear Ce-Nd isotope mantle array given by the empirical equation $\varepsilon^{143}Nd = -8.7 \times \varepsilon^{138}Ce + 0.83$. Within uncertainty, the Ce-Nd mantle array intersects with the non-carbonaceous chondritic $^{138}Ce/^{136}Ce$ value of this study shows no overlap with the carbonaceous chondritic $^{138}Ce/^{136}Ce$ value of this study. (Figure 27 B).

In the same way, the $^{138}La/^{136}Ce$ mean values for carbonaceous and non-carbonaceous chondrites were determined. The carbonaceous chondritic $^{138}La/^{136}Ce$ mean value of this study is 0.1980±65 (2. s.e., n = 8) and the non-carbonaceous chondritic $^{138}La/^{136}Ce$ mean value of this study is 0.1804±80 (2. s.e., n = 11). In the study of Bellot et al. (2015) no $^{138}La/^{138}Ce$ were determined. In the study of Willig and Stracke (2019) the carbonaceous chondritic $^{138}La/^{136}Ce$ mean value is 0.1900±51 (2. s.e., n = 7) and the non-carbonaceous chondritic $^{138}La/^{136}Ce$ mean value 0.1851±147 (2. s.e., n = 6). As a consequence, the carbonaceous and non-carbonaceous chondritic value of this study and Willig and Stracke (2019) overlap within uncertainties and we recommend to calculate the mean values from both studies. As a consequence, the carbonaceous chondritic $^{138}La/^{136}Ce$ mean value is 0.1946±43 (2. s.e., n = 14) and the non- carbonaceous chondritic $^{138}La/^{136}Ce$ mean value is 0.1823±46 (2. s.e., n = 17).

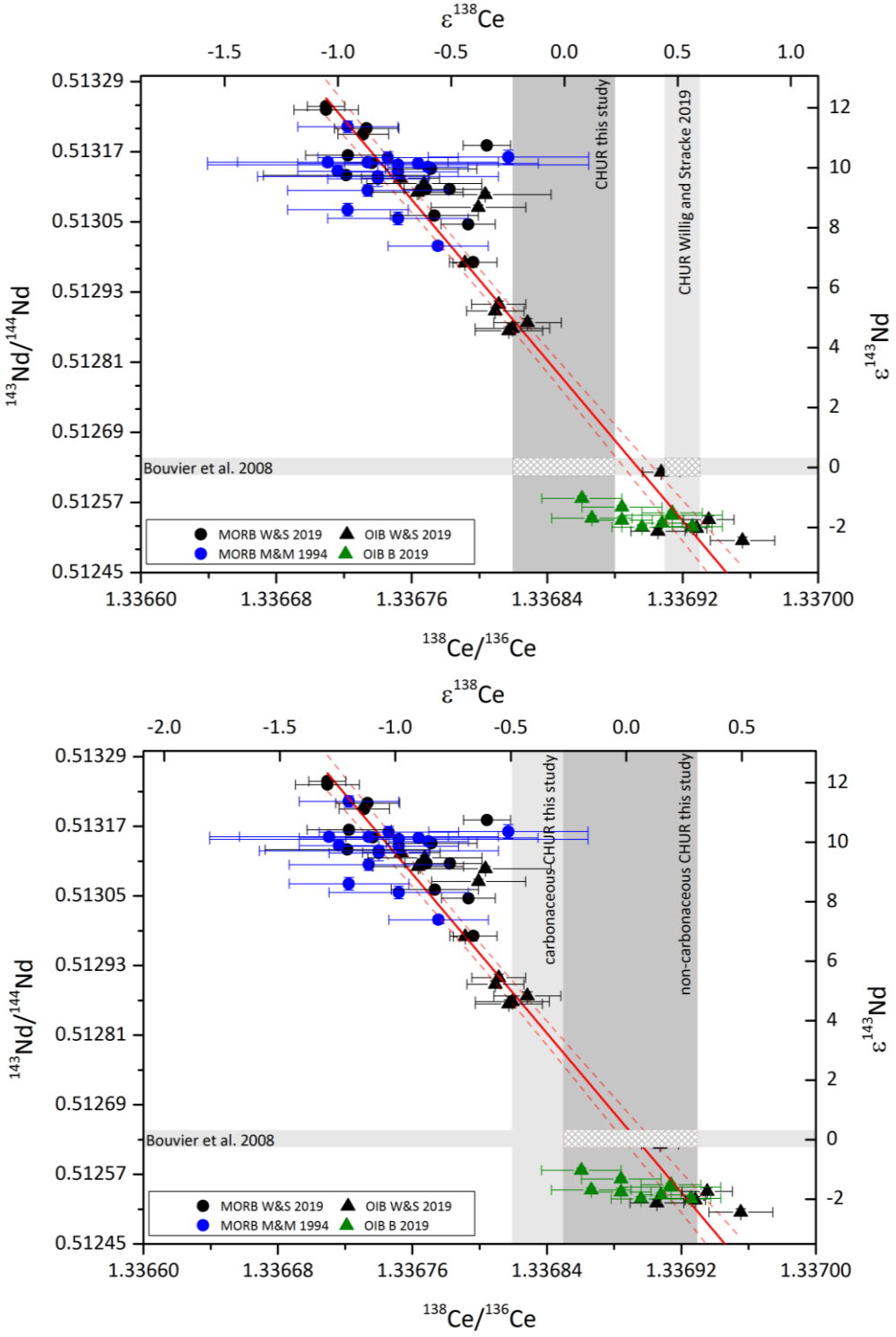

Figure 27 Comparison of published $^{138}Ce/^{136}Ce$ vs. $^{143}Nd/^{144}Nd$ isotope data for MORBs and OIBs with different CHUR estimates. MORB and OIB literature data are from Willig and Stracke (2019) (W&S 19), Makashima and Masuda (1994) (M&M 94) and Boyet et al. (2019) (B 2019). In Figure 22 A the chondritic $^{138}Ce/^{136}Ce$ CHUR values determined in this study and in the study of Willig and Stracke (2019) and the $^{143}Nd/^{144}Nd$ CHUR value from Bouvier et al. (2008) are shown. The Ce-Nd mantle array is defined by the equation $\varepsilon^{143}Nd = -8.7\varepsilon^{138}Ce+3.4$. (A) (this study). Both chondritic $^{138}Ce/^{136}Ce$ values show no overlap within the uncertainties of the Ce-Nd mantle array. In Figure 22 B the MORB and OIB data are shown using the carbonaceous (1.33684±4 2 s.e) and non-carbonaceous chondritic (1.33689±4 2 s.e.) $^{138}Ce/^{136}Ce$ mean value of this study. Within uncertainties, an overlap of the Ce-Nd mantle array with the non- carbonaceous chondritic $^{138}Ce/^{136}Ce$ mean value is observed.

3.5. Conclusions

In this study, we define the ^{138}La-^{138}Ce CHUR reference values more accurately by analyzing 22 carbonaceous, ordinary and enstatite chondrites of petrologic types 1 to 6. Both ^{147}Sm-^{143}Nd and ^{138}La-^{138}Ce isotope data were determined on the same meteorite aliquots to combine the ^{138}La-^{138}Ce isotope system with the more popular ^{147}Sm-^{143}Nd system. The ^{147}Sm-^{143}Nd isotope data are in good agreement with literature data (Bouvier et al. (2008), Patchett et al. (2012), Boyet and Carlson (2005), Carlson et al, (2007), Bouvier et al. (2008)) (Figure 21). While Bouvier et al. (2008) suggested using only unequilibrated chondrites for the Lu-Hf and Sm-Nd CHUR values even the Sm-Nd CHUR value of unequilibrated chondrites overlap with the mean value of all chondrites. In line with Sm-Nd patterns, we use all chondrites of this study for the determination of the ^{138}La-^{138}Ce CHUR parameters. Some outliers with clearly disturbed La/Ce ratios have been excluded. In this study, twenty meteorites were used to determine the chondritic ^{138}La/^{136}Ce value 0.1864±66. Our chondritic ^{138}La/^{136}Ce value overlaps within uncertainties with the chondritic ^{138}La/^{136}Ce value from Willig and Stracke (2019) and we recommend a chondritic ^{138}La/^{136}Ce value of 0.1868±40 (2. s.e, n=33). In Appendix B Table 21 informations which chondrites are used are given.

Our chondritic ^{138}Ce/^{136}Ce value of 1.33686±3 (2 s.e.) is in excellent agreement with that of Bellot et al. (2015) (1.33684±3, 2 s.e.). As supported by a t-test, the chondritic ^{138}Ce/^{136}Ce mean value proposed by Willig and Stracke (2019) deviates significantly from the mean value obtained in this study and by Bellot et al. (2015). For this reason, we recommend using the chondritic ^{138}Ce/^{136}Ce mean value calculated from the combined results of Bellot et al. (2015) and this study, yielding a ^{138}Ce/^{136}Ce of 1.33685±3 (2 s.e.).

When the combined Ce-Nd literature data for MORBs and OIBs (Makashima and Masuda (1994), Willig and Stracke (2019) and Boyet et al. (2019)) are considered, the Ce-Nd isotope data define a Ce-Nd mantle array (Figure 27 A and 27 B). Using the chondritic ^{138}Ce/^{136}Ce of Willig and Stracke (2019), some OIBs yield inconsistent ε^{176}Hf, ε^{143}Nd and ε^{138}Ce values. Using our newly determined chondritic ^{138}Ce/^{136}Ce value this problem is solved and all MORB and OIBs data show negative ε^{143}Nd and positive ε^{138}Ce and vice versa as expected from the opposing relative incompatibilities of the Sm/Nd and La/Ce parent-daughter ratios. However, both chondritic mean values show no overlap within uncertainties with the Ce-Nd mantle array. Due to the ongoing debate which group and petrological type of chondrites reflects the building blocks of the Earth (e.g. Warren (2011), Boyet et al. (2018)) both carbonaceous and non-carbonaceous chondritic ^{138}Ce/^{136}Ce mean values were calculated. The carbonaceous chondritic ^{138}Ce/^{136}Ce mean value is 1.33684±2 (2 s.e., n = 11, relative to Mainz-AMES) and was calculated from this study and the result from Bellot et al. (2015) because the carbonaceous chondritic ^{138}Ce/^{136}Ce mean value of Willig and Stracke (2019) shows no

overlap within uncertainties. The non-carbonaceous chondritic $^{138}Ce/^{136}Ce$ mean value of this study, the study of Bellot et al. (2015) and Willig and Stracke (2019) overlap within uncertainties and our recommended non-carbonaceous chondritic $^{138}Ce/^{136}Ce$ mean value is 1.33689±4 (2 s.e., n=17) and within uncertainties, the Ce-Nd mantle array as known to date intersects with the non-carbonaceous chondritic $^{138}Ce/^{138}Ce$ mean value of this study. However, further $^{138}Ce/^{136}Ce$ measurements of ordinary and enstatite chondrites are needed to determine the non-carbonaceous and enstatite $^{138}Ce/^{136}Ce$ value more precisely. Additionally, there are only a few MORB and OIB data available and the first study shows large uncertainties (~±0.75 $\varepsilon^{138}Ce$ units). Therefore, no statement can presently be made about the question if the accessible silicate Earth is subchondritic or supra-chondritic in its Ce isotope composition, but the importance of accurately determining the $^{138}Ce/^{136}Ce$ value becomes evident.

The non-carbonaceous chondritic $^{138}La/^{136}Ce$ mean value of this study is 0.1823±46 (2 s.e., n=17) and the carbonaceous chondritic $^{138}La/^{136}Ce$ mean value of this study is 0.1946±43 (2 s.e., n=14). Both $^{138}La/^{136}Ce$ mean values show no overlap within uncertainties. This difference is highly significant, once age-corrected initial Ce isotope ratios are calculated for example older terrestrial samples. Recalculating the non-carbonaceous and carbonaceous chondritic value of this study to an age of the oldest rocks on Earth $3.8*10^9$ years would cause a difference of 1.2 $\varepsilon^{138}Ce$. This significant difference would affect the interpretation of the data with respect to crust-mantle differentiation processes.

Chapter 4

Combined ^{138}La-^{138}Ce, ^{147}Sm-^{143}Nd and ^{176}Lu-^{176}Hf isotope systematics in early Archean rocks from southern West Greenland and South Africa

4.1. Introduction

The long-lived radionuclide decay system ^{138}La-^{138}Ce is a powerful tool to study the behavior of the LREE. The potential application of the ^{138}La-^{138}Ce radioactive decay system to geochronology was first introduced in the 1980's (Makashima and Masuda (1982)). The application in geochemistry is based on the higher incompatibility of the parent nuclide ^{138}La relative to the daughter nuclide ^{138}Ce during partial melting processes and also on the refractory-lithophile nature of both elements. The application of the ^{138}La-^{138}Ce system to geochronology and isotope chemistry has been limited because of the requirement of an efficient separation technique and a highly precise isotope analysis (see Chapter 2).

As for Archean rocks, until now, one single study (Shimizu et al. (1988)) combined the ^{138}La-^{136}Ce geochronometer with the more popular ^{147}Sm-^{143}Nd radioactive decay system for Archean Amîtsoq gneisses from West Greenland. In several other studies, the more popular ^{176}Lu-^{176}Hf and ^{147}Sm-^{143}Nd decay system have been used to constrain the evolution of the mantle-crust differentiation processes during Earth's history (e.g. Hoffman et al. (2011), Schneider et al. (2018, 2019), van de Löcht et al. (2018), Blichert-Toft et al. (1999), Vervoort et al. (1996), Kramers (2007)). During mantle-crust differentiation processes, the parent-daughter ratios of La/Ce are fractionated inversely compared to Lu/Hf or Sm/Nd. A depleted mantle is characterized by higher Sm/Nd and Lu/Hf ratios but lower La/Ce ratios (compared to CHUR), whereas an enriched crust will produce complementary parent-daughter ratios. Consequently, with increasing time, the continental crust will evolve towards lower ε^{176}Hf and ε^{143}Nd values but higher ε^{138}Ce values, whereas depleted mantle domains will evolve towards higher ε^{176}Hf and ε^{143}Nd values but lower ε^{138}Ce (Figure 6, Chapter 1). Due to the similar fractionation of Sm/Nd and Lu/Hf during geological processes, both systems are strongly coupled. However, in some early Archean rock suites there is a strong decoupling of Nd and Hf isotope compositions (e.g. Caro et al. (2005), Hiess et al. (2009), Hoffmann et al. (2011), Rizo et al., (2011)). Until now, three models have been proposed. One possibility is the metasomatism (overprint one of the source rock changing the chemical and mineralogical composition) of depleted mantle with a subduction-derived component (e.g., Jenner et al. (2009), Hoffmann et al. (2011)). Alternatively, this apparent decoupling of Hf and Nd isotopes

might be caused by late post-emplacement metamorphic events (e.g., Moorbath et al. (1997), Frei et al. (2002), Hoffmann et al. (2011), van de Löcht (2019)) or by fractionation of Ca and Mg perovskite during magma ocean crystallization (Rizo et al. (2011), Hoffmann et al. (2011), Puchtel et al. (2016))

A major open question in unveiling Earth's geological history is how geodynamic processes worked during the Hadean and Archean. There is an ongoing debate when mantle-crust differentiation processes started and when modern Phanerozoic-style plate tectonics began to take place (Chapter 1). It is still unclear, if the extraction of an enriched crustal reservoir from a chondritic mantle occurred as early as 4.4 Ga (Harrison et al. (2005), (2008) Blichert-Toft and Albaréde (2008), Shirey et al. (2008) and references therein), or if such differentiation processes began at 4.2-4.3 Ga. (Vervoort et al. (1999)), or possibly even later (Kemp et al. (2015), Pettersson et al. (2019)). These geochemical issues are accompanied by the (so far) unanswered question of how strong the mantle in the Archean had been depleted. Some ^{176}Lu-^{176}Hf isotope studies yielded extremely high initial ε^{176}Hf values which could imply an early highly depleted mantle (Hoffman et al. (2011), Nebel et al. (2014)) whereas the studies of Kemp et al. (2010 and 2015) and Peterson et al. (2019) show evidence that the mantle has been chondritic until ca. 3.7 Ga ago.

Here, we present the application of the ^{138}La-^{138}Ce geochronometer on some of the oldest known Archean rocks from the Itsaq Gneiss Complex (IGC), southwest Greenland, and the Ancient Gneiss Complex (AGC) and Barberton Greenstone Belt (BGB), South Africa.

4.2. Geological Overview

The samples used in this study have been collected from two different localities: South West Greenland and South Africa. In the following, a short geological overview is given about the samples.

The 3900 to 3600 Ma old IGC (Figure 28) is made up of two Eoarchean terranes, the Færingehavn and the Isukasia Terrane. Both terranes consist of up to 90% TTGs with ages that range from 3650 to 3890 Ma (Nutman et al. (1996), Horie et al. (2010), Næraa et al. (2012)). These TTGs intruded into supracrustal fragments (mainly amphibolites and rare metasedimentary rocks), that were deformed and metamorphosed prior to the intrusion of the TTGs (e.g., Nutman et al. (2009), Hoffmann et al. (2011)). In addition, small ultramafic enclaves occur in both Eoarchean terrains of the IGC. The IGC represents the largest fragment of Eoarchean continental crust, predominantly comprising TTG gneisses (Nutman et al. (1996)).

The Isua supracrustal belt (ISB) also represents one of the oldest and best preserved Archean successions and is emplaced within the Itsaq Gneiss Complex (Nutman et al. (1996)). This greenstone belt comprises different varieties of (ultra-)mafic metavolcanic rocks as well as

metasediments and more differentiated plutonic rocks (e.g., Nutman et al. (1984), Rosing and Rose (1993), Appel et al. (1998)). Nutman et al. (2009) inferred that the ISB is divided into two distinct belts of different ages (~3700 Ma and the ~3800 Ma) that are separated by a mylonitic contact shear zone of Eoarchean age (Figure 28). Both terranes are dominated by amphibolites (e.g., Polat and Hofmann (2003), Jenner et al., (2009)) and from the ~3800 Ma terrane two amphibolites samples JEH 2007-08 and JEH 2007-19 have been collected (Hoffmann et al. (2011)).

Furthermore, six well preserved TTG samples JEH 10-18, JEH 10-19, JEH 10-24, JEH 10-25, JEH 10-38, JEH 10-39 have been collected the IGC in the Isukasia terrane southwest of the ISB (SOISB) (Hoffmann et al. (2014)). This area is very suitable for collecting early Archean rocks, as it was only affected by tectonic low strain events in the Mesoarchean. Predominantly, rocks from this area are ca. 3.70-3.85 Ga old, whereas all sampled TTGs are about 3800 Ma old. The IGC sample set also includes mafic-ultramafic inclusion, including mantle peridotites 10-12B originating from the Narssaq ultramafic body (NUB) which is located in the Færingehavn terrane (van de Löcht et al. (2018)). Additional to the whole rock samples mentioned above, the mineral separates 10-11-A1 (amphibole), 10-20C-A1 (amphibole) and 10-36-A1 (amphibole) were also investigated in this study (Table 12).

The oldest fragment of continental crust in South Africa and Swaziland is the second locality that was studied here (Figure 29). 21 samples of the 3660-3200 Ma (Hoffmann and Kröner, in press) along the Southern Side of the BGB were selected. The evolution of the AGC covers almost the entire Paleoarchean, with the oldest gneisses yielding protolith ages of up to 3666 Ma (e.g. Compston and Kröner (1988), Schoene et al. (2008), Zeh et al. (2011), Kröner et al. (2014)), and the youngest components having ages of ca. 3.2 Ga (e.g. Kröner et al. (1991, 1996)). The AGC rocks are intruded by the ca. 3100 Ma Piggs Peak batholith and several smaller granite plutons at ca. 2700 Ma (Figure. 29; e.g., Wilson (1989), Zeh et al. (2011), Mukasa et al. (2013)). The oldest component of the AGC is the 3606-3450 Ma Ngwane Gneiss, represented in this study by the 3442 Ma grey gneiss sample AGC 352, the granitic gneiss sample AGC 351 and Mtimanre River metagabbro AGC 350 (ca. 3450 Ma). The Ngwane Gneiss is intruded by the 3478–3430 Ma homogeneous and variably foliated dioritic to tonalitic Tsawela Gneiss (TG) (e.g. Kröner et al. (2007), Zeh et al. (2011), Hoffmann et al. (2016)), granitoid gneisses of the ca. 3230 Ma Usutu Intrusive Suite (Schoene et al. (2009)), and the 3.1 Ga Pigg's Peak batholith (Murphy (2015)) which divides the AGC from the BGB in the north, as well as several other smaller plutons with ages up to 2700 Ma (e.g. Zeh et al. (2011)). Additionally, in northwest Swaziland a small inlier (Piggs Peak inlier) of 3660 Ma AGC gneisses occurs in faulted and sheared contact with ca. 3450 Ma BGB rocks. From this Piggs Peak inlier the samples AGC 370 (tonalite, 3552 Ma) and AGC 445 (grey gneiss, 3216 Ma) were selected. The most prominent and largest supracrustal succession within the AGC is the 3450 Ma

Dwalile Greenstone Remnant (DGR; Kröner and Tegtmeyer (1994)) that is located west of Mankayane town. From the DGR the four samples AGC 45 (amphibolite, 3460 Ma; Kröner and Tegtmeyer (1994)), AGC 50 (meta-komatiite, ca. 3450 Ma), AGC 49 (amphibolite) and AGC 473 (throndjemitic gneiss, 3241 Ma) were selected. The Tsawela Gneiss is a younger (ca. 3450 Ma) plutonic suite from west-central Swaziland sample AGC 75 (tonalitic gneiss, 3478 Ma) was chosen from the TG. Additionally to the two amphibolites (AGC 45 and AGC 50) which are described above, a third amphibolite AGC 222 (>3400 Ma) from the Kubuta area of southern Swaziland was selected. Moreover, the 3216 Ma granodiorite AGC 368 from the Usutu Suite was analyzed.

The 3530–3200 Ma BGB and surrounding ca. 3200-3510 Ma plutons (Steynsdorp, Theespruit, Stolzburg, Nelshoogte, and Kaap Valley plutons) are tectonically separated from the AGC. The oldest unit of the BGB is the Onverwacht Group, which comprises (ultra-)mafic volcanic rocks that are interlayered with subordinate felsic rocks. From this area one meta-tholeiite ZA-32a (3482 Ma) and a komatiitic basalt ZA 51 (3482 Ma) of the Komati Formation were selected. From the Theespruit Formation the amphibolites KS-BA 182 (3530 Ma), KS-BA 184 (3530 Ma), BA 156 (3530 Ma) and BA 155 (3538 Ma) were selected. Also, the tonalitic grey gneiss BA 128 was collected in this area. From the Sandspruit Formation, the amphibolite KS-BA 171 was collected.

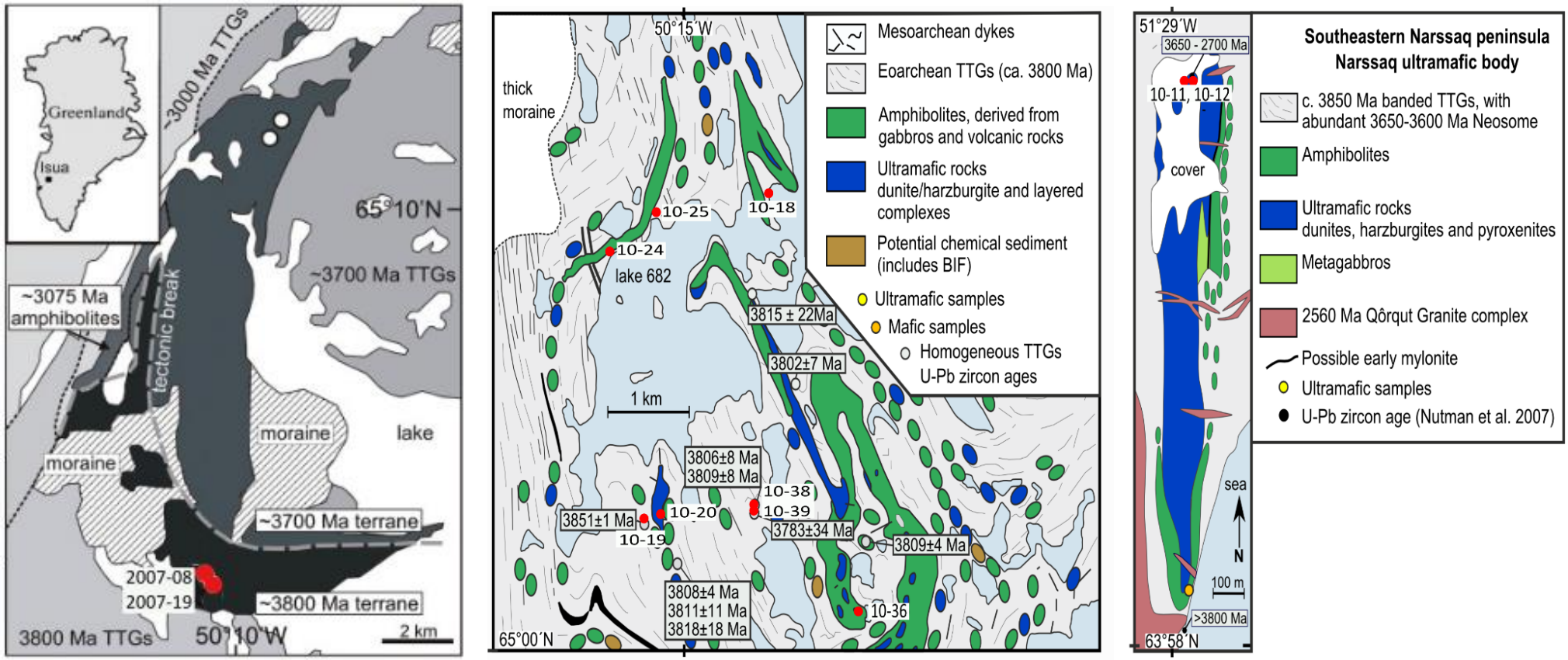

Figure 28 Geological map of the western part (left panel) and southern part (right panel) of the Isua supercrustal Belt (SOIB) from the Itsaq Gneiss Complex, South West Greenland. Red dots mark sample localities of the felsic and mafic/ultramafic rocks used in this study. Map modified after Hoffmann et al. (2011) and van de Löcht (2019)

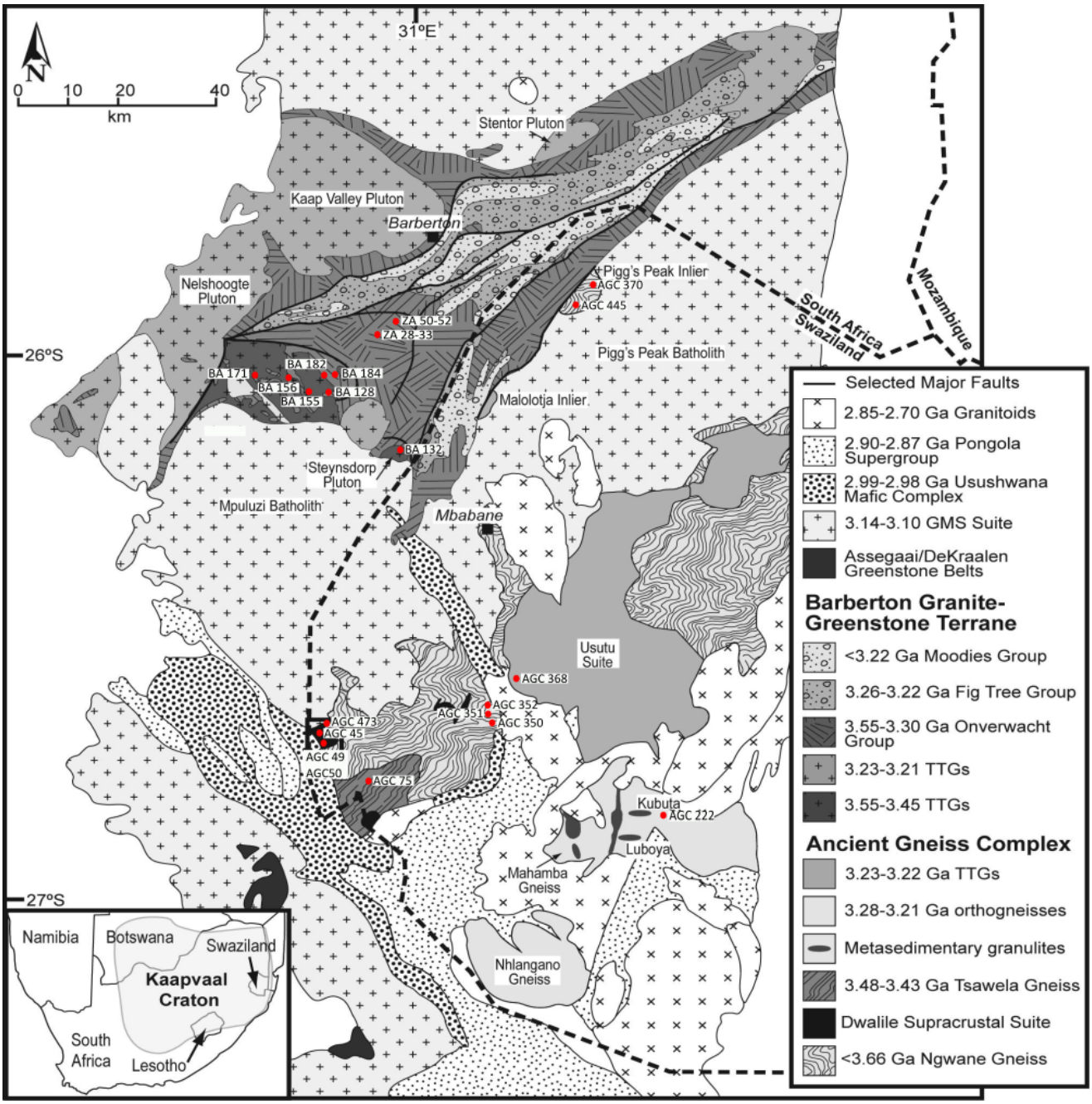

Figure 29 Geological map of the Ancient Gneiss Complex and Barberton Greenstone Belt, South Africa. Red dots mark sample localities of the felsic and mafic rocks used in this study. Map modified after Van Schijndel et al. (2017).

4.3. Analytical methods

4.3.1. Sample preparation and ion-exchange chromatography

Sample preparation and ion-exchange chromatography were performed following the analytical protocol described in Chapter 2. Single-distilled concentrated HF (24M), HCl (10M), HNO_3 (14M) and reagent grade H_2O_2 (30%) and $KBrO_3$ (purity ≥ 99.8%) were used. Chemistry blanks were checked before the measurement. Total chemistry blanks were less than 500 pg Ce and can be neglected. 120-240 mg powdered samples were digested in a 1:1 mixture of

HF (24N) and HNO_3 (14N) at 120°C in Savillex® beakers on a hotplate. After 24h on the hotplate, the acids were dried down and the residue re-dissolved in a 3:2 mixture of HF (24N) and HNO_3 (14N) and put in Parr Bombs® at 180°C to ensure complete dissolution of refractory minerals. After that, 1 mL of $HClO_4$ was added to prevent fluorides and the samples were dried down, re-dissolved 3 times in 2 mL HNO_3 (14N) and dried down again. The complete dissolution of the samples was verified by re-dissolving the sample in 10 mL 6N HCl solution for 12 h. After these digestion steps, all samples were completely dissolved. Each sample was split into a ca. 90% Ce isotope measurement cut (Ce IC) and a ca. 10% La Ce isotope dilution (ID) cut. The ID cut was spiked with a mixed ^{138}La-^{142}Ce isotope tracer (La-Ce mix I). The isotope tracer was prepared and calibrated at the University of Cologne (see details in Chapter 2). The cuts were dried down again and La and Ce were isolated from major elements following the separation procedure of Chapter 2.

4.3.2. **Mass spectrometry**

Isotope analyses of La and Ce were performed at the University of Cologne on a ThermoFinnigan™ Neptune MC-ICP-MS, broadly following the protocol of Chapters 2 and 3. Cerium isotope measurements were performed using a Cetac ARIDUS II™ desolvation system and a PFA nebulizer with an uptake rate of ca. 50 µL min^{-1}. 0.14N HNO_3 was used as a measurement solution. A Ni sample cone and a X-type Skimmer cone were used to further increase the elemental sensitivity. All Ce isotopes (136, 138, 140 and 142) were measured in static mode and in low resolution mode (R = 300). In order to be able to measure the extremely high abundance of ^{140}Ce relative to the much smaller ^{136}Ce and ^{138}Ce isotopes, 10^{10} Ω amplifier was used for mass 140. Three amplifiers equipped with 10^{13} Ω resistors were applied to monitor ^{134}Xe, ^{137}Ba and ^{144}Nd ion currents for interference correction. The detailed Faraday cup configuration and interferences are shown in Chapter 2 and Chapter 3. Interference correction of the isobars ^{136}Xe, ^{136}Ba, ^{138}Ba, ^{138}La and ^{142}Nd and mass fractionation correction followed the method described in Chapter 2. Each analysis consisted of 60 cycles (2 blocks of 30 cycles with 8.389 s integration time). Mass bias correction was also performed as described in Chapter 2 using ^{136}Ce/^{140}Ce of 0.002124072 (Makashima and Nakamura (1991), Makashima et al. (1987)) and the exponential law to correct the measured ^{138}Ce/^{136}Ce isotopic ratio.

In this study, three different synthetic reference materials were used: Johnson Matthey reference material JMC-304 (batch 15952), Cologne-AMES and Mainz-AMES (see details in Chapter 2). Due to the limited amount of available Mainz-AMES, our in house JMC-304 standard was used to perform standard-sample bracketing with all samples. The Mainz-AMES standard was measured 1-2 times before and after the standard sample bracketing block for quality control. All three used reference standards were calibrated against each other (Chapter

2). All reported data are reported relative to $^{138}Ce/^{136}Ce$ of 1.33738±1 (2 s.e.) for the Mainz-AMES standard (Willbold (2007)). $\varepsilon^{138}Ce(0)$ values are calculated after the Equation 10:

$$\varepsilon^{138}Ce(0)_{chondritic} = \left[(^{138}Ce/^{136}Ce)_{sample}/(^{138}Ce/^{136}Ce)_{chondritic} - 1\right] * 10^4 \quad \text{Equation 10}$$

$\varepsilon^{138}Ce(t)$ values are calculated in the same way, where age-corrected $^{138}Ce/^{136}Ce_{CHUR}$ is used. All La/Ce isotope dilution measurements were performed on the Thermo Finnigan Neptune MC-ICP-MS at Cologne with a Scott-type glass spray chamber and a 50µL glass nebulizer was used to avoid memory effects. The detailed Faraday Cup configuration is shown in Chapter 2. Age corrected $\varepsilon^{138}Ce(t)$ values were calculated using the ^{138}La-^{138}Ce CHUR values determined in Chapter 3 and the ^{138}La decay constant λ_{β^-}=2.37 (±0.10)*10^{-12} y^{-1} (Tanimizu (2000)).

4.4. Results

In this study, we present our ^{138}La-^{138}Ce data combined with ^{147}Sm-^{144}Nd and ^{176}Lu-^{176}Hf data from the literature (Hoffmann et al. (2011), Hoffmann et al. (2014), Schneider et al. (2018), Schneider et al. (2019), van de Löcht et al. (2018) and van de Löcht (2019)) for mafic and felsic samples from Greenland and South Africa. The isotope data for the ^{138}La-^{138}Ce, ^{147}Sm-^{143}Nd and ^{176}Lu-^{176}Hf systematics are listed in Table 12-14 and their present-day isotope compositions are shown in Figure 30.

Table 12 La-Ce, Sm-Nd and Lu-Hf from the Itsaq Gneiss Complex, South West Greenland. Samples 10-36-A1, 10-11-A1 and 10-20C-A1 are amphibole separates. Initial values $\varepsilon^{138}Ce(t)_{chondritic}$ were calculated using the $^{138}La/^{136}Ce$ 0.1868±40 (2 s.e.) and $^{138}Ce/^{136}Ce$ 1.33685±3 (2 s.e.) of Chapter 3. Initial values $\varepsilon^{138}Ce(t)_{non\text{-}carbonaceous}$ were calculated using the $^{138}La/^{136}Ce$ 0.1823±45 (2 s.e.) and $^{138}Ce/^{136}Ce$ 1.33689±4 (2 s.e.) of Chapter 3. Initial values $\varepsilon^{138}Ce(t)_{carbonaceous}$ were calculated using the $^{138}La/^{136}Ce$ 0.1946±43 (2 s.e.) and $^{138}Ce/^{136}Ce$ 1.33684±2 (2 s.e.) of Chapter 3.

	Itsaq Gneiss Complex, South West Greenland												
	felsic							**mafic and ultramafic**					
	JEH 10-39	**JEH 10-19**	**JEH10-39**	**JEH10-38**	**JEH10-25**	**JEH10-24**	**JEH10-18**	**2007-08**	**2007-19**	**10-12B**	**10-36-A1**	**10-11-A1**	**10-20C-A1**
Alter (Ma)	3806±8	3851±1	3806±8	3806±8	ca. 3800	ca. 3800	ca. 3800	ca. 3803	ca. 3803	3810	3810	3810	3810
Ce [ppm]	7.83	12.5	8.60	9.82	31.9	26.1	28.3	13.5	12.4	1.11	14.6	5.86	5.74
La [ppm]	3.90	7.35	4.21	5.26	19.9	17.0	18.7	4.79	4.84	0.45	5.72	1.91	1.91
La/Ce	0.4979	0.5847	0.4896	0.5357	0.6260	0.6501	0.6627	0.3552	0.3898	0.4063	0.3918	0.3255	0.3324
$^{138}La/^{136}Ce$	0.2424	0.2846	0.2383	0.2608	0.3047	0.3164	0.3226	0.1729	0.1897	0.1976	0.1907	0.1585	0.1618
$^{138}Ce/^{136}Ce(0)$	1.33712	1.33739	1.33720	1.33729	1.33731	1.33738	1.33748	1.33679	1.33692	1.33712	1.33696	1.33794	1.33667
Error [2 s.e.]	0.00003	0.00003	0.00003	0.00003	0.00002	0.00002	0.00003	0.00003	0.00002	0.00010	0.00006	0.00010	0.00006
$\varepsilon^{138}Ce(0)$	2.02	4.06	2.59	3.32	3.45	3.96	4.70	-0.46	0.53	2.01	0.82	8.14	-1.33
$^{138}Ce/^{136}Ce(t)$	1.33492	1.33478	1.33504	1.33493	1.33456	1.33452	1.33456	1.33522	1.33520	1.33533	1.33523	1.33650	1.33521
$\varepsilon^{138}Ce(t)_{chondritic}$	**-1.76**	**-2.66**	**-0.90**	**-1.69**	**-4.53**	**-4.82**	**-4.50**	**0.48**	**0.33**	**1.28**	**0.55**	**10.07**	**0.36**
$\varepsilon^{138}Ce(t)_{carbonaceous}$	**-1.15**	**-2.05**	**-0.30**	**-1.09**	**-3.93**	**-4.22**	**-3.89**	**1.08**	**0.93**	**1.88**	**1.15**	**10.67**	**0.96**
$\varepsilon^{138}Ce(t)_{non\text{-}carbonaceous}$	**-2.36**	**-3.26**	**-1.51**	**-2.30**	**-5.13**	**-5.43**	**-5.10**	**-0.13**	**-0.28**	**0.67**	**-0.05**	**9.45**	**-0.25**
Error [2 s.e.]	**0.32**	**0.32**	**0.26**	**0.26**	**0.19**	**0.16**	**0.30**	**0.28**	**0.24**	**0.96**	**0.57**	**0.99**	**0.62**
Ce/Ce*	0.919	0.765	0.971	0.817	0.800	0.738	0.810	1.02	1.00	0.958	1.08	1.14	1.09
Sm(ppm)	1.53	1.39	1.53	1.58	2.60	2.40	2.46	2.96	2.31	0.227	3.16	1.51	1.56
Nd(ppm)	6.44	8.23	6.44	6.82	17.7	15.1	16.2	9.69	8.16	0.730	8.61	4.30	4.62
$^{147}Sm/^{144}Nd$	0.1433	0.1021	0.1433	0.1401	0.09211	0.09487	0.09164	0.1846	0.1709	0.1894	0.2216	0.2124	0.2035
$^{143}Nd/^{144}Nd_{(0)}$	0.511357	0.510347	0.511357	0.51129	0.510167	0.51022	0.510162	0.512337	0.51204	0.512588	0.513510	0.513130	0.5129135
Error [2 s.e.]	11	10	11	10	10	10	10	6	5	8	2	2	1
$\varepsilon^{143}Nd(t)$	**+1.1**	**+2.2**	**+1.1**	**+1.4**	**+3.1**	**+2.8**	**+3.1**	**-0.1**	**+0.8**	**+2.4**	**+4.6**3810	**+1.7**	**+1.8**
Error	0.4	0.4	0.4	0.4	0.4	0.4	0.4	0.4	0.4	0.4	0.45	0.45	0.26
Lu [ppm]								0.326	0.206	0.0386	1.56	0.161	0.314
Hf [ppm]								2.22	1.69	0.0866	2.12	0.510	0.985
$^{176}Lu/^{177}Hf_{(0)}$	0.002351	0.001425	0.002351	0.002391	0.002391	0.001443	0.001496	0.02086	0.01737	0.0439	0.104151	0.044936	0.045303
$^{176}Hf/^{177}Hf_{(0)}$	0.280495	0.280444	0.280495	0.280498	0.280498	0.280477	0.280490	0.281848	0.2816	0.283316	0.287638	0.283515	0.283704
Error [2 s.e.]	8	8	11	5	5	6	7	6	9	9	11	15	12
εHf(t)	**+1.10**	**+2.00**	**+1.10**	**+0.40**	**+2.30**	**+2.20**	**+2.30**	**0.00**	**+0.30**	**-8.00**	**-11.2**	**-3.8**	**+2.0**
Error	0.40	0.40	0.40	0.50	0.40	0.40	0.40	0.40	0.40	0.50	0.81	0.56	0.65
Referenz	Hoffmann et al. (2014)							Hoffmann et al. (2011)			Van de Löcht et al. (2019)		

Table 13 La-Ce, Sm-Nd and Lu-Hf from the Ancient Gneiss Complex, South Africa. Initial values $\varepsilon^{138}Ce(t)_{chondritic}$ were calculated using the $^{138}La/^{136}Ce$ 0.1868±40 (2 s.e.) and $^{138}Ce/^{136}Ce$ 1.33685±3 (2 s.e.) of Chapter 3. Initial values $\varepsilon^{138}Ce(t)_{non\text{-}carbonaceous}$ were calculated using the $^{138}La/^{136}Ce$ 0.1823±45 (2 s.e.) and $^{138}Ce/^{136}Ce$ 1.33689±4 (2 s.e.) of Chapter 3. Initial values $\varepsilon^{138}Ce(t)_{carbonaceous}$ were calculated using the $^{138}La/^{136}Ce$ 0.1946±43 (2 s.e.) and $^{138}Ce/^{136}Ce$ 1.33684±2 (2 s.e.) of Chapter 3.

	Ancient Gneiss Complex, South Africa											
				felsic				**mafic**				
	AGC351	**AGC370**	**AGC75**	**AGC352**	**AGC368**	**AGC473**	**AGC445**	**AGC50**	**AGC350**	**AGC 49**	**AGC45**	**AGC222**
Alter (Ma)	3455±1.2	3553	3478	3442±1.4	3261	3240.5±2.9	3220	3450	3450	3450	3459	3400
Ce [ppm]	96.6	22.9	53.8	27.7	75.0	57.2	86.2	9.18	32.8	20.0	11.7	13.9
La [ppm]	44.2	21.2	26.7	17.2	43.5	35.9	43.1	3.81	12.0	8.94	4.19	5.34
La/Ce	0.4570	0.9249	0.4959	0.6221	0.5804	0.6271	0.5008	0.4151	0.3661	0.4474	0.3578	0.3837
$^{138}La/^{136}Ce$	0.2224	0.4501	0.2414	0.3028	0.2825	0.3053	0.2438	0.2021	0.1782	0.2178	0.1741	0.1868
$^{138}Ce/^{136}Ce(0)$	1.33705	1.33774	1.33730	1.33734	1.33743	1.33764	1.33729	1.33702	1.33680	1.33703	1.33680	1.33689
Error [2 s.e.]	0.00002	0.00002	0.00001	0.00002	0.00002	0.00005	0.00002	0.00002	0.00002	0.00002	0.00002	0.00001
$\varepsilon^{138}Ce(0)$	1.46	6.66	3.37	3.63	4.36	5.88	3.32	1.25	-0.38	1.31	-0.38	0.33
$^{138}Ce/^{136}Ce(t)$	1.33522	1.33393	1.33530	1.33486	1.33524	1.33528	1.33543	1.33536	1.33534	1.33524	1.33537	1.33538
$\varepsilon^{138}Ce(t)_{chondritic}$	**-0.73**	**-10.01**	**-0.01**	**-3.48**	**-1.20**	**-0.95**	**0.05**	**0.31**	**0.15**	**-0.59**	**0.40**	**0.66**
$\varepsilon^{138}Ce(t)_{carbonaceous}$	**-0.18**	**-9.44**	**0.55**	**-2.93**	**-0.67**	**-0.42**	**0.58**	**0.87**	**0.70**	**-0.04**	**0.96**	**1.20**
$\varepsilon^{138}Ce(t)_{non\text{-}carbonaceous}$	**-1.31**	**-10.60**	**-0.59**	**-4.06**	**-1.76**	**-1.51**	**-0.50**	**-0.26**	**-0.43**	**-1.17**	**-0.18**	**0.08**
Error [2 s.e.]	**0.25**	**0.23**	**0.15**	**0.16**	**0.16**	**0.53**	**0.17**	**0.19**	**0.16**	**0.29**	**0.12**	**0.12**
Ce/Ce*	0.914	0.653	1.01	0.759	0.86	0.940	**1.06**	**1.03**	**1.04**	1.00	1.07	1.03
Sm(ppm)	14.6	1.97	3.80	3.71	4.90	4.93	6.80	1.36	6.09	3.01	2.21	2.85
Nd(ppm)	65.2	13.7	21.8	18.4	30.2	30.5	37.5	5.16	22.4	11.8	7.68	9.41
$^{147}Sm/^{144}Nd$	0.1350	0.08680	0.1050	0.1220	0.09791	0.09780	0.1095	0.1592	0.1642	0.1544	0.1743	0.1830
$^{143}Nd/^{144}Nd_{(0)}$	0.511314	0.510137	0.510548	0.511004	0.510422	0.510545	0.510736	0.511775	0.511922	0.511734	0.512138	0.512410
Error [2 s.e.]	15	13	11	16	8	6	7	9	10	14	9	8
$\varepsilon^{143}Nd(t)$	**+1.5**	**+1.4**	**+0.2**	**+1.4**	**-1.85**	**-1**	**-1.1**	**-0.3**	**+0.5**	**+1.21**	**+0.05**	**+1.6**
Lu [ppm]	1.38	0.0988	0.216	0.222		0.111	0.0840	0.120	0.488	0	0.289	0.414
Hf [ppm]	16.9	4.47	3.64	4.47		4.62	5.23	0.952	3.12	0	1.74	2.22
$^{176}Lu/^{177}Hf_{(0)}$	0.01163	0.003138	0.008431	0.007050		0.003429	0.002289	0.01789	0.02220	0	0.02360	0.02647
$^{176}Hf/^{177}Hf_{(0)}$	0.281427	0.280755	0.281164	0.281134		0.280894	0.280854	0.28179	0.2821	0	0.2822	0.2825
Error [2 s.e.]	7	7	5	6		7	11	22	5	0	10	7
εHf(t)	**+3.80**	**+2.09**	**+2.41**	**+4.00**		**-0.30**	**+0.23**	**+1.70**	**+2.80**		**+2.33**	**+6.00**
Error	0.40			0.40								
Referenz	Schneider et al. (2018)											

Table 14 La-Ce, Sm-Nd and Lu-Hf from the Barberton Greenstone Belt, South Africa Initial values $\varepsilon^{138}Ce(t)_{chondritic}$ were calculated using the $^{138}La/^{136}Ce$ 0.1868±40 (2 s.e.) and $^{138}Ce/^{136}Ce$ 1.33685±3 (2 s.e.) of Chapter 3. Initial values $\varepsilon^{138}Ce(t)_{non\text{-}carbonaceous}$ were calculated using the $^{138}La/^{136}Ce$ 0.1823±45 (2 s.e.) and $^{138}Ce/^{136}Ce$ 1.33689±4 (2 s.e.) of Chapter 3. Initial values $\varepsilon^{138}Ce(t)_{carbonaceous}$ were calculated using the $^{138}La/^{136}Ce$ 0.1946±43 (2 s.e.) and $^{138}Ce/^{136}Ce$ 1.33684±2 (2 s.e.) of Chapter 3.

	Barberton Greenstone Belt, South Africa									
	felsic		**mafic**							
	BA128	**BA132**	**BA155**	**Ba156**	**Ba156**	**KS-Ba171**	**BA182**	**KS-BA184**	**ZA-32a**	**ZA-51**
Alter (Ma)	3465	3509	3538	3538	3538	3553	3530	3530	3482	3482
Ce [ppm]	13.7	33.1	4.79	8.90	8.92	11.1	40.8	60.0	11.4	6.05
La [ppm]	8.82	21.9	1.76	3.22	3.21	4.36	18.0	27.8	4.46	2.29
La/Ce	0.6454	0.6616	0.3677	0.3618	0.3599	0.3938	0.4410	0.4627	0.3904	0.3781
$^{138}La/^{136}Ce$	0.3142	0.3221	0.1790	0.1761	0.1752	0.1917	0.2147	0.2252	0.1901	0.1841
$^{138}Ce/^{136}Ce(0)$	1.33746	1.33745	1.33670	1.33673	1.33678	1.33691	1.33711	1.33714	1.33691	1.33683
Error [2 s.e.]	0.00002	0.00002	0.00003	0.00002	0.00003	0.00002	0.00004	0.00003	0.00002	0.00002
$\varepsilon^{138}Ce(0)$	4.58	4.46	-1.13	-0.87	-0.50	0.45	1.96	2.18	0.44	-0.14
$^{138}Ce/^{136}Ce(t)$	1.33487	1.33476	1.33519	1.33525	1.33531	1.33529	1.33531	1.33525	1.33533	1.33531
$\varepsilon^{138}Ce(t)_{chondritic}$	**-3.28**	**-4.00**	**-0.64**	**-0.20**	**0.24**	**0.14**	**0.20**	**-0.23**	**0.23**	**0.03**
$\varepsilon^{138}Ce(t)_{carbonaceous}$	**-2.72**	**-3.43**	**-0.07**	**0.37**	**0.80**	**0.71**	**0.77**	**0.33**	**0.79**	**0.59**
$\varepsilon^{138}Ce(t)_{non\text{-}carbonaceous}$	**-3.86**	**-4.58**	**-1.22**	**-0.78**	**-0.35**	**-0.44**	**-0.38**	**-0.81**	**-0.35**	**-0.55**
Error [2 s.e.]	**0.20**	**0.23**	**0.25**	**0.18**	**0.26**	**0.23**	**0.42**	**0.29**	**0.19**	**0.22**
Ce/Ce*	0.798	0.856	0.982	1.04	1.04	1.02	1.00	0.988	1.03	1.09
Sm [ppm]	1.85	3.44	1.34	2.14	2.14	2.07	5.27	6.45	2.10	1.17
Nd [ppm]	8.67	18.9	3.90	6.54	6.54	6.96	22.2	30.2	7.31	3.77
$^{147}Sm/^{144}Nd$	0.1290	0.1097	0.2078	0.1984	0.1983	0.1795	0.1431	0.1291	0.1738	0.1871
$^{143}Nd/^{144}Nd_{(0)}$	0.511105	0.510609	0.512944	0.512728	0.512728	0.512260	0.511384	0.511053	0.512134	0.512440
Error [2 s.e.]	20	13	7	7	7	11	6	6	8	7
$\varepsilon^{143}Nd(t)$	**+0.2**	**-0.4**	**+0.7**	**+0.8**	**+0.9**	**+0.3**	**-0.2**	**-0.3**	**+0.29**	**+0.3**
Lu [ppm]	0.0766	0.221	0.250	0.368	0.368	0.311	0.444	0.561	0.295	0.215
Hf [ppm]	3.68	4.27	0.982	1.69	1.69	1.86	3.85	4.93	1.70	1.07
$^{176}Lu/^{177}Hf_{(0)}$	0.002957	0.007350	0.03612	0.03096	0.03096	0.02375	0.01637	0.01617	0.02463	0.02862
$^{176}Hf/^{177}Hf_{(0)}$	0.280738	0.281014	0.283054	0.282689	0.282689	0.28219	0.281651	0.281608	0.282255	0.282532
Error [2 s.e.]	7	5	8	6	6	11	9	10	5.216	3
εHf(t)	**+0.10**	**-4.30**	**+3.40**	**+3.00**	**+2.98**	**+2.90**	**+1.40**	**+0.40**	**+2.60**	**+2.90**
Referenz	Schneider et al. (2019)									

4.4.1. **Present day $\varepsilon^{143}Nd(0)/\varepsilon^{176}Hf(0)$ and $\varepsilon^{138}Ce(0)$ values**

Due to the relative compatibilities La<Ce and Sm>Nd, Lu>Hf; all samples should plot in the - $\varepsilon^{143}Nd/+\varepsilon^{138}Ce$; - $\varepsilon^{176}Hf/+\varepsilon^{138}Ce$ or in the + $\varepsilon^{143}Nd/-\varepsilon^{138}Ce$; + $\varepsilon^{176}Hf$ /- $\varepsilon^{138}Ce$ quadrant (Figure 30). The samples 10-12B, 10-11-A1, 10-36-A1, 10-20C-A1, 10-18 and AGC 473 have high Ba contents in the Ce IC cuts. As Ba interferences can cause too high $^{138}Ce/^{136}Ce$ ratios all samples with too high Ba interferences are excluded for the further interpretation of the data (See Chapter 2 for more details). Except of 3 mafic samples (AGC 350, AGC 45 and 2007-08) which show small negative $\varepsilon^{138}Ce$ and $\varepsilon^{143}Nd/\varepsilon^{176}Hf$ values and sample BA 156 which plot in the negative $\varepsilon^{138}Ce$ and $\varepsilon^{176}Hf$ space all other samples plot in the - $\varepsilon^{143}Nd/+\varepsilon^{138}Ce$ or in the - $\varepsilon^{143}Nd/+\varepsilon^{138}Ce$ quadrants within uncertainties. The mafic samples show $\varepsilon^{138}Ce$ present-day values from -1.33 to +2.18 and the felsic samples show higher $\varepsilon^{138}Ce$ values from +1.48 to +6.66. As a result, a separation between mafic and felsic samples can be seen in Figure 30.

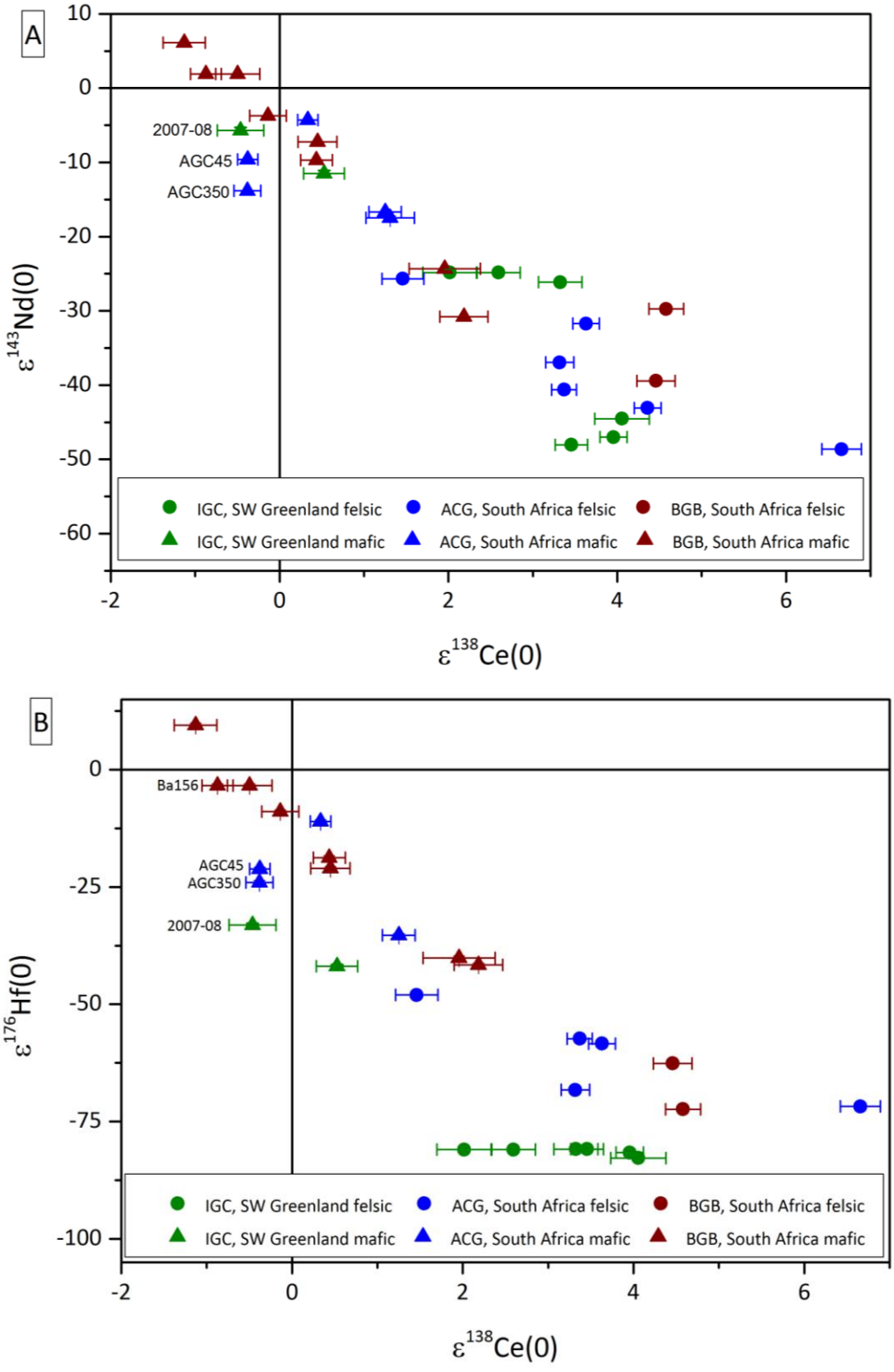

Figure 30 results of Ce isotope measurements presented as present-day ε^{138}Ce vs. ε^{143}Nd (A) and ε^{138}Ce vs. ε^{176}Hf (B). The samples AGC 350, AGC 45 and 2007-08 plot in both figures in the -ε^{143}Nd, Hf/-ε^{138}Ce space. All other samples plot due to the negative correlation of the relative compatibilities in the +ε^{176}Hf, ^{143}Nd/-ε^{138}Ce and -ε^{176}Hf, ^{143}Nd/+ε^{138}Ce space, respectively Additional ε^{143}Nd and ε^{176}Hf data from Hoffmann et al. (2011), Hoffmann et al. (2014), van de Löcht (2019), Schneider et al. (2018) and Schneider et al. (2019)

4.4.2. $\varepsilon^{143}Nd(t)/\varepsilon^{176}Hf(t)$ and $\varepsilon^{138}Ce(t)$ values

In Figure 31 all samples were recalculated to the respective crystallization age using the CHUR value of Bouvier et al. (2008) for ^{176}Lu-^{176}Hf and ^{147}Sm-^{143}Nd and that of Chapter 3 for ^{138}La-^{138}Ce. Almost all mafic samples show an offset from about +0.3 $\varepsilon^{138}Ce$ from the chondritic $\varepsilon^{138}Ce$ value. The $\varepsilon^{138}Ce(t)$ values range from -0.14 to +1.77. Except of two felsic samples AGC 75 and AGC 445 which show slightly positive $\varepsilon^{138}Ce(t)$ values of about +0.3 $\varepsilon^{138}Ce(t)$, all other felsic samples show negative $\varepsilon^{138}Ce(t)$ values from -10.01 to -0.28. Additionally, the felsic samples show a larger spread in $\varepsilon^{138}Ce(t)$ and in $\varepsilon^{143}Nd(t)$ values than the mafic samples which is expected from their more variable La/Ce ratios. One felsic sample AGC 370 shows a highly negative $\varepsilon^{138}Ce(t)$ value of about -10.01. In contrast to all other samples, this sample shows very high $^{138}La/^{136}Ce$=0.45 (Table 13, Figure 31) and very low $^{147}Sm/^{144}Nd$=0.0868 which implies some isotopic disturbance during post-crystallization metamorphism and migmatization (Kröner et al. (2014)).

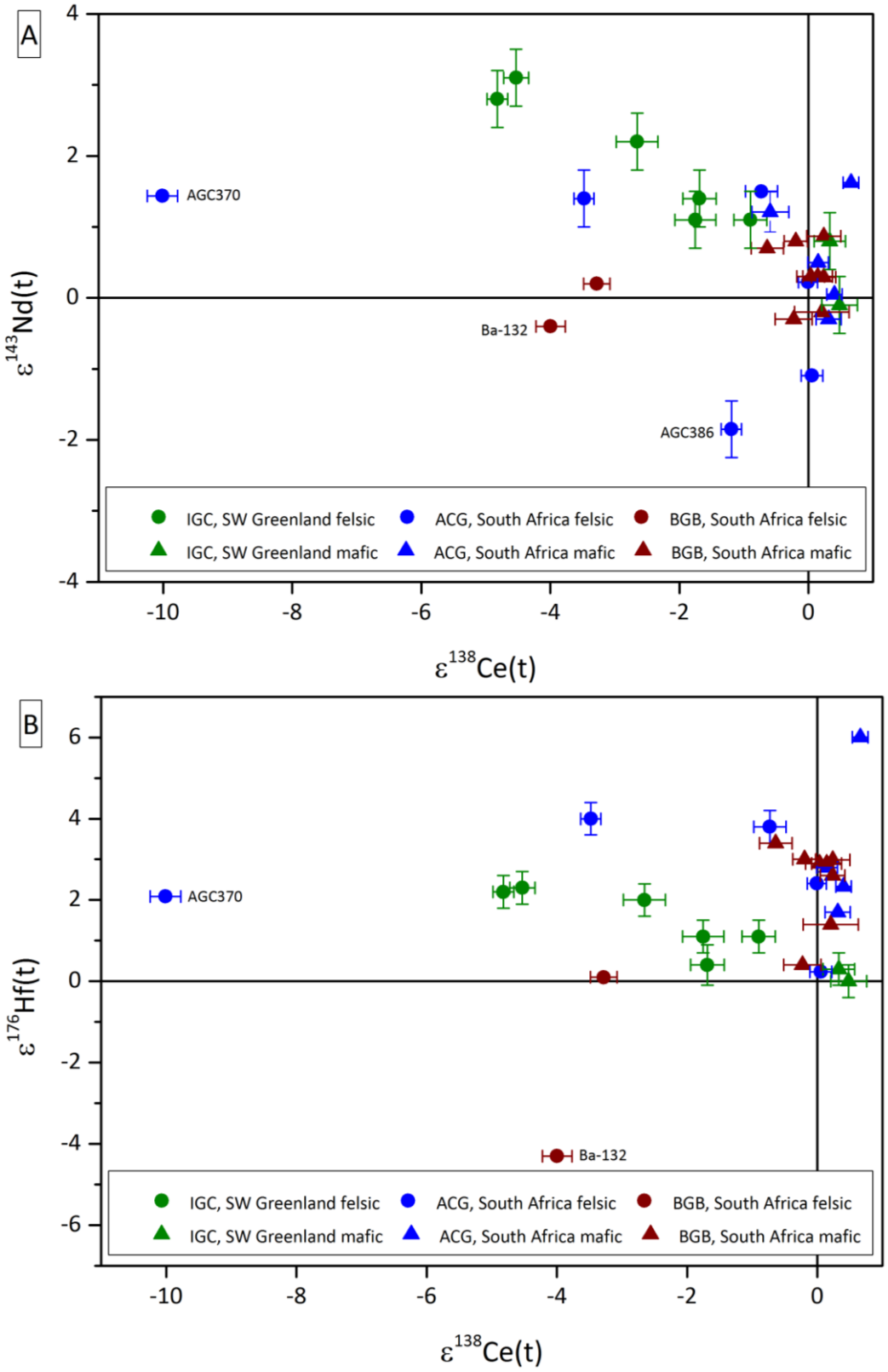

Figure 31 results of initial $\varepsilon^{138}Ce$ vs. $\varepsilon^{143}Nd$ (A) and $\varepsilon^{138}Ce$ vs. $\varepsilon^{176}Hf$ (B). ε-values were calculated using the CHUR values of Bouvier et al. (2008) for Hf and Nd and the chondritic ^{138}La-^{138}Ce value of Chapter 3 for Ce. The sample AGC 370 has an extremely negative $\varepsilon^{138}Ce$ value. Additionally, all felsic samples from southwest Greenland and from the BCB South Africa show unexpected high negative $\varepsilon^{138}Ce$ values. Additional $\varepsilon^{143}Nd$ and $\varepsilon^{176}Hf$ data from Kröner et al. (1994), Hoffmann et al. (2011), Hoffmann et al. (2014), Kröner et al. (2014), Schneider et al. (2018), Schneider et al. (2019) and van de Löcht et. al. (2019).

In Figure 32 $^{147}Sm/^{144}Nd$ and $^{176}Lu/^{176}Hf$ are plotted versus $^{138}La/^{136}Ce$. The samples show an anti-correlation between La/Ce and Lu/Hf, Sm/Nd systems which is expected from magmatic fractionation. Felsic samples show higher $^{138}La/^{136}Ce$ but lower $^{147}Sm/^{144}Nd$ and $^{176}Lu/^{176}Hf$ values than mafic samples. All mafic samples have $^{138}La/^{136}Ce$ ratios between 0.16 and 0.23 whereas felsic samples show $^{138}La/^{136}Ce$ ratios between 0.22 and 0.45. This allows a clear discrimination between mafic and felsic samples from their $^{138}La/^{136}Ce$ ratios.

Hoffmann et al. (2011) divided the Greenland TTGs into two groups based on their $\varepsilon^{176}Hf(t)$ and $\varepsilon^{143}Nd(t)$ values (green dots in all figures of this chapter). The samples 10-18 (not shown), 10-19, 10-24 and 10-25 belong to group 1 and the samples 10-38 and 10-39 (duplicate) belong to group 2. Group 1 has $\varepsilon^{143}Nd(t)$ values from +2.2 to +3.1 and $\varepsilon^{176}Hf(t)$ values from +2.0 to +2.3. Instead group 2 shows significant lower $\varepsilon^{143}Nd(t)$ values of +1.1 and +1.4 and $\varepsilon^{176}Hf(t)$ values of +0.4 and +1.1. This is supported by the fact that samples 10-38 and 10-39 of group 2 show significantly lower $\varepsilon^{138}Ce(t)$ values than the other Greenland TTGs. All Greenland felsic samples show a negative correlation of $\varepsilon^{143}Nd(t)$ vs. $\varepsilon^{138}Ce(t)$ and $\varepsilon^{176}Hf(t)$ vs. $\varepsilon^{138}Ce(t)$, whereas the samples show unexpected low $\varepsilon^{138}Ce(t)$ values (between -1.26 and -4.33). Notably, the felsic samples 10-25 and 10-18 show coherent results in $\varepsilon^{143}Nd(t)$ and $\varepsilon^{138}Ce(t)$ space (Figure 26, Table 12) which could be a hint on the same origin. These two groups of TTG's can also be seen in Figure 32 where $^{147}Sm/^{144}Nd$ is plotted versus $^{138}La/^{136}Ce$. Group 1 includes the samples JEH 10-25, JEH 10-24, 10-19 and 10-18 (not shown) from southwest Greenland that shows low $^{147}Sm/^{144}Nd$ ratios (≤ 0.01). These trends cannot be confirmed in the $^{176}Lu/^{176}Hf$ vs $^{138}La/^{136}Ce$ plot, where all TTG samples show a low but relatively constant $^{176}Lu/^{176}Hf$ value around ca. 0.002. In general, the results of the ^{138}La-^{138}Ce isotope system support the results of the ^{147}Sm-^{143}Nd and ^{176}Lu-^{176}Hf isotope systems because of the same trends as the division in group 1 and group 2 and inverse behavior of the ^{138}La-^{138}Ce isotope system compared to the ^{147}Sm-^{143}Nd and ^{176}Lu-^{176}Hf isotope systems. But the unexpected low $\varepsilon^{138}Ce(t)$ values for the TTG sample could be a hint on a La/Ce isotope disturbance.

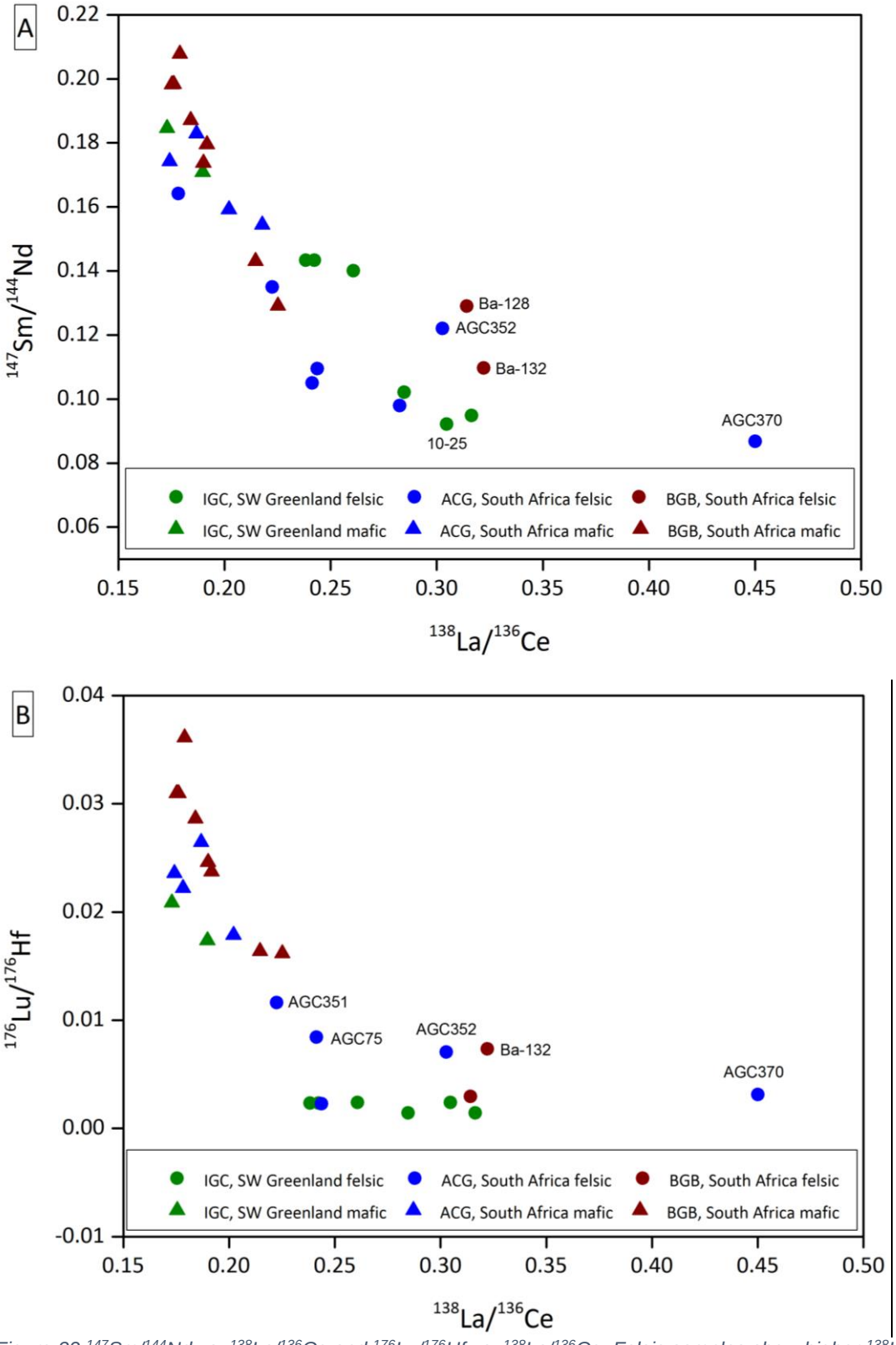

Figure 32 $^{147}Sm/^{144}Nd$ vs. $^{138}La/^{136}Ce$ and $^{176}Lu/^{176}Hf$ vs. $^{138}La/^{136}Ce$. Felsic samples show higher $^{138}La/^{136}Ce$ and lower $^{147}Sm/^{144}Nd$ or $^{176}Lu/^{176}Hf$ values than mafic samples. All mafic samples show a $^{138}La/^{136}Ce$ ratio of 0.16 to 0.23, whereas all felsic samples have higher $^{138}La/^{136}Ce$ ratios of 0.22 to 0.45. The sample AGC 370 show a high $^{138}La/^{138}Ce$ and low $^{143}Nd/^{144}Nd$ value. The samples AGC 368 and AGC 49 are not shown in the $^{176}Lu/^{176}Hf$ vs. $^{138}La/^{138}Ce$ plot because no Hf data are available. Additional $\varepsilon^{143}Nd$ and $\varepsilon^{176}Hf$ data from Kröner et al. (1994), Hoffmann et al. (2011), Hoffmann et al. (2014), Kröner et al. (2014), Schneider et al. (2018), Schneider et al. (2019) and van de Löcht et. al. (2019)

4.5. Discussion

Due to the relative compatibilities La<Ce and Sm>Nd, Lu>Hf all samples should plot in the - ε^{143}Nd/+ε^{138}Ce; -ε^{176}Hf/+ε^{138}Ce or in the +ε^{143}Nd/-ε^{138}Ce; +ε^{176}Hf /-ε^{138}Ce quadrant. In Figures 30, 31 and 32 several samples are marked because they show an offset in the appropriate Figure. In Figure 31 Ce isotope measurements presented as present-day ε^{138}Ce vs. ε^{143}Nd (A) and ε^{138}Ce vs. ε^{176}Hf (B) is shown. Samples 2007-08, AGC 45 and AGC 350 plot in the - ε^{143}Nd/- ε^{138}Ce and +ε^{176}Hf /-ε^{138}Ce quadrants (Figure 30 A and B). Additionally, sample Ba 156 plots in the +ε^{176}Hf /-ε^{138}Ce quadrant. In Figure 31 the results of initial ε^{138}Ce vs. ε^{143}Nd (A) and ε^{138}Ce vs. ε^{176}Hf (B) are presented. In Figure 31 A the sample AGC 370 plot in the appropriate quadrat (+ε^{143}Nd/-ε^{138}Ce) but shows an unexpected high ε^{138}Ce(t) = -10. The same result for sample AGC 370 can be seen in Figure 31 B. Sample BA 132 plots in Figure 31 A and B in the -ε^{143}Nd/-ε^{138}Ce and -ε^{176}Hf /-ε^{138}Ce. Sample AGC 386 plots in the -ε^{143}Nd/-ε^{138}Ce quadrant. Additional to these outliers almost all felsic samples show an ε^{138}Ce(t) = 0.3. In Figure 32 all samples are plotting in the ^{147}Sm/^{144}Nd vs. ^{138}La/^{136}Ce (A) and ^{176}Lu/^{176}Hf vs. ^{138}La/^{136}Ce (B) space. It can be seen that the sample AGC 370 shows an unexpected high ^{138}La/^{136}Ce value and low ^{176}Lu/^{176}Hf and ^{147}Sm/^{144}Nd values. The samples Ba 128 and Ba 132 which are mentioned above show an offset in Figures 32 A and B with higher ^{147}Sm/^{144}Nd and ^{176}Lu/^{176}Hf values than the most remaining felsic samples. In the following chapter, four different possibilities (Alteration, Cerium anomalies, Sediments and ^{138}La-^{138}Ce CHUR value) are discussed to identify disturbed samples.

4.5.1. Influence of alteration and metamorphism on the La-Ce isotope composition

In general, results of different studies have shown that Zr is one of the least mobile elements during post-magmatic disturbances (Winchester and Floyd (1977), Pearce and Peate (1995) and references therein). Consequently, Zr can be used as an alteration-independent tracer in geochemistry (Murton et al. (1992), Pearce et al. (1992)). If immobile elements such as REE, high field strength element (HFSE), Al, Cr and Ni correlate clearly with Zr, it can be concluded that these elements were only affected minority by alteration and that the different elemental abundances are largely controlled by olivine and pyroxene fractionation (e.g. Arndt (1994) and references therein). Nevertheless, these elements can be mobile during carbonate alteration and metamorphism which can be seen in non-coherent patterns normalized to trace elements diagrams. (e.g. Arndt et al. (1989), Gruau et al. (1992), Lahaye et al. (1995)). Thus, Polat et al. (2002) defined alteration criteria:

1) immobile elements have to correlate with the least mobile element Zr in binary diagrams

2) unaltered samples have to be characterized by Ce anomalies that are higher than 0.9 and lower than 1.1

3) unaltered samples have to be characterized by <2% of carbonate and silica enrichment, and

4) samples need to have <6% wt.% of loss on ignition.

Figure 33 shows the co-variation diagrams of La/Ce and Sm/Nd vs. Zr to identify post-magmatic disturbances. A clear difference between mafic and felsic samples can be seen. The samples 10-19, and AGC 370 show higher La/Ce values than the other felsic samples and are marked with open symbols. The sample AGC 445 shows lower La/Ce values than the other felsic samples and is also marked with an open symbol because this sample could be disturbed. The mafic sample AGC 350 shows a high Zr content in contrast to the other mafic samples and also marked with an open symbol.

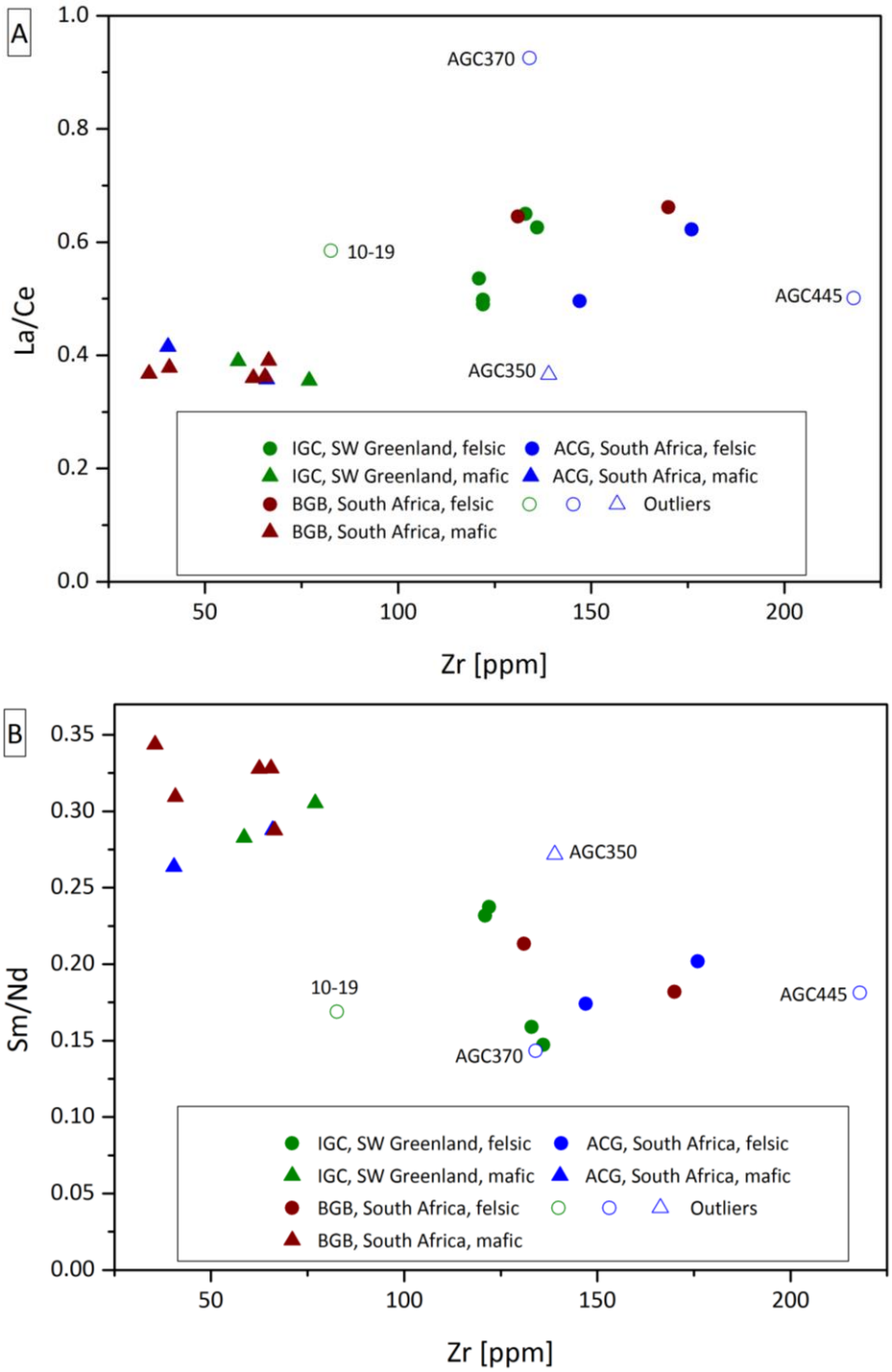

Figure 33 Sm/Nd and La/Ce ratios plotted versus Zr content. In the La/Ce versus Zr plot the samples 10-19, AGC 350, AGC 370 and AGC 445 (open symbols) plot offset the co-variation line between La/Ce versus Zr. Interestingly, the same samples are also offset in the Sm/Nd versus Zr space. These samples could be disturbed. In general, the offset in Sm/Nd versus Zr space is smaller than from La/Ce versus Zr.

LREE, MREE and HREE have similar chemical properties but they can be fractionated from each other by magmatic processes. Individual REE anomalies (except for Eu) are not caused by these processes and as a result, non-coherent REE patterns are often the result of post-magmatic alteration processes (Humphris (1984)). Especially the LREE (La and Ce) show often mobility during post-depositional alteration processes and the LREE are more sensitive to the secondary alteration than HREE (Polat and Hofman (2003)). This is also reported in

other studies (e.g., Gruau et al. (1996), Moorbath et al. (1997), Nutman (2001)) that combined Lu-Hf and Sm-Nd isotope system where Hf isotope compositions were regarded pristine whereas Nd isotope compositions were subsequently altered.

4.5.2. **Cerium anomalies**

In contrast to the other REE, Ce and Eu can occur in the tetravalent and divalent states, respectively. Cerium may therefore fractionate from REE^{3+} in an oxidizing environment. Therefore, it is common to define a Cerium anomaly (Ce/Ce*, Equation 1) to account for the difference between the actually measured and predicted Ce concentration (inferred from the Nd and La concentration of the individual samples). Thus, by the determination of Ce/Ce*, further information about processes modifying the LREE inventory may be obtained. For the calculation of the Ce anomalies, the La and Ce data obtained in this study by isotope dilution were normalized to CI abundances (Lodders (2003)). The Pr data are taken from literature data (Kröner et al. (1994), Hoffmann et al. (2011), Hoffmann et al. (2014), Kröner et al. (2014), Schneider et al. (2018), Schneider et al. (2019) and van de Löcht et. al. (2019)). For sample AGC 368 and the three mineral separates (not shown) no Pr data are available and therefore the Ce/Ce* value was calculated after Equation 1 (Chapter 1).

Polat et al. (2002) defined samples showing a Ce/Ce* ratios between 0.9 and 1.1 as the least altered samples, whereas samples that deviate from that range are regarded as variably altered. In Figure 34 it is demonstrated that the mafic samples have Ce/Ce* values ranging from 0.98 to 1.09. Interestingly, sample AGC 350 shows no Ce anomaly although it plots offset in the La/Ce, Sm/Nd versus Zr plot (Figure 33).

The felsic samples have Ce/Ce* values between 0.65 and 1.00 whereas only the three samples AGC 351, AGC 45 and 10-39 show no Ce anomaly (Ce/Ce* = 0.91-1.00). As explained earlier, the sample AGC 370 shows a high negative $\varepsilon^{138}Ce(t)$ value and a significantly higher La/Ce ratio (Figure 32) compared to other samples within this study. Taking into account that this sample has a Ce/Ce* value of 0.64, it appears reasonable that a significant portion of LREE including La and Nd were enriched relative to Ce during secondary alteration. As previously assumed by Kröner et al. (2014) this sample has isotopic disturbance during post-crystallization metamorphism and migmatization.

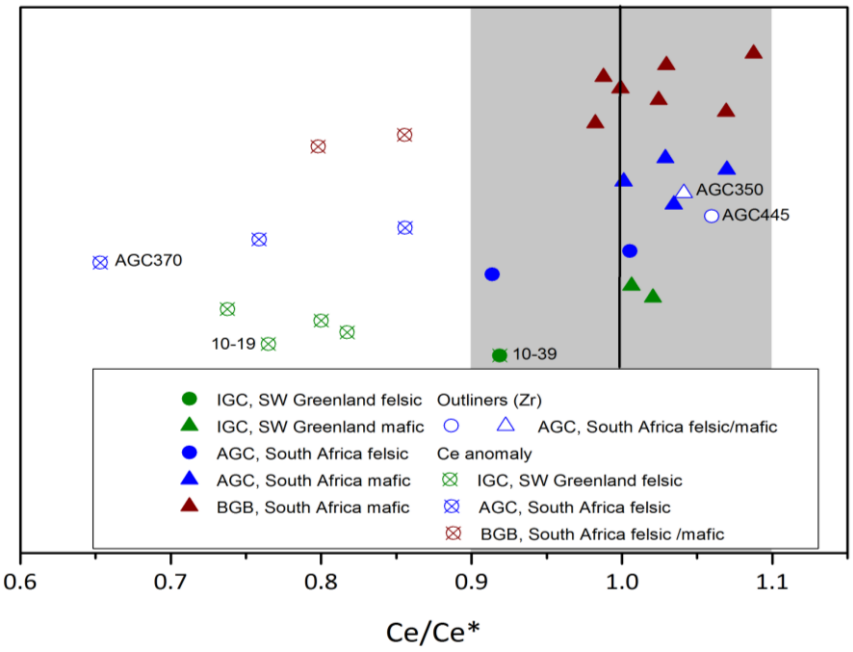

Figure 34 Cerium anomalies of all samples from this study. Samples with a Cerium anomaly are marked with an open symbol and crosses. The felsic samples 10-19 and AGC 370 also plot offset the La/Ce and Sm/Nd versus Zr plot. *The samples AGC 350 and AGC 445 which plot offset the La/Ce and Sm/Nd versus Zr plot show no Cerium anomaly and are therefore marked with an open symbol.*

Figure 35 illustrates the strong correlation between $\varepsilon^{138}Ce(t)$ and Ce anomalies. Especially felsic samples that have a negative Ce anomaly show extremely negative $\varepsilon^{138}Ce(t)$ values. The sample AGC 370 which has the lowest Ce/Ce* value has the highest negative $\varepsilon^{138}Ce(t)$.

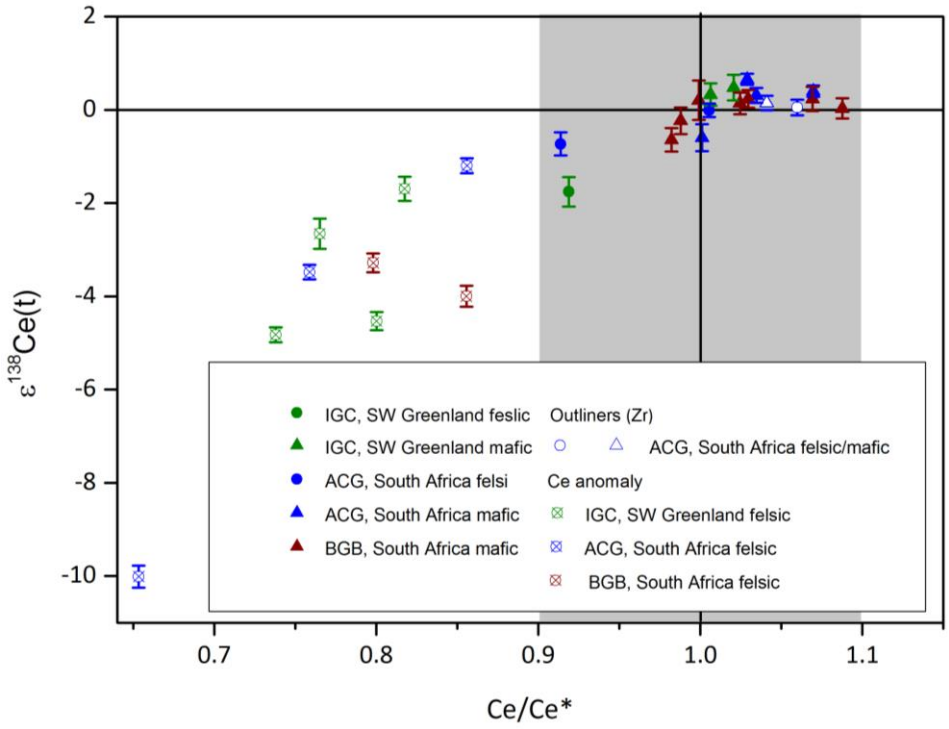

Figure 35 $\varepsilon^{138}Ce(t)$ values plotted against Ce/Ce values. Samples with a Cerium anomaly are marked with an open symbol and crosses. Samples AGC 350 and AGC 445 are marked with an open symbol because these samples plot offset the La/Ce versus Zr and Sm/Nd versus Zr plot although these samples show no Cerium anomaly.*

4.5.3. **Effects of Sediment recycling on source compositions**

Since the pioneering study of White and Patchett (1984) the influence of sediments on different isotopic systems (^{176}Hf-^{176}Lu, ^{147}Sm-^{144}Nd and ^{87}Rb-^{87}Sr) was investigated (e.g. Dickin (1987), Vervoort et al. (2011), Plank and Langmuir (1998), Spandler and Pirard (2013)). In general, Cerium can be fractionated in the marine environment relative to the other REE because dissolved trivalent cerium can be oxidized to the insoluble tetravalent state while other REE remain trivalent (see also paragraph on Ce anomalies). Subducted sediments will generate higher La/Ce ratios and therefore higher ^{138}Ce/^{136}Ce isotope ratios in subduction components and overprint the composition of more depleted mantle sources that were not affected by a sedimentary influx (e.g. MORB). Sediment formation commonly results in LREE enrichment relative to HREE in the sediment and thus sediment recycling has a more significant effect on LREE inventory, such as La, Ce, Sm and Nd. Moreover, the accumulation of monazite in sediments commonly produces even higher enrichment of Ce (+/- La) in the sediments relative to the other LREEs. Therefore, sediment recycling has commonly a more significant effect on the ^{138}La-^{138}Ce isotope system than on the ^{147}Sm-^{143}Nd isotope systems. In general, sediments are also a possible cause for the slightly positive ε^{138}Ce(t) values in some mafic samples (Figure 35) because the concentrations of many elements are much higher than in the mantle source. Isotope systems and trace element ratios can be influenced by continues injection of sediment into the mantle. The analyzed samples were screened for negative Nb/Ta anomalies relative to La. The samples from Schneider et al. (2019) show no negative Nb/Ta anomalies relative to La. In contrast, the samples from Hoffmann et al. (2011) and van de Löcht et al. (2019) show negative Nb/Ta anomalies and sediment recycling could be a reason.

4.5.4. **^{138}La-^{138}Ce CHUR value**

The selection of a representative and accurate ^{138}La-^{138}Ce value is crucial as it will have severe implications. This is demonstrated in Figure 36 where our samples are recalculated to several CHUR values. There it is demonstrated that the resulting εCe(t) values change severely depending on whether a chondritic (Figure 36 A), a carbonaceous chondritic (Figure 36 B) or a non-carbonaceous chondritic reference value (Figure 36 C) is used. Using the chondritic ^{138}La-^{138}Ce value, a difference of +0.57 ε^{138}Ce-units is obtained in contrast to the carbonaceous chondritic ^{138}La-^{138}Ce value. Using the chondritic ^{138}La-^{138}Ce value, a difference of -0.58 ε^{138}Ce-units is obtained in contrast to the non-carbonaceous chondritic ^{138}La-^{138}Ce value. These results underline the importance of the precise determination of the ^{138}La-^{138}Ce value. Due to a strong coupling and similar fractionation between the La-Ce, Sm-Nd and Lu-Hf pairs during geological processes, we would expect that these samples should have predominantly

negative $\varepsilon^{138}Ce(t)$ values in the range of 0 to -0.5 $\varepsilon^{138}Ce(t)$. As mentioned above, using the chondritic ^{138}La-^{138}Ce value all undisturbed felsic samples show a positive offset of +0.3 $\varepsilon^{138}Ce(t)$. The carbonaceous chondritic ^{138}La-^{138}Ce value also causes too positive $\varepsilon^{138}Ce(t)$ values of up to one $\varepsilon^{138}Ce(t)$ (Figure 36 B). Using the non-carbonaceous chondritic ^{138}La-^{138}Ce value and taking into account the uncertainties of each sample, most samples indeed show negative $\varepsilon^{138}Ce(t)$ values. Consequently, our data show that for the ^{138}La-^{138}Ce system the bulk Earth is best described with a non-carbonaceous chondrite compositions.

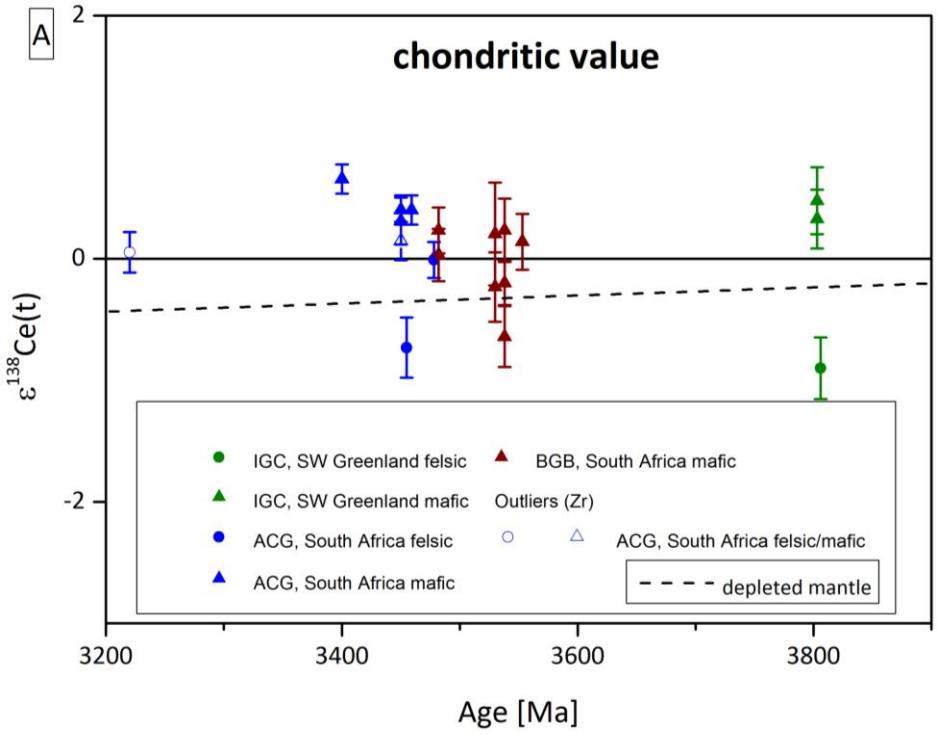
A
chondritic value
2
0
-2
ε^{138}Ce(t)
IGC, SW Greenland felsic
IGC, SW Greenland mafic
ACG, South Africa felsic
ACG, South Africa mafic
BGB, South Africa mafic
Outliers (Zr)
ACG, South Africa felsic/mafic
depleted mantle
3200
3400
3600
3800
Age [Ma]

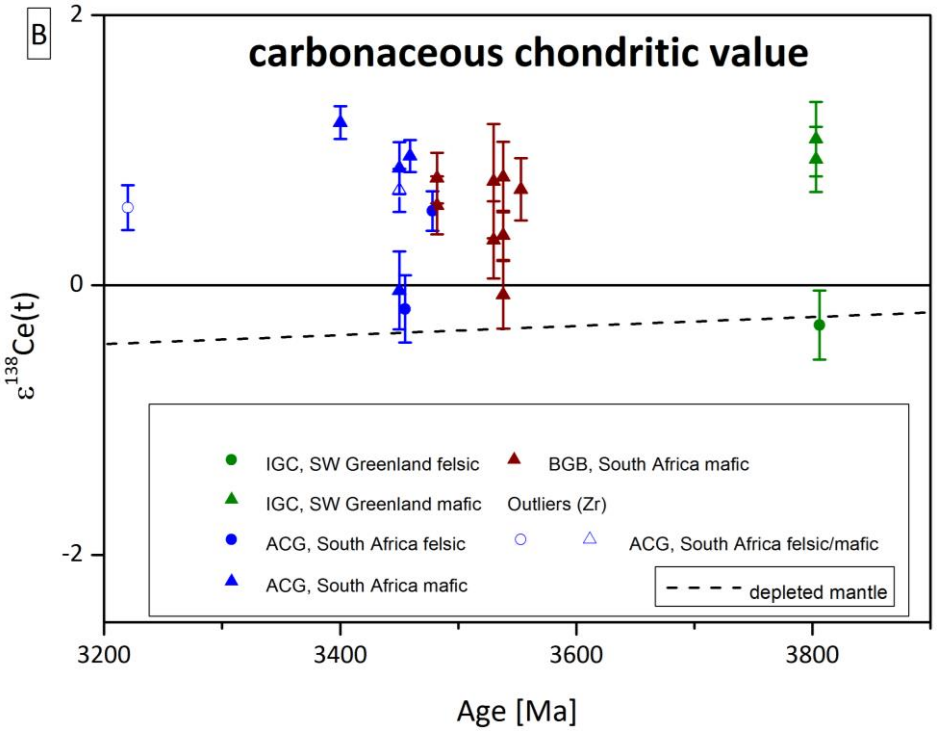
B
carbonaceous chondritic value
2
0
-2
ε^{138}Ce(t)
IGC, SW Greenland felsic
IGC, SW Greenland mafic
ACG, South Africa felsic
ACG, South Africa mafic
BGB, South Africa mafic
Outliers (Zr)
ACG, South Africa felsic/mafic
depleted mantle
3200
3400
3600
3800
Age [Ma]

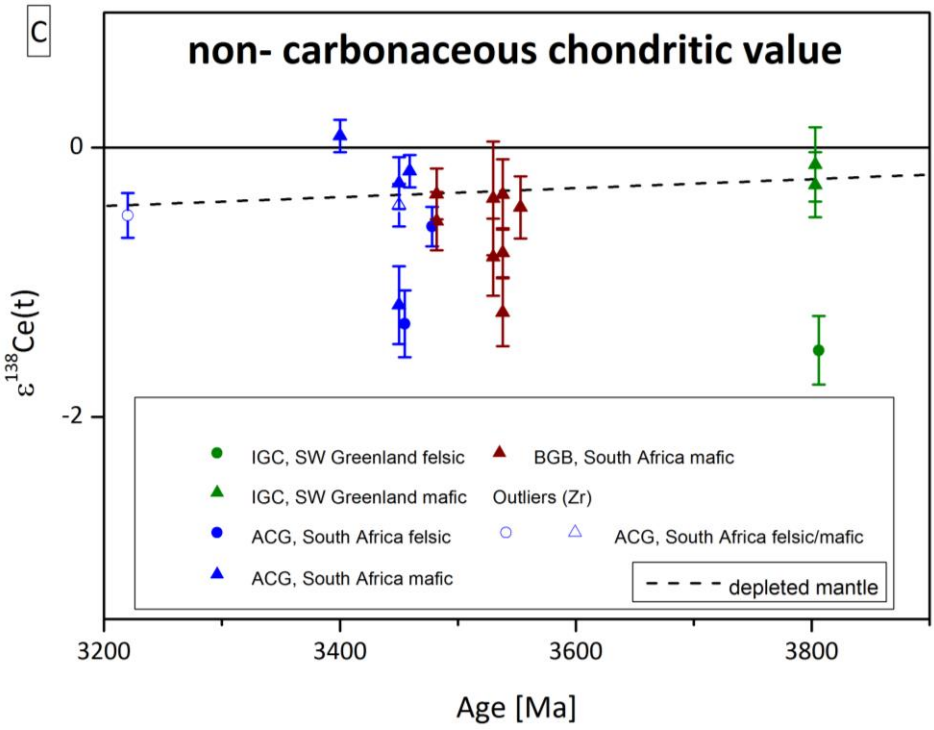

Figure 36 results $\varepsilon^{138}Ce(t)$ versus age [Ma] for undisturbed samples using the chondritic ($^{138}La/^{136}Ce$=0.1868±40, $^{138}Ce/^{136}Ce$=1.33685±3 (all 2 s.e.) (A), carbonaceous chondritic ($^{138}La/^{136}Ce$=0.1946±43, $^{138}Ce/^{136}Ce$=1.33684±2 (all 2 s.e.) (B) and non-carbonaceous chondritic ($^{138}La/^{136}Ce$=0.1823±46, $^{138}Ce/^{136}Ce$=1.33689±4 (all 2 s.e.) (C) ^{138}La-^{138}Ce values of Chapter 3. AGC 350 and AGC 445 are marked with an open symbol. Using the chondritic ^{138}La-^{138}Ce values, the undisturbed samples show a difference of about +0.57 $\varepsilon^{138}Ce$ units to the carbonaceous chondritic ^{138}La-^{138}Ce value and a difference of -0.58 $\varepsilon^{138}Ce$ to the non- carbonaceous chondritic ^{138}La-^{138}Ce value. Depleted mantle value taken from literature ($\varepsilon^{138}Ce(0)$= -1.5, Tazoe et al. (2007), Tazoe et al. (2011), Willig and Stracke (2019), Bonnand et al. (2019)).

In Figure 37 $\varepsilon^{138}Ce(t)$ versus $\varepsilon^{143}Nd(t)$ for undisturbed samples using the chondritic (A), carbonaceous chondritic (B) and non-carbonaceous chondritic (C) ^{138}La-^{138}Ce values of Chapter 3 are shown. The chondritic ^{138}La-^{138}Ce value, which is used as CHUR value for the ^{147}Sm-^{143}Nd and ^{176}Lu-^{176}Hf isotope system, shows an offset of about 0.45 $\varepsilon^{138}Ce(t)$ (Figure 33 A). The carbonaceous chondritic ^{138}La-^{138}Ce value causes even a higher offset of about +0.7 $\varepsilon^{138}Ce(t)$ (Figure 37 B). Using the non-carbonaceous chondritic ^{138}La-^{138}Ce value only an offset of about +0.12 $\varepsilon^{138}Ce(t)$ is caused. Within uncertainty the Ce-Nd correlation trend intersects with the non- carbonaceous chondritic ^{138}La-^{136}Ce value. This result is also in good agreement with the result of the Ce-Nd mantle array. In Figure 28 (Chapter 3) is shown that the chondritic and non-carbonaceous chondritic $^{138}Ce/^{136}Ce$ values show no overlap with the Ce-Nd mantle array. Instead, the carbonaceous chondritic $^{138}Ce/^{136}Ce$ value intersects within uncertainties with the Ce-Nd mantle array. This result is in good agreement with other studies. The study of Warren (2011) and references therein show the division of carbonaceous and non-carbonaceous chondrites for Ti, Cr and Ni isotope ratios. The positive (0 to +5) $\varepsilon^{50}Ti$ values of carbonaceous chondrites are well separated from negative (0 to -2) $\varepsilon^{50}Ti$ values of non-carbonaceous chondrites, the Earth, the Moon and the Mars. This systematic trend can also be seen in $\varepsilon^{54}Cr$ values. The carbonaceous chondrites show positive (0 to +1.6) $\varepsilon^{54}Cr$ values

and the non-carbonaceous chondrites, the Earth, the Moon and the Mars show negative (+0.2 to -1.0) ε^{54}Cr values. Again, the same classification can be seen for ε^{62}Ni where carbonaceous chondrites show positive (0 to +0.3) ε^{62}Ni values and non-carbonaceous chondrites show negative (0 to -0.2) ε^{62}Ni. In the study of Barrat et al. (2016) and references therein Tm/Tm* anomalies were determined in different chondrites. Carbonaceous chondrites show Tm/Tm* ratios relative to CI values ≥ 1 and non-carbonaceous chondrites show Tm/Tm* values ≤ 1. This distribution in carbonaceous and non-carbonaceous chondrites can also be seen for Y/Ho (Pack et al. (2007)). Carbonaceous chondrites have a Y/Ho ratio of 25.94 ± 0.08 (2 σ) and the non-carbonaceous chondrites show higher common Y/Ho ratios: 1.3% for L- and H-chondrites and 5.1% for EL 6 enstatite chondrites. Besides the assumption that the building blocks of the Earth are non-carbonaceous chondrites or enstatite chondrites (e.g. Waaren (2011), Boyet et al. (2018)), there is the possibility that the Earth is chondritic and a hidden reservoir explains the ε^{138}Ce difference between the Earth and chondrites.

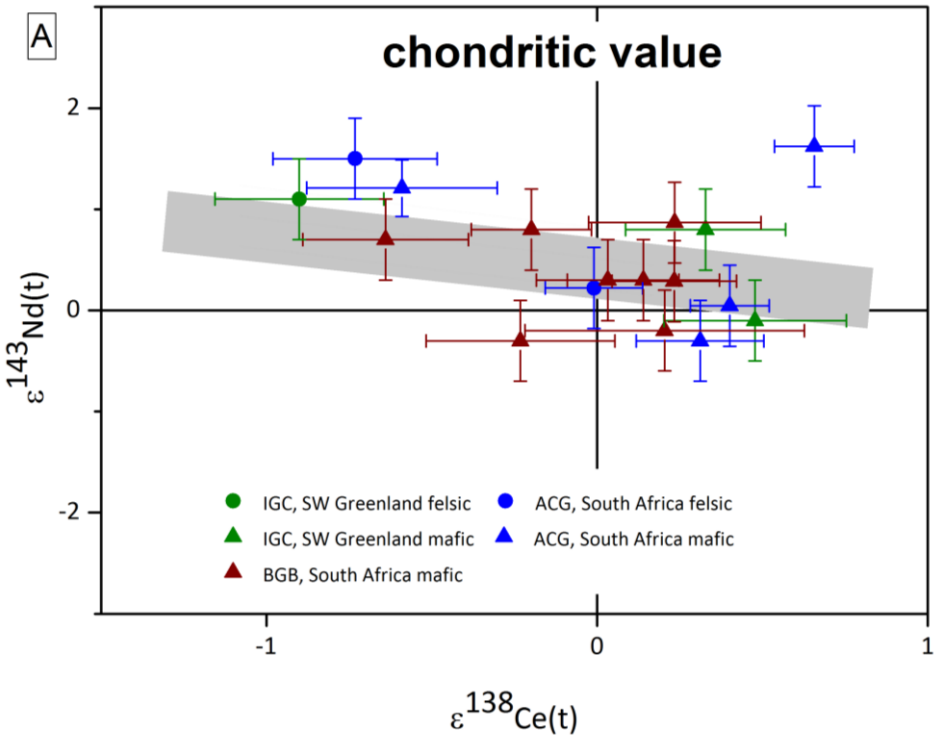

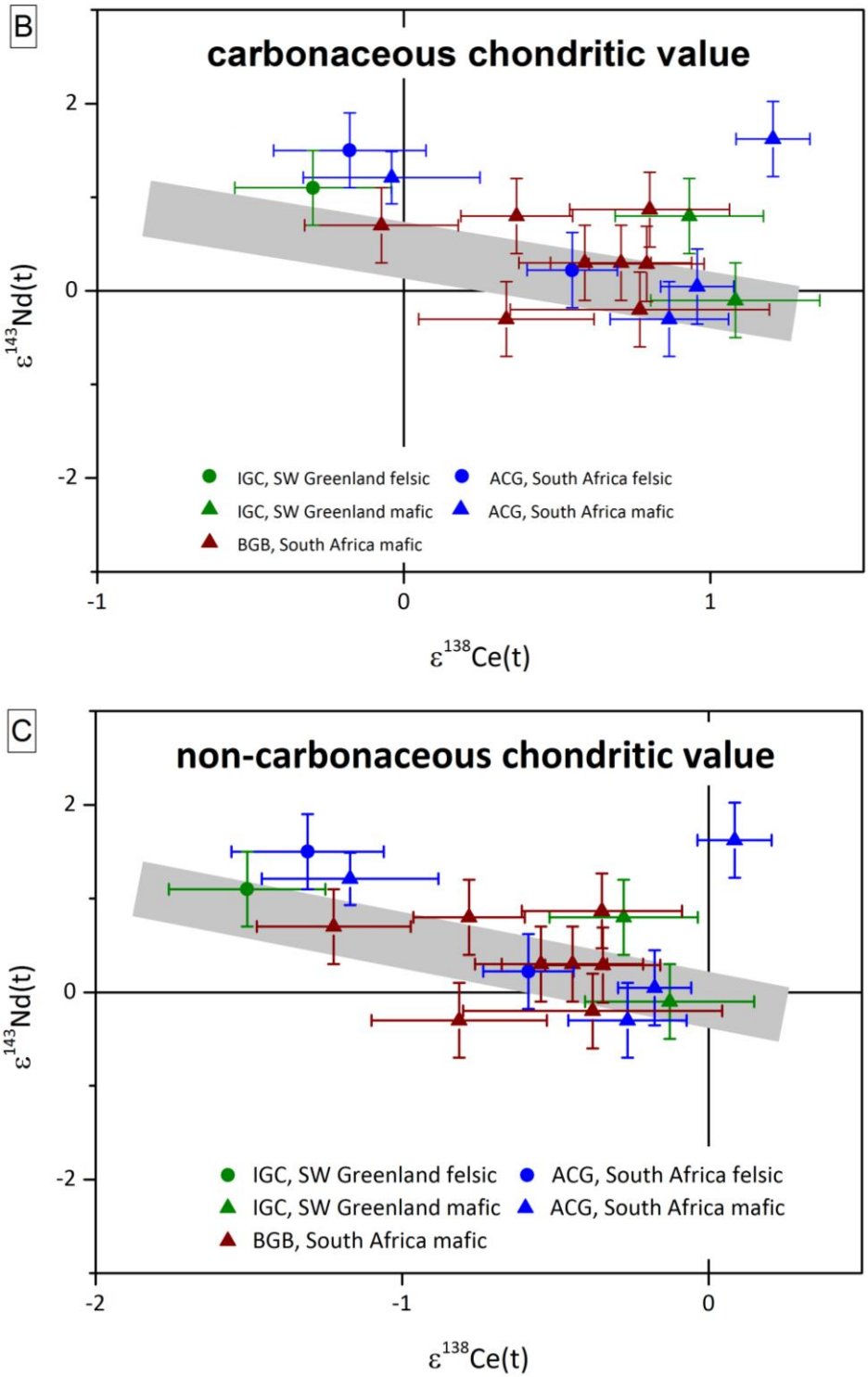

Figure 37 results $\varepsilon^{138}Ce(t)$ versus $\varepsilon^{143}Nd(t)$ for undisturbed samples using the chondritic (A), carbonaceous chondritic (B) and non-carbonaceous chondritic (C) ^{138}La-^{138}Ce values of Chapter 3. AGC 350 and AGC 445 are marked with an open symbol. The samples define a Ce-Nd relation given by $\varepsilon^{143}Nd = -0.324\varepsilon^{138}Ce+0.451$ for the chondritic ^{138}La-^{138}Ce value (A), $\varepsilon^{143}Nd = -0.504\varepsilon^{138}Ce+0.703$ for the carbonaceous chondritic ^{138}La-^{138}Ce value (B) and $\varepsilon^{143}Nd = -0.534\varepsilon^{138}Ce+0.121$ for the carbonaceous chondritic ^{138}La-^{138}Ce value (C).

4.6. Conclusion

In this chapter, the first $\varepsilon^{138}Ce(t)$ data for mafic and felsic Archean rocks from South Africa and Greenland are presented. Present-day values of $\varepsilon^{138}Ce$ and $\varepsilon^{143}Nd$ show a strong correlation

(Figure 30). If the appropriate isotope composition at the age of these samples is recalculated using the chondritic ^{138}La-^{138}Ce mean value of Chapter 3 several samples show $\varepsilon^{138}Ce(t)$ values from -10 to +0.5. Several samples show a Ce anomaly and were excluded due to post-magmatic disturbance of the ^{138}La-^{138}Ce system. As expected from the incompatible behavior of La, Ce, Sm and Nd during magmatic processes, the samples of this study should be characterized by negative $\varepsilon^{138}Ce(t)$ values. Excluding all samples with a negative Ce anomaly, the remaining samples show constant positive $\varepsilon^{138}Ce(t)$ of ca. +0.3 $\varepsilon^{138}Ce(t)$ when normalized to chondritic ^{138}La-^{138}Ce value. Three possibilities that might cause these apparently too high $\varepsilon^{138}Ce$ values in our dataset were discussed above: input of sediment, post magmatic disturbances of the ^{138}La-^{138}Ce system or an inaccurate ^{138}La-^{138}Ce CHUR value that differs strongly between different chondrite classes. Although, alteration and sediments could cause a positive shift of +0.3 $\varepsilon^{138}Ce(t)$ values for the mafic samples. In Figure 36 all undisturbed samples are shown using the chondritic (A), the carbonaceous chondritic (B) and the non-carbonaceous chondritic (C) ^{138}La-^{138}Ce value. For the first time, the difference between using different (chondritic, carbonaceous chondritic and non-carbonaceous chondritic) ^{138}La-^{138}Ce values for age-corrected samples is shown. Undisturbed samples plot near to the expected depleted mantle value when the ^{138}La-^{138}Ce value of non-carbonaceous chondrites is usesd. In Figure 37 all disturbed samples are plotted in the $\varepsilon^{143}Nd(t)$ versus $\varepsilon^{138}Ce(t)$ space. Within uncertainty the Ce-Nd correlation trendline intersects with the non-carbonaceous chondritic ^{138}La-^{136}Ce value in contrast to the chondritic and carbonaceous chondritic ^{138}La-^{136}Ce values. This result is a good agreement with other studies for example Tm/Tm* (Barrat et al. (2016)), Y/Ho (Pack et al. (2007)) and $\varepsilon^{50}Ti$, $\varepsilon^{54}Cr$ and $\varepsilon^{62}Ni$ (Warren (2011)). As a result, the use of the non-carbonaceous chondritic ^{138}La-^{138}Ce value for older samples is recommended.

References

Allègre, C.J., Brévart, O., Dupré, B., Minster, J.-F., 1980. Isotopic and Chemical Effects Produced in a Continuously Differentiating Convecting Earth Mantle. Philos. Trans. R. Soc. London Ser. A, 297, 447–477.

Allègre, C.J., Rousseau, D., 1984. The growth of the continent through geological time studied by Nd isotope analysis of shales. Earth Planet. Sci. Lett. 67, 19–34. https://doi.org/10.1016/0012-821X(84)90035-9

Amakawa, H., Ingri, J., Masuda, A., Shimizu, H., 1991. Isotopic compositions of Ce, Nd and Sr in ferromanganese nodules from the Pacific and Atlantic Oceans, the Baltic and Barents Seas, and the Gulf of Bothnia. Earth Planet. Sci. Lett. 105, 554–565. https://doi.org/10.1016/0012-821X(91)90192-K

Andreasen, R., Sharma, M., 2006. Solar Nebula Heterogeneity in p-process Samarium and Neodymium Isotopes. Science (80-.). 806–809.

Appel, P.W.U., Fedo, C.M., Moorbath, S., Myers, J.S., 1998. Recognizable primary volcanic and sedimentary features in a low-strain domain of the highly deformed, oldest known (~ 3.7-3.8 Gyr) Greenstone Belt, Isua, West Greenland. Terra Nov. 10, 57–62. https://doi.org/10.1046/j.1365-3121.1998.00162.x

Armstrong, R.L., 1991. The persistent myth of crustal growth. Aust. J. Earth Sci. 38, 613–630. https://doi.org/10.1080/08120099108727995

Arndt, N.T., Teixeira, N.A., White, W.M., 1989. Bizarre geochemistry of komatiites from the Crixás greenstone belt, Brazil. Contrib. to Mineral. Petrol. 101, 187–197. https://doi.org/10.1007/BF00375305

Arndt, N.T., 1994, Archean komatiites. In: Condie, K.C. (Ed.), Archean Crustal Evolution. Elsevier, Amsterdam, pp. 11–44.

Baker, J., Waight, T., Ulfbeck, D., 2002. Rapid and highly reproducible analysis of rare earth elements by multiple collector inductively coupled plasma mass spectrometry. Geochim. Cosmochim. Acta 66, 3635–3646. https://doi.org/Pii S0016-7037(00)00921-3

Barrat, J.A., Zanda, B., Moynier, F., Bollinger, C., Liorzou, C., Bayon, G., 2012. Geochemistry of CI chondrites: Major and trace elements, and Cu and Zn Isotopes. Geochim. Cosmochim. Acta 83, 79–92. https://doi.org/10.1016/j.gca.2011.12.011

Bédard JH (2006) A catalytic delamination-driven model for coupled genesis of Archaean crust and sub-continental lithospheric mantle. Geochim. Cosmochim. Acta 70, 1188-1214. DOI: 10.1016/j.gca.2005.11.008

Bellot, N., Boyet, M., Doucelance, R., Pin, C., Chauvel, C., Auclair, D., 2015. Ce isotope systematics of island arc lavas from the Lesser Antilles. Geochim. Cosmochim. Acta 168, 261–279. https://doi.org/10.1016/j.gca.2015.07.002

Bennett, V.C., Nutman, A.P., McCulloch, M.T., 1993. Nd isotopic evidence for transient, highly depleted mantle reservoirs in the early history of the Earth. Earth Planet. Sci. Lett. 119, 299–317. https://doi.org/10.1016/0012-821X(93)90140-5

Bennett, V.C., Nutman, A.P., Esat, T.M., 2002. Constraints on mantle evolution from $^{187}Os/^{188}Os$ isotopic compositions of Archean ultramafic rocks from southern West Greenland (3.8 Ga) and Western Australia (3.46 Ga). Geochim. Cosmochim. Acta 66, 2615–2630. https://doi.org/10.1016/S0016-7037(02)00862-1

Berglund, M., Wieser, M.E., 2011. Isotopic compositions of the elements 2009 (IUPAC Technical Report). Pure Appl. Chem. 83, 397–410. https://doi.org/10.1351/PAC-REP-10-06-02

Bischoff, A., 2001. Meteorite classification and the definition of new chondrite classes as a result of successful meteorite search in hot and cold deserts. Planet. Space Sci. 49, 769–776. https://doi.org/10.1016/S0032-0633(01)00026-5

Blichert-Toft, J., Albarède, F., 1997. The Lu-Hf isotope geochemistry of chondrites and the evolution of the mantle–crust system. Earth Planet. Sci. Lett. 148, 243–258. https://doi.org/10.1016/s0012-821x(97)00198-2

Blichert-Toft, J., Albarède, F., Rosing, M., Frei, R., Bridgwater, D., 1999. The Nd and Hf isotopic evolution of the mantle through the Archean. Results from the Isua supracrustals, West Greenland, and from the Birimian terranes of West Africa. Geochim. Cosmochim. Acta 63, 3901–3914. https://doi.org/10.1016/S0016-7037(99)00183-0

Blichert-Toft, J., Albarède, F., 2008. Hafnium isotopes in Jack Hills zircons and the formation of the Hadean crust. Earth Planet. Sci. Lett. 265, 686–702. https://doi.org/10.1016/j.epsl.2007.10.054

Bonnand, P., Israel, C., Boyet, M., Doucelance, R., Auclair, D., 2019. Radiogenic and stable Ce isotope measurements by thermal ionisation mass spectrometry. J. Anal. At. Spectrom. https://doi.org/10.1039/C8JA00362A

Bouvier, A., Vervoort, J.D., Patchett, P.J., 2008. The Lu-Hf and Sm-Nd isotopic composition of CHUR: Constraints from unequilibrated chondrites and implications for the bulk composition of terrestrial planets. Earth Planet. Sci. Lett. 273, 48–57. https://doi.org/10.1016/j.epsl.2008.06.010

Bouvier, A., Wadhwa, M., 2010. The age of the Solar System redefined by the oldest Pb-b age of a meteoritic inclusion. Nat. Geosci. 3, 637–641. https://doi.org/10.1038/ngeo941

Bouvier, A., Boyet, M., 2016. Primitive Solar System materials and Earth share a common initial^{142}Nd abundance. Nature 537, 399–402. https://doi.org/10.1038/nature19351

Bowring, S.A., Housh, T., 1995. The Earth's Early Evolution. Nature 269, 1535–1540.

Bowring, S.A., Williams, I.S., 1999. Priscoan (4.00-4.03 Ga) orthogneisses from northwestern Canada. Contrib. to Mineral. Petrol. 134, 3–16. https://doi.org/10.1007/s004100050465

Boyet, M., Carlson, R.W., 2005. 142Nd Evidence for Early (>4.53 Ga) Global Differentiation of the Silicate Earth. Science. 309, 576–581. https://doi.org/10.1126/science.1227608

Boyet, M., Carlson, R.W., 2006. A new geochemical model for the Earth's mantle inferred from ^{146}Sm-^{142}Nd systematics. Earth Planet. Sci. Lett. 250, 254–268. https://doi.org/10.1016/j.epsl.2006.07.046

Boyet, M., Bouvier, A., Frossard, P., Hammouda, T., Garçon, M., Gannoun, A., 2018. Enstatite chondrites EL3 as building blocks for the Earth: The debate over the ^{146}Sm–^{142}Nd systematics. Earth Planet. Sci. Lett. 488, 68–78. https://doi.org/10.1016/j.epsl.2018.02.004

Boyet, M., Doucelance, R., Israel, C., Bonnand, P., Auclair, D., Suchorski, K., Bosq, C., 2019. New constraints on the origin of the EM-1 component revealed by the measurement of the La-Ce isotope systematics in Gough Island lavas. Geochemistry, Geophys. Geosystems 1–15. https://doi.org/10.1029/2019gc008228

Burbidge, E.M., Burbidge, G.R., Fowler, W.A., Hoyle, F., 1957. Synthesis of the Elements in Stars. Rev. Mod. Phys. 29, 547–655.

Braukmüller, N., Wombacher, F., Hezel, D.C., Escoube, R., Münker, C., 2018. The chemical composition of carbonaceous chondrites: Implications for volatile element depletion, complementarity and alteration. Geochim. Cosmochim. Acta 239, 17–48. https://doi.org/10.1016/j.gca.2018.07.023

Burkhardt, C., Kleine, T., Oberli, F., Pack, A., Bourdon, B., Wieler, R., 2011. Molybdenum isotope anomalies in meteorites: Constraints on solar nebula evolution and origin of the Earth. Earth Planet. Sci. Lett. 312, 390–400. https://doi.org/10.1016/j.epsl.2011.10.010

Burkhardt, C., Borg, L.E., Brennecka, G.A., Shollenberger, Q.R., Dauphas, N., Kleine, T., 2016. A nucleosynthetic origin for the Earth's anomalous ^{142}Nd composition. Nature 537, 394–398. https://doi.org/10.1038/nature18956

Busso, M., Gallino, R., Wasserburg, G.J., 1999. Nucleosynthesis in Asymptotic Giant Branch Stars: Relevance for Galactic Enrichment and Solar System Formation. Annu. Rev. Astrom. Astrophys. 37, 239–309.

Cameron, A.G.W., 1957. NUCLEAR REACTIONS IN STARS AND NUCLEOGENESIS. Astron. Soc. Pacific 69, 201–222.

Carlson, R.W., Boyet, M., Horan, M., 2007. Chondrite Barium, Neodymium, and Samarium Isotopic Heterogeneity and Early Earth Differentiation. Science 316, 1175–1178. https://doi.org/10.1016/j.epsl.2004.07.008

Caro G., Bourdon B., Wood B. J. and Corgne A. (2005) Trace-element fractionation in Hadean mantle generated by melt segregation from a magma ocean. Nature 436, 246.

Caro, G., Bourdon, B., 2010. Non-chondritic Sm/Nd ratio in the terrestrial planets: Consequences for the geochemical evolution of the mantle-crust system. Geochim. Cosmochim. Acta 74, 3333–3349. https://doi.org/10.1016/j.gca.2010.02.025

Caro, G., 2011. Early Silicate Earth Differentiation. Annu. Rev. Earth Planet. Sci. 39, 31–58. https://doi.org/10.1146/annurev-earth-040610-133400

Chen, J.H., Papanastassiou, D.A., Wasserburg, G.J., 2010. Ruthenium endemic isotope effects in chondrites and differentiated meteorites. Geochim. Cosmochim. Acta 74, 3851–3862. https://doi.org/10.1016/j.gca.2010.04.013

Christensen, U.R., Hofmann, A.W., 1994. Segregation of subducted oceanic crust in the convecting mantle. J. Geophys. Res. 99, 19867–19884.

Collerson, K.D., Campbell, L.M., Weaver, B.L., Palacz, Z.A., 1991. Evidence for extreme mantle fractionation in early Archaean ultramafic rocks from northern Labrador. Nature 349, 209–214. https://doi.org/10.1038/349209a0

Compston, W., Kröner, A., 1988. Multiple zircon growth within early Archaean tonalitic gneiss from the Ancient Gneiss Complex, Swaziland. Earth Planet. Sci. Lett. 87, 13–28. https://doi.org/10.1016/0012-821X(88)90061-1

Compston W, Pidgeon RT (1986) Jack Hills, evidence of more very old detrital zircons in Western Australia. Nature 321:766

Condie, K.C., 1997. Plate Tectonics and Crustal Evolution.

Condie KC (2005) TTGs and adakites: are they both slab melts? Granitic Syst 80:33–44. DOI: 10.1016/j.lithos.2003.11.001

Dauphas, N., Pourmand, A., 2015. Thulium anomalies and rare earth element patterns in meteorites and Earth: Nebular fractionation and the nugget effect. Geochim. Cosmochim. Acta 163, 234–261. https://doi.org/10.1016/j.gca.2015.03.037

Dauphas, N., 2017. The isotopic nature of the Earth's accreting material through time. Nature 541, 521–524. https://doi.org/10.1038/nature20830

Defant MJ, Drummond MS (1990) Derivation of some modern arc magmas by melting of young subducted lithosphere. Nature 347:662

DePaolo, D.J., Wasserburg, G.J., 1976. Nd isotopic variations and petrogenic models. Geophys. Res. Lett. 3, 249–252. https://doi.org/10.1029/GL003i005p00249

Dickin, A.P., 1987. Cerium isotope chemistry of ocean island basalts. Nature 326, 283–284.

Dickin, A.P., Jones, N.W., Thirlwall, M.F., Thompson, R.N., 1987. A Ce/Nd isotope study of crustal contamination processes affecting Palaeocene magmas in Skye, Northwest Scotland. Contrib Miner. Pet. 96, 455–464.

Dickin, A.P., 1988. Mantle and crustal Ce/Nd isotope systematics. Nature 33, 403.

Doucelance, R., Bellot, N., Boyet, M., Hammouda, T., Bosq, C., 2014. What coupled cerium and neodymium isotopes tell us about the deep source of oceanic carbonatites. Earth Planet. Sci. Lett. 407, 175–186. https://doi.org/10.1016/j.epsl.2014.09.042

Fischer-Gödde, M., Kleine, T., 2017. Ruthenium isotopic evidence for an inner Solar System origin of the late veneer. Nature 541, 525–527. https://doi.org/10.1038/nature21045

Fitoussi, C., Bourdon, B., 2012. Silicon Isotope Evidence Against an Enstatite Chondrite Earth. Science ,335, 1477–1480.

Frei R, Rosing MT, Waight TE, Ulfbeck DG (2002) Hydrothermal-metasomatic and tectonometamorphic processes in the Isua supracrustal belt (West Greenland): a multi-isotopic investigation of their effects on the earth's oldest oceanic crustal sequence. Geochim Cosmochim Acta 66:467–486. doi: 10.1016/S0016-7037(01)00781-5

Gannoun, A., Boyet, M., Rizo, H., El Goresy, A., 2011. ^{146}Sm-^{142}Nd systematics measured in enstatite chondrites reveals a heterogeneous distribution of ^{142}Nd in the solar nebula. Proc. Natl. Acad. Sci. U. S. A. 108, 7693–7697. https://doi.org/10.1073/pnas.1017332108

Goldschmidt V. M. (1937). The principles of distribution of chemical elements in minerals and rocks. Journal of the Chemical Society: 655 – 673

Gruau, G., Tourpin, S., Fourcade, S., Blais, S., 1992. Loss of isotopic (Nd, O) and chemical (REE) memory during metamorphism of komatiites: new evidence from eastern Finland. Contrib. to Mineral. Petrol. 112, 66–82. https://doi.org/10.1007/BF00310956

Gruau, G., Rosing, M., Bridgwater, D., Gill, R.C.O., 1996. Resetting of Sm-Nd systematics during metamorphism of > 3.7-Ga rocks: Implications for isotopic models of early Earth differentiation. Chem. Geol. 133, 225–240. https://doi.org/10.1016/S0009-2541(96)00092-7

Hamilton, P.J., O'Nions, R.K., Bridgwater, D., Nutman, A.P., 1983. Sm-Nd studies of Archaean metasediments and metavolcanics from West Greenland and their implications for the Earth's early history. Earth Planet. Sci. Lett. 62, 263–272. https://doi.org/10.1016/0012-821X(83)90089-4

Hans, U., Kleine, T., Bourdon, B., 2013. Rb-Sr chronology of volatile depletion in differentiated protoplanets: BABI, ADOR and ALL revisited. Earth Planet. Sci. Lett. 374, 204–214. https://doi.org/10.1016/j.epsl.2013.05.029

Harrison, T.M., Blichert-Toft, J., Müller, W., Albarède, F., P., H., Mojzsis, S.J., 2005. Heterogeneous Hadean Hafnium : Evidence of Continental Crust at 4.4 to 4.5 Ga. Science 310, 1947–1950. https://doi.org/10.1126/science.1117926

Harrison, T.M., Watson, E.B., Aikman, A.B., 2007. Temperature spectra of zircon crystallization in plutonic rocks. Geology 35, 635–638. https://doi.org/10.1130/G23505A.1

Harrison, T.M., Schmitt, A.K., McCulloch, M.T., Lovera, O.M., 2008. Early (4.5 Ga) formation of terrestrial crust Lu–Hf, δ18O, and Ti thermometry results for Hadean zircons.pdf. Earth Planet. Sci. Lett. 268, 476–486.

Harper, C.L., Jacobsen, S.B., 1992. Evidence from coupled ^{147}Sm-^{143}Nd and ^{146}Sm-^{142}Nd systematics for very early (4.5 Gyr) differentiation of Earth´s mantle. Lett. To Nat. 360, 728–732.

Hiess J., Bennett V. C., Nutman A. P. and Williams I. S. (2009) In situ U–Pb, O and Hf isotopic compositions of zircon and olivine from Eoarchaean rocks, West Greenland: New insights to making old crust. Geochim. Cosmochim. Acta 73, 4489–4516.

Hirahara, Y., Chang, Q., Miyazaki, T., Takahashi, T., Kimura, J., 2012. Improved Nd chemical separation technique for ^{143}Nd/^{144} Nd analysis in geological samples using packed Ln resin columns. JAMSTEC Rep. Res. Dev. 15, 27–33.

Hofmann, A.W., 1988. Chemical differentiation of the Earth: the relationship between mantle, continental crust, and oceanic crust. Earth Planet. Sci. Lett. 90, 297–314. https://doi.org/10.1016/0012-821X(88)90132-X

Hoffmann, J.E., Münker, C., Polat, A., König, S., Mezger, K., Rosing, M.T., 2010. Highly depleted Hadean mantle reservoirs in the sources of early Archean arc-like rocks, Isua

supracrustal belt, southern West Greenland. Geochim. Cosmochim. Acta 74, 7236–7260. https://doi.org/10.1016/j.gca.2010.09.027

Hoffmann, J.E., Münker, C., Polat, A., Rosing, M.T., Schulz, T., 2011. The origin of decoupled Hf-Nd isotope compositions in Eoarchean rocks from southern West Greenland. Geochim. Cosmochim. Acta 75, 6610–6628. https://doi.org/10.1016/j.gca.2011.08.018

Hoffmann, J.E., Nagel, T.J., Münker, C., Næraa, T., Rosing, M.T., 2014. Constraining the process of Eoarchean TTG formation in the Itsaq Gneiss Complex, southern West Greenland. Earth Planet. Sci. Lett. 388, 374–386. https://doi.org/10.1016/j.epsl.2013.11.050

Hoffmann, J.E., Kröner, A., Hegner, E., Viehmann, S., Xie, H., Iaccheri, L.M., Schneider, K.P., Hofmann, A., Wong, J., Geng, H., Yang, J., 2016. Source composition, fractional crystallization and magma mixing processes in the 3.48-3.43 Ga Tsawela tonalite suite (Ancient Gneiss Complex, Swaziland) - Implications for Palaeoarchaean geodynamics. Precambrian Res. 276, 43–66. https://doi.org/10.1016/j.precamres.2016.01.026

Horie, K., Nutman, A.P., Friend, C.R.L., Hidaka, H., 2010. The complex age of orthogneiss protoliths exemplified by the Eoarchaean Itsaq Gneiss Complex (Greenland): SHRIMP and old rocks. Precambrian Res. 183, 25–43. https://doi.org/10.1016/j.precamres.2010.06.016

S. E. Humphris, 1984. The mobility of the rare earth elements in the crust. In: Henderson, P. (Ed.), Rare Earth Element Chemistry. Elsevier, Amsterdam, pp. 317 – 342

Iizuka, T., Komiya, T., Ueno, Y., Katayama, I., Uehara, Y., Maruyama, S., Hirata, T., Johnson, S.P., Dunkley, D.J., 2007. Geology and zircon geochronology of the Acasta Gneiss Complex, northwestern Canada: New constraints on its tectonothermal history. Precambrian Res. 153, 179–208. https://doi.org/10.1016/j.precamres.2006.11.017

Jacobsen, S.B., Wasserburg, G.J., 1980. Sm-Nd isotopic evolution of chondrites. Earth Planet. Sci. Lett. 50, 139–155. https://doi.org/10.1016/0012-821X(80)90125-9

Jacobsen, S.B., 1988. Isotopic and chemical constraints on mantle-crust evolution. Geochim. Cosmochim. Acta 52, 1341–1350. https://doi.org/10.1016/0016-7037(88)90205-0

Jenner, F.E., Bennett, V.C., Nutman, A.P., Friend, C.R.L., Norman, M.D., Yaxley, G., 2009. Evidence for subduction at 3.8 Ga: Geochemistry of arc-like metabasalts from the southern edge of the Isua Supracrustal Belt. Chem. Geol. 261, 83–98. https://doi.org/10.1016/j.chemgeo.2008.09.016

Jochum, K.P., Weis, U., Schwager, B., Stoll, B., Wilson, S.A., Haug, G.H., Andreae, M.O., Enzweiler, J., 2015. Reference Values Following ISO Guidelines for Frequently Requested Rock Reference Materials. Geostand. Geoanalytical Res. 40, 333–350. https://doi.org/10.1111/j.1751-908x.2015.00392.x

Kamber B, Ewart A, Collerson K, et al (2002) Fluid-mobile trace element constraints on the role of slab melting and implications for Archaean crustal growth models. Contrib Mineral Petrol 144:38–56. doi: 10.1007/s00410-002-0374-5

Kemp, A.I.S., Wilde, S.A., Hawkesworth, C.J., Coath, C.D., Nemchin, A., Pidgeon, R.T., Vervoort, J.D., DuFrane, S.A., 2010. Hadean crustal evolution revisited: New constraints

from Pb-Hf isotope systematics of the Jack Hills zircons. Earth Planet. Sci. Lett. 296, 45–56. https://doi.org/10.1016/j.epsl.2010.04.043

Kemp, A.I.S., Hickman, A.H., Kirkland, C.L., Vervoort, J.D., 2015. Hf isotopes in detrital and inherited zircons of the Pilbara Craton provide no evidence for Hadean continents. Precambrian Res. 261, 112–126. https://doi.org/10.1016/j.precamres.2015.02.011

Kramers, J.D., 2007. Hierarchical Earth accretion and the Hadean Eon. J. Geol. Soc. London. 164, 3–17. https://doi.org/10.1144/0016-76492006-028

Kratz, K.L., Farouqi, K., Pfeiffer, B., 2007. Nuclear physics far from stability and r-process nucleosynthesis. Prog. Part. Nucl. Phys. 59, 147–155. https://doi.org/10.1016/j.ppnp.2006.12.024

Kröner, A., Byerly, G.R., Lowe, D.R., 1991. Chronology of early Archaean granite-greenstone evolution in the Barberton Mountain Land, South Africa, based on precise dating by single zircon evaporation. Earth Planet. Sci. Lett. 103, 41–54. https://doi.org/10.1016/0012-821X(91)90148-B

Kröner, A., Tegtmeyer, A., 1994. Gneiss-greenstone relationships in the Ancient Gneiss Complex of southwestern Swaziland, southern Africa, and implications for early crustal evolution. Precambrian Res. 67, 109–139. https://doi.org/10.1016/0301-9268(94)90007-8

Kröner, A., Hegner, E., Wendt, J.I., Byerly, G.R., 1996. The oldest part of the Barberton granitoid-greenstone terrain, South Africa: Evidence for crust formation between 3.5 and 3.7 Ga. Precambrian Res. 78, 105–124.

Kröner, A., 2007. Chapter 5.2 The Ancient Gneiss Complex of Swaziland and Environs: Record of Early Archean Crustal Evolution in Southern Africa. Dev. Precambrian Geol. 15, 465–480. https://doi.org/10.1016/S0166-2635(07)15052-0

Lahaye, Y., Arndt, N., Byerly, G., Chauvel, C., Fourcade, S., Gruau, G., 1995. The influence of alteration on the trace-element and Nd isotopic compositions of komatiites. Chem. Geol. 126, 43–64. https://doi.org/10.1016/0009-2541(95)00102-1

Lee, S.-G., Masuda, A., Shimizu, H., Yong-Sun, S., 2001. Crustal evolution history of Korean Peninsula in East Asia : The significance of Nd, Ce isotopic and REE data from the Korean Precambrian gneisses. Geochemical J. 35, 175–187.

Löcht, J. Van De, Hoffmann, J.E., Li, C., Wang, Z., Becker, H., Rosing, M.T., Kleinschrodt, R., 2018. Earth ' s oldest mantle peridotites show full record of late accretion. Geol. Soc. Am. 46, 10–20. https://doi.org/10.1130/G39709.1

Löcht, J. Van de, 2019, Geochemistry and petrology of ~ 3.8 Ga mafic-ultramafic enclaves in the Itsaq Gneiss Complex, SW Greenland, Ph.D. thesis, University of Cologne

Luais, B., Le Carlier de Veslud, C., Géraud, Y., Gauthier-Lafaye, F., 2009. Comparative behavior of Sr, Nd and Hf isotopic systems during fluid-related deformation at middle crust levels. Geochim. Cosmochim. Acta 73, 2961–2977. https://doi.org/10.1016/j.gca.2008.12.026

Lodders, K., 2003. SOLAR SYSTEM ABUNDANCES AND CONDENSATION TEMPERATURES OF THE ELEMENTS Katharina Lodders. Astrophys. J. 591, 1220–1247. https://doi.org/http://dx.doi.org/10.1086/375492

Martin H (1986) Effect of steeper Archean geothermal gradient on geochemistry of subduction-zone magmas. Geology 14:753–756. doi: 10.1130/0091-7613(1986)14<753:EOSAGG>2.0.CO;2

Makishima, A., Shimizu, H., Masuda, A., 1987. Precise Measurement of Cerium and Lanthanum Isotope Ratios. Mass Spectrosc. 35, 64–72.

Makishima, A., Nakamura, E., 1991. Precise measurement of cerium isotope composition in rock samples. Chem. Geol. 94, 1–11.

Makishima, A., Masuda, A., 1993. Primordial Ce isotopic composition of the solar system. Chem. Geol. 106, 197–205. https://doi.org/10.1016/0009-2541(93)90026-F

Makishima, A., Masuda, A., 1994. Ce isotope ratios of N-type MORB. Chem. Geol. 118, 1–8. https://doi.org/10.1016/0009-2541(94)90166-X

Makishima, A., Masuda, A., 1994. Search for p-isotopic anomaly of cerium in the bulk Allende meteorite. Geochem. J. 28, 115–122.

Martin, P.M., Mason, B., 1974. Major and trace elements in the Allende meteorite. Nature 249, 333–334. https://doi.org/10.1038/249333a0

Masuda, A., Shimizu, H., Nakai, S., Makishima, A., Lathi, S., 1988. 138La - beta decay constant estimated from geochronological studies. Earth Planet. Sci. Lett. 89, 316–322.

Menneken M, Nemchin AA, Geisler T, et al (2007) Hadean diamonds in zircon from Jack Hills, Western Australia. Nature 448:917

Merrill, P.W., 1952. Measurements in the Spectra of four long-period variable stars of Class Me. Am. Astron. Soc. 344–347. https://doi.org/10.1017/CBO9781107415324.004

Moorbath, S., Allaart, J.H., Bridgwater, D., McGregor, V.R., 1977. Rb-Sr ages of early Archean supracrustal rocks and Amitsoq gneisses at Isua. Nature 270, 43–45.

Moorbath, S., Whitehouse, M.., Kamber, B.., 1997. Extreme Nd-isotope heterogeneity in the early Archaean—fact or fiction? Case histories from northern Canada and West Greenland. Chem. Geol. 135, 213–231. https://doi.org/10.1016/s0009-2541(98)00032-1

Mukasa, S.B., Wilson, A.H., Young, K.R., 2013. Geochronological constraints on the magmatic and tectonic development of the Pongola Supergroup (Central Region), South Africa. Precambrian Res. 224, 268–286. https://doi.org/10.1016/j.precamres.2012.09.015

Murphy, R.C.L 2015. Stabilising a craton: the origin and emplacement of the 3.1 Ga Mpuluzi Batholith, Ph.D. thesis, Macquarie University, Sydney

Murton, B.J., Peate, D.W., Arculus, R.J., Pearce, J.A., Van Der Laan, S., 1992. Trace-element geochemistry of volcanic rocks from Site 786: the Izu- Bonin Forearc. Proc. Ocean Drill. Progr. 125, 211–236.

Næraa, T., Scherstén, A., Rosing, M.T., Kemp, A.I.S., Hoffmann, J.E., Kokfelt, T.F., Whitehouse, M.J., 2012. Hafnium isotope evidence for a transition in the dynamics of continental growth 3.2 Gyr ago. Nature 485, 627–630. https://doi.org/10.1038/nature11140

Nakamura, N., Tatsumoto, M., Ludwig, K.R., 1984. Applicability of La-Ce systematics to planetary samples. J. Geophys. Res. 89, B438–B444. https://doi.org/10.1017/CBO9781107415324.004

Nebel, O., Campbell, I.H., Sossi, P.A., Van Kranendonk, M.J., 2014. Hafnium and iron isotopes in early Archean komatiites record a plume-driven convection cycle in the Hadean Earth. Earth Planet. Sci. Lett. 397, 111–120. https://doi.org/10.1016/j.epsl.2014.04.028

Nebel-Jacobsen Y, Münker C, Nebel O, et al (2010) Reworking of Earth's first crust: Constraints from Hf isotopes in Archean zircons from Mt. Narryer, Australia. Precambrian Res 182:175–186. doi: 10.1016/j.precamres.2010.07.002

Newman, K., 2012. Effects of the sampling interface in MC-ICP-MS: Relative elemental sensitivities and non-linear mass dependent fractionation of Nd isotopes. J. Anal. At. Spectrom. 27, 63–70. https://doi.org/10.1039/c1ja10222b

Nica, N., 2018. Nuclear Data Sheets for A=147. Nucl. Data Sheets 154, 1–403. https://doi.org/10.1016/j.nds.2018.11.002

Nutman, A.P., Bridgwater, D., Fryer, B.J., 1984. The iron-rich suite from the Amîtsoq gneisses of southern West Greenland: early Archaean plutonic rocks of mixed crustal and mantle origin. Contrib. to Mineral. Petrol. 87, 24–34. https://doi.org/10.1007/BF00371399

Nutman, A.P., Allaart, J.H., Bridgwater, D., Dimroth, E., Rosing, M., 1984. Stratigraphic and geochemical evidence for the depositional environment of the early archaean isua supracrustal belt, southern West Greenland. Precambrian Res. 25, 365–396. https://doi.org/10.1016/0301-9268(84)90010-X

Nutman, A.P., McGregor, V.R., Friend, C.R.L., Bennett, V.C., Kinny, P.D., 1996. The Itsaq Gneiss Complex of southern West Greenland; the world's most extensive record of early crustal evolution (3900-3600 Ma). Precambrian Res. 78, 1–39.

Nutman, A.P., 2001. On the scarcity of > 3900 Ma detrital zircons in ≥ 3500 Ma metasediments. Precambrian Res. 105, 93–114. https://doi.org/10.1016/S0301-9268(00)00106-6

Nutman, A.P., Friend, C.R.L., Paxton, S., 2009. Detrital zircon sedimentary provenance ages for the Eoarchaean Isua supracrustal belt southern West Greenland: Juxtaposition of an imbricated ca. 3700 Ma juvenile arc against an older complex with 3920-3760 Ma components. Precambrian Res. 172, 212–233. https://doi.org/10.1016/j.precamres.2009.03.019

OHNO, T., HIRATA, T., 2013. Determination of Mass-Dependent Isotopic Fractionation of Cerium and Neodymium in Geochemical Samples by MC-ICPMS. Anal. Sci. 29, 47–53. https://doi.org/10.2116/analsci.29.47

Pack, A., Russell, S.S., Shelley, J.M.G., Van Zuilen, M., 2007. Geo- and cosmochemistry of the twin elements yttrium and holmium. Geochimica et Cosmochimica Acta 71, 4592–4608. DOI:10.1016/j.gca.2007.07.010.

Palme, H., Lodders, K., Jones, A., 2014. Solar System Abundances of the Elements, in: In Treatise on Geochemistry. Elsevier Ltd., pp. 15–21. https://doi.org/10.1007/978-3-642-10352-0_8

Papanastassiou, D.A., Wasserburg, G.J., 1968. Initial strontium isotopic abundances and the resolution of small time differences in the formation of planetary objects. Earth Planet. Sci. Lett. 5, 361–376. https://doi.org/10.1016/s0012-821x(68)80066-4

Patchett, P.J., Tatsumoto, M., 1980. A routine high-precision method for Lu-Hf isotope geochemistry and chronology. Contrib. to Mineral. Petrol. 75, 263–267. https://doi.org/10.1007/BF01166766

Patchett, P.J., 1983. Importance of the Lu-Hf isotopic system in studies of planetary chronology and chemical evolution. Geochim. Cosmochim. Acta 47, 81–91. https://doi.org/10.1016/0016-7037(83)90092-3

Pearce, J.A., Van Der Laan, S., Arculus, R.J., Murton, B.J., Ishii, T., Peate, D.W., Parkinson, I.J., 1992. Boninite and harzburgite from Leg 125 (Bonin-Mariana Forearc): a case study of magma genesis during the initial stages of subduction. Proc. Ocean Drill. Progr. 125, 623–662.

Pearce, J.A., Peate, D.W., 1995. Tectonic implications of the composition of volcanic arc magmas. Annu. Rev. Earth Planet. Sci. 23, 251–185.

Peters, S.T.M., Münker, C., Wombacher, F., Elfers, B.M., 2015. Precise determination of low abundance isotopes (^{174}Hf, ^{180}W and ^{190}Pt) in terrestrial materials and meteorites using multiple collector ICP-MS equipped with $10^{12}\Omega$ Faraday amplifiers. Chem. Geol. 413, 132–145. https://doi.org/10.1016/j.chemgeo.2015.08.018

Petersson, A., Kemp, A.I.S., Hickman, A.H., Whitehouse, M.J., Martin, L., Gray, C.M., 2019. A new 3.59 Ga magmatic suite and a chondritic source to the east Pilbara Craton. Chem. Geol. 511, 51–70. https://doi.org/10.1016/j.chemgeo.2019.01.021

Pfeifer, M., Lloyd, N.S., Peters, S.T.M., Wombacher, F., Elfers, B.M., Schulz, T., Münker, C., 2017. Tantalum isotope ratio measurements and isotope abundances determined by MC-ICP-MS using amplifiers equipped with 10^{10}, 10^{12} and 10^{13} Ohm resistors. J. Anal. At. Spectrom. 32, 130–143. https://doi.org/10.1039/c6ja00329j

Pin, C., Gannoun, A., 2017. Integrated Extraction Chromatographic Separation of the Lithophile Elements Involved in Long-Lived Radiogenic Isotope Systems (Rb-Sr, U-Th-Pb, Sm-Nd, La-Ce, and Lu-Hf) Useful in Geochemical and Environmental Sciences. Anal. Chem. 89, 2411–2417. https://doi.org/10.1021/acs.analchem.6b04289

Plank, T., Langmuir, C.H., 1998. The chemical composition of subducting sediment and its consequences for the crust and mantle. Chem. Geol. 145, 325–394. https://doi.org/10.4045/tidsskr.17.0952

Polat, A., Hofmann, A.W., Rosing, M.T., 2002. Boninite-like volcanic rocks in the 3.7-3.8 Ga isua greenstone belt, West Greenland: Geochemical evidence for intra-oceanic subduction zone processes in the early earth. Chem. Geol. 184, 231–254. https://doi.org/10.1016/S0009-2541(01)00363-1

Polat, A., Hofmann, A.W., 2003. Alteration and geochemical patterns in the 3.7-3.8 Ga Isua greenstone belt, West Greenland. Precambrian Res. 126, 197–218. https://doi.org/10.1016/S0301-9268(03)00095-0

Pourmand, A., Dauphas, N., Ireland, T.J., 2012. A novel extraction chromatography and MC-ICP-MS technique for rapid analysis of REE, Sc and Y: Revising CI-chondrite and Post-Archean Australian Shale (PAAS) abundances. Chem. Geol. 291, 38–54. https://doi.org/10.1016/j.chemgeo.2011.08.011

Puchtel IS, Blichert-Toft J, Touboul M, et al (2016) The coupled 182W-142Nd record of early terrestrial mantle differentiation. Geochem Geophys Geosystems 17:2168–2193. doi: 10.1002/2016GC006324

Raczek, I., Stoll, B., Hofmann, A.W., Jochum, K.P., 2001. High-precision trace element data for the USGS reference materials BCR-1, BCR-2, BHVO-1, BHVO-2, AGV-1, AGV-2, DTS-1, DTS-2, GSP-1 and GSP-2 by ID-TIMS and MIC-SSMS. Geostand. Newsl. 25, 77–86. https://doi.org/10.1111/j.1751-908X.2001.tb00789.x

Rehkämper, M., Gärtner, M., Galer, S.J.G., Goldstein, S.L., 1996. Separation of Ce from other rare-earth elements with application to Sm-Nd and La-Ce chronometry. Chem. Geol. 129, 201–208.

Richard, P., Shimizu, N., Allègre, C.J., 1976. $^{143}Nd/^{146}Nd$, A natural Tracer: An Application to Oceanic Basalts. Earth Planet. Sci. Lett. 31, 269–278.

Rizo H., Boyet M., Blichert-Toft J. and Rosing M. (2011) Combined Nd and Hf isotope evidence for deep-seated source of Isua lavas. Earth Planet. Sci. Lett. 312, 267–279. doi: 10.1016/j.epsl.2011.10.014

Rosing, M.T., Rose, N.M., 1993. The role of ultramafic rocks in regulating the concentrations of volatile and non-volatile components during deep crustal metamorphism. Chem. Geol. 108, 187–200. https://doi.org/10.1016/0009-2541(93)90324-C

Saji, N.S., Wielandt, D., Paton, C., Bizzarro, M., 2016. Ultra-high-precision Nd-isotope measurements of geological materials by MC-ICPMS. J. Anal. At. Spectrom. 31, 1490–1504. https://doi.org/10.1039/c6ja00064a

Salters, V.J.M., Stracke, A., 2004. Composition of the depleted mantle. Geochemistry, Geophys. Geosystems 5, 1–27. https://doi.org/10.1029/2003GC000597

Savage, P.S., Moynier, F., 2013. Silicon isotopic variation in enstatite meteorites: Clues to their origin and Earth-forming material. Earth Planet. Sci. Lett. 361, 487–496. https://doi.org/10.1016/j.epsl.2012.11.016

Schatz, H., Aprahamian, A., Göres, J., Wiescher, M., Rauscher, T., Rembges, J.F., Thielemann, F.K., Pfeiffer, B., Möller, P., Kratz, K.L., Herndl, H., Brown, B.A., Rebel, H., 1998. Rp-Process Nucleosynthesis At Extreme Temperature and Density Conditions. Phys. Rep. 294, 167–263. https://doi.org/10.1016/S0370-1573(97)00048-3

Schatz, H., Aprahamian, A., Barnard, V., Bildsten, L., Cumming, A., Ouellette, M., Rauscher, T., Thielemann, F.K., Wiescher, M., 2001. Endpoint of the rp process on accreting neutron stars. Phys. Rev. Lett. 86, 3471–3474. https://doi.org/10.1103/PhysRevLett.86.3471

Schneider, K.P., Hoffmann, J.E., Boyet, M., Münker, C., Kröner, A., 2018. Coexistence of enriched and modern-like ^{142}Nd signatures in Archean igneous rocks of the eastern Kaapvaal Craton, southern Africa. Earth Planet. Sci. Lett. 487, 54–66. https://doi.org/10.1016/j.epsl.2018.01.022

Schneider, K.P., Hoffmann, J.E., Münker, C., Patyniak, M., Sprung, P., Roerdink, D., Schönberg, D.G., Kröner, A., 2019. Petrogenetic evolution of metabasalts and metakomatiites of the lower Onverwacht Group, Barberton Greenstone Belt (South Africa). Chem. Geol. 511, 152–177. https://doi.org/10.1016/j.chemgeo.2019.02.020

Schoene, B., de Wit, M.J., Bowring, S.A., 2008. Mesoarchean assembly and stabilization of the eastern Kaapvaal craton: A structural-thermochronological perspective. Tectonics 27, 1–27. https://doi.org/10.1029/2008TC002267

Schoene, B., Dudas, F.O.L., Bowring, S.A., de Wit, M., 2009. Sm-Nd isotopic mapping of lithospheric growth and stabilization in the eastern Kaapvaal craton. Terra Nov. 21, 219–228. https://doi.org/10.1111/j.1365-3121.2009.00877.x

Schulz, T., Münker, C., Peters, S.T.M., 2013. P-Process ^{180}W anomalies in iron meteorites: Nucleosynthetic versus non-nucleosynthetic origins. Earth Planet. Sci. Lett. 362, 246–257. https://doi.org/10.1016/j.epsl.2012.11.009

Shimizu, H., Tanaka, T., Masuda, A., 1984. Meteoritic ^{138}Ce/^{142}Ce ratio and its evolution. Nature 307, 251–252.

Shimizu, H., Nakai, S., Tasaki, S., Masuda, A., Bridgwater, D., Nutman, A.P., Baadsgaard, H., 1988. Geochemistry of Ce and Nd isotopes and REE abundances in the Amitsoq gneisses, West Greenland. Earth Planet. Sci. Lett. 91, 159–169.

Shimizu, H., Umemoto, N., Masuda, A., Appel, P.W.., 1990. Sources of iron-formations in the archean isua and malene supracrustals, West Greenland: Evidence from La-Ce and Sm-Nd isotopic data and REE abundances. Geochim. Cosmochim. Acta 54, 1147–1154. https://doi.org/10.1016/0016-7037(90)90445-Q

Shimizu, H., Sawatari, H., Kawata, Y., Dunkley, P.N., Masuda, A., 1992. Ce and Nd isotope geochemistry on island arc volcanic rocks with negative Ce anomaly : existence of sources with concave REE patterns in the mantle beneath the Solomon and Bonin island arcs. Contrib Miner. Pet. 110, 242–252.

Shimizu, H., Lee, S.-G., Masuda, A., Mamoru, A., 1996. Geochemistry of Nd and Ce isotopes and REE abundances in Precambrian orthogneiss clasts from the Kamiaso conglomerate, central Japan. Geochem. J. 30, 57–69.

Shirey, S.B., Kamber, B.S., Whitehouse, M.J., Mueller, P.A., Basu, A.R., 2008. A review of the isotopic and trace element evidence for mantle and crustal processes in the Hadean and Archean: Implications for the onset of plate tectonic subduction. Geol. Soc. Am. Spec. Pap. 440 2440, 1–29. https://doi.org/10.1130/2008.2440(01)

Smithies, R.H., 2000. The Archaean tonalite-trondhjemite-granodiorite (TTG) series is not an analogue of Cenozoic adakite. Earth Planet. Sci. Lett. 182, 115–125. https://doi.org/10.1016/S0012-821X(00)00236-3

Sonzogni, A.A., 2003. Nuclear Data Sheets for A = 138 *. Nucl. Data Sheet 98, 515–664.

Spandler, C., Pirard, C., 2013. Element recycling from subducting slabs to arc crust: A review. Lithos 170–171, 208–223. https://doi.org/10.1016/j.lithos.2013.02.016

Stracke, A., Palme, H., Gellissen, M., Münker, C., Kleine, T., Birbaum, K., Günther, D., Bourdon, B., Zipfel, J., 2012. Refractory element fractionation in the Allende meteorite: Implications for solar nebula condensation and the chondritic composition of planetary bodies. Geochim. Cosmochim. Acta 85, 114–141. https://doi.org/10.1016/j.gca.2012.02.006

Sun, S.S., 1980. Lead Isotopic Study of Young Volcanic Rocks from Mid-Ocean Ridges, Ocean Islands and Island Arcs. Philos. Trans. R. Soc. London Ser. A, 297, 409–445.

Stern, R.A., Bleeker, W., 1998. Age of the world's oldest rocks refined using Canada's SHRIMP: the Acasta Gneiss Complex, Northwest Territories, Canada. Geosci. Canada.

Tanaka., T., A., Masuda, 1982. The La-Ce geochronometer: A new dating method. Nature 300, 515–518.

Tanaka, T., Shimizu, H., Kawata, Y., Masuda, A., 1987. Combined La-Ce and Sm-Nd isotope systematics in petrogenetic studies. Nature 327, 113–117.

Tanimizu, M., 2000. Geophysical determination of the ^{138}La β^- decay constant. Phys. Rev. 62, 140–143. https://doi.org/10.1103/PhysRevC.62.017601

Tanimizu, M., Tanaka, T., 2002. Coupled Ce – Nd isotope systematics and rare earth elements differentiation of the moon. Geochim. Cosmochim. Acta 66, 4007–4014.

Tatsumoto, M., 1978. Isotopic Composition of Lead In Oceanic Basalt and Its Implication to Mantle Evolution. Earth Planet. Sci. Lett. 38, 63–87.

Tazoe, H., Obata, H., Gamo, T., 2007. Determination of cerium isotope ratios in geochemical samples using oxidative extraction technique with chelating resin. J. Anal. At. Spectrom. 22, 616. https://doi.org/10.1039/b617285g

Tazoe, H., Obata, H., Gamo, T., 2011. Coupled isotopic systematics of surface cerium and neodymium in the Pacific Ocean. Geochemistry, Geophys. Geosystems 12, 1–14. https://doi.org/10.1029/2010GC003342

Thirlwall, M.F., 1991. Long-term reproducibility of multicollector Sr and Nd isotope ratio analysis. Chem. Geol. 94, 85–104. https://doi.org/10.1016/S0009-2541(10)80021-X

Valley JW, Cavosie AJ, Ushikubo T, et al (2014) Hadean age for a post-magma-ocean zircon confirmed by atom-probe tomography. Nat Geosci 7:219–223

van Schijndel, V., Stevens, G., Zeh, A., Frei, D., Lana, C., 2017. Zircon geochronology and Hf isotopes of the Dwalile Supracrustal Suite, Ancient Gneiss Complex, Swaziland: Insights into the diversity of Palaeoarchaean source rocks, depositional and metamorphic ages. Precambrian Res. 295, 48–66. https://doi.org/10.1016/j.precamres.2017.04.025

Van Schmus, W.R., Wood, J.A., 1967. A chemical-petrologic classification for the chondritic meteorites. Geochim. Cosmochim. Acta 31, 747–765.

Vervoort, J.D., Patchett, P.J., Gehrels, G.E., Nutman, A.P., 1996. Constraints on early Earth differentiation from hafnium and neodymium isotopes. Nature 379, 624–627. https://doi.org/10.1038/379624a0

Vervoort, J.D., Blichert-Toft, J., 1999. Evolution of the depleted mantle: Hf isotope evidence from juvenile rocks through time. Geochim. Cosmochim. Acta 63, 533–556. https://doi.org/10.1007/978-94-007-7365-3_5

Warren, P.H., 2011. Stable-isotopic anomalies and the accretionary assemblage of the Earth and Mars: A subordinate role for carbonaceous chondrites. Earth Planet. Sci. Lett. 311, 93–100. https://doi.org/10.1016/j.epsl.2011.08.047

Weisberg, M.K., McCoy, T.J., Krot, A.N., 2006. Systematics and Evaluation of Meteorite Classification. Meteorites early Sol. Syst. II 19–52.

White, W.M., Patchett, J., 1984. HfNdSr isotopes and incompatible element abundances in island arcs: implications for magma origins and crust-mantle evolution. Earth Planet. Sci. Lett. 67, 167–185. https://doi.org/10.1016/0012-821X(84)90112-2

Willbold, M., 2007. Determination of Ce isotopes by TIMS and MC-ICPMS and initiation of a new, homogeneous Ce isotopic reference material. J. Anal. At. Spectrom. 22, 1364. https://doi.org/10.1039/b705306a

Wilde, S.A., Valley, J.W., Peck, W.H., Graham, C.M., 2001. Evidence from detrital zircons for the existence of continental crust. Nature 409, 175–178. https://doi.org/10.1038/35051550

Willig, M., Stracke, A., 2019. Earth's chondritic light rare earth element composition: Evidence from the Ce–Nd isotope systematics of chondrites and oceanic basalts. Earth Planet. Sci. Lett. 509, 55–65. https://doi.org/10.1016/j.epsl.2018.12.004

Winchester, J.A., Floyd, P.A., 1977. Geochemical discrimination of different magma series and their differentiation products using immobile elements. Chem. Geol. 20, 325–343. https://doi.org/10.1016/0009-2541(77)90057-2

Wood, B.J., Smythe, D.J., Harrison, T., 2019. The condensation temperatures of the elements: A reappraisal. Am. Mineral. 104, 844–856. https://doi.org/10.2138/am-2019-6852CCBY

Xiao, Y.K., Liu, W.G., Zhou, Y.M., 1994. Precise measurement of the isotopic composition of cerium and its atomic weight. Int. J. Mass Spectrom. Ion Process. 136, 181–189. https://doi.org/10.1016/0168-1176(94)04014-1

Yokoyama, T., Walker, R.J., 2016. Nucleosynthetic isotope variations of siderophile and chalcophile elements in the solar system. Rev. Mineral. Geochemistry 81, 107–160. https://doi.org/10.2138/rmg.2016.81.03

Zambardi, T., Poitrasson, F., Corgne, A., Méheut, M., Quitté, G., Anand, M., 2013. Silicon isotope variations in the inner solar system: Implications for planetary formation, differentiation and composition. Geochim. Cosmochim. Acta 121, 67–83. https://doi.org/10.1016/j.gca.2013.06.040

Zeh, A., Gerdes, A., Millonig, L., 2011. Hafnium isotope record of the Ancient Gneiss Complex, Swaziland, southern Africa : evidence for Archaean crust-mantle formation and crust

reworking between 3.66 and 2.73 Ga. J. Geol. Soc. London. 168, 953–963. https://doi.org/10.1144/0016-76492010-117.

Danksagung

Es gibt sehr viele Personen, denen ich an dieser Stelle danken möchte. Ohne euch wäre diese Arbeit gar nicht möglich gewesen.

Zuerst möchte ich mich bei meinen Doktorvätern Carsten und Erik danken. Bei Carsten möchte ich mich bedanken, dass du bereit warst einer Chemikerin Kosmochemie und Geologie beizubringen. Vielen Dank für diese Möglichkeit. Bei beiden möchte ich mich für die Unterstützung und die vielen Diskussionen in den letzten Jahren bedanken.

Bei meinen Kollegen möchte ich mich bedanken. Die Arbeit im Reinraumlabor wäre ohne euch viel langweiliger gewesen. Einen besonderen Dank gelten Bo und Julia, die immer ein offenes Ohr für meine kosmochemischen und geologischen Fragen hatten und zusätzlich möchte ich beiden für die moralische Unterstützung der letzten Jahre danken. Ninja möchte ich für die angenehme Bürozeit und den vielen netten Diskussionen danken. Bei Eric möchte ich mich für die Laborvertretung während meiner Schwangerschaft bedanken. Der Wahnsinnsplan ist geschafft. Uwe möchte ich gerne für die besondere moralische Unterstützung der letzten Jahre, aber auch für die handwerkliche Unterstützung danken.

Bei allen Mitarbeitern des Instituts für Geologie und Mineralogie möchte ich mich für die nette Arbeitsatmosphäre bedanken.

Zum Schluss möchte ich mich bei meiner Familie und meine Freunden bedanken. Meinen Eltern möchte ich dafür danken, dass sie mir mein Studium ermöglicht haben und mich immer unterstützt haben. Meiner restlichen Familie möchte sehr gerne für die Unterstützung danken. Meinem Mann Björn möchte ich für die Unterstützung und die vielen Diskussionen danken. Meiner Tochter Elisabeth Sophie möchte ich für die Ablenkung nach einem stressigen Arbeitstag danken. Meinen Freunden in Köln möchte ich danken, dass ihr mich aufgenommen habt und dazu beigetragen habt, dass ich mich in Köln heimisch fühle. Meinen Freundinnen Theresa, Christine und Martina möchte ich für die langjährige Freundschaft und Unterstützung danken.

Appendix

4.7. Appendix A

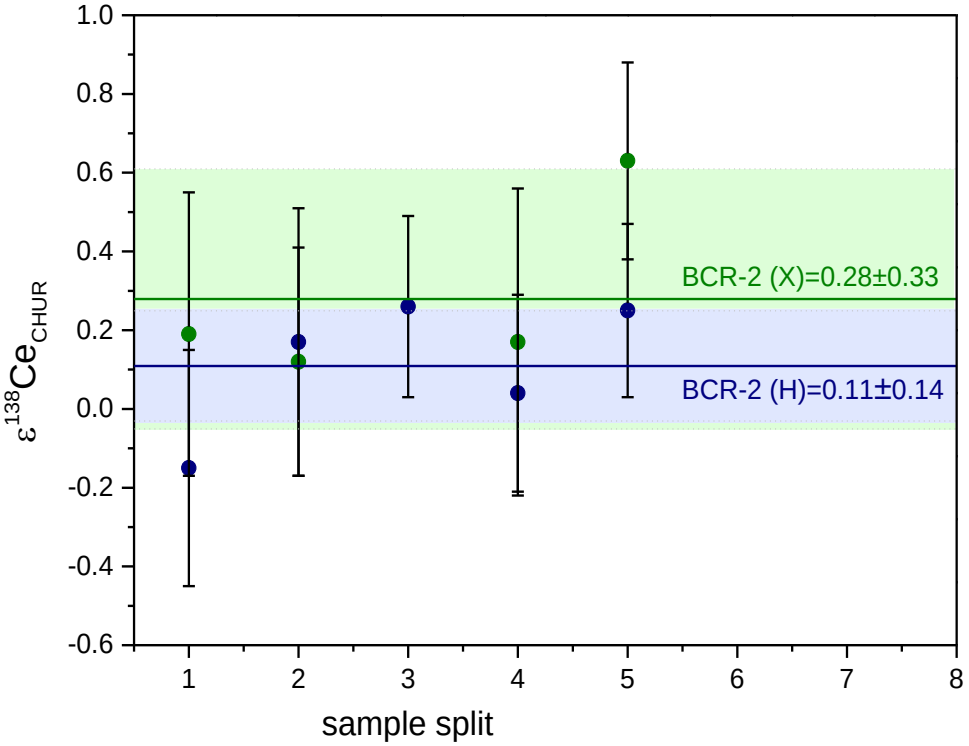

Figure 38 Cerium isotope ratios obtained for rock standard BCR-2. The results are expressed in $\varepsilon^{138}Ce$ relative to CHUR (Bellot et al. (2015)[3]). The mean value for the 5 BCR-2 samples using a standard Ni sample cone and a H-type skimmer cone is analytically indistinguishable from the mean value for the 4 BCR-2 samples using a standard Ni sample cone and a X-type skimmer cone.

Table 15 Typical MC-ICP-MS instrument operating conditions during Ce isotope ratio measurements

Operation power [W]	1200
Sample gas flow rate [L/min]	0.9
Auxiliary gas flow rate [L/min]	0.7
Cooling gas flow rate [L/min]	15
Nebulizer	100µL/min MicroFlow PFA
ARIDUS II™ sweep gas flow rate [L/min]	5.6
ARIDUS II™ nitrogen gas flow rate [L/min]	0.06

Table 16 Effects of interfering Ba, Ce and Nd on the accuracy of measured $\varepsilon^{138}Ce$ and $\varepsilon^{142}Ce$ values. Analyses were performed using a 600 ppb JMC-304 solution doped with variable amounts of the interfering elements Ba, La and Nd.

ratio	$\varepsilon^{138}Ce$	$\varepsilon^{142}Ce$
$^{137}Ba/^{140}Ce$		
4.22E-06	0.17±0.23	
2.45E-05	0.78±0.31	
1.18E-04	4.20±0.38	
2.33E-04	8.42±0.35	
1.17E-03	41.05±1.11	
$^{139}La/^{140}Ce$		
2.37E-04	-0.25±0.35	
1.72E-03	-0.28±0.38	
1.91E-02	-0.08±0.39	
9.50E-02	1.22±0.44	
1.96E-01	4.02±0.27	
$^{144}Nd/^{140}Ce$		
5.00E-06		-0.19±0.17
2.48E-05		-0.12±0.14
2.54E-04		-0.23±0.17
6.18E-03		-1.37±0.19
1.34E-02		-2.57±0.19
2.60E-02		-4.93±0.25
5.18E-02		-9.65±0.20

*Table 17 Results for long term Ce isotope measurements of (i) Cologne-AMES and (ii) Mainz-AMES. The weighted means of ε138Ce are +0.83±11ppm for Cologne-AMES and +2.61±9ppm for Mainz-AMES (all 2 r.s.d). *measurement session, where data were collected using an X-s skimmer cone.*

Standard	number of measurements	Session	$\varepsilon^{138}Ce$ (JMC-304)	2 r.s.e [ppm]
Cologne-AMES	3	Session 1	0.67	0.16
	3	Session 2	0.89	0.04
	3	Session 3	0.98*	0.04
	2	Session 4	0.76	0.03
	2	Session 5	1.11	0.13
	4	Session 6	0.99	0.28
	11	Session 7	0.76	0.11
	15	Session 8	0.54	0.09
	15	Session 9	0.67	0.07
	15	Session 10	0.77	0.08
Mainz-AMES	3	Session 1	2.66	0.12
	3	Session 2	2.57	0.04
	3	Session 3	2.67*	0.15
	2	Session 4	2.54	0.07
	3	Session 5	2.83	0.29
	3	Session 6	2.61	0.18
	11	Session 7	2.46	0.14

Table 18 Results of repeated measurements of the absolute $^{138}Ce/^{136}Ce$ ratio of the Mainz-AMES standard. In our study, the $^{138}Ce/^{136}Ce$ ratios were measured using $^{136}Ce/^{140}Ce$ 0.002124072[21,36] or $^{136}Ce/^{142}Ce$=0.01688[36] as normalization ratio.

number of measurements	$^{138}Ce/^{136}Ce$ rel $^{136}Ce/^{140}Ce$	2 r.s.d [abs]	$^{138}Ce/^{136}Ce$ rel $^{136}Ce/^{142}Ce$	2 r.s.d [abs]
2	1.33732	0.00001	1.33731	0.00001
3	1.33741	0.00001	1.33759	0.00009
18	1.33736	0.00002	1.33726	0.00004
3	1.33755	0.00001	1.33767	0.00009
3	1.33759	0.00001	1.33761	0.00005
3	1.33746	0.00003	1.33746	0.00006
2	1.33759	0.00001	1.33761	0.00005
3	1.33755	0.00004	1.33736	0.00005
3	1.33749	0.00002	1.33730	0.00005
11	1.33747	0.00002	1.33730	0.00001
mean±2 r.s.e	**1.33748±0.0003**		**1.33745±0.0004**	

*Table 19 Cerium isotope results for different interface cone combinations used during MC-ICP-MS measurements. *The sample BCR-2 Batch 1 was measured 4 times in one analytical session to investigate the reproducibility of X cone combinations. Reported uncertainties correspond to 2 s.e.*

Sample	$\varepsilon^{138}Ce$(CHUR) H	2 s.e	$\varepsilon^{138}Ce$(CHUR) X	2 s.e	$\varepsilon^{138}Ce$(CHUR) J	2 s.e	$\varepsilon^{138}Ce$(CHUR) X/J	2 s.e
JG-1 Batch 1	0.06	0.21	0.19	0.22				
JA-2 Batch 1	-0.24	0.21			-0.40	0.22		
BCR-2 Batch 1	-0.07	0.26	0.09	0.20	-0.26*	0.20		
BCR-2 Batch 2	-0.22	0.22			-0.11	0.24	-0.29	0.19
BCR-1 Batch 1	-0.17	0.24	-0.41	0.30	-0.34	0.20		
BCR-1 Batch 2	-0.16	0.26					-0.54	0.20
JB-1b Batch 1	-0.78	0.21			-0.93	0.23		
AGV-1 Batch 1	-0.76	0.20	-0.62	0.20	-1.00	0.18		
AGV-1 Batch 2	-0.70	0.20					-0.86	0.19
LP-1 Batch 1	-1.32	0.24	-1.35	0.24	-1.38	0.17		
LP-1 Batch 2	-1.29	0.19					-1.20	0.24
BHVO-2 Batch 1	-1.30	0.22	-1.12	0.30	-1.56	0.22		
BHVO-2 Batch 2	-1.62	0.24					-1.71	0.19
JB-3 Batch 1	-1.57	0.22	-1.38	0.14	-1.57	0.21		
JB-1b Batch 2	-0.50	0.30					-0.56	0.23

4.8. Appendix B

Table 20 Comparison of $^{147}Sm/^{144}Nd$ and $^{143}Nd/^{144}Nd$ data for Allende, Vigarano, Chainpur and Karoonda from this study and literature data.

Meteorite	$^{147}Sm/^{144}Nd$	$^{143}Nd/^{144}Nd$	Reference
Allende (mean value) Smithsonian	0.1940±5	0.512571±13	Patchett et al. (2004), Boyet and Carlson (2005), Carlson et al. (2007), Bouvier et al. (2008)
Allende A		0.512602±8	Willig and Stracke (2019)
Allende B		0.512597±7	Willig and Stracke (2019)
Allende#1 MS	0.1942	0.512741±29	This study
Allende#2 MS	0.1944	0.512744±35	This study
Vigarano	0.1951	0.512609±10	Bouvier et al. (2008)
	0.1931	0.512596±18	This study
Chainpur	0.1956	0.512623±8	Bouvier et al. (2008)
	0.1950	0.512640±22	This study
Karoonda	0.1951	0.512602±7	Patchett et al. (2004)
	0.1948	0.512633±15	This study

Table 21 Comparison of La and Ce concentration data determined for standard reference materials and meteorites in recent studies

Sample	La[ppm]	Ce[ppm]	La/Ce	$^{138}La/^{136}Ce$	method	Ref.
BCR-2	24.8	53.5	0.4641	0.2259	MC-ICP-MS	Pourmand et al. (2012)
	19.1	43.1	0.4432	0.2157	SF-ICP-MS	Braukmüller et al. (2018)
	25.2	53.4	0.4725	0.2300	ID-MC-ICP-MS	Chapter 2
	24.9	52.9	0.4707	0.2291	ID-TIMS	Raczek et al. (2001)

Table 21 continued

Sample	La[ppm]	Ce[ppm]	La/Ce	$^{138}La/^{136}Ce$	method	Ref.
	25.1	53.1	0.4721	0.2298	database	Jochum (2016)
	24.9	53.6	0.4646	0.2261	SF-ICP-MS	Stracke et al. (2012)
BHVO-2	15.2	37.5	0.4053	0.1973	SF-ICP-MS	Barrat et al. (2012)
	15.1	38.2	0.3948	0.1921	MC-ICP-MS	Pourmand et al. (2012)
	12.0	31.8	0.3774	0.1837	SF-ICP-MS	Braukmüller et al. (2018)
	15.4	37.9	0.4053	0.1973	ID-MC-ICP-MS	Chapter 2
	15.2	37.5	0.4053	0.1971	ID-TIMS	Raczek et al. (2001)
	15.2	37.5	0.4053	0.1971	database	Jochum (2016)
	15.1	37.8	0.3995	0.1944	SF-ICP-MS	Stracke et al. (2012)
Allende	0.516	1.29	0.4000	0.1947	SF-ICP-MS	Barrat et al. (2012)
	0.548	1.374	0.3986	0.1940	MC-ICP-MS	Pourmand et al. (2012)
-Smiths.	0.471	1.21	0.3886	0.1891	SF-ICP-MS	Braukmüller et al. (2018)
-MS	0.481	1.17	0.4111	0.2001	SF-ICP-MS	
	0.486	1.24	0.3916	0.1906	SF-ICP-MS	Willig and Stracke (2019)
	0.474	1.21	0.3917	0.1907	SF-ICP-MS	
-MS	0.671	1.56	0.4312	0.2098	ID-MC-ICP-MS	This study
-MS	0.673	1.55	0.4332	0.2108	ID-MC-ICP-MS	
Nogoya	0.312	0.806	0.3871	0.1884	SF-ICP-MS	Braukmüller et al. (2018)
	0.337	0.842	0.3996	0.1945	ID-MC-ICP-MS	This study
Cold Bokkeveld	0.291	0.758	0.3839	0.1869	SF-ICP-MS	Braukmüller et al. (2018)
	0.487	0.974	0.4997	0.2432	ID-MC-ICP-MS	This study
Jbilet Winselwan	0.311	0.829	0.3752	0.1826	SF-ICP-MS	Braukmüller et al. (2018)
	0.424	1.03	0.4101	0.1996	SF-ICP-MS	Willig and Stracke (2019)
MET1070	0.295	0.768	0.3841	0.1870	SF-ICP-MS	Braukmüller et al. (2018)
	0.386	0.909	0.4252	0.2069	ID-MC-ICP-MS	This study

Table 22 used meteorites for the recommended chondrite, carbonaceous chondrite and non-carbonaceous chondrite $^{138}La/^{136}Ce$ and chondrite, carbonaceous chondrite and non-carbonaceous chondrite $^{138}Ce/^{136}Ce$ values

chondritic $^{138}La/^{136}Ce$ value	**chondritic $^{138}Ce/^{136}Ce$ value**	**carbonaceous chondrite $^{138}La/^{136}Ce$ value**	**carbonaceous chondrite $^{138}Ce/^{136}Ce$ value**	**non-carbonaceous chondrite $^{138}La/^{136}Ce$ value**	**non-carbonaceous chondrite $^{138}Ce/^{136}Ce$ value**
0.1868±40 (2. s.e)	1.33685±3 (2 s.e.)	0.1946±43 (2. s.e.)	1.33684±2 (2 s.e.)	0.1823±46 (2. s.e.)	1.33689±4 (2. s.e.)
MET01070 this study	Karoonda this study	MET01070 this study	Karoonda this study	Dimmit this study	Dimmit this study
Nogoya this study	MET01070 this study	Nogoya this study	MET01070 this study	Chainpur this study	Chainpur this study
Vigerano This study	Nogoya this study	Vigerano This study	Nogoya this study	Etter this study	Etter this study
Acfer082 this study	Cold Bokkeveld this study	Acfer082 this study	Cold Bokkeveld this study	Ramsdorf this study	Ramsdorf this study
Isna this study	Vigerano This study	Dar al Gani067 this study	Vigerano This study	EET96341 this study	EET96341 this study
Dar al Gani067 this study	Acfer082 this study	Vigerano this study	Acfer082 this study	Happy Canyon-1 this study	Happy Canyon-2 this study
Allende-MS 2x this study	Isna this study	Allende-MS 2x this study	Dar al Gani067 this study	Happy Canyon-2 this study	Saharah Bellot et al. (2015)
Dimmit this study	Dar al Gani067 this study	Isna this study	Allende-MS 2x this study	Khairpur-1 this study	Homestead Willig and Stracke (2019)
Chainpur this study	Allende-MS 2x this study	Allende A Willig and Stracke (2019)	Isna this study	Khairpur-2 this study	Indarch Willig and Stracke (2019)
Etter this study	Dimmit this study	Allende B Willig and Stracke (2019)	Allende Bellot et al. (2015)	Atlanta this study	Knyahinya Willig and Stracke (2019)
Ramsdorf this study	Chainpur this study	Murchinson Willig and Stracke (2019)		Neuschwanstein this study	Parnallee Willig and Stracke (2019)
EET96341 this study	Etter this study	Ninqiang Willig and Stracke (2019)		Homestead Willig and Stracke (2019)	Pultusk Willig and Stracke (2019)
Happy Canyon-1 this study	Ramsdorf this study	NWA6015 Willig and Stracke (2019)		Indarch Willig and Stracke (2019)	Tuxtuac Willig and Stracke (2019)
Happy Canyon-2 this study	EET96341 this study	Ornans Willig and Stracke (2019)		Knyahinya Willig and Stracke (2019)	Holbrook Willig and Stracke (2019)
Ilafegh002 this study	Happy Canyon-2 this study			Parnallee Willig and Stracke (2019)	
Atlanta this study	Ilafegh this study			Pultusk Willig and Stracke (2019)	
Neuschwanstein this study	Allende Bellot et al. (2015)			Tuxtuac Willig and Stracke (2019)	

Table 22 continued

Chondritie ^{138}**La/**^{136}**Ce value**	Chondritie ^{138}Ce/^{136}Ce value	carbonaceous chondrite ^{138}La/^{136}Ce value	carbonaceous chondrite ^{138}La/^{136}Ce value	non-carbonaceous chondrite ^{138}La/^{136}Ce value	non-carbonaceous chondrite ^{138}Ce/^{136}Ce value
Khairpur-1 this study	Saharah Bellot et al. (2015)			Holbrook Willig and Stracke (2019)	
Khairpur-2 this study					
Allende A Willig and Stracke (2019)					
Allende B Willig and Stracke (2019)					
Homestead Willig and Stracke (2019)					
Indarch Willig and Stracke (2019)					
Knyahinya Willig and Stracke (2019)					
Murchinson Willig and Stracke (2019)					
Ninqiang Willig and Stracke (2019)					
NWA6015 Willig and Stracke (2019)					
Ornans Willig and Stracke (2019)					
Parnallee Willig and Stracke (2019)					
Pultusk Willig and Stracke (2019)					
Tuxtuac Willig and Stracke (2019)					
Holbrook Willig and Stracke (2019)					

Erklärung

Ich versichere, dass ich die von mir vorgelegte Dissertation selbständig angefertigt, die benutzten Quellen und Hilfsmittel vollständig angegeben und die Stellen der Arbeit − einschließlich Tabellen, Karten und Abbildungen −, die anderen Werken im Wortlaut oder dem Sinn nach entnommen sind, in jedem Einzelfall als Entlehnung kenntlich gemacht habe; dass diese Dissertation noch keiner anderen Fakultät oder Universität zur Prüfung vorgelegen hat; dass sie − abgesehen von unten angegebenen Teilpublikationen − noch nicht veröffentlicht worden ist, sowie, dass ich eine solche Veröffentlichung vor Abschluss des Promotionsverfahrens nicht vornehmen werde. Die Bestimmungen der Promotionsordnung sind mir bekannt. Die von mir vorgelegte Dissertation ist von Prof. Dr. Carsten Münker betreut worden

Nachfolgend genannte Teilpublikationen liegen vor:

Schnabel, C., Münker, C., Strub, E., 2017. La-Ce isotope measurements by multicollector-ICPMS. J. Anal. At. Spectrom. 32, 2360–2370. https://doi.org/10.1039/c7ja00256d

Chapter 2

Appendix A

Datum Unterschrift